University of Sussex

An Experimental Investigation of Micro- and Macrocracking Mechanisms in Rocks by Freeze–Thaw Cycling

Vikram Maji

This thesis is submitted for the Degree of

Doctor of Philosophy

University of Sussex

Declaration

This thesis contains no material that has been accepted for the award of any degree in another university and, to the best of my knowledge and belief, it contains no material previously published by another person except where due reference is made in the text of the thesis.

Vikram Maji

Abstract

The fracture of rock during freezing and thawing poses a serious threat to rock slope stability and represents an important geohazard in cold regions. However, mechanistic understanding of microcracking processes, controls and rates, and the transition from micro- to macrocracking during freeze–thaw is limited. To investigate the mechanisms of cracking, two physical modelling experiments supplemented by compressive tests were performed on specimens of chalk and sandstone, monitoring and imaging micro- and macroscale deformation due to freeze–thaw cycling.

The microscale experiment repeatedly scanned two water-saturated specimens 20 mm in diameter and 30 mm high, subject to downward freezing in a climate cabinet. Successive micro-computed tomography (μ-CT) images quantified the progressive development of structure and strain during 20 freeze–thaw cycles. The macroscale experiment imposed 12 bidirectional (upward and downward) freezing cycles on three 300 mm cubic blocks over the course of 315 days, simulating an active layer above permafrost. Eight acoustic emission sensors recorded the timing, location and energy released during microcracking events, while rock temperature, surface heave and settlement, and subsurface strain were monitored continuously.

The microscale experiment generated different probability functions that correlate points, clusters and linear movements of the progressive fracture phase extracted from scanned images and showed dominantly vertical rather than horizontal microcrack growth. The macroscale experiment brecciated a chalk block near modal depths of the 0^{o}C isotherm during thaw, and indicated high tensional activity and limited shearing. Ice segregation during thawing produced more microcracking events than volumetric expansion produced during freezing. A statistical model is proposed that distinguishes the mechanism of fracture propagation during freezing and thawing.

Acknowledgements

The work presented in the thesis owes a great deal to numerous wonderful people, both professionally and personally. Firstly I would like to express my sincere gratitude to my supervisor, Prof. Julian Murton and co-supervisor Prof. Robert Prance for their guidance, support and patience. Most of all, I am grateful to Julian for understanding me and providing constant supervision throughout the journey of my PhD years. Long, energetic discussions with him have greatly expanded my knowledge, helped to develop ideas and resolve challenges or difficulties. It was a genuine pleasure to work with him and learn useful research skills.

I would like to express my gratitude to the University of Sussex for funding my doctoral studies through a Global Studies Studentship and a Chancellor's International Research Scholarship. Without this financial support, my PhD research would not have been possible.

I find myself lucky to have had the opportunity to explore the unique facility of using the Permafrost Laboratory at Sussex. Tim Cane in the Department of Geography, and James Archer and Paul O'Neil in the Sensor Technology Research Centre, Department of Engineering and Design, at Sussex kindly provided valuable help and guidance with experimental design, equipment fabrication, sensor technology and data acquisition. Barry Jackson, in Engineering at Sussex, provided assistance with electronics. Dr Simon Carr, Lucy Diggens and Michele Day at the Centre for Micromorphology, Queen Mary University, London, are thanked for providing access to micro-computing tomography and guidance about image processing and analysis. Dr Friederike Günzel at the geotechnical testing facility, University of Brighton, provided access to compressive strength testing. Dr Rhys Pullin and Dr Matthew Pearson in the Institute of Mechanical and Manufacturing Engineering at Cardiff University provided guidance about acoustic emissions and access to rock testing apparatus. Marcus Dodds, Ed Haslam and Russell Swift of the British Geological Survey, Keyworth, provided advice about acoustic emissions and strain gauges. Special thanks to my office colleagues, who have joined and left throughout the duration of my stay. And a special mention to the University of Sussex campus and Brighton city for bringing colour, diversity and happiness in PhD days.

Finally, I would like to thank my mother, family and friends for their endless support. To my late father, I hope you are seeing me from above. There is one more person to thank—my fiancé, Anita, for her continual encouragement during the ups and downs throughout the PhD life.

Contents

List of Figures

List of Tables

Chapter 1

Introduction

1.1 Motivation

According to the Circum-Arctic Map of Permafrost and Ground Ice Conditions, around one-fifth to one-fourth of the Earth's land surface area is underlain by permafrost (Brown et al., 1997). Due to the effect of global temperature rise, an estimated 25–44% retreat of permafrost is expected during the next century according to some models (Anisimov and Nelson, 1996; Grosse et al., 2016) that consider a 2°C increase in the mean annual air temperature. Degradation of permafrost is considered as one of the "striking environmental changes in the middle Holocene" (Prager et al., 2008) that caused abundant rock slope failure activity in the Italian Dolomites, the Tyrolean Alps, the Bavarian Alps, and the Swiss Central Alps (Jerz, 1999; Soldati et al., 2004; Tinner et al., 2005). With continued climate warming, the degradation of permafrost increases the risk of geohazards in alpine environments due to extensive rock fall activity and slow deformation of rock. Such hazards pose a serious threat to infrastructure constructed on permafrost rocks (Krautblatter et al., 2013). Specifically, cracking and melt of ice within cracks may damage structures such as dams, bridges, roads and pipelines developed on porous rocks containing permafrost as many of the structures were not designed to cope with stability problems arising from degrading permafrost.

A number of experimental investigations have been conducted on frost-susceptible soils and rocks subject to various freeze-thaw regimes (Penner, 1986; Harris, 1996; Matsuoka, 2001; Harris et al., 2007) in order to obtain mechanistic understanding of cryogenic processes and their controlling factors (e.g. Harris et al., 2008). Factors such as coupled heat transfer, moisture migration and force balance, accompanied by the change in pore water pressure due to phase change, were principally considered to develop a thermo-hydro-mechanical model (Rempel 2007, 2010, 2011; Thomas et al., 2009). Murton et al. (2001, 2006, 2016a, 2016b) conducted several freeze-thaw experiments on limestone (chalk) by simulating natural permafrost conditions, producing a brecciated layer at the base of the active layer and the top of the permafrost. Upward freezing due to the dominance of the ice-segregation process can form propagating ice-filled fractures that might act as a slip plane during thawing (Matsuoka and Murton, 2008). Changes in the temperature gradient modify both the mechanical properties of

rock (compressive and tensile strength) and ice (creep and cohesion). Krautblatter et al. (2013) illustrated how the present dynamic nature of permafrost triggered rock slope instability due to increasing shear stresses and reducing shear resistance. The repetitive action of alternating freezing and thawing cycles imparts an effect similar to fatigue-induced failure (Jia et al., 2015).

The present study investigates the major factors that influence the initiation and development of fractures in porous sedimentary rocks by simulating natural freezing and thawing in controlled laboratory experiments. Two different rock types are considered (limestone and sandstone). The experiments were designed in three phases. The first phase evaluated the mechanical properties of unfrozen specimens under compressive testing. The second test analysed microstructure development due to repetitive freeze–thaw cycles using repeat scans generated by micro-computed tomography (μ-CT). The third experiment used highly sensitive sensors to quantify the various thermal and mechanical stimuli that induce micro- and macrocracking during freezing and thawing.

1.2 Research problems and gaps

During cooling of water-saturated rocks at sub-zero temperature, the processes of volumetric expansion and ice segregation are thought to operate at varying locations, times and magnitudes (Walder and Hallet, 1985; Matsuoka, 1990). As liquid water changes phase during freezing it expands in volume. Additionally, ice lenses sometimes form and grow in size, slowly building up pressure that can trigger reactivation of pre-existing slope failures (Matsuoka, 2001; Harris et al., 2007), develop new cracks, heave the ground surface and slowly degrade the rock mass (Jia et al., 2015). However, the mechanistic understanding of micro- and macrocracking within rocks as a consequence of volumetric expansion and ice segregation is limited because it involves a complex integration of the thermal–hydraulic–mechanical balance (Rempel, 2007, 2010, 2011; Thomas et al., 2009). To increase such understanding requires further experimental investigation to evaluate the existing models. Various factors that interplay with the thermodynamic equilibrium during repeated freezing and thawing are difficult and expensive to monitor in the field over long periods appropriate to investigate crack initiation and development. Moreover, it is often complex in the field to isolate the effect of any single parameter on the processes of cracking.

Several research gaps can be identified that physical experiments on rock freezing and thawing can help to address. First, with rising global temperature, it is important to simulate in a laboratory experiment the consequences of increasing active-layer depth in order to assess

temperature-induced damage within bedrock. This has direct relevance to geomorphic systems where frost-susceptible bedrock occurs at or near the ground surface as well as to infrastructure built on such bedrock.

Second, recent frost-weathering experiments have focussed on the development of horizontal to subhorizontal cracks and their relationship to ice segregation (e.g. Murton et al., 2006). Little has been discussed about vertical or subvertical cracks in rock. The initiation and growth of vertical cracks has been proven during some freezing experiments on frost-susceptible soil (Arenson et al., 2008) but their characteristics and relationship with water migration require detailed investigation. No freezing experiments to date have sought to elucidate vertical cracking in rock.

Third, acoustic emission (AE) activity has been measured during stable thermal boundary conditions in rock freezing experiments (Hallet et al., 1991). Now it is timely to analyse changes in AE under dynamic thermal boundary conditions that better simulate natural field conditions. As dynamic freezing experiments involve changes in temperature gradients, temperature-induced strain is difficult to separate from mechanical strain produced by ice.

Fourth, digitised time series imaging requires assessing progressive fracture development. The lineal path function has been used in material science to define the linearity of a phase within a material containing multiple other phases (Torquato, 2002). What is needed in experimental studies of frost weathering is to track changes in linear relationships of a developing fracture phase after different numbers of freezing cycles.

Fifth, the properties of empty cracks and cracks filled with other material vary under compressive loading. Experimental studies conducted on rocks containing single hole or multiple hole arranged in an array to infer the behaviour of cracking (Wong et al., 2006; Lin et al., 2015). Now it is timely to investigate the crack propagation mechanisms when fracture is obstructed by an infilled hole of different composition to the surrounding material.

1.3 Hypotheses

The present study seeks to increase mechanistic understanding of cracking in rock at sub-zero temperature by testing several hypotheses, as set out below.

Hypothesis 1 (H1): Vertical cracks act as effective conduits for water supply towards the freezing front and ice lenses on the cold side of the frozen fringe. In addition to the vertical cracks, rocks with a distinct directional discontinuity like bedding planes can also function in a similar way to cracks.

The magnitude of thermodynamic processes operating within the thin film of water in vertically oriented cracks during freezing differs from that of cracks formed horizontally (Arenson et al., 2008). Vertical cracks in which veins of ice may later form are thought to provide passage to water migration as the permeability of the system is reduced by the formation of pore ice (Chamberlain and Gow, 1979; Konrad and Samson, 2000a; Konrad and Samson, 2000b). As transportation of water has been identified as one of the principle drivers in ice segregation and frost weathering (Taber, 1929; Gilpin, 1980; Walder and Hallet, 1985), an investigation of vertical cracks provides useful information to understand the mechanisms of frost weathering.

Hypothesis 2 (H2): Changes in active-layer depth favour the development of a new brecciated layer at a different depth within rock.

The frozen fringe is considered as an active zone of cracking in soil when ground temperature falls below the freezing point and pore water changes phase (Miller, 1972). The brecciated zone formed experimentally in chalk as a result of cracking due to ice segregation during bidirectional freezing was best developed near the base of the simulated active layer and the top of the underlying permafrost (Murton et al., 2006, 2016). Therefore, changes in active-layer depth are likely to produce multiple (or amalgamated) weak, brecciated layers that pose serious concerns for rock slope stability. In frost-susceptible soils, a newly developed brecciated layer in pre-existing slopes can act as a plane of weakness during thawing as periglacial solifluction or active-layer detachment come into operation (Matsuoka, 2001; Harris et al., 2007).

Hypothesis 3 (H3): Tension and shearing activity during cracking of rock vary during different stages of freezing and thawing.

Although the tensile strength of soil in the frozen fringe increases with decreasing temperature (Akagawa and Nishisato, 2009; Azmatch et al., 2011), cracking in the frozen fringe occurs when freezing-induced tensile stress exceeds the tensile strength of the material. It is suggested here that a growing ice lens inside a pore exerts a tensile stress that fractures rock during freezing, while melting of pore ice and ice lenses during thawing develops a potential weak slip surface that favours shearing. The existence of thin films of pre-melted unfrozen water around pore ice (Taber, 1929; Wettlaufer and Worster, 2006) reduces the coefficient of friction along the boundary contrast and makes it vulnerable to shearing.

Hypothesis 4 (H4): As the principle crack grows during freezing and thawing of rock, it bifurcates at a higher separation distance than cracks developed under compression in unfrozen rock.

Compression tests with single and multiple holes that simulate voids in rock specimens resulted in the development of wing cracks (Wong et al., 2006; Lin et al., 2015). A different fracture pattern developed in blocks of chalk subject to simulated seasonal freezing and perennial freezing (Murton et al., 2016b). Therefore, it is proposed that the separation distance at which wing cracks develop varies with the nature of stress applied and with the thermal conditions of the rock.

1.4 Aims and objectives

Aim 1 (A1): To form micro-and macrocracks in porous sedimentary rocks, primarily by simulating natural freezing conditions.

Objective 1.1 (O1.1): Design and carry out a microscale experiment in a climate cabinet, with 20 freeze–thaw cycles applied to cores of chalk and sandstone (20 mm diameter, 30mm long) and scanned repeatedly by μ-CT.

Objective 1.2 (O1.2): Design and carry out a macroscale experiment in the permafrost laboratory, with twelve cycles of bidirectional freezing (simulating an active layer above permafrost) on cubic blocks of chalk and sandstone (300 X 300 X 300 mm) equipped with sensors monitoring heave, strain, temperature and acoustic emissions (AEs).

Objective 1.3 (O1.3): Design and carry out compression tests on unfrozen specimens of chalk and sandstone to assess their mechanical properties under compression and compare the macrocracks with those induced during freezing experiments.

Aim 2 (A2): To understand mechanistically the development of freezing-induced micro cracking.

Objective 2.1 (O2.1): Quantify and analyse microstructure development in chalk and sandstone during freeze–thaw cycling by image analysis of repeated μ-CT images.

Objective 2.2 (O2.2): Estimate the progressive strain of rock cylinders from μ-CT scans.

Objective 2.3 (O2.3): Assess the probabilistic occurrence of the development of the horizontal and vertical fracture phase by applying a two-point probability function, a lineal path probability function and a two-point cluster function on the repeated μ-CT images.

Aim 3 (A3): To investigate the mechanisms and transition of micro- and macrocracking during repeated freezing and thawing.

Objective 3.1 (O3.1): Determine heave and settlement of rock during freeze–thaw cycles using linear variable differential transformers (LVDT) and strain using miniature strain gauges.

Objective 3.2 (O3.2): Determine the 3D location of individual cracking events within a chalk block using eight AE sensors, and detect and analyse waveforms emitted during these events.

Objective 3.3 (O3.3): Identify the distribution, abundance and mechanical characteristics of cracks during (a) freezing, (b) freezing to thawing transition, (c) thawing and (d) thawing to freezing transition by examining the relations between chalk freezing and the timing of cracking events captured by AE sensors.

Objective 3.4 (O3.4): Distinguish between cracking modes I and II (tension and shear) during repeated freezing and thawing by analysing waveform parameters.

Aim 4 (A4): To evaluate the influence of thermal conditions and material properties on micro- and macrocracking during freezing and thawing.

Objective 4.1 (O4.1): Determine the depth relationship between the base of the active layer (0^{o}C isotherm) and the focus of macrocracking.

Objective 4.2 (O4.2): Evaluate how the orientation of fossil fragments and voids influences the location or growth of micro- and macrocracks.

Objective 4.3 (O4.3): Examine how stratification (directional discontinuities) influences the thermal conditions and deformation of horizontally versus vertically oriented sandstone blocks.

Objective 4.4 (O4.4): Assess stress concentration near rock boundaries of contrasting density during compression tests and analyse the pattern of changes in the direction of cracking.

Aim 5 (A5): To categorize the extent of linear growth of the microfracture phase according to its probabilistic occurrence in various directions.

Objective 5.1 (O5.1): Relate the continuous linear growth of the microfracture phase along various directions by examining the information extracted from repeatedly scanned images for chalk and sandstone.

Objective 5.2 (O5.2): Determine the zones of inherent flaws, intense microcracking and weak microcracking during freezing based on the probabilistic occurrence and extent of microcracks.

Aim 6(A6): To develop a statistical model on crack propagation during freezing and thawing.

Objective 6.1 (O6.1): Construct three boundary conditions that reproduce different modes of crack propagation (unidirectional, inside–outward and outside–inward).

Objective 6.2 (O6.2): Propose a statistical model that assesses the distance and angular relationship of neighbouring cracking events arranged in their temporal order of occurrence.

Objective 6.3 (O6.3): Compare the patterns of fracture propagation for three boundary conditions with those of cracks observed and captured using AEs in chalk in the macroscale experiment.

1.5 Structure of the thesis

Chapter 1 sets out the research problem, aims and objectives and describes the rock types used in the experiments. Chapter 2 discusses some background theory, illustrating how volumetric expansion and ice segregation build up the pressure to initiate new cracks or reactivate inherited cracks. The application of acoustic emission sensing during fracturing of rock and concrete is also reviewed. Chapter 3 describes the methods adopted in three laboratory experiments. The first experiment is a destructive test to assess the material strength and fracture pattern developed under a compressive stress regime. The second experiment involves repeated μ-CT scanning of small core specimens subject to repeated freeze-thaw cycles in a temperature-controlled climate cabinet to analyse the progress of microcracking. The third experiment simulates seasonal freezing within an active layer above permafrost in cubic blocks of chalk and sandstone, and involves logging temperature, heave, strain and acoustic activity throughout the duration of the experiment. Chapter 4 reports data that visualise the growth of microcracks after repeated freeze-thaw cycles in three dimensions and analyses them using correlation probability functions. Chapter 5 describes the behaviour of the rock specimens under compression loading to illustrate the cracking pattern developed. Chapter 6 presents the results on AEs, strain, temperature and macrocracks to understand the extent of impact imposed by volumetric expansion and ice segregation on rock fracture (brecciation) mechanisms. Chapter 7 integrates and evaluates the results from chapters 4, 5, and 6 to review the aims and objectives set out in chapter 1 about the mechanisms of cracking due to sub-zero cooling. Finally, chapter 8 identifies the key conclusions and limitations from this study and outlines recommendations for future work.

1.6 Rock types

The experiments were conducted on two different types of sedimentary rock, tuffeau chalk and Ardingly Sandstone.

1.6.1 Tuffeau chalk

Tuffeau is a siliceous chalk with the proportion of $CaCO_3$ ranging from 46.5 to 54.5%, and a substantial content of detrital quartz embedded in a matrix of micrite and opal-cristobalite (Murton et al., 2000). The tuffeau is of Turonian (Upper Cretaceous) age. One block of tuffeau was obtained from Lucet Quarry, Brézé-Saint-Cyr-en-Bourg, France.

1.6.2 Ardingly Sandstone

Ardingly Sandstone is a pale coloured, fine to medium grained, poorly cemented, ripple-laminated sandstone of Lower Cretaceous age. It accumulated in non-marine depositional environment in the Wealden district of southeast England (Radley and Allen, 2012). Two blocks of Ardingly Sandstone were quarried from Philpots Quarry, West Hoathly, West Sussex (Robinson and Williams, 1976).

1.6.3 Rationale

The two rock types with different physical properties were selected to conduct the experiment for the following reasons.

The tuffeau is a fine-grained rock whose freezing behaviour is similar to frost-susceptible silt-clay sediments. Previous experiments conducted on the tuffeau reproduced a brecciated layer under a limited number of freeze-thaw cycles. The rock is naturally brecciated within a few metres of the ground surface in the Loire Valley around Saumur and Vendôme, in the Vienne Valley around Chinon.

The tuffeau is in broad terms relatively homogeneous, but contains small fragments of fossils which were used to orient the specimen for repeated scanning. The fossil fragments were also used as markers to estimate strain.

The Ardingly Sandstone is laminated and therefore contains a directional dicontinuity along the direction of the lamination. Therefore, the effect of any directional defect on cracking mechanisms can be tested.

The density and compressive strength of Ardingly Sandstone (2130 kg/m^3 and 72 MPa) are relatively high compared to the density of the tuffeau chalk (1350 kg/m^3 and 18 MPa).

Overall, therefore, the same freezing conditions can be tested on a soft frost-susceptible, relatively homogeneous chalk compared to relatively hard nonfrost-susceptible, inhomogeneous sandstone containing a directional lamination.

1.7 Novel contributions

The present study provides several novel contributions to experimental studies of rock weathering. The macroscale bidirectional freezing experiment is the first to simulate degrading permafrost in the laboratory by increasing the active-layer depth part way through the experiment. In particular, the study investigates AE responses within chalk under dynamic temperature boundary conditions. Twelve continuous freezing and thawing cycles (315 days) were performed to initiate and develop cracks in a relatively slow process compared to destructive compressive laboratory testing for the investigations of fracture. Based on the varying AE responses under bidirectional freezing, the transitions between freezing to thawing and thawing to freezing were investigated in addition to the freezing and thawing periods within the cycles. It is identified that the freeze to thaw transition period correlates with degrading permafrost. A concept of dummy strain gauge was designed in the macroscale freezing experiment to eliminate the strain effect due to changing thermal boundary condition and record only the mechanical strain.

Second, repeated micro-CT scanning was conducted on two sedimentary rocks types to assess the structural changes that resulted from unidirectional freezing and thawing. In this novel experiment, repeated imaging of the same specimen provides a time series of microstructural rock change during frost weathering. Also new was the testing of three low-order probability functions to correlate the relationships between points, clusters and linearity within the progressing fracture phase of rocks during unidirectional freezing. Out of these three probability functions, the lineal path function was identified as important in describing microstructural changes. Therefore, this function was used to further investigate changes in linearity along 49 different 3D directions on repeated micro-CT images.

A third new contribution is the comparison of fracture types developed on the same rock types during compression testing and repeated freezing and thawing. The fractures were explored based on the distance and angle at which a progressing crack bifurcates. A new statistical model is proposed to understand the mechanism of crack propagation based on the spatial interrelationship of the locations of AE hypocentres arranged in their temporal order of occurrence.

Chapter 2

Background Theory

2.1 Introduction

The aim of this chapter is to introduce some background concepts that form the basis of the work presented in the thesis. Different models that describe the frost-heave phenomenon are discussed and the equations that control heave during freezing at sub-zero temperature are set out. Also the mechanism of fracture initiation and propagation due to repeated freeze-thaw effects are explained. The sensing of acoustic emissions (AEs) during fracture events, particularly during freezing of rock and fracture of concrete, is also reviewed.

2.2 Expansion resulting from solidification

When water freezes, its volume increases by about 9%. This expansion tends to force remaining unfrozen water away from freezing sites in soil or rock. In a closed system, where unfrozen water is trapped, freezing causes pressure to build up at the ice-rock interface. This led scientists to attribute frost-induced weathering in cold-climate regions to break up of rock due to additional pressure as a consequence of volumetric expansion of water during solidification. To test this hypothesis, Taber (1929, 1930) carried out pioneering freezing experiments on soils in which he replaced water with fluid that contracts upon freezing (benzene and nitro-benzene). He observed substantial heave of the soil surface; in fact heave in excess of that which would result from volumetric expansion of freezing water. Remarkably, he noted that water moved towards, rather than away from, the freezing front, which contradicts the volumetric expansion hypothesis. From experimental observations he concluded that frost weathering requires an open system that allows unfrozen water to migrate towards the freezing front. Despite these important discoveries, some unresolved questions remained. Why does unfrozen water exist below freezing temperature between soil-ice interfaces and what mechanism(s) allows water to move towards the freezing front?

2.3 Frost heave and ice-lens formation

Frost heave signifies the upward or outward movement of the ground surface (or objects on, or in, the ground) caused by the formation of ice in the soil (van Everdingen, 2005, p. 36). Taber's experiment (1929, 1930) revealed that the role of water migrating from unfrozen regions

towards the 0° C isotherm leads to the formation of lenses of segregated ice whose growth provides the necessary force to separate the soil mass. This mechanism can heave the soil surface provided that there is sufficient water supply (Beskow, 1935). Two mathematical models established since Taber's work describe the frost-heave phenomenon: the primary frost heave or capillary model and the secondary frost heave or frozen-fringe model.

2.3.1 Primary frost heave or capillary model

The capillary model applies the Clapeyron equation at thermodynamic equilibrium in a system at temperature T and containing ice at pressure P_i and water at pressure P_w (Jackson and Chalmers, 1958; Black, 1995):

$$P_i - P_w = \frac{\rho_w}{T_m} L_f (T_m - T) \qquad (2.1)$$

where ρ_w is the density of the water, L_f is the latent heat of fusion at the freezing temperature T_m. The Clapeyron equation takes into account the pressure melting term of the ice $(\rho_w/\rho_{i-1})(P_{atm} - P_i)$ where P_{atm} is atmospheric pressure. As $P_w \rightarrow P_i$, the term becomes small and hence is neglected here.

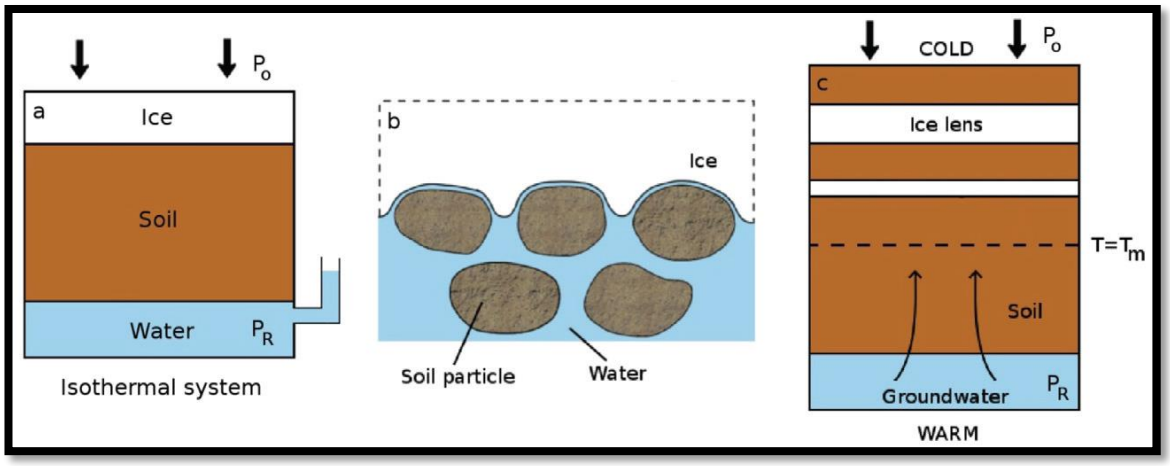

Figure 2.1. Schematic diagrams for the frost-heave process: (a) a simple isothermal model of frost heave; (b) microscopic view of the soil particles at the ice–soil interface; and (c) a typical column of soil with two ice lenses. The soil is freezing from the top downward. Source: Peppin et al. (2013).

A simple system of the frost-heave mechanism is illustrated in Figure 2.1a (Jackson and Chalmers, 1958). A layer of saturated soil is supplied by a reservoir of water at pressure P_r at the base and underlies a layer of ice, together simulating the natural freezing condition. The temperature of the frozen part of the system is $T<T_m$. Water retained within the pores is

unfrozen as the pores have narrow throats that ice cannot invade (Gibbs–Thompson effect). Figure 2.1b shows the detailed view of the ice lens-soil interface. If the ice pressure of the system is P_o (overburden pressure), then the water pressure, P_{cl} (often called the Clapeyron pressure) at equilibrium is:

$$P_{cl} = P_o - \frac{\rho_w L_f}{T_m}(T_m - T) \qquad (2.2)$$

If the reservoir pressure equals the Clapeyron pressure ($P_r = P_{cl}$), no water flows through the soil column. With constant P_o, if the temperature of the system decreases, then, following equation 2.2, the value of P_{cl} also decreases. This leads to a situation where the fluid pressure at the reservoir (P_r) exceeds the fluid pressure at the freezing front, where the ice lens forms. Water migrating towards the freezing front allows the ice to thicken, if sufficient water is available. Water flow within the soil column can be controlled either by reducing P_r or by increasing P_o. Such flow of water through the soil layer and accumulation of additional ice at the freezing front form the basic theoretical background for frost heave, referred to as the capillary theory (Smith, 1985).

Continuous supply of water is required for the ice lens to grow at the soil–ice interface, but a difficulty arises when the soil–ice interface is considered (Figure 2.1b). The only location where water can attach to the soil particles is along the pore throat as the soil particles are frozen to ice at one side. This restricts the growth of a continuous ice lens, whereas Taber (1929, 1930) suggested that a thin film of water separates the soil particle and ice surfaces, allowing water to flow around the particles and the ice lens to thicken evenly. Later research has confirmed the existence of a thin film of liquid around the soil particles caused by the molecular attraction between the particles and ice (Dash et al., 2006).

2.3.1.1 Maximum frost-heave pressure

Capillary theory is based on the assumption that ice cannot invade soil pores as temperature drops below T_m. This can be explained by the Young-Laplace equation of pressure difference along the ice-water interface (Everett, 1961):

$$P_i - P_w = \frac{2\gamma_{iw}}{r} \qquad (2.3)$$

Where γ_{iw} is the ice–water surface energy, r is the radius of ice adjacent to the pore and r_p, is the radius of pore. When $r > r_p$, ice cannot intrude the pore spaces between soil particles; it can only penetrate if $r = r_p$ while the pressure difference is large enough. Therefore the critical pressure difference required for ice entry is:

$$\Delta P_{max} = \frac{2\gamma_{iw}}{r} \qquad (2.4)$$

Combining equation 2.1 and 2.4 forms the Gibbs–Thomson equation (Everett, 1961; Jackson et al., 1966), which explains the temperature T_p at which ice penetrates soil pores:

$$T_p = T_m \left(1 - \frac{2\gamma_{iw}}{\rho_w L_f r_p}\right) \qquad (2.5)$$

Following the capillary model, when $T \leq T_p$, ice cannot further penetrate the soil pores, thereby preventing water from migrating towards the growing lens and stopping heaving the surface. This leads to estimation of the maximum frost-heave pressure, P_m while the reservoir pressure remains $\geq$ liquid pressure at the freezing front. While applying the equation to soils, it is assumed that the Laplace equation can be applicable to the pore scale:

$$P_m = P_r + \frac{2\gamma_{iw}}{r} \qquad (2.6)$$

The mechanism of frost heave can be explained well by equations 2.6 for uniform-sized particles where pressure drops at the leading edge of the warmest ice lens, and therefore draws water to accumulate ice at the leading edge, causing thickening of the ice lens and heaving the ground.

2.3.1.2 Limitations of the capillary theory

There are a number of limitations of the capillary theory. First, estimates of the maximum frost-heave pressure are in good agreement with uniformly-sized soils (Miller et al., 1960), but they become significantly larger when polydispersed soils (Loch and Miller, 1975) are considered. Second, combining the Darcy law with the capillary theory leads to estimates of the fluid flow rate (V) towards the ice lens through a soil column of uniformly-sized particles (Style and Peppin, 2012):

$$V = \frac{k}{\mu}\frac{P_R - P_f}{z_h} \qquad (2.7)$$

where k is the permeability of the frozen soil, μ is the dynamic viscosity of water, $z_h$is the distance between the ice lens and reservoir and P_f is the liquid pressure adjacent to warmest ice lens. But for frost-heave experiment, measured values of V are several orders of magnitude higher than predicted ones. Third, the significant feature of frost heave (multiple ice lenses, often within bands) cannot be explained by the capillary theory.

2.3.2 Secondary frost heave or frozen-fringe model

The secondary frost-heave model postulates that ice lenses continue to grow at temperatures below T_p i.e., after ice invades pore spaces and forms a frozen fringe (Figure 2.2). The existence of a thin film of liquid at temperatures below T_p allows slow migration of water through the

partially frozen soil (Dash et al., 2006). The thermo-molecular pressure gradient within the premelted film is considered as the driving force for fluid migration (Rempel et al., 2004).

Harlan (1973) first proposed the equation for heat and mass flow in a frozen fringe:

$$\rho_s c_{ps} \frac{\partial T}{\partial t} = \frac{\partial}{\partial z}\left(k_s \frac{\partial T}{\partial z}\right) + \rho_i L_f \frac{\partial \varphi_i}{\partial t} \qquad (2.8)$$

where P_s, c_{ps} and K_s are the density, specific heat capacity and thermal conductivity of the partially frozen soil, z is the distance from a fixed reference height, t is time and φ_i is volume fraction of ice within the pore space, where $\varphi_i + \varphi_w + \varphi_p = 1$. Equation 2.8 illustrates the diffusion of heat through the partially frozen fringe with an added term to balance the latent heat released during freezing of the liquid fraction.

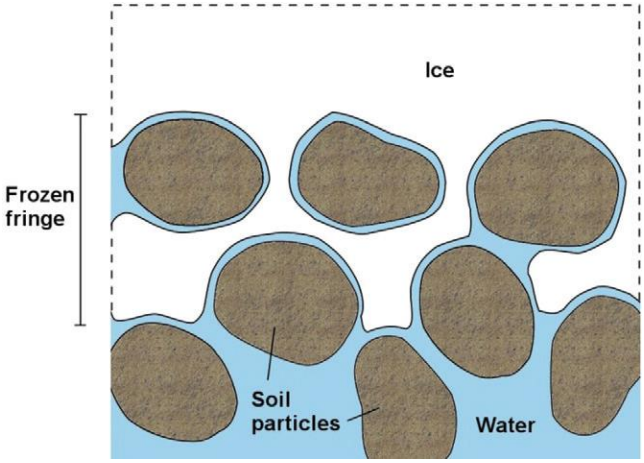

Figure 2.2. Schematic diagram of a freezing soil with a frozen fringe. Source: Peppin et al. (2013).

The frozen-fringe model explains the mechanism of continuous growth of ice lenses after ice intrudes into the pore space that was restricted due to the maximum frost-heave pressure, P_m in the capillary model. The formation of ice within pores in the frozen fringe restricts the transportation of water towards the growing lens, and therefore heave occurs slowly at temperatures far below the freezing temperature.

Miller (1977, 1978) assumed that new ice lenses form only if the effective stress between the soil particles is either zero or negative. Using the Harlan model, Miller estimated the temperature and fluid pressure at the frozen fringe and used these values to determine the ice pressure. The effective compressive stress between the soil particles becomes zero under certain conditions, leading to the formation of a new ice lens. Rempel et al. (2004) and Rempel (2007) derived an expression for fluid migration in the frozen fringe that considers fluid flow within the thin film of liquid. A force balance equation on the particles within the fringe

separates the parameter regime for the formation of a single lens, development of multiple lenses and freezing of the pore spaces without formation of any ice lenses (Figure 2.3). The diagram plots a dimensionless freezing velocity vs a dimensionless overburden pressure, where G is the ambient temperature gradient imposed on the freezing soil. Rempel estimated that three different scenarios can occur as the soil starts to freeze. The first scenario (light grey region) emphasises the formation of single ice lens (low V and P_o) in a stable manner, moving the soil particles ahead of it. The second (white region), at a higher freezing rate, results in multiple ice lenses. Third, at excessive overburden pressure, no ice lens can form. Rempel et al. (2004) also pointed out the presence of hysteresis near the separation boundaries (marked as dashed lines).

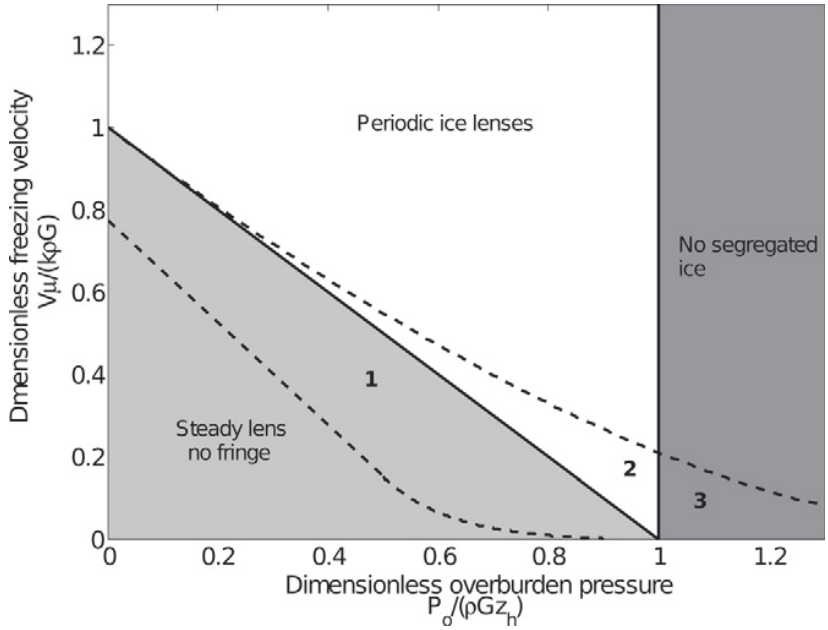

Figure 2.3. Regime diagram for soil freezing behaviour at different freezing speeds and overburden pressures P_o, modified from Rempel et al., (2004).

A fundamental question that separates the capillary and frozen fringe model is whether the ice lenses develop within a frozen fringe or whether ice lenses always form without entering the pore space.

Freezing experiments on rocks show the development of ice lenses within the frozen fringe. Water migrates into the large or small pores and microcracks within the rock. On subsequent cooling, the pore space or the microcracks lead to the development and propagation of cracks and finally fracture the rock (Walder and Hallet, 1985; Vlahou and Worster, 2010). Hallet et al.

(1991) showed that the pressure required to open new cracks and to fracture the rock is sufficiently large when the temperature decreased well below the freezing temperature.

Because the thermal characteristics of the frozen and unfrozen soil differ, Akagawa (1988) estimated the thermal conductivity of frozen soil. Soil retaining ice lenses had higher thermal conductivity relative to the unfrozen region of the soil.

2.4 Revised capillary theory

2.4.1 Deviation of maximum frost-heave pressure in polydispersed soil

The maximum heave pressure can be predicted accurately using the capillary theory only for monodispersed soils. The results deviate substantially for soils with an extended particle-size distribution. A sorting phenomenon occurs when ice grows adjacent to a soil surface to reduce the effective pore space. Therefore, larger particles tend to be incorporated within the prograding ice interface, while relatively smaller particles are excluded and accumulate ahead of the growing ice (Rempel and Worster, 1999). Thus a layer consisting of relatively small particles develops adjacent to the growing ice lens and the size of interparticle pore decreases substantially. This implies that the pore size during ice entry is relatively smaller compared to the pore size during air entry.

2.4.2 Failure of Clapeyron equation outside equilibrium

Given that the viscosity of the thin premelted film between soil–ice interfaces becomes substantial at finite freezing rates (Jackson et al., 1966), the Darcy pore pressure of the ice lens at P_f can be estimated using a generalised Clapeyron equation consisting a kinetic term:

$$P_f = P_o - \frac{\rho_w L_f}{T_m}(T_m - T) + Vf(T_m - T) \qquad (2.9)$$

where V is the growth rate of an ice lens and f is a function of temperature calculated by considering the geometry of the soil particles. The additional term in equation 2.9 quantifies how the frost-heave process depends on the size of particles.

2.4.3 Formation of periodic ice lenses

Beskow (1935) noted that the region ahead of a growing ice lens becomes progressively supercooled, therefore allowing to nucleate a new ice lens in an existing pore or flaw. He also pointed out the resemblance of fracture growth to that of ice-lens growth and hypothesised that the supercooling state ahead of a growing ice lens possibly supply the required energy to nucleate a new ice lens.

2.5 Frost-induced fracturing of rocks

During winter nearly half of the Earth's land surface experiences sub-zero temperatures. In addition to thermal expansion and contraction due to temperature changes, freeze–thaw cycles in moist rocks play an important role on physical weathering of rocks (Yang and Chen, 2004). Water-to-ice phase transition and its impact on brittle rock degradation are reflected by the propagation of cracks under freezing-induced pressure.

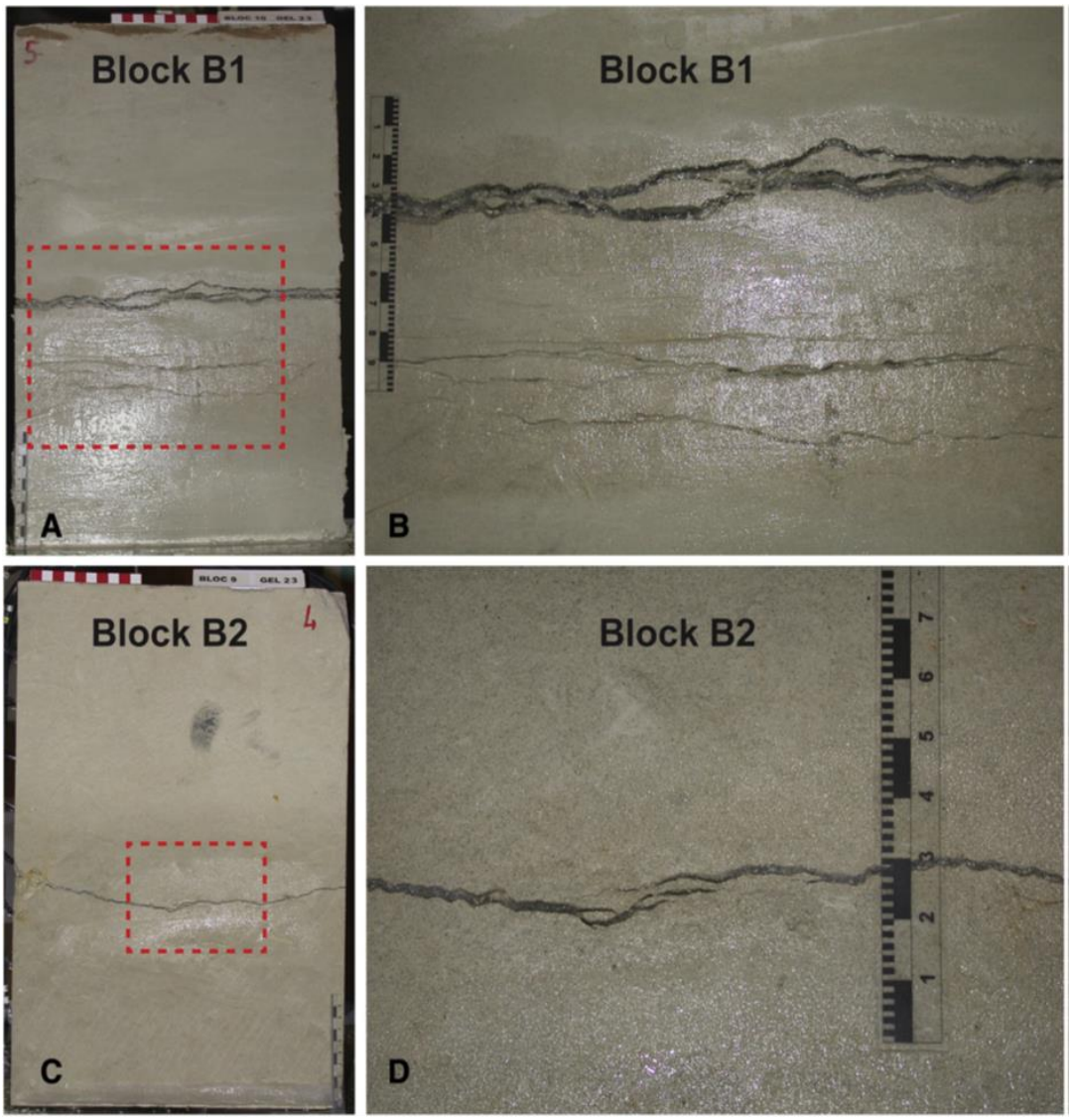

Figure 2.4. Macrocrack networks formed in tuffeau chalk at the end of a bidirectional freezing experiment. The blocks are frozen and the cracks are filled with segregated ice. Scales in centimetres. Source: Murton et al. (2016b).

Experimental observations in soils show that considerable frost heave occurs when ice lenses push soil particles apart and continue to thicken if sufficient supply of water is available (sections

2.2–2.4). Frost-induced fracture in frost-susceptible rocks follows the same principle as frost heave in soils, where the ice-filled pores and cavities within rocks resemble pore ice and ice lenses in soils (Hallet et al., 1991). The early assumption to explain frost weathering in rocks was the volumetric expansion of water by 9% during freezing, as extensively used in soil science. The volumetric expansion theory can apply to rocks where there are no further spaces available for water to escape within cracks or pore spaces during freezing, which causes the pressure to build up (Taber, 1929; Matsuoka, 1990).

That water expands in volume by 9% on freezing requires a minimum level of saturation about 91% to increase pressure within the pore spaces of rock. Otherwise the water would simply move into air-filled spaces within pores and cracks, and a raise in pressure due to volume expansion of water would not develop. One freezing experiment, however, showed that the saturation level did not exceed 65% when fracturing began in chalk (Murton et al., 2006). During intense freezing, fracturing of the chalk occurred in short bursts due to the immediate effect of volumetric expansion (Murton et al., 2016b). This experiment also suggested, from measurement of gradual and small amounts of heave of the rock surface, that microcracking activity and ice segregation occurred during thawing periods, when the active layer was at or close to its maximum depth.

Recent studies have introduced the concept of ice segregation, where ice-filled pores or cavities in rocks function in a similar role to ice lenses in soils (Walder and Hallet, 1985; Murton et al., 2006). The concept is strengthened by the fact that thin and interconnected films of water around mineral particles exist at sub-zero temperature (Dash et al., 2006), and some of this water migrates towards the freezing front (Fukuda, 1983). As reviewed by Matsuoka & Murton (2008), a temperature gradient in frozen rocks builds up a suction pressure in the unfrozen water films, which draws water towards freezing sites. Rempel et al. (2004) discussed the flow of unfrozen water triggered by disjoining pressure at ice–rock interfaces that initiate suction within the premelted films of water, and developed a model for growth of multiple ice lenses (Rempel et al., 2007). Freeze–thaw experiments on rocks simulating a permafrost table beneath an active layer produced intense brecciation and abundant segregated ice (Figure 2.4) at the upper part of the simulated permafrost and the basal part of the active layer (Murton et al., 2000, 2001, 2016a, 2016b).

2.6 Acoustic emission sensing

Acoustic Emission (AE) sensing has been extensively used both in engineering and earth sciences to detect the mechanism of cracking in heterogeneous material under various stress

configurations. During cracking, material experiences irreversible changes in its internal structure that cause sudden release of strain energy in the form of elastic waves that propagate through the material and are captured by the piezoelectric AE sensors (Hardy, 2003).Such capturing of AE events may record the formation of new microcracks or the opening, closing or sliding of pre-existing cracks.

The AE technique has been successfully implemented on rocks both in the laboratory (Scholz, 1968a, 1968b; Lockner et al., 1991; Hallet et al., 1991) and field (Amitrano et al., 2012; Collins et al., 2018). The behaviour of materials and structures can be monitored over a long period of time without moving any of the components of AE sensors (Grosse & Ohtsu, 2008).

Despite the extensive use of AE, the mechanism of cracking is poorly understood because of the complexity involved in fracturing. When materials fail under constant loading or compression, the transition from stable nucleation to unstable dynamic movement is manifested by the sudden increase in the fracture propagation rate before final rupture (Lockner et al., 1991). On the other hand, fractures induced during freezing and thawing develop slowly compared to fractures developed under compression. Therefore, freezing-induced fracture provides more complex information on understanding the mechanisms of cracking. There is still a requirement to understand the mechanisms of fracture nucleation and propagation within rocks under dynamic freezing and thawing conditions.

2.6.1 Acoustic emission in fracture detection

Following the similarities between fault-induced earthquakes and strike-slip friction (Brace and Bayerlee, 1966), AE methods were implemented in the laboratory to investigate the failure mechanism (Scholz, 1968a, 1968b). The rates of occurrence of microcracking in a rock were monitored using AE sensing in a triaxial experiment. The AE rate increased rapidly at 90% of the peak strength of the material (Scholz, 1968a). Scholz (1968b) also noted that microcracks coalesced with each other along an eventual fault plane.

The use multiple AE sensors in appropriate structural arrays provides useful information about the location of microcracking and damage accumulation during deformation within rocks (Duca et al., 2014). The mechanisms of crack nucleation and propagation under quasi-static conditions in the laboratory were explained by Lockner et al. (1991). A triaxial compression test was conducted on Westerly granite of 76.2 mm in diameter under constant confining pressure to prevent unstable fracture growth. As shown in the Figure 2.5, AE locations were scattered throughout the specimen at the beginning of the loading. Near the point of peak load, clustering of the AE locations was observed near the edge of the specimen. The cracking activity then

quasi–statically shifted from the scattered nucleation sites to an intense region of activity that gradually developed the plane of failure.

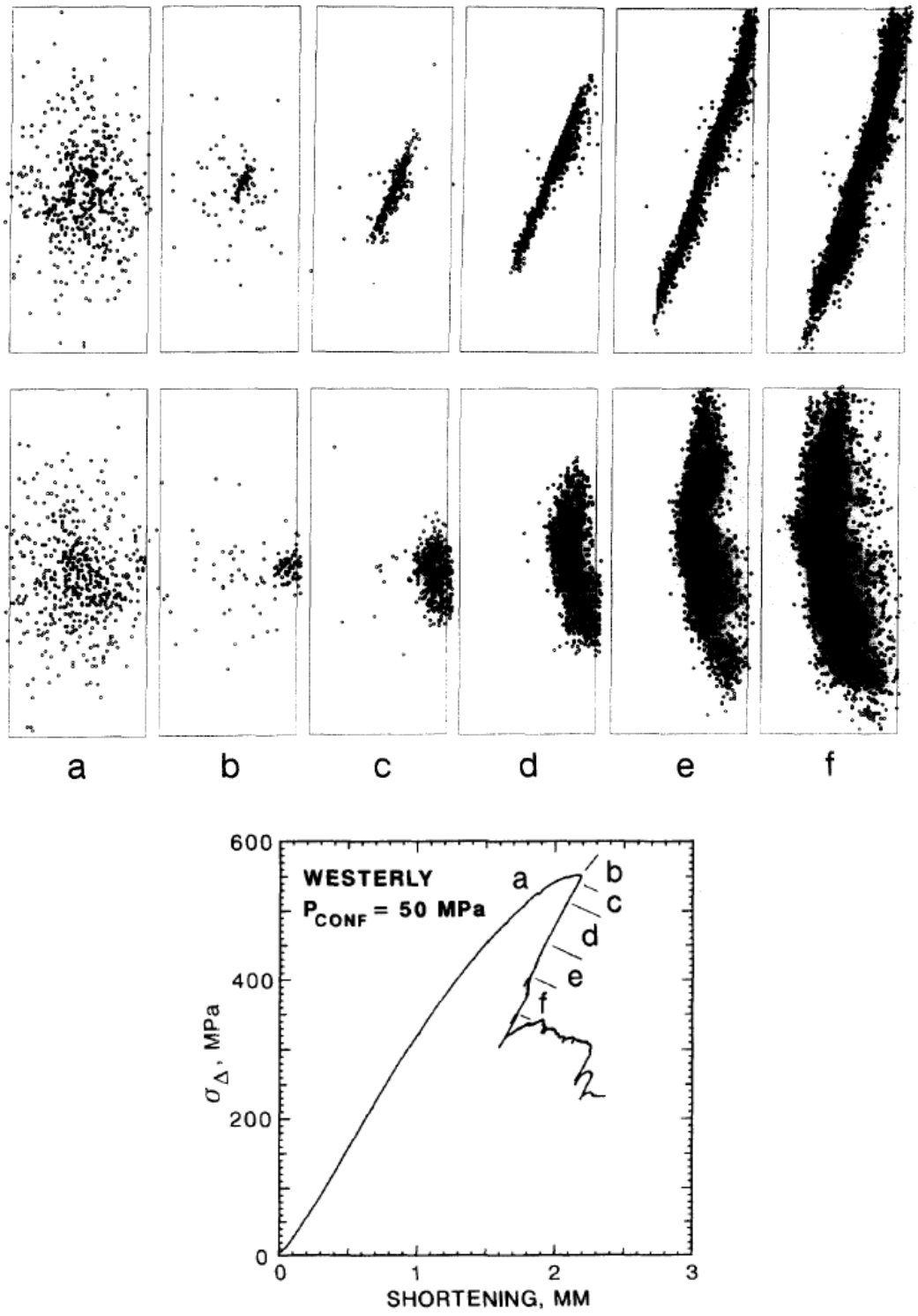

Figure 2.5. Fault nucleation and quasi-static propagation under AE feedback loading. Location periods (a) to (f) are indicated in stress–strain diagram at the bottom. (a) Pre-nucleation activity, (b) fracture nucleation, (c) to (f) fracture propagation. Source: Lockner et al. (1991).

Lei et al. (2000) developed a fast acquisition system to capture significant quantities of AE events prior to rock failure. Under a constant confining pressure and loading, a specimen of hornblende schist experienced fracture. Figure 2.6 shows the hypocentres of the AE events within the rock, where AE locations were resolved into the fracture plane and plotted as a function of depth and time. The locations of the AE activity propagate through the entire specimen before the final rupture. The clustering of AE events near the end platens could indicate the stress concentration due to unidirectional movement of the loading piston.

The locations of the AE activities were also studied by Zang et al. (1998, 2000) to map the progress of a process zone around a crack tip. As with initiation of new cracks, closure of existing cracks can also induce AE activity, but occurrences are limited compared to the crack shearing process (Moradian et al., 2010).

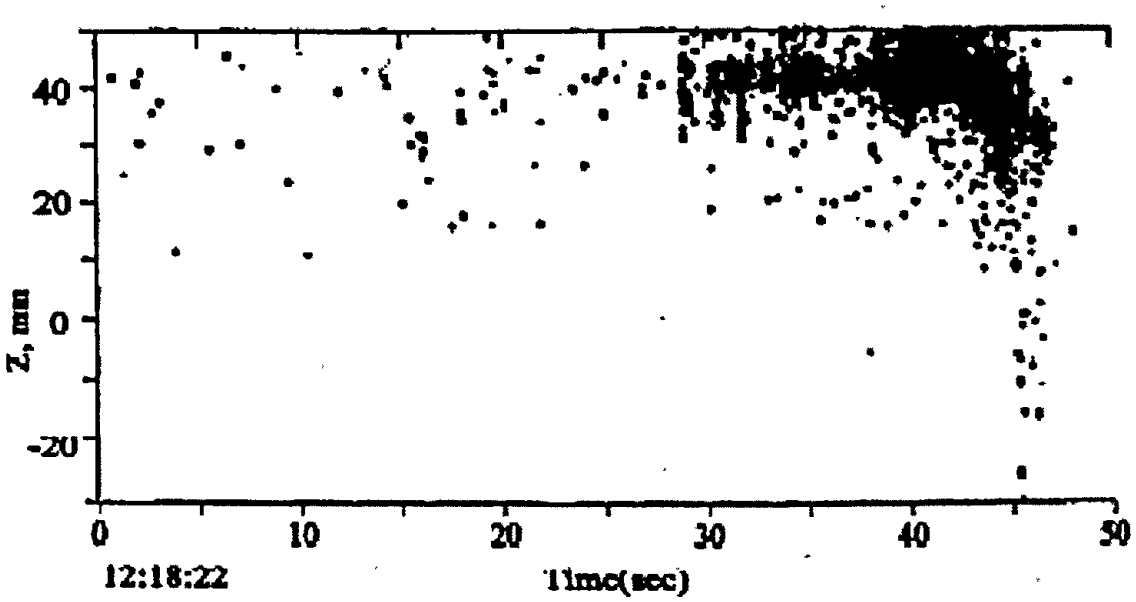

Figure 2.6. Fracture nucleation and quasi–static propagation in a specimen hornblende schist under constant stress conditions. AEs are resolved into the fracture plane and plotted with time as a function of depth (Z) of sample. Source: Lei et al. (2000).

2.6.2 Acoustic emissions during freezing and thawing

The effect of cooling rock to sub-zero temperature was first studied using AE methods by Hallet et al. (1991). A rectangular block of Berea Sandstone (50 X 50 X 300 mm) was frozen unidirectionally and, when the temperature gradient became fixed, AE events were counted and located as a function of time and temperature. The study confirmed that increased AE activity resulted from steepening of the thermal gradient as the temperature of the cooler side of the specimen was lowered. This increase in AE activity was followed by a gradual decrease in activity

(Figure 2.7). Although AE events were scattered over a major portion of the rock specimen, like material under compressive loading, 90% of the AE activity was noted between –3 and –6 °C and 50% between –4 and –5 °C (Figure 2.8). The experimental results suggested that nucleation of frost-induced microcracking does not require falling temperature because most of the AE events occurred when the temperature gradient was held constant.

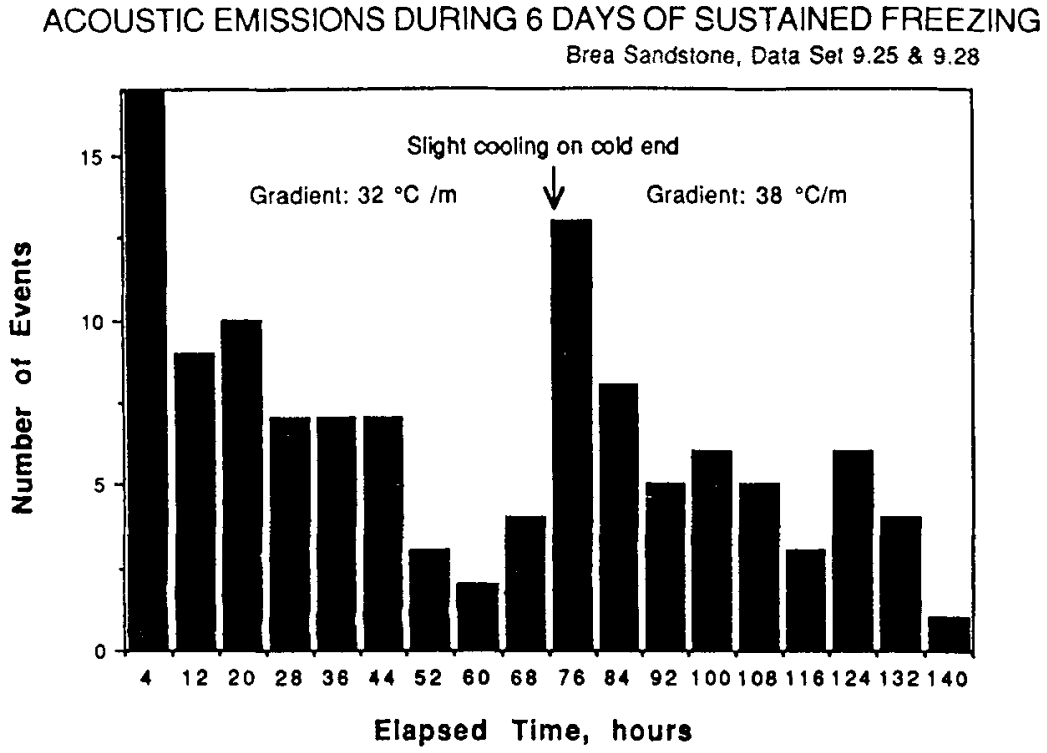

Figure 2.7. Time series of AE activity for a six-day experimental run showing a typical decrease in AE activity following the establishment of a steady temperature profile, and the reactivation of AE events following a step decrease in the temperature of the cold end of the specimen. Source: Hallet et al. (1991).

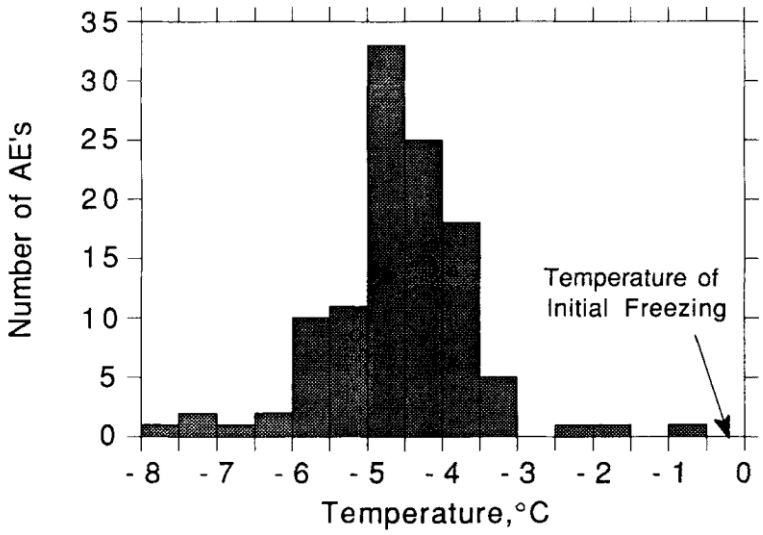

Figure 2.8. Thermal distribution of AE events located by relative arrival times. The plot shows the number of AE events relative to rock temperature. All but 10% of the AE occurred between –3 and –6 °C, and 50% between –4 and –5 °C. None of the located AEs occurred above 0 °C. Source: Hallet et al. (1991).

Duca et al. (2014) measured AE activity within a specimen of Arolla gneiss in which microcracking was artificially induced by thermal changes (including thermal shock) above 0 °C prior to the main freezing experiment. After this thermal pretreatment, the block was subjected to a fixed thermal gradient, with the upper and lower ends of the specimen at 5 and –12.7 °C, respectively, for a period of three months. Most of the AE events were recorded within a temperature range of –0.5 to –2.7 °C, which is consistent with the process of ice segregation. To estimate the precise location of hypocentres of the AE events, segmented velocity profiles were implemented on the frozen and unfrozen parts of the gneiss. The hypocentres occurred within a band that approximated the depth of the frozen fringe.

Amitrano et al. (2012) expanded the use of AE sensing into a high-alpine cliff of granitic gneiss to understand rockfall activity in an area of mountain permafrost. Most of the AE events were recorded during the night, when the temperature fell below 0 °C. Not only did temperature fluctuations play an important role in AE activity, but so did the availability of moisture.

In addition to investigating freezing effects in rocks, AE methods have also been applied to rock in a hot environment to understand the mechanics of exfoliation joints in the field (Collins et al., 2018). Intense AE activity in a granitic dome in California, USA, was recorded during the day, suggesting that thermal expansion of the rock mass can generate significant AE activity (Figure 2.9).

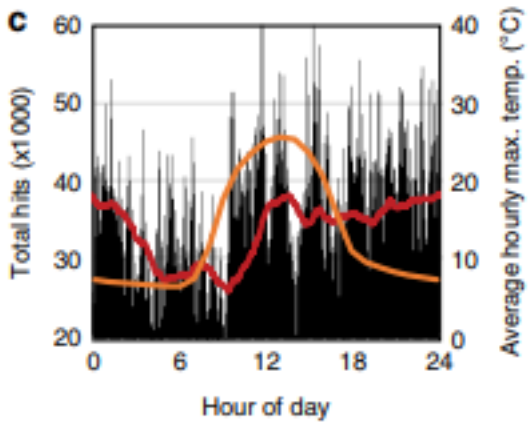

Figure 2.9. Plot showing total AE hits from six sensors between October 2014 and March 2015, indicating that subcritical cracking occurred after the 2014 fracture events. Note the sharp increase in 3-hr hit running average (red line) peaks with maximum temperatures (orange line). Source: Collins et al. (2018).

2.6.3 Acoustic emission in concrete

Significant research has been conducted on parameter-based AE techniques to assess the degree of damage in concrete structures (Grosse and Ohtsu, 2008) as the nucleation and growth of cracks can be monitored and detected in real time. The generation and characteristics of AE signals under compressive loading have been related to the volumetric changes in concrete, and the 'Kaiser effect' (the absence of detectable acoustic emissions until the previously imposed stress level is exceeded) has been detected up to 75% of the failure load (Ohtsu, 1988; Grosse and Ohtsu, 2008). The rapid increase in AE activity above 75% of the failure load is related to the increase in Poisson's ratio. It is also noted that with an increase in Poisson's ratio, the acoustic wave velocity eventually decreases (L'Hermite, 1960). AE activity has also been observed even during the unloading process (Robinson, 1968).

Yoon et al. (2000) conducted an experimental investigation on corroded reinforced concrete (RC) beams and concluded that the frequency of AE events and rate of AE generation depend on the degree of corrosion of reinforcing steel (Figure 2.10). The rate process analysis was introduced by Ohtsu and Watanabe (2001) to quantify the changes in AE waveform due to the development of damage. The rate process theory consists of a (hyperbolic) probability function of occurrence of AE events within the small changes in stress level. The total number of AE events (N) is related to the applied stress level (V %) as

$$N = CV^a e^{bV} \qquad (2.10)$$

where a and b are empirical coefficients and C is the integration constant.

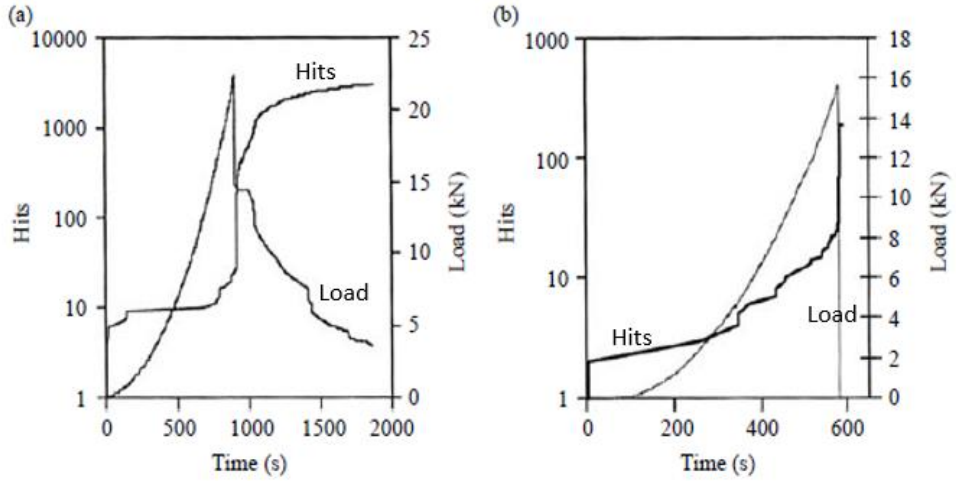

Figure 2.10. Load and AE history for concrete specimens with (a) 1.5% steel fibres and (b) 0% fibres (the AE hits, on the y axis, are plotted on a logarithmic scale). Source: Soulioti et al. (2009).

To quantify the damage in concrete structures, an important parameter named the *b*-value has been introduced (Tanigawa et al., 1977; Colombo et al., 2003). The *b*-value is estimated from the negative gradient of the log-linear plot of frequency magnitude following the protocol used in seismology (Ohtsu, 1996; Weiss, 1997; Colombo et al., 2003; Rao and Prasanna Lakshmi, 2005). In the context of AEs, the correlation between frequency and magnitude of AE waveform follows the Gutenberg–Richter relationship for seismic waves and is given by

$$\log_{10} N(M) = a - b\left[\frac{A_{dB}}{20}\right] \qquad (2.11)$$

where *N(M)* is the number of AE events above a predefined magnitude (≥ *M*), *b* is the *b*-value and A_{dB} is the peak amplitude. An attempt to correlate between the *b*-value and strain within steel and concrete was conducted by Vidya Sagar (2010). An improved version of the *b*-value (*Ib*) was also proposed to precisely quantify the damage in concrete structures (Shiotani et al., 2001). *Ib* is estimated from the slope of the peak amplitude of the AE events (Grosse and Ohtsu, 2008; Shiotani et al., 2000; Rao and Prasanna Lakshmi, 2005). As the amplitude of the AE activities varies with time, therefore, peak amplitude, *Ib,* is calculated by:

$$Ib = \frac{\log N(\mu-\alpha_1\sigma)-\log N(\mu+\alpha_1\sigma)}{(\alpha_1+\alpha_2)\sigma} \qquad (2.12)$$

where μ is the mean value of the amplitude distribution, σ is standard deviation, and α_1 and α_2 are coefficients related to the smaller amplitude and fracture level amplitude. Predominant occurrences of microcracks were indicated by a larger *b*-value, whereas a smaller *b*-value relates to the macrocracking activity, as shown in Figure 2.11 (Colombo et al., 2003).

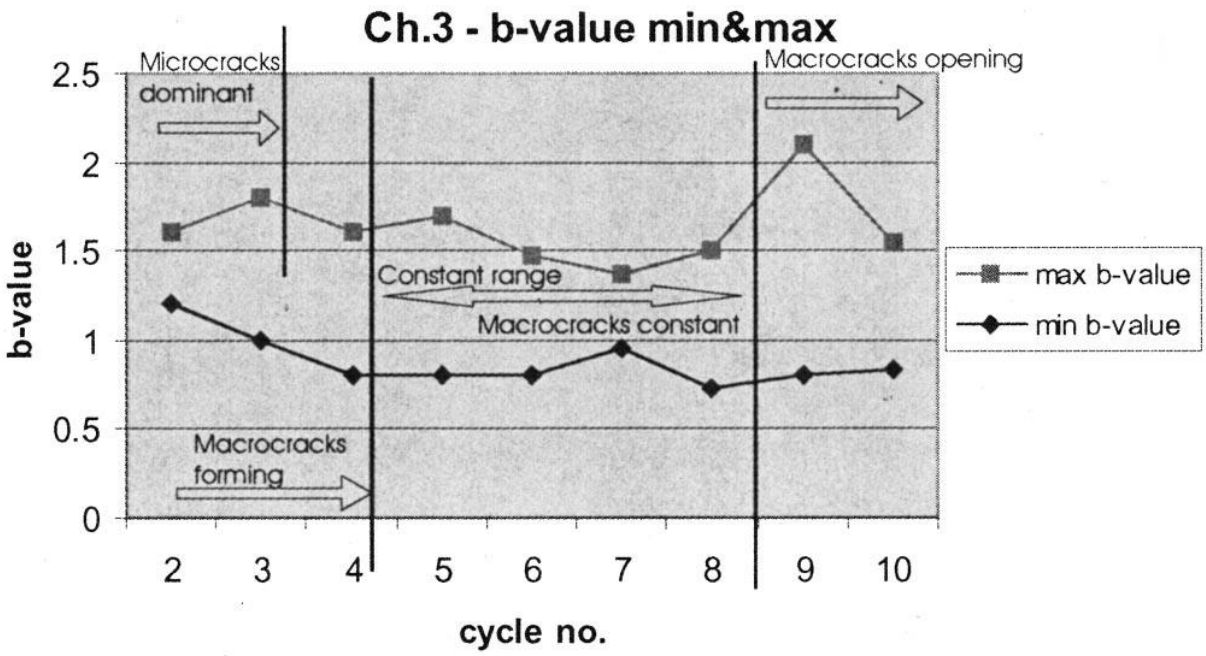

Figure 2.11. Variation of maximum and minimum b-values for reinforced concrete beam designed as representative of a bridge. Vertical lines show different stages of cracking indicated by arrows and cycles refers to the number of loading and unloading cycles. Source: Colombo et al. (2003).

Research has also been conducted to correlate the wide range of experimental results related to the fracturing in concrete with the lattice model (van Mier, 1997), assuming spherical-shaped aggregates. The nature of AE activity generated during fracturing in concrete was correlated with the lattice model of fracturing (Vidya Sagar et al., 2010).

The rapid release of strain energy during fracturing is considered as an important phenomenon to quantify the fracturing mechanism. A relationship between released AE energy and fracture energy of concrete (Figure 2.12; Landis et al., 2002; Vidya Sagar et al., 2010) shows that the release of AE energy takes place once the peak load is reached. If the characteristics of the emitted wavelength is less than the size of the constituent aggregate, then internal deflection may cause scattering of AE waves. The nature of AE wave scattering is strongly influenced by the heterogeneity and distribution of the composite material.

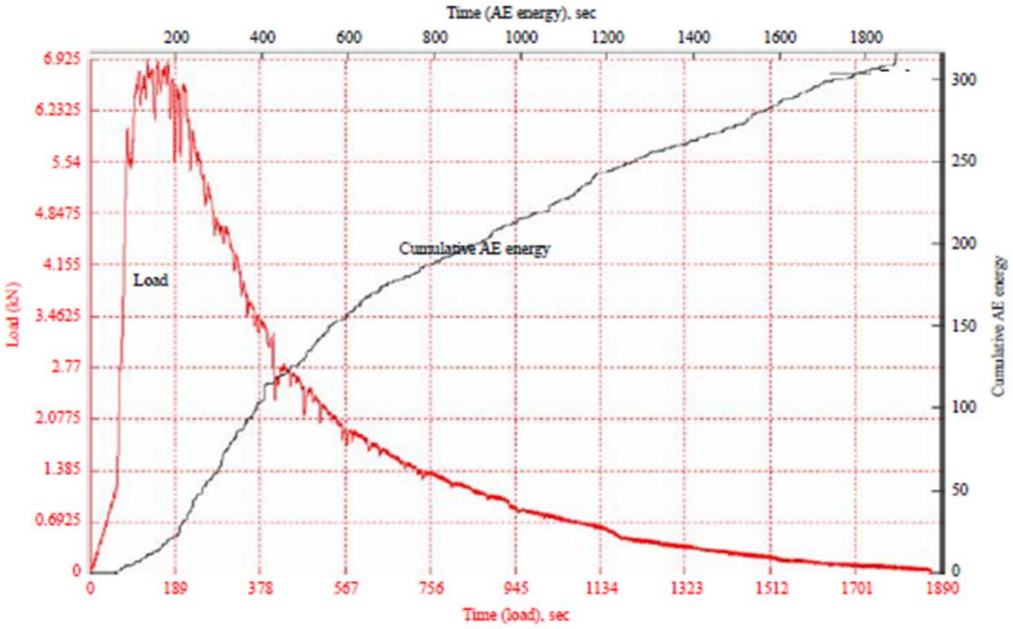

Figure 2.12. Changes in AE energy during fracturing in concrete. Source: Landis et al. (2002).

With the progression of fracturing, the modes of cracking change from tensile (mode–I) to shear (mode–II) types. Crack opening coincides with mode–I cracking, while shearing along pre-existing cracks develops mode–II cracks. A generalised classification of mode–I and mode–II crack types was introduced in concrete based on two different approaches in AE studies. One is a parametric-based approach where the proportion of 'average frequency (counts/duration)' and 'RA values (rise time/amplitude)' was considered to separate the tensile and shear component of a microcrack (Figure 2.13; JCMS-IIIB5706, 2003). The other approach is 'Simplified Green's functions for moment tensor analysis (SiGMA)' procedure, also known as the signal-based method (Ohtsu, 1991). The moment tensor inversion method has proven successful in quantifying the kinematics of crack orientation and slip vector of AE sources and the types of crack. According to the SiGMA analysis on reinforced concrete (RC) beam, tensile cracks develop in the early stage of cracking followed by mixed mode of tensile and shear types of cracking, and finally shear type cracking dominates (Yuyama et. al., 1999). The parameter-based analysis developed from an empirical relation, whereas the SiGMA procedure was based on the generalized theory of AE.

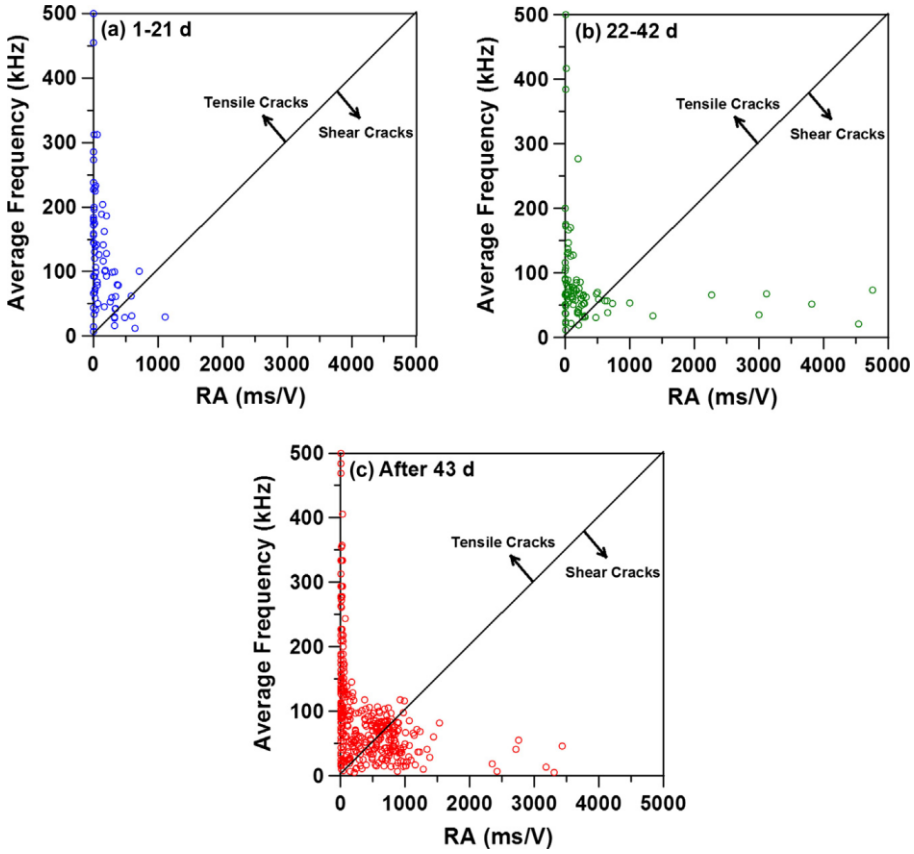

Figure 2.13. Relationship between average frequency (AF) and RA index for concrete specimen prepared using reactive agents during (a) 1–21 days, (b) 22–42 days, and (c) after 43 days. Source: Farnam et al. (2015).

Chapter 3

Methodology

3.1 Introduction

Chapter 3 describes the methodologies adopted to carry out three experiments on rock cracking under laboratory conditions. Section 3.3 describes the freezing and thawing conditions imposed on small cylinders of rock in a climate cabinet and the protocol followed in the μ-CT acquisition and processing of repeated scans of the specimens to detect progressive crack development following the objective 1.1 (O1.1) outlined in chapter one. The details of the equipment and sensors used in compressive tests performed on unfrozen rock specimens are described in section 3.4 addressing the objective 1.3 (O1.3). Section 3.5 details the macroscale freezing experiment conducted in the Permafrost Laboratory for 315 days of continuous data acquisition to accomplish objective 1.2 (O1.2). It also documents the signal conditioning (converting the measured electrical pulses into their respective physical parameters) of various sensors measuring the physical changes during bidirectional freezing and the mechanical changes of the chalk and sandstone blocks.

3.2 Rationale for experimental investigations

The present research aims to investigate the mechanisms of cracking in Ardingly Sandstone and tuffeau chalk during subzero freezing by conducting laboratory experiments at micro- and macroscales. Assessment of the parameters that initiate and develop cracks during freeze–thaw cycling in field conditions is difficult and expensive to monitor, particularly as cracking in rocks tends to be slow and incremental, requiring extended periods of data acquisition. Furthermore, frost weathering involves a complex set of processes (Matsuoka and Murton, 2008), and it can be difficult to isolate the influence of any single parameter in the field on one particular process.

Laboratory experiments, on the other hand, allow careful control and monitoring of environmental parameters. They also circumvent the natural variability of field conditions in space and time, favouring development of mechanistic understanding of cracking. Experimental studies conducted on soils have developed ice lenses during the initial cycles of freezing (Miller, 1977; Arenson et al., 2008), but due to the plastic nature of soil, the stress induced during freezing was released in various directions. By contrast, in rock, the induced stress initiates networks of cracks that reveal valuable information about the mechanical instability.

3.3 Micro-CT imaging and analysis

3.3.1 Sample preparation

The resolution of the scanning system depends on the size and shape of the specimen. Small samples allow higher resolution compared to large samples. The scanning system captures and compares images obtained from 360° around the object to detect the internal morphological features. Therefore, small cylindrical plugs 30 mm long and 20 mm in diameter of chalk and sandstone (Figure 3.1) were used in the experiment to assess the development of microcracks as a consequence of freeze–thaw cycling. The size of the specimens fitted easily within the field of view of the µ-CT scanning system, minimizing the loss of information during scanning. The geometry of the specimen induces certain acquisition artefacts during scanning. For example, the penetration strength of the x-rays within a single material differs for a sample with cubic geometry during a 360° scan as x-rays must travel further along the direction diagonally inward from the corners of intersecting faces compared to the direction normal to each face. Using a cylindrical geometry reduces such scanning-induced artefacts and was therefore implemented in the present experiment. A drill press with a diameter of 20 mm was used to obtain a rock core, the top and bottom of which were flattened using an angular hand grinder. The small core specimens were firmly encased within a small block of floral foam to prevent movement during scanning in the µ-CT system (Figure 3.2).

Figure 3.1. Small core cylinders of Ardingly Sandstone (left) and tuffeau chalk (right) 30 mm long and 20 mm in diameter.

Figure 3.2. Ardingly Sandstone core encased within floral foam to prevent movement during micro- CT scanning.

Prior to freezing, the specimens were wetted by capillary rise. A water table 5 mm above the base of the sample allowed the rocks to draw water by capillary action and saturate the porosity. This procedure was repeated prior to each freezing cycle to facilitate frost weathering.

3.3.2 Climate cabinet

The climate cabinet is a temperature-controlled closed chamber with an internal and external dimension (W x D x H) of 585 x 530 x 1260 mm and 740 x 720 x 2000 mm, respectively. The temperature range varies from –40 to 100°C and is programmable, which enables automatic cycling between various temperatures, over a set period of time. The present freezing was experiment conducted at the University of Sussex in an ECO 400 climate cabinet manufactured by Temperature Applied Science Ltd, UK.

3.3.3 Temperature regime

Natural winter and summer cycles were simulated inside the climate cabinet. The rock cores were insulated beneath and around them using blocks of polystyrene (Figure 3.3) during temperature cycling to prevent lateral heat transfer during downward freezing from the top. This imposed a vertical thermal gradient along the direction of their length. For the first 10 freeze–thaw cycles the temperature ranged from –5°C during freezing periods to 5°C during thawing periods, with a duration of 24 hours for each cycle (Figure 3.4a). From the 11th cycle

onwards, the thermal regime was changed, from –10 to 10°C with a duration of 5 days for each freezing and thawing period (Figure 3.4b). The increases in duration and temperature range were implemented to accelerate cracking during freezing.

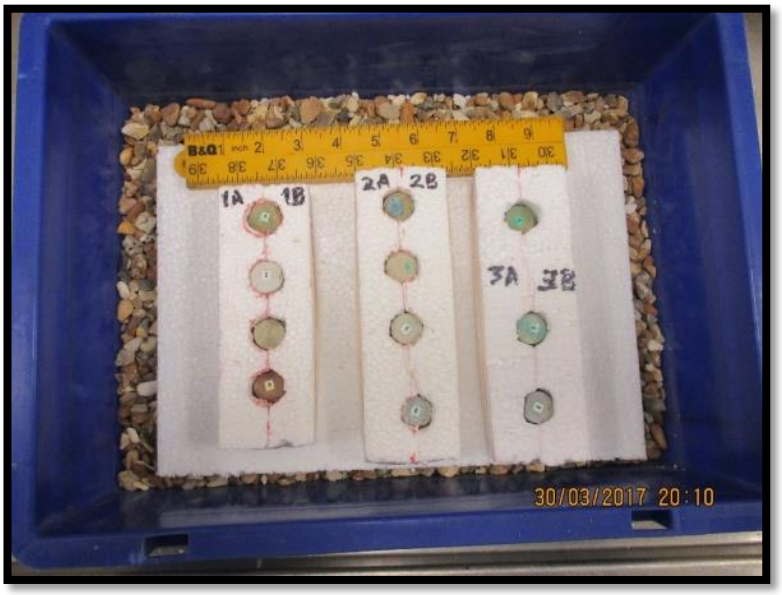

Figure 3.3. Specimens encased within polystyrene to minimize lateral heat transfer during freeze–thaw cycles.

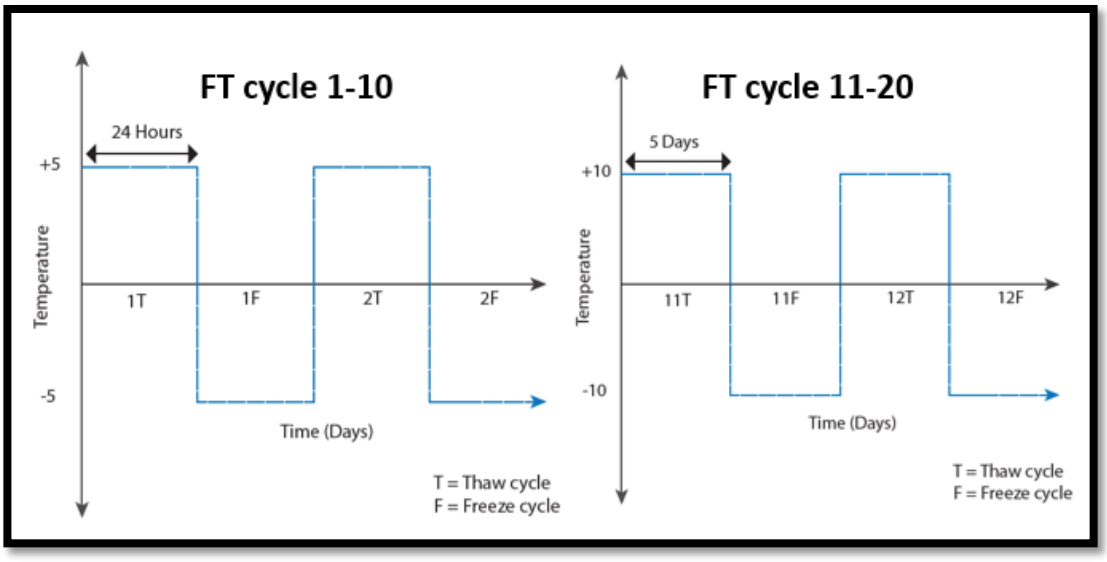

Figure 3.4. Duration and temperature regime in climate cabinet during freeze–thaw cycles (a) 1–10 and (b) 11–20.

3.3.4 Scanning protocol

3.3.4.1 Scanning principle

Micro-computed tomography (µ-CT) scanning is a powerful non-destructive method of investigating the internal morphology of objects. The variable penetration of X-rays through material is the basis for µ-CT imaging technique, which is mathematically illustrated by Beer's law. The transmitted intensity I of a monochromatic X-ray beam passing through an object is

$$I = I_0 e^{-\int \mu(s) ds} \qquad (3.1)$$

where I_0 is the intensity of incident X-ray beam and $\mu(s)$ is the linear attenuation coefficient along the ray path$s$. $\mu(s)$ depends on the photoelectric effect, coherent (Rayleigh) scattering, incoherent (Compton) scattering and pair production. Using a rotating stage for objects under scanning in combination with an X-ray source and detector system, a series of projections from different angle is captured. The images are further rendered using appropriate reconstruction algorithms by assigning definite grey scale value for each voxel inside the volume.

3.3.4.2 Description of CT scanning system

The µ-CT scanning of small rock specimens was undertaken by the Nikon Metrology XT H-225 tomography system (Figure 3.5) in the Centre for Micromorphology at Queen Mary University, London. The system has an X-ray source, a rotating stage and an X-ray detector consisting 1000 x 1000 pixels. A cone-shaped X-ray beam is produced by bombarding a tungsten metal target with electrons, which is focused on an object sitting on the rotating stage. The stage can rotate 360^o and the detector panel captures a series of two-dimensional (2D) projections (radiographs) at every 0.2^o interval. The radiographs measure the amount of X-ray energy transmitted through the object under scanning. A series of 2D radiographs is then used to reconstruct the 3D volume using computer software.

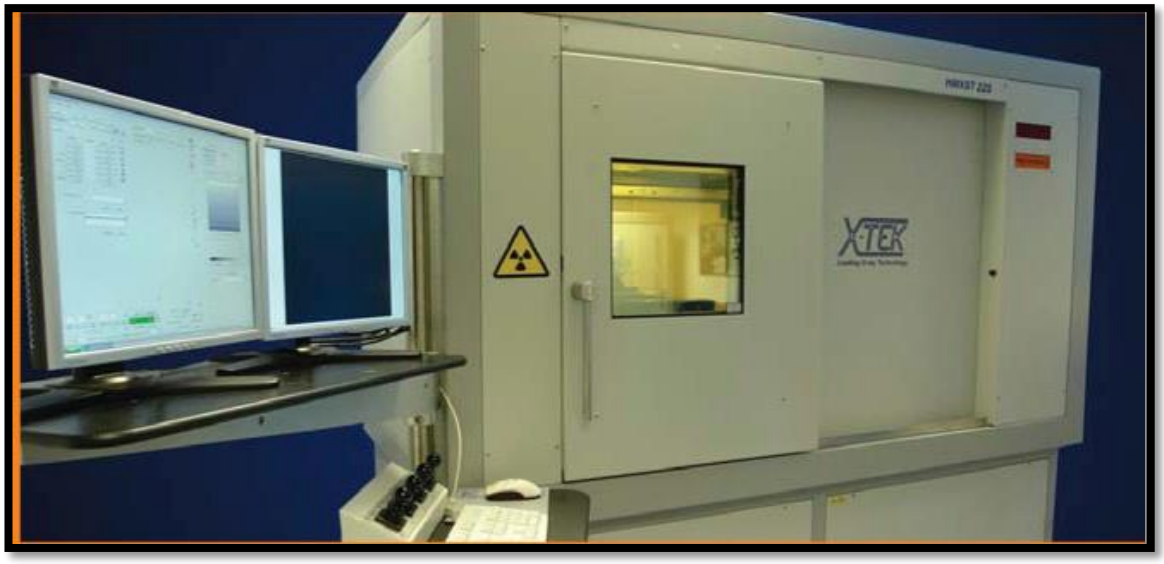

Figure 3.5.Main components of the XT H 225 CT system. On the left are two monitors, one showing the live X-ray image (right) and the other with the main controls (left). The specimen, X-ray gun and detector is housed in a lead-lined sample chamber.

3.3.4.3 Data acquisition

Before scanning, the system is auto-conditioned to the correct operating voltage for some time to ensure that scanning is undertaken at a stable operating voltage. Once the system has been auto-conditioned (several minutes if the system is on), the specimen is loaded on the rotating stage between X-ray source and detector. The specimen is firmly encased within a block of floral foam to prevent any movement during acquisition and placed as centrally as possible on the rotating stage to enhance the accuracy. Then a pilot 360^{o} rotation and subsequent adjustment to align the specimen centrally ensures that the object fits inside the field of view of the detector. The position of the stage (X, Y and Z co-ordinates of the stage with reference to x-ray source and detector) is saved into the workstation and used during repeated scanning to eliminate any spatial error.

After the sample is centred, the energy parameters are set. Penetration strength (and radiograph contrast) of the X-ray beam is mainly determined by the voltage, whereas the number of X-rays (and radiograph brightness) is largely determined by the current. The operation is based on a grey-scale histogram analysis to get the best range of grey scale values possible between 9,000 and 60,000. Other acquisition parameters such as exposure time, digital gain, number of projections, frames per projection, frames to average, filtering material and thickness are set accordingly in the Inspect-X software prior to scanning (Table 3.1). As the

objective of the experiment involves multiple scanning of the same specimen, the initial settings of the scanning parameters are restored and repeatedly used to ensure data comparability. Each scan of the entire specimen takes around 3 to 4 hours to complete.

Acquisition parameters during scanning	
Target metal	Tungsten (W)
Filter	1 mm thick copper (Cu)
Voltage	186 kV
Current	250 µA
Exposure time	1000 ms
Gain	12 dB
Digital gain	1X
Number of projection	1571
Number of images for shading correction	3
Frames to average	4

Table 3.1. Listing the values of acquisition parameters during µ-CT scanning.

3.3.4.4 Reconstruction

Once the scanning is complete, the projections are aligned centrally in a radial pattern to reconstruct the 3D volume. The pixels along each row of the detector become a slice. Therefore using the method of back projection a cross section of the specimen is created from each row of pixels in the radiograph. A µ-CT reconstruction is thus a 3D matrix in which each element consists of a voxel with a definite grey scale value of 16 bits. The grey scale value is a function of the linear attenuation coefficient of the material under scanning, which is a measure of the absorption and scattering of an X-ray beam while passing through the material. The value of the coefficient also largely depends on the density and thickness of the material. The magnification of the object on the detector screen determines the size of the voxel.

The reconstruction was conducted using CT-Pro 3D software, which reassembles a series of 2D sequential scanning projections into a 3D volume. The operation generates a 16-bit TIFF image slice stack for further processing and visualisation.

Task	Step	Process
Acquisition	Sample preparation	Using drilling and grinding techniques to prepare 30 mm long and 20 mm diameter core plugs
	Set up live imaging	Set up the position of rotating stage to ensure the object is under detector for all the positions in a 360° rotation
	Set up CT scan	Set the acquisition parameters in Inspect X software
Reconstruction	Transfer data to reconstruction PC	Data saved and transfer to reconstruction PC from acquisition PC
	Reconstruction	Reconstruct 2D projections into 3D volume using CT Pro software
Render	Convert to RAW	The image format converted to RAW format for easy handling using Image J software
	Drishti import	The raw images imported into Drishti Import for further operation in Drishti
	Visualisation	The 3D volume of the specimen is visualised in Drishti using transfer function
Analysis	Data analysis	Image information converted into matrix form for analysis in Matlab

Table 3.2. Workflow of the μ-CT analysis.

3.3.5 Data analysis based on statistical correlation functions

Several low-order statistical correlation functions were applied to determine the progressive changes and damage to rock specimens caused by freeze–thaw cycles to accomplish objective 2.3 (O2.3). The functions can be applied to material classes such as random heterogeneous materials, amorphous solids and materials with directional bonding (Torquato, 1991; Torquato, 2002). It is assumed that the microstructures resulting from freeze–thaw cycles were static (or approximately static) during times when the rock specimens were maintained at ambient laboratory temperature during pauses in freeze–thaw cycling. Therefore any realization ω that describes the microstructures of heterogeneous rock materials must be independent of time.

Any realization ω of the two-phase random media (i.e. fracture phase and material phase) is based on the probability of occurrence of events described in that realization and occupies a subset ν in the three-dimensional (3-D) Euclidean space, $\nu \in \mathbb{R}$. The subset ν constitutes the volume fraction of fracture phase $\nu_f(\omega)$ and material phase $\nu_m(\omega)$. In practice, the indicator function $\mathbb{I}^f(x;\omega)$ creates a Boolean array by repeatedly checking a given condition or realisation ω for the fracture phase $x \in \nu_f(\omega)$ and is defined as

$$\mathbb{I}^f(x;\omega) = \begin{cases} 1, \ if \ x \in v_f(\omega), \\ 0, \ otherwise, \end{cases} \qquad (3.2)$$

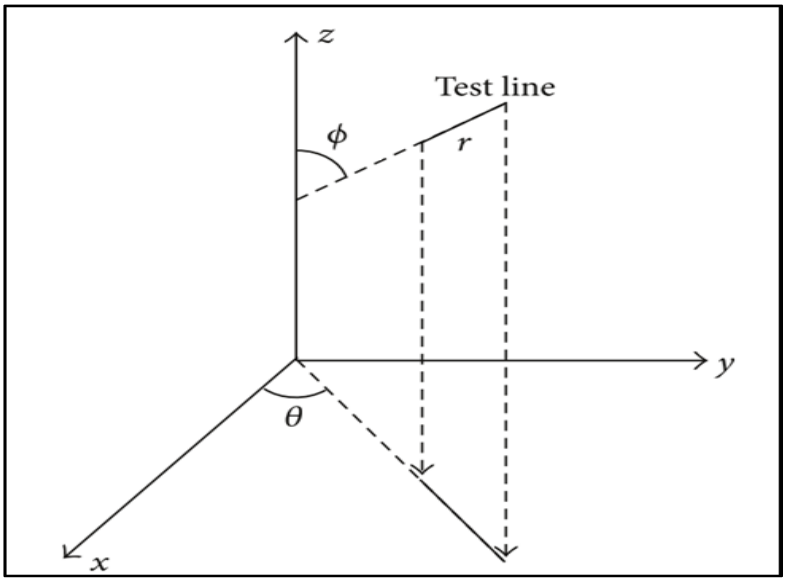

Figure 3.6. Description of different parameters in 3-dimensional space used to estimate the correlation functions. Modified from Chung et al. (2015).

3.3.5.1 Two-point probability function

For the fracture phase *f*, the two-point probability function S_f is defined as the expectation of the product $\mathbb{I}^f(x_1;\omega).\mathbb{I}^f(x_2;\omega)$, i.e., the probability that the two points x_1 and x_2 belong to the fracture phase and is denoted as

$$S_f(x_1, x_2) \equiv \langle \, \mathbb{I}^f(x_1;\omega) \, . \, \mathbb{I}^f(x_2;\omega) \, \rangle \qquad (3.3)$$

The two-point probability function $S_f(r)$ was calculated by projecting a line segment of length $r \equiv |r|$ within the defined 3-D space and oriented in a specific direction (Torquato, 2002). The phase information at the end two points of the projected line was repeatedly considered to check whether the two points were in the same phase or different phases, and accordingly a Boolean array was created to calculate the probability of occurrence with varying degrees of separation. The boundary conditions for the two-point correlation function are as follows:

$$\lim_{r\to 0} S_{ff}(r,\theta,\phi) = v_f$$

$$\lim_{r\to 0} S_{fm}(r,\theta,\phi) = 0 \qquad (3.4)$$

$$(f \neq m)$$

$$\lim_{r\to \infty} S_{ff}(r,\theta,\phi) = [v_f]^2$$

$$\lim_{r\to\infty} S_{fm}(r,\theta,\phi) = [v_f][v_m] \qquad (3.5)$$

$$(f \neq m)$$

where v_f is the volume fraction of the fracture phase and v_m is the volume fraction of the material (or non-fracture) phase. Equation 3.4 indicates that when the separation between the two points approaches zero, the probability of both the end points in the same phase converges to the volume fraction of the fracture phase. In other cases, the probability of finding different phases at a point becomes zero. Equation 3.5 illustrates that as ***r*** increases to infinity, $S_{fm}(r)$ becomes the product of the volume fraction of constituent phases. No additional information in between the two bounding points was considered in this function.

Brown (1955) introduced the two-point probability function to determine the effective directional transport properties in random heterogeneous material. The function $S_f(r)$ simply measures how the end points of a vector ***r*** were correlated with each other in the fracture phase.

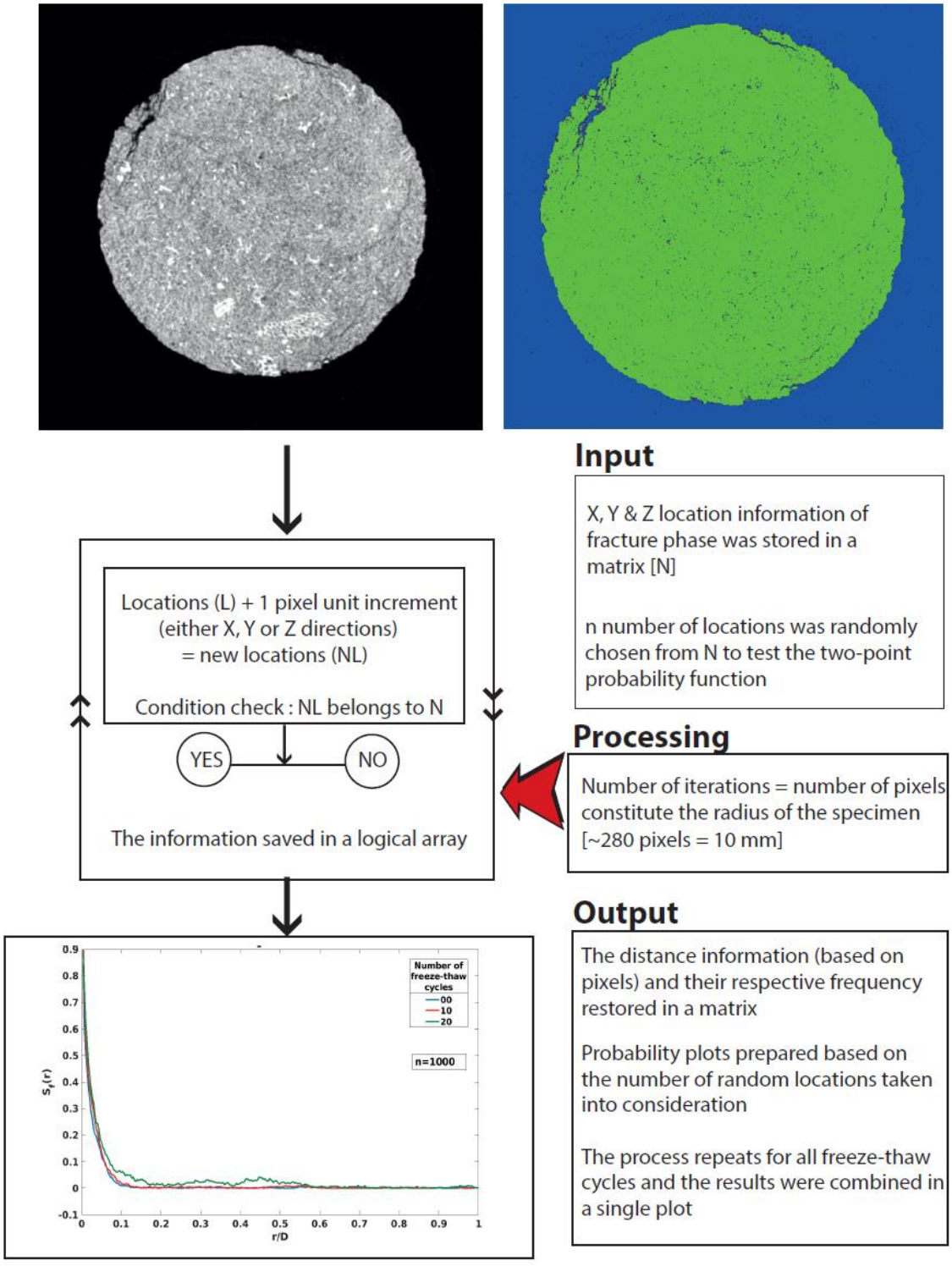

Figure 3.7 Flow chart illustrating the data input, processing and output for two-point probability function.

To calculate the two-point probability function, 1000 3-D random points were selected in the fractured phase extracted from image analysis (Figure 3.7). Each point was incremented at a unit distance of one pixel (one pixel = 34.78 μm) along the orthogonal direction (X-, Y- and Z-

directions) until the boundary condition was reached and the phase information was analysed and restored in a Boolean array to calculate their probabilistic occurrence with increasing distance. In each operation, *r* is the distance between the two points considered and *D* is the diameter of the specimen (20 mm). Therefore, the ratio r/D represents the dimension of cracking activity with respect to the dimension of the specimen. The two-point probability function measures the continuity of a phase along definite directions. Reiteration of the function after several freeze–thaw cycles captured the progressive development of the fracture phase along predefined directions.

3.3.5.2 Two-point cluster function

Another interesting two-point descriptor used to describe the microstructures in heterogeneous material is the two-point cluster function (Torquato, 2002). This function $C_f(x_1, x_2)$ calculates the probability of finding any two points $x_1 \text{and } x_2$ in the same cluster of the fracture phase. $C_f(x_1, x_2)$ is useful in determining the connectivity of both the phase distribution and phase cluster, even if the phase connectivity is interrupted by another phase along a specific direction. The boundary conditions for the two-point cluster function are:

$$\lim_{r \to 0} C_f(r, \theta, \phi) = v_f \qquad (3.6)$$

$$\lim_{r \to \infty} C_f(r, \theta, \phi) = 0 \qquad (3.7)$$

where v_f is the volume fraction of the fracture phase. Unlike other probability functions, when the distance between the arbitrarily chosen two points approaches zero, the probability of finding the two points in the same phase or cluster reaches the volume fraction of the fracture phase, as illustrated by equation 3.6. Equation 3.7 explains that when the separation between the two points is close to infinity then the chances of getting them in same phase or cluster approaches zero.

Lee and Torquato's (1989) method was adopted in the present study to calculate the two-point cluster function. A randomly chosen pair of arbitrary points (n=100000) tested if they were part of the same fracture phase (Figure 3.8). The phase information and the distance between the pair of randomly selected points were therefore measured and the process repeated for different freeze–thaw cycles to estimate the progressive changes in the two-point cluster function.

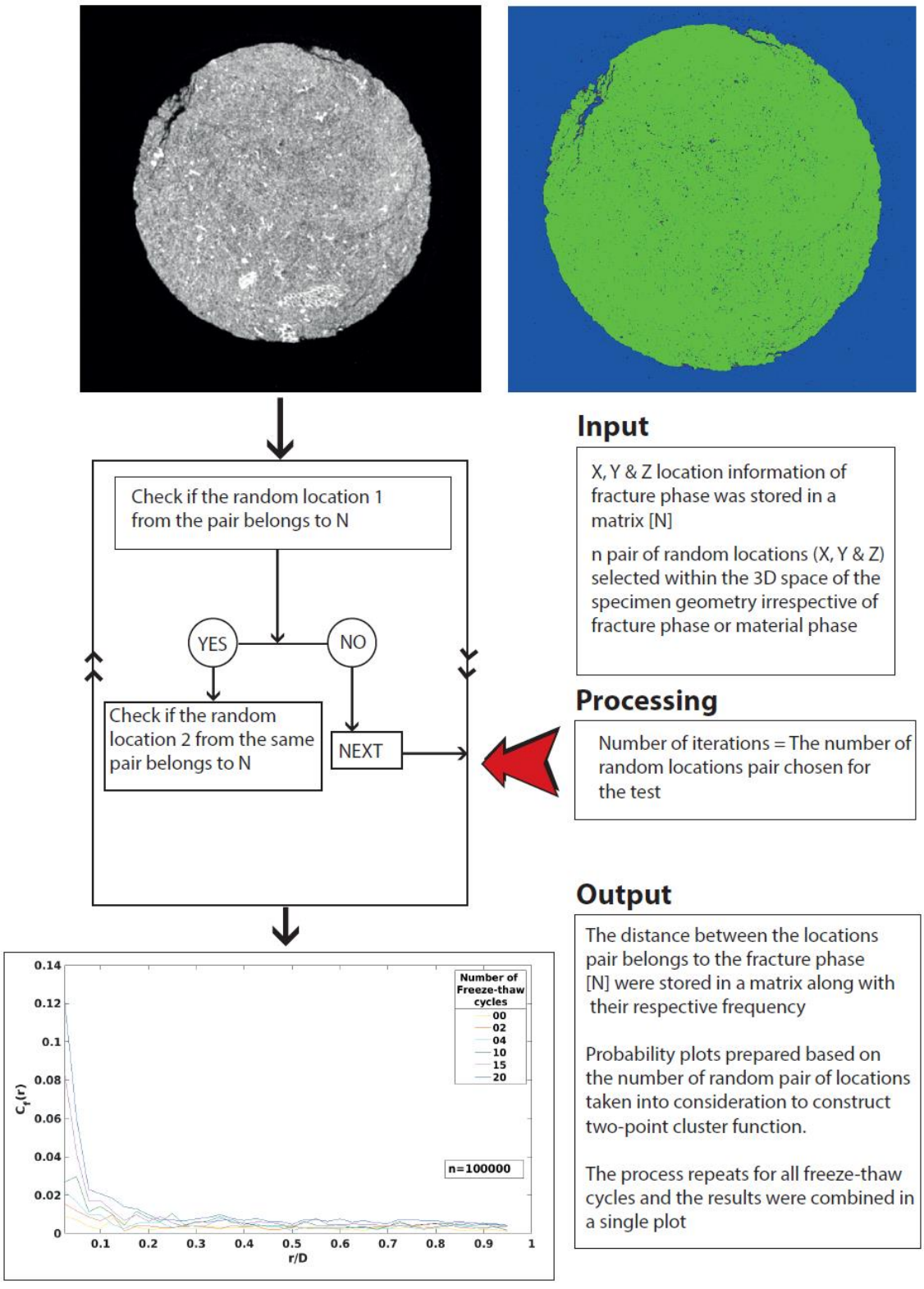

Figure 3.8. Flow chart illustrating the data input, processing and output for two-point cluster function.

3.3.5.3 Lineal path function

The lineal path function $L_f(r)$ calculates the probability that a line segment of length r lies completely in the fracture phase when randomly placed into the volume space (Torquato, 2002). Unlike the two-point probability function, the lineal path function retains phase information at each point on the projected line under consideration and measures the level of continuous connectivity of the fracture phase in a specific direction. The limits for the lineal path function are as follows:

$$\lim_{r\to 0} L_f(r,\theta,\phi) = v_f \qquad (3.8)$$

$$\lim_{r\to \infty} L_f(r,\theta,\phi) = 0 \qquad (3.9)$$

where v_f is the volume fraction of fracture phase. Equation 3.8 indicates that when the length of the test line approaches zero, the probability of finding the same phase at the other end of the moving line converges to the volume fraction of the fracture phase. On the other hand, as the length of the test line increases to infinity (Equation 3.9), the probability of finding connected fracture phase reaches to zero.

The present study followed the methods adopted by Coker and Torquato (1995) to measure the lineal path function for thermally treated rock specimens. To estimate the lineal path function $L_f(r)$, 1000 random points were selected inside the fracture phase and the phase information at a definite direction was measured by increasing the length of the test line by one unit (i.e. equivalent to the length of one voxel) for each iteration (Figure 3.9). The process was repeated until the test line encountered a different phase. The information about the continuous length of various randomly oriented lines (combination of a range of values of azimuth and zenith angle, θ & ϕ, Figure 3.6) within the progressive fracture phase and its respective progress were accessed to estimate the changes in lineal path function due to freezing and thawing.

The connectivity of the fracture phase along a specific direction can be measured using the lineal path function as the function retains continuous phase information of all the points of the line segment.

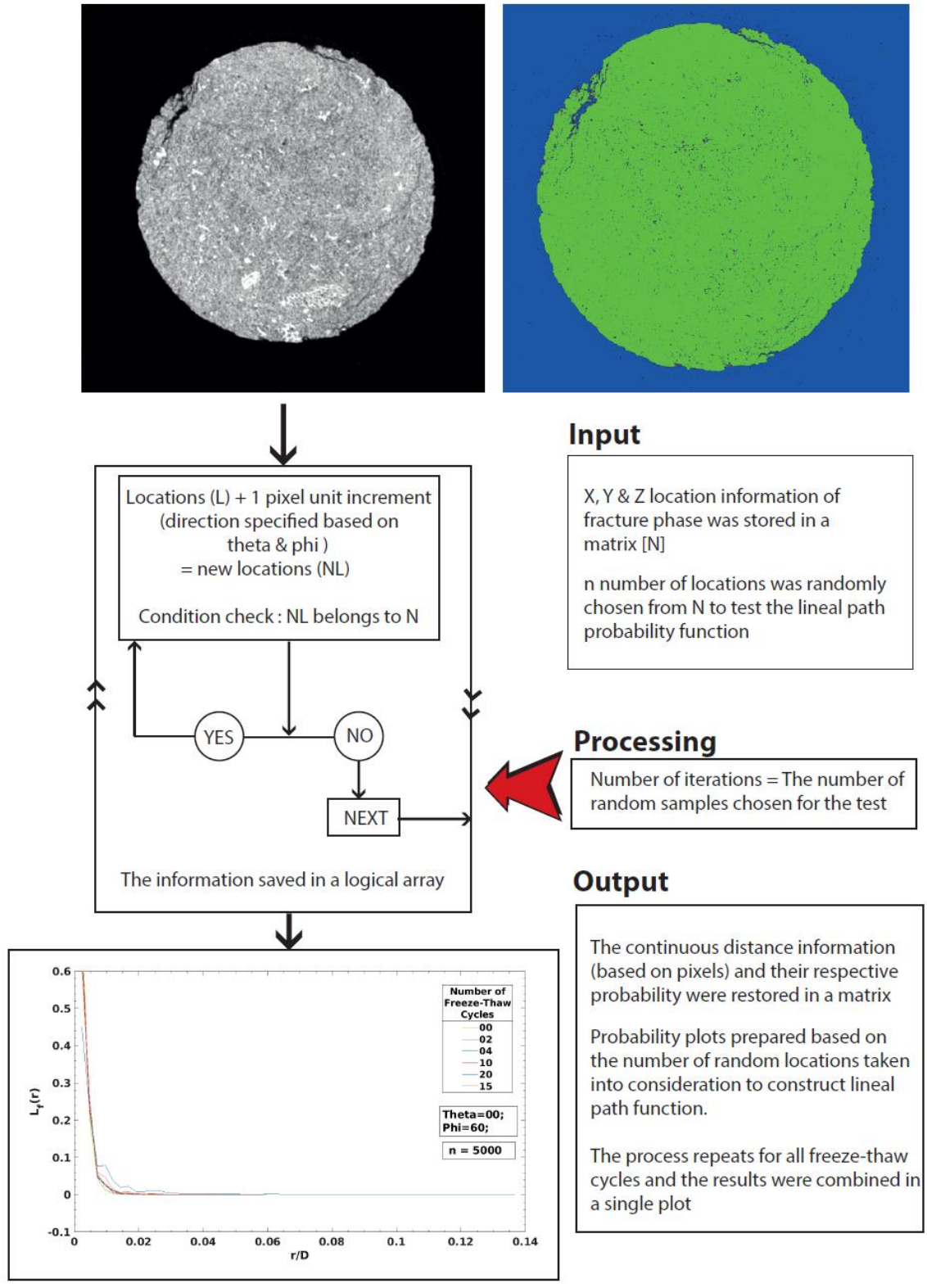

Figure 3.9. Flow chart illustrating the data input, processing and output for lineal path function.

3.4 Compression Test

3.4.1 Objective

Prior to conducting both the freezing experiments, destructive tests were performed to determine the geomechanical characteristics of the rock specimens and assess the fracture mechanism under compressive loading. The effect on fracture propagation due to the presence of rock of variable density was also assessed by combining two rock types during compressive loading to address objective 4.4 (O4.4). The resulting information on geomechanical properties and fracture propagation is used to analyse and interpret the experiments on freezing-induced fracture of rock.

3.4.2 Sample preparation

Special attention was taken to prepare the samples such that the combined effect of both rock types can be estimated during compressive loading. A rectangular block of each rock type, with dimensions of 200 x 100 x 50 mm, was prepared to ensure that the material failed purely under compression and other factors contributing to failure were minimised (e.g. bending of elongated samples). The blocks were cut in the rock-cutting facility at the University of Sussex, with care taken to ensure that the surface faces of the blocks were smooth. Each block was then drilled to remove a 35 mm diameter core from the centre of the 200 x 100 mm face along the direction of minimum thickness (Figure 3.10). The core of chalk (50 mm long, 35 mm in diameter) was inserted into the centre of the sandstone block, and vice versa. A thick paste of gypsum ($CaSO_4$, $2H_2O$) was used to bond the cores firmly inside each block and dried at room temperature for several days to strengthen the bonding.

3.4.3 Rationale for specimen

The mechanism of fracturing involves three principle steps: (1) initiation of cracks; (2) propagation of cracks; and (3) coalescence of cracks, which causes the ultimate failure of rock. Pre-existing microcracks, voids, grain boundaries, and inclusions within an elastic solid act as defects that initiate fracture. According to Griffith's tensile theory (1921), tensile cracking initiates at the tips of minute defects that he represented as elliptical flaws. Hoek (1965) discussed the transition from open cracks to closed cracks, because in most of geologic materials tensile cracks originate at the grain boundaries, which are usually cemented together and have to be considered as closed cracks rather than open cracks. To incorporate the effect of closed cracks, two different rock types were combined under compressive loading. The experiment simulated the effect of the presence of low-density macropores encased within a high-density material (Specimen 1—chalk core within sandstone) and vice versa (Specimen 2— sandstone core within chalk).

3.4.4 Instrumentation

Six strain gauges were mounted at different locations and orientations on a single surface measuring 200 x100 mm of each block (Figure 3.10). For the sandstone block containing a chalk core, four strain gauges were mounted on the sandstone surface, three in a direction of axial loading and the fourth in transverse direction (to measure the lateral strain). The remaining two strain gauges were attached to the face of the chalk core, one in the direction of axial loading and the other of transverse loading. The same protocol was applied to mount the strain gauges on the chalk block containing a sandstone core. The strain gauges used consisted of a 120 Ω resistor with a gauge factor of two and manufactured by RS Component (RS Pro wire lead strain gauge, Part no–632-124). To ensure good bonding between the rock and the strain gauges, the rock surface was filed with sandpaper prior to gluing on the gauges. A two-component epoxy (X-60 two component adhesive, HBM) containing a powder and a solution were mixed in appropriate ratio to attach the strain gauges firmly on the surface.

Two linear variable differential transformers (LVDTs), with their foot resting on opposite vertical faces (100 x 50 mm) of the rock specimen, measured lateral movement during axial loading. The LVDTs were manufactured by OMEGA Engineering Inc. (Part no–LD620 - 50).

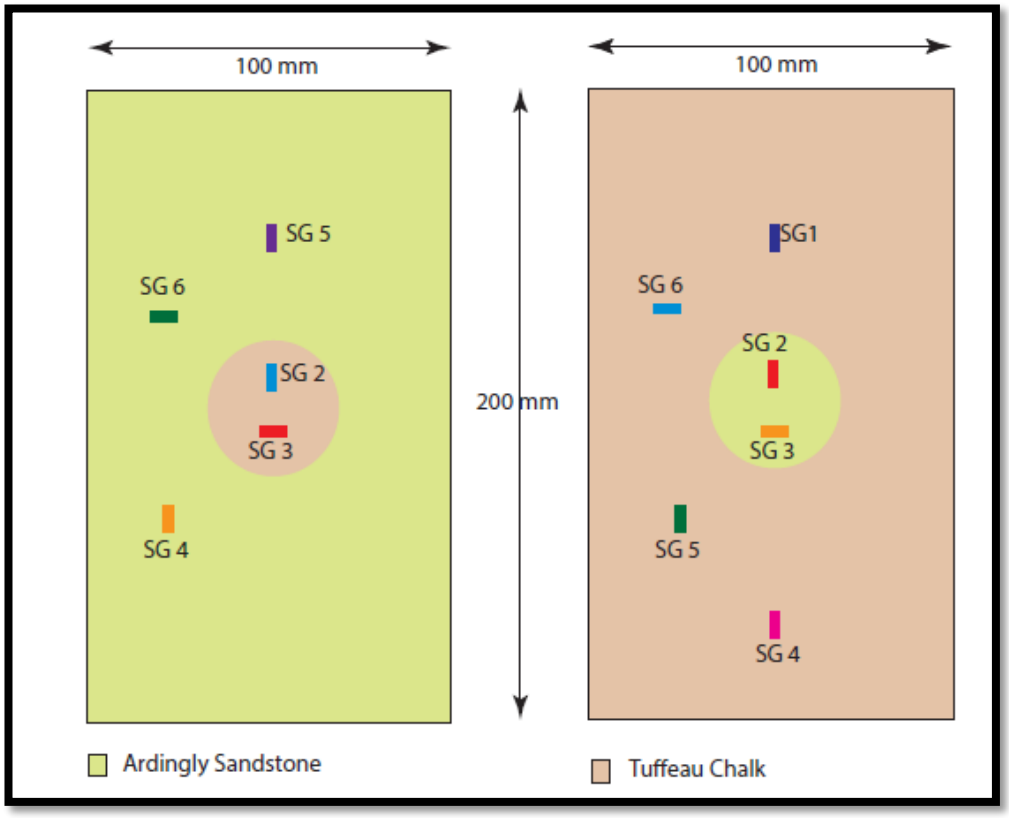

Figure 3.10. Location and orientation of strain gauges mounted in sandstone and chalk.

3.4.5 Data acquisition system

The compression test was carried out at the geotechnical testing facility at the University of Brighton. The compression system consists of an Instron 8500 digital control with a 4000 N load cell (Figure 3.11). The rate of displacement of the load cell was set to 0.04 mm/second until failure occurred. Strain and LVDT data were acquired using a NI DAQ system with individual modules for strain and LVDT acquisition, respectively (NI–9237), plugged into a chassis board (cDAQ–9178) connected to a laptop. Strain, LVDT and loading data were acquired at intervals of 0.5 seconds and saved in Excel file format for analysis. Several photographic images were captured during the compression tests to record the successive intervals of crack initiation and propagation, leading to the development of fractured surfaces.

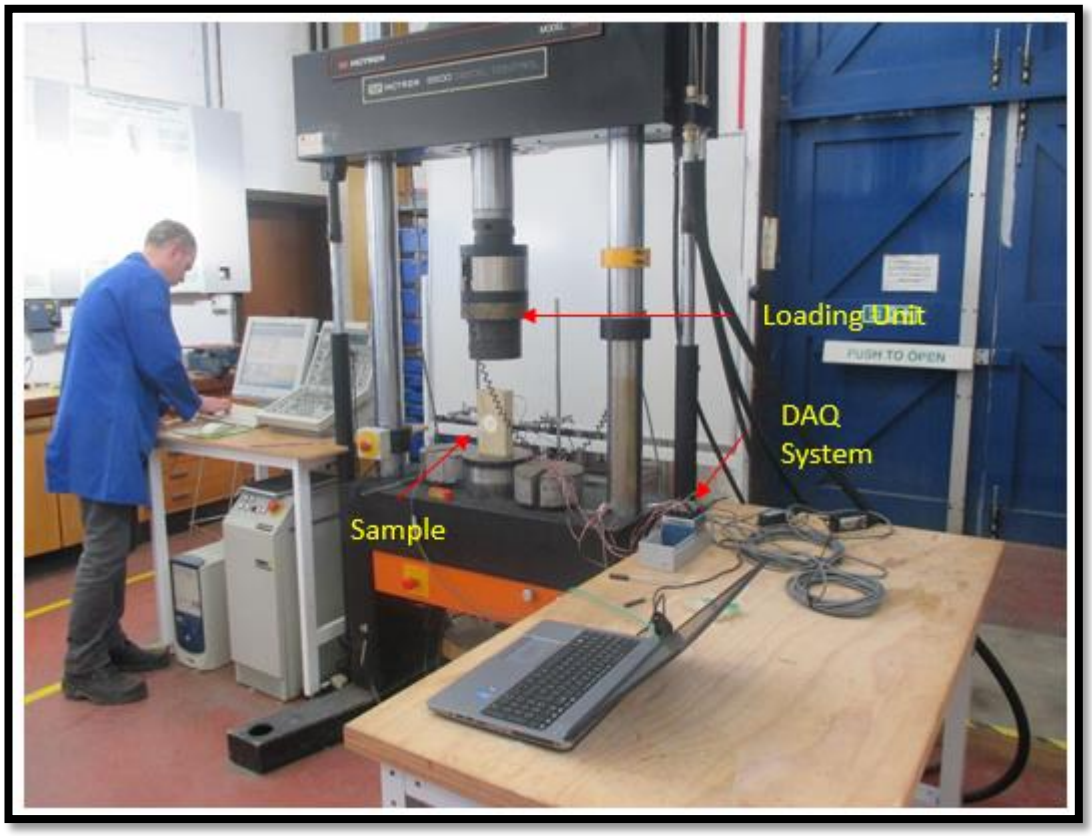

Figure 3.11. Set up for compression testing Instron 8500 digital control system.

3.5 Macroscale experiment

3.5.1 Sample preparation

The two rock types were cut into three cubic blocks measuring 300 x 300 x 300 mm. Blocks 1 and 2 were Ardingly Sandstone (B1 and B2), and block 3 was tuffeau chalk (B3). The block size is sufficient for macroscale fractures to develop at a size almost comparable to those at field scale (Murton et al., 2001, 2006). To examine the effect of defects (bedding planes) on cracking mechanisms, the two sandstone blocks were placed at different orientations in the freezing tank. Block 1 had its bedding oriented horizontally to simulate the common scenario where bedding planes are aligned parallel to isotherms beneath a horizontal land surface. Block 2 had its bedding oriented vertically, at right angle to the isotherms, to test the effect of anisotropic permeability on rock response to freeze–thaw cycling following objective 4.3 (O4.3). The three blocks were air dried in ambient laboratory conditions.

The blocks were drilled prior to placing them in the experimental tank and installing sensors. Five holes 6 mm in diameter and 45 mm long were drilled horizontally to contain the temperature sensor (Pt-100 resistor) in each block. The holes were aligned along the central vertical axis on the vertical face D for each block, with 50 mm apart from each other (Figures 3.12–3.14) in order to monitor the vertical thermal profile of the blocks. Eight acoustic emission (AE) sensors were mounted on the chalk block (B3), with two on vertical faces A, B and C, one on face D and one on the top (Figure 3.14), as detailed in section 3.5.4.2.

Strain gauges were mounted on the vertical face using a two-component epoxy (X-60 two component adhesive, HBM) and aligned along the vertical axis, which was 10 mm apart from the central vertical axis. The dummy gauges were mounted on a ruler of 300 mm length (which is similar to the height of each blocks of rock). To fix the dummy gauges next to the actual gauges, two additional holes, 3 mm in diameter and ~25 mm long, were drilled near the top and the bottom of the samples such that the ruler containing the dummy gauges could be placed adjacent to their real counterparts. The foot of the LVDT sensors rested on the top face of each block to detect any vertical movement (i.e. heave and settlement) during the experiment.

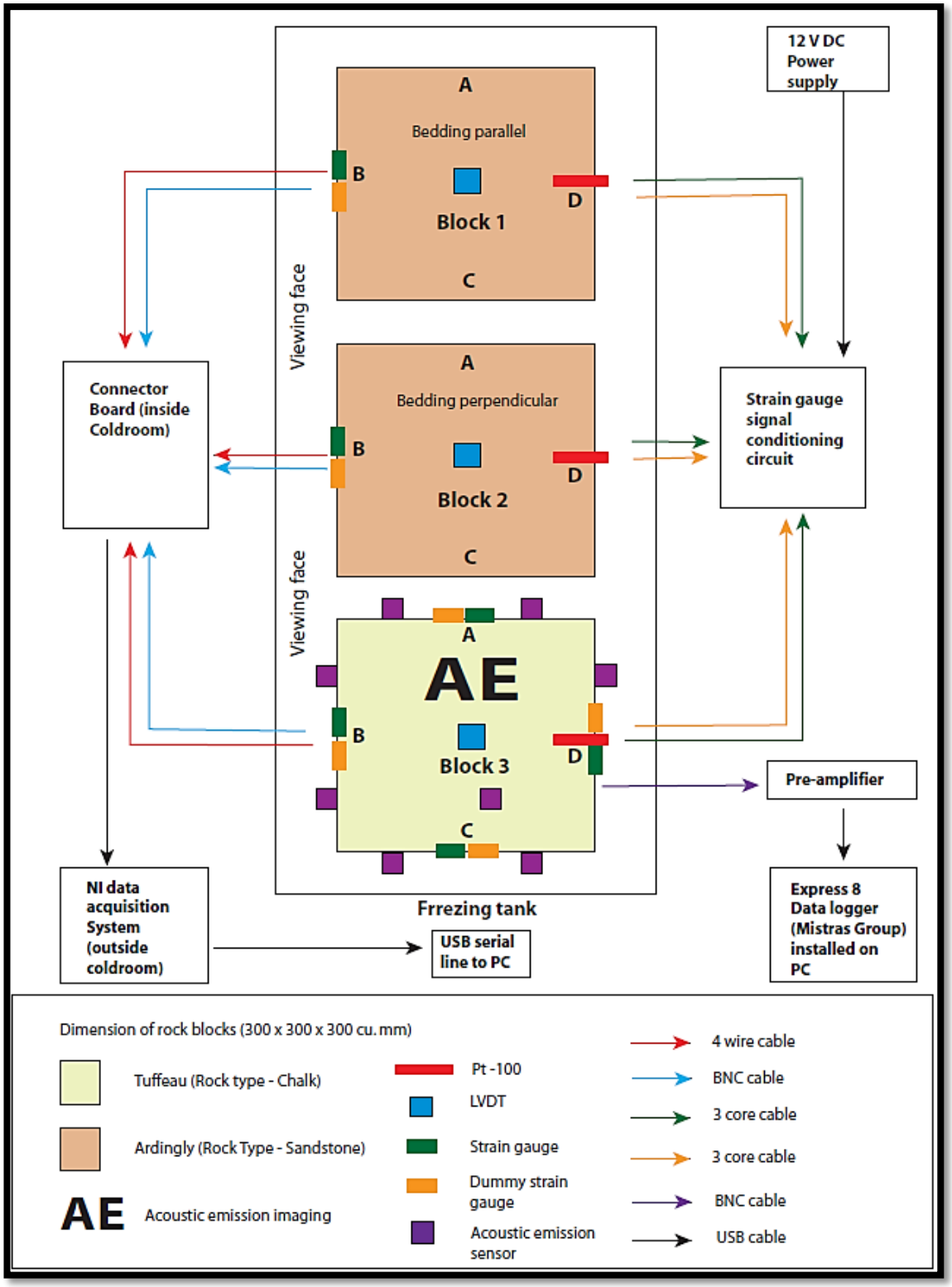

Figure 3.12. Plan view of macroscale freezing experiment in the Permafrost Laboratory.

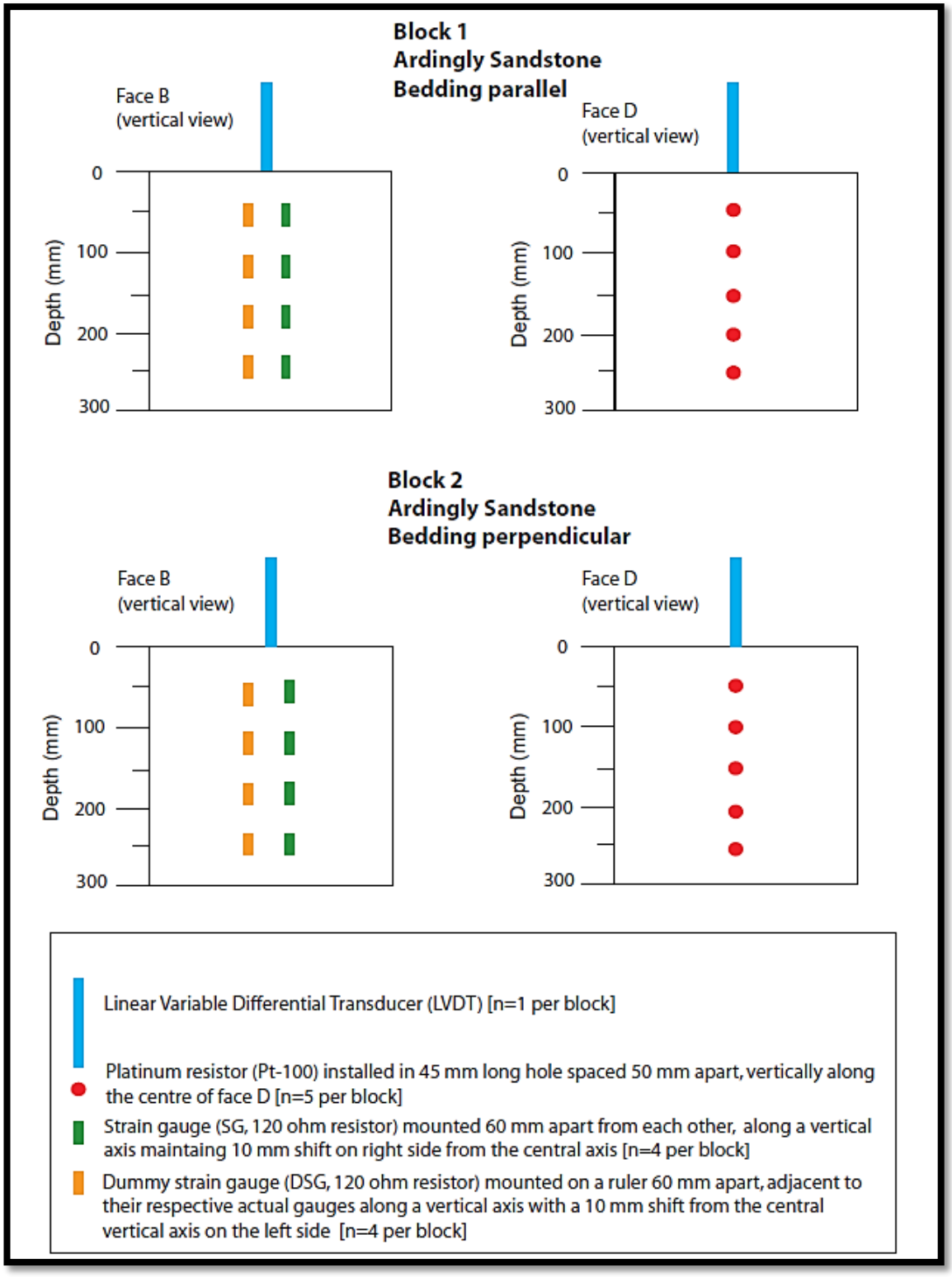

Figure 3.13. Diagram showing the location of Pt-100s, LVDTs and strain gauges in the block of Ardingly Sandstone.

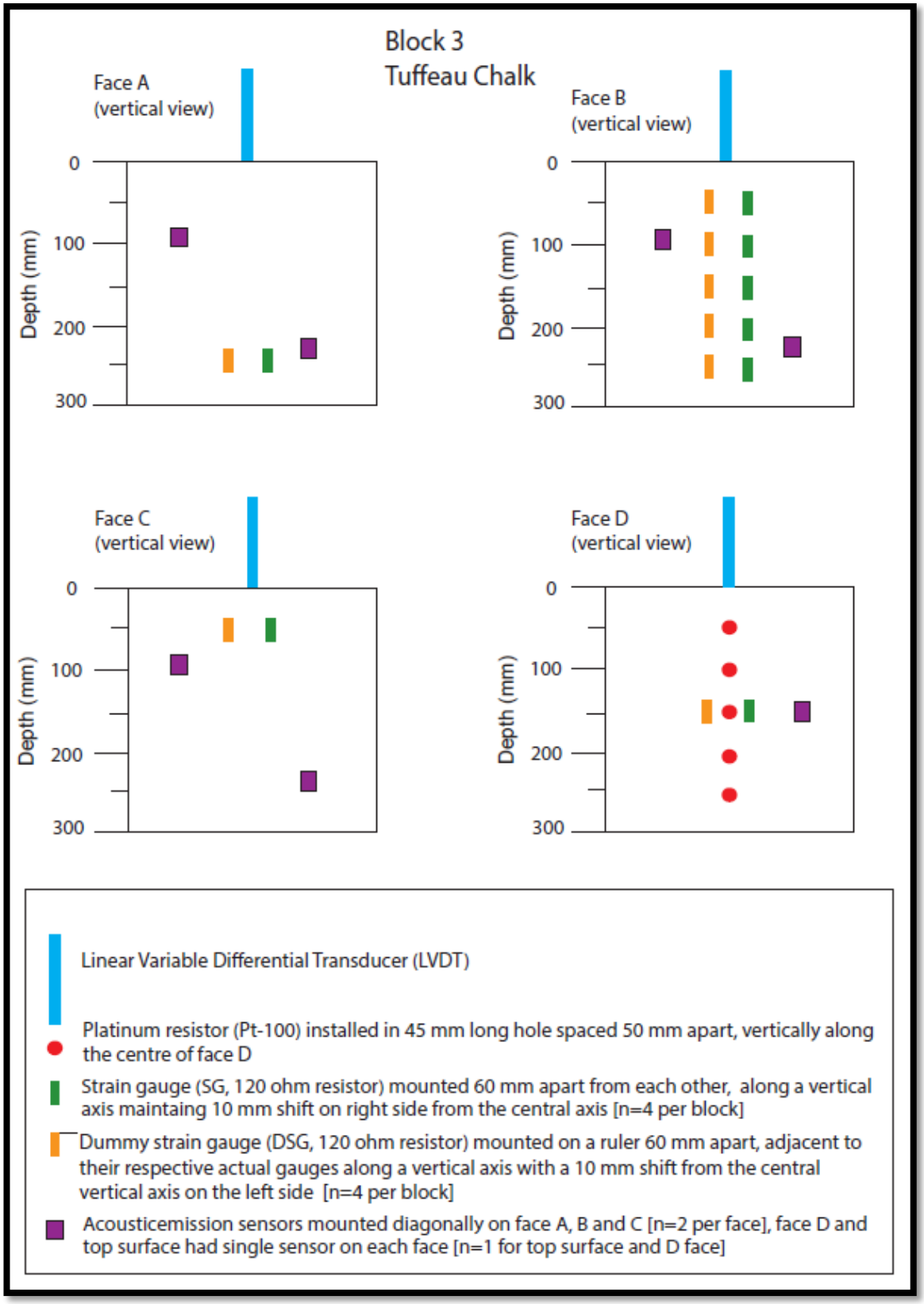

Figure 3.14. Diagram showing the location of Pt100s, LVDTs, strain gauges and AE sensors in the block of tuffeau chalk.

3.5.2 Freezing system and cold-room description

The cold room has two types of freezing system. One controls the ambient air temperature to simulate winter, while the other one controls the temperature of a cooling plate that can simulate permafrost independently of air temperature. The air and cooling plate temperature can be set from –20 to +20^{o}C and adjusted in the control panel located outside the cold room. The temperature control has been changed during freeze–thaw cycling to accomplish objective 4.1 (O4.1).

Air temperature allows the rock blocks to cool progressively downward, while the cooling plate underneath the rock blocks causes upward freezing of each block. To simulate thaw cycles (summers), the air cooling system is turned off and the door of the cold room is opened. This allows warm air to enter the cold room and initiate downward thawing from the top surface of the blocks. During freezing cycles, the air cooling system initiates downward freezing of the blocks, while the basal cooling plate initiates upward freezing. These produce sub-zero temperatures throughout the blocks and simulate frozen-ground conditions. During thaw cycles, the zero degree isotherm fluctuates between 100 and 150 mm depth from the top face, simulating an active layer above the permafrost table.

The cold room contains an aluminium tank with internal length, width and height of 1895 X 750 X 500 mm, respectively. The cooling plate is a tabular block with dimensions of 1500 X 600 X 50 mm, hollow inside and connected to a gas container that circulates cooling fluid into the hollow space inside to reach the require freezing temperature. The cooling plate rests upon a polystyrene sheet that separates it from the aluminium tank bottom and insulates the bottom.

Each block of rock was laid upon the cooling plate using four acetyl pillars with a diameter and thickness of 40 and 10 mm, respectively, placed beneath the corners. Water was added into the tank to set a water table ~10 mm from base of the blocks such that water could be drawn into them by capillary action. The rate of capillary rise varied between the three blocks. The sandstone block with bedding oriented vertically (B2) had the fastest capillary rise front, while the block of chalk (B3) had the slowest rate. The sandstone block with the bedding horizontally oriented (B1) had an intermediate rate of capillary rise (Figure 3.15). The blocks were left out in the laboratory for several days with the imposed water table in order to saturate completely as evident by the capillary front reaching the top horizontal surface prior to begin the experiment.

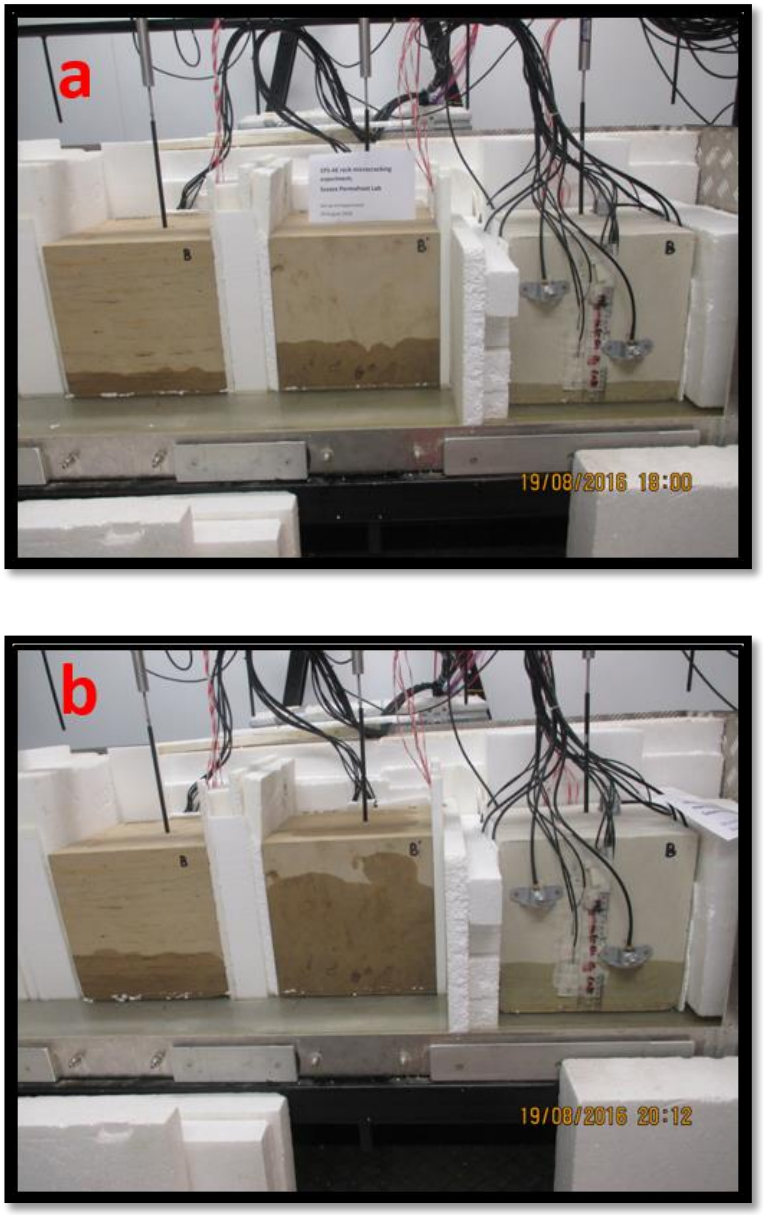

Figure 3.15.Photographs showing the rising capillary front during different stages of block wetting (a) Initial stage, (b) two hours later. Note the more rapid wetting of block 2 (vertical lamination) compared to block 1 (horizontal lamination) of Ardingly Sandstone. The tuffeau block is on the right.

The space between the aluminium tank and the vertical faces of the blocks was filled with polystyrene block of various sizes to provide insulation and minimise lateral heat transfer. The purpose of this was to set up a vertical temperature gradient during the freeze–thaw cycles.

All three blocks started freezing from the surface downward, controlled by the chilled air system. When the temperature at the bottom of the blocks reached –10^{o}C, the cooling plate beneath

the blocks was turned on to maintain permafrost in the lower part of the blocks throughout the experiment. The experiment consisted of consecutive freeze (air temperature < 0°C) and thaw (air temperature > 0°C) cycles.

A total of 12 freeze–thaw cycles was conducted over a duration of 315 days. This period of time is subdivided into three phases: P1 (freeze–thaw cycles 1–4), P2 (freeze–thaw cycles 5–8) and P3 (freeze–thaw cycles 9–12). The location of the 0°C isotherm was interpolated from the temperature profile plot of the blocks to estimate the depth of the active layer during each thawing period (simulated summer).

3.5.3 Monitoring strategy

The strategy for monitoring the rock samples during the experiment equipped them with sensors to compare the changes developed during repeated freeze–thaw cycles. The experimental setup permits assessment of the influence of rock type, bedding orientation and weathering status on fracture initiation and development. The experiment was designed to record continuously measurements of imposed thermal gradient, surface heave and settlement, mechanical deformation, and elastic energy released during mechanical deformation and their corresponding locations. A single time clock was maintained for all data acquisition during the experiment to maximise confidence on correlating events captured by various sensors (Table 3.3). Several digital photographs were taken before, during and at the end of the experiment and analysed to correlate crack development with monitoring data.

Method	**No. of sensors/ Measurement**	**Sampling Frequency**	**Measurement Duration**
Temperature	5 per block, 3 blocks	Averaged over 10 min period	Instant
Heave	1 per block, 3 blocks	Averaged over 10 min period	Instant
Strain	For sandstone, 4 per block, 2 block For Chalk, 8 per block, 1 block	Averaged over 10 min period	Instant
Acoustic Emission	8 per block, Chalk block	Minimum 4 hits for each event	Continuous

Table 3.3. Data acquisition parameters and measurement protocol for the macroscale experiment in the Permafrost Laboratory.

3.5.4 Acoustic Emission System: Microcracking activity

3.5.4.1 Working principle

Acoustic Emissions (AEs) are defined as "The class of phenomena whereby transient elastic waves are generated by the rapid release of energy from localised sources within a material, or the transient waves so generated" (ASTM E1316-2010). AE detection is a non-destructive method of testing material based on detection and conversion of high-frequency elastic waves into measureable discrete electrical signals (Goszczyn´ska et al., 2014). Such action is accomplished by coupling piezoelectric transducers directly mounted on the surface of the material or structure tested.

The transducer element used in an AE sensor is a piezoelectric crystal that responds with high sensitivity to motion in the low ultrasonic frequency range (10–2000 kHz). While the AE wave front arrives at the surface of the test specimen, minute mechanical movements of the surface molecules are detected by the transducer and converted to useable electrical signal. The captured electrical signal is then amplified and split into discrete waveforms with characteristics such as amplitude, absolute energy and rise time for further analysis.

While multiple sensors are arranged in a definite array within a structure, the location of any AE activity can be estimated in three-dimensional (3D) space using complex algorithms. The calculation considers the velocity of the elastic wave within the material and the difference in hit arrival times among the sensors to precisely locate the source. By arranging multiple sensors in an order, it is possible to inspect an entire structure remotely.

3.5.4.2 Instrumentation

Eight AE sensors (R-15 alpha, Mistras Group) were mounted on five faces of the chalk block (B3) to explore objective 3.2. A 3D Cartesian co-ordinate system was introduced and the sensors were distributed to capture any single cracking event. On each vertical face A, B and C, two AE sensors were mounted diagonally, while in vertical face D and the top horizontal surface contains only one sensor each. The sensor on the top monitored the depth of cracking and therefore is thought to have improved the vertical resolution for detecting the 3D cracking locations (Figures 3.12 and 3.14).

The AE sensors were mounted on the vertical face with silicon grease epoxy (Pro silicone grease 494-124, RS Component) to establish a good contact between the smooth ceramic sensor face

and the rough rock surface. The use of permanent epoxy damages the sensors and provides a restriction on using them further in the future. The epoxy used in the present experiment could not hold the sensors indefinitely on the vertical faces, and therefore a metal cage was introduced to hold the sensors securely in place (Figure 3.16).

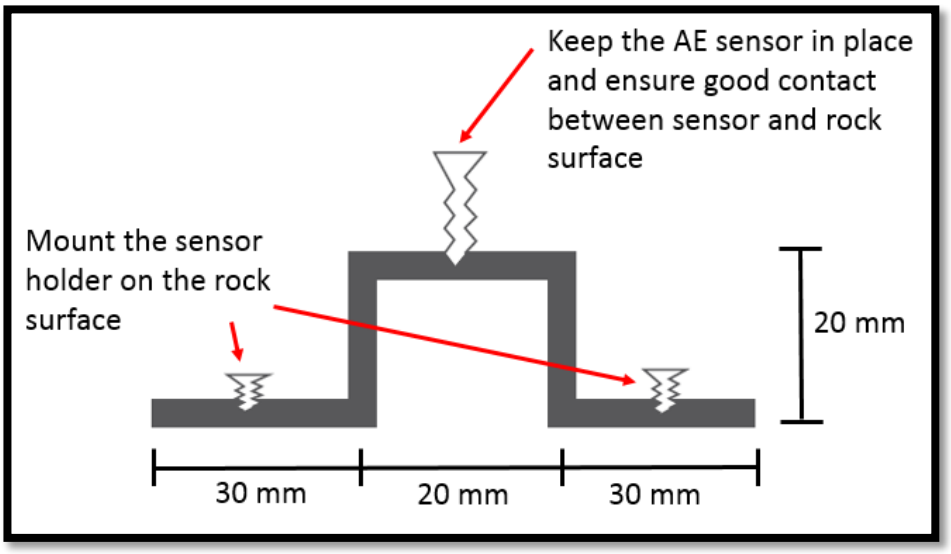

Figure 3.16. Geometry of the acoustic emission sensor holder.

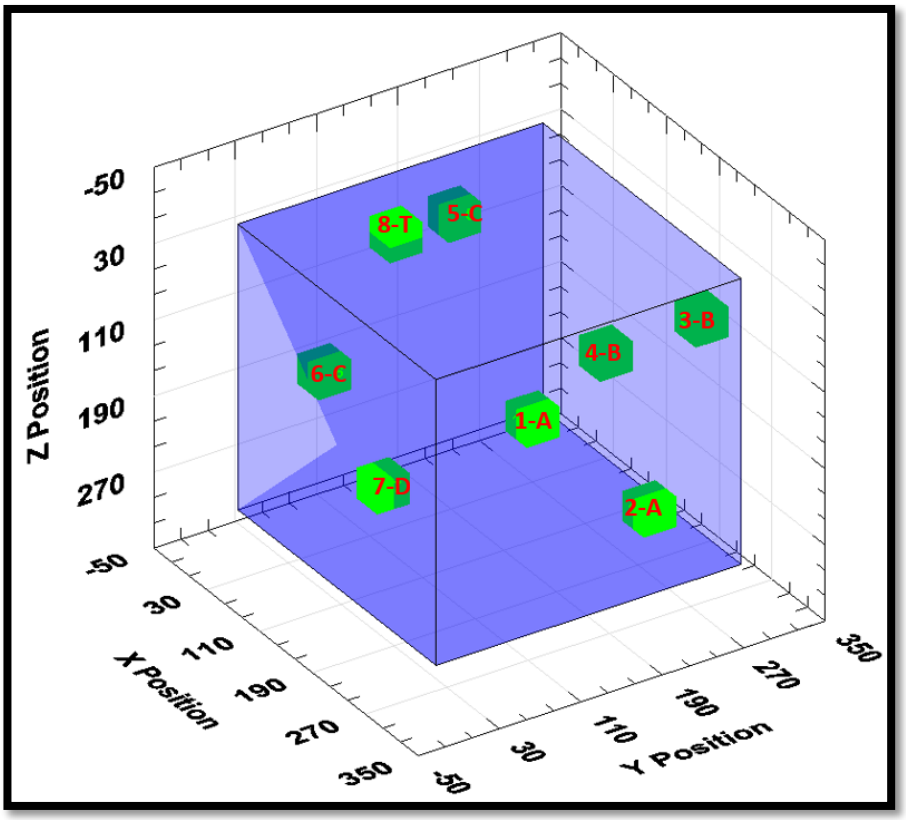

Figure 3.17. Layout of eight acoustic emission sensors in 3D Cartesian co-ordinates (Scale in mm). Number indicates the serial number of the sensors and the letter indicates the face of the block. Source: AEWin3D location detection software.

Two additional holes were drilled (3 mm in diameter and ~25 mm long) to mount each cage. Plastic raw plugs were inserted into the holes to anchor the cage firmly with screws. The sensors were pushed further towards the rock face by providing an additional linear torque that is adjusted by a screw on the top of the cage. Thus, the sensors were firmly pressed against the vertical faces during the experiment.

The sensors were connected to a preamplifier (IL40S with 32–1100 kHz, Mistras Group) with a cable 1.5 m long and placed inside a box in the cold room. The operating temperature of the sensors and preamplifier was within the limits of the temperature regime used in the experiment. The preamplifiers were activated by a 28V DC phantom power supply from the PCI Express-8 data card installed in the workstation. A 10-meter-long BNC cable was used to connect the preamplifiers and data card installed in the workstation outside the cold room.

3.5.4.3 Data acquisition system and measurement protocol

The data acquisition system for AEs was manufactured by Mistras Group. The signals captured by the sensors were routed through a preamplifier and sent to a PCI Express-8 card installed in the workstation located outside the cold room. The rest of the operation is controlled by AEWin software with an added plug-in capable of detecting the location released energy.

A threshold of 40 dB was set to separate noise induced in the laboratory from signals of microcracking events. The preamplifier added a 40 dB gain to the signal captured by the sensors. The analog and digital filters used in the preamplifier had ranges of 20–400 and 8–40 kHz, respectively. The sampling rate was set to 1 MHz and the values for peak definition time (PDT), hit definition time (HDT) and hit lockout time (HLT) were set at 200, 800 and 1000 microseconds, respectively. Every hit captured by the sensors included the parameters amplitude, energy, counts, duration, average signal level (ASL), rise time, average frequency, signal strength and absolute energy.

The data acquisition system continuously collected the data and recorded if any event was detected. The AE events were classified on the basis of the number of minimum hits (n=4) captured by AE sensors. The events were displayed on a graphical interface in AEWin, showing their location within the block. The number of hits and amplitude were considered to eliminate and filter out the noise generated due to the freezing system. The system produced a file containing the details of events at 12-hour intervals.

3.5.4.4 3D location detection principle

An additional plug-in code was added to the AEWin software to detect the 3D location from where AE signals originated. This took into account the array of sensors around the block with respect to a fixed Cartesian reference frame and the velocity of acoustic waves propagating through the material (longitudinal wave velocity, shear wave velocity, surface wave velocity). Hits and events were classified based on their arrival times at different sensors around the block. The 3D locations were visualised on a graphical interface in which the sources of the acoustic waves were plotted within a transparent cubic block.

The acoustic wave velocity of the entire block was assumed to remain constant throughout the experiment. This assumption is reasonable when the rock was frozen (i.e. during the middle to late stages of freezing cycles). However, during the thawing cycles slight differences in acoustic wave velocity may have developed between the permafrost and active layer above it.

3.5.5 Temperature: Freeze–thaw cycles

3.5.5.1 Working principle

There are various methods available for measuring temperature, but resistance temperature detector (RTD) has the best accuracy over a wide range of temperature. The Pt-100 sensors have a resistance of 100 ohms at 0°C, with a good linearity and repeatability over a broad range of temperature (–15 to 30°C). The resistance–temperature relationship is not perfectly linear, and therefore some standards are used to approximate the linearity. Two equations are used to measure the temperature above and below 0°C (International Electrotechnical Commission 60751:2008),

$$R_T = R_0(1 + AT + BT^2), \quad T > 0 \qquad (3.10)$$

$$R_T = R_0[1 + AT + BT^2 + C(T - 100)T^3], \quad T < 0 \qquad (3.11)$$

where T is the temperature; R_T and R_0 are the resistance at temperature T and 0°C, respectively; and A, B and C are known as Callender-Van Dusen coefficients. There are different wire configurations for measuring temperature with RTDs, but the 4-wire configuration reduces any error caused by wire resistance.

3.5.5.2 Instrumentation

Each block of rock was equipped with five Pt-100 sensors (British Rototherm Co Ltd.) in a linear array along the central vertical axis of face D. The sensors have a metallic cover around the 4-wire platinum resistor and a calibration of 100 Ω at 0 °C. The resistance changes linearly with changes in the ambient temperature. The sensors were installed within holes 6 mm in diameter

and 45 mm long drilled along the central vertical axis of a vertical face, spaced 50 mm apart. After inserting the sensors into the holes the gaps were filled with a mixture of rock dust (produced during drilling of the blocks) and gypsum (2:3 ratio). A dilute solution of gypsum ($CaSO_4$, $2H_2O$) was used to seal the outer part of each hole. Overall, such filling ensures a good contact between the temperature sensors and the rock (ASTM C842). Prior to installation, the sensors were calibrated in an ice–water bath (0°C) and checked by a digital thermometer (Fisherbrand Traceable Digital Thermometer, FB50266) with a precision of up to three decimal places.

3.5.5.3 Data acquisition system and measurement protocol

Electrical pulses detected by the sensors were acquired using the National Instruments (NI) Compact DAQ multiplexed USB data acquisition system (Model NI cDAQ - 9172) and processed using the graphical interface LabVIEW. Each chassis can accommodate up to eight modules and is powered by 12V DC power supply. The module used in the experiment (9205) can accommodate either 16 differential-ended analog inputs or 32 single-ended analog inputs, or a combination of them. Acquisition channels and acquisition data types can be configured and adjusted using the NI-Max interface. The DAQ system can measure the signals ranging from +10V to –10V.

The differential voltage data from the Pt-100 sensors were routed through the NI-DAQ system into a workstation located outside the cold room, where the temperature profiles were displayed on graphical interface of LabVIEW using 10-minute live streaming.

Mean values of continuous 10 minute logging data were recorded into a text (.txt) file format at 10 minutes intervals and the LabVIEW virtual interface was programmed to generate a single text file of all the temperature data recorded at 24-hr intervals.

3.5.6 Surface heave and settlement

3.5.6.1 Working principle

Surface heave and settlement were measured with linear variable differential transformers (LVDTs) to achieve objective 3.1 (O3.1). An LVDT is an electromechanical transducer that converts linear motion into electrical signal. LVDTs are mechanically coupled with a sample and any changes in the position of the sample is reflected as a linear motion that is converted into electrical signal to measure the linear motion. The moving component of an LVDT (the core) can move freely along the central axis within the cylinder inside a coil. The core is composed of magnetically permeable material. The primary winding P in an LVDT is energised by an alternating current of appropriate amplitude and frequency, known as primary excitation. The

output signal is the difference in AC voltage between the two secondary windings S_1 and S_2, which changes with the relative position of the core within the LVDT coil (Figure 3.18). AC output voltage is then converted into suitable DC voltage.

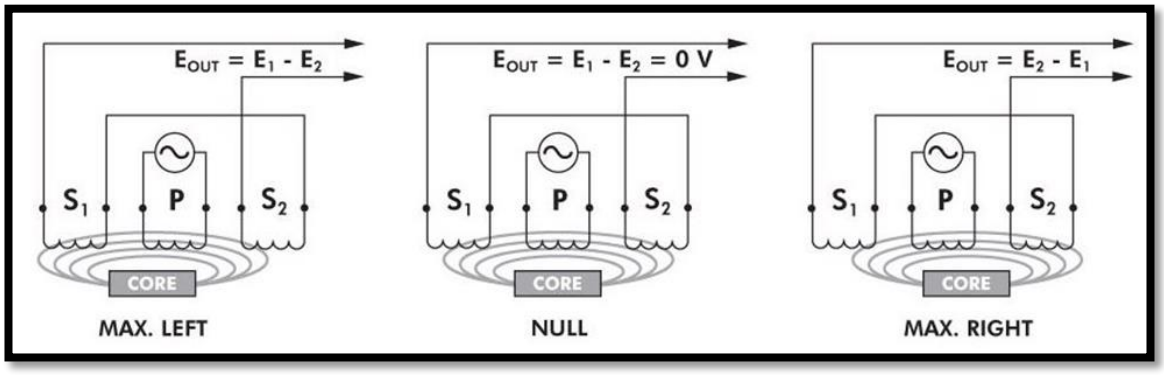

Figure 3.18. Working principle for LVDT to measure movement. The figure illustrates three cases when the LVDT core is in different axial positions. . Source: TE connectivity - LVDT tutorial.

3.5.6.2 Instrumentation

Heave and settlement of the block tops were measured by LVDT model LDC 1000C, manufactured by RDP Group. The foot of the LVDT rested on the middle of the top face of each rock block. Each LVDT was calibrated individually using different metal slips of known thickness (1–10 mm), using a metric gauge block set (Block-47, Grade-1, No. 090155), prior to the experiment. A linear correlation function between the voltage and the displacement was established for each LVDT and later used to convert the acquired voltage values into detectable vertical displacement. An additional acetyl rod (8 mm in diameter) of adjusted length was screwed on to each LVDT leg such that the voltage value reaches the most sensitive state in response to any small vertical displacement (near the centre of the core).

3.5.6.3 Data acquisition system and measurement protocol

Data acquired used the NI Compact DAQ multiplexed USB data acquisition system and were processed with LabVIEW, similar to the set up used for temperature acquisition. The system continuously logged data and 10 minutes mean value were recorded into a text (.txt) format with a date and time stamp and generated an individual file every 24 hrs (see section 3.5.5.3 for more details).

3.5.7 Strain: Mechanical deformation

3.5.7.1 Working principle

Strain is a quantitative measure of the deformation of a body as a consequence of external stress force acting on it and can be either positive (tensile) or negative (compressive). Strain gauges

are generally used as a direct method for measuring strain. They are based on the principle that the electrical resistance of strain gauge component wire changes in response to the amount of strain retained within the body. Gauges are mounted on the face of test specimen using epoxy, such that strain retained within the deformed body can be transferred into the gauges.

A quantitative parameter called the gauge factor (GF) is used to measure the sensitivity of the strain gauge. This takes into account the ratio of fractional change in electrical resistance (R) to the fractional change in length (ε, strain):

$$GF = \frac{\Delta R/R}{\Delta L/L} = \frac{\Delta R/R}{\varepsilon} \qquad (3.12)$$

The small changes in resistance within the gauge are measured using a Wheatstone bridge configuration (Figure 3.19), with an excitation voltage (DC) supply. The Wheatstone bridge configuration consists of four arms each with a resistance. An excitation voltage V_{EX} is then applied across the bridge with an output voltage V_O, which is a function of resistors used in the bridge and the external power supply:

$$V_0 = \left[\frac{R_3}{R_3+R_4} - \frac{R_2}{R_1+R_2}\right] V_{EX} \qquad (3.13)$$

From the equation, it is apparent that when $R_1/R_2 = R_4/R_3$, the voltage output V_O is zero and the bridge is said to be balanced. Any change in resistance in any arm of the bridge results in a nonzero output voltage.

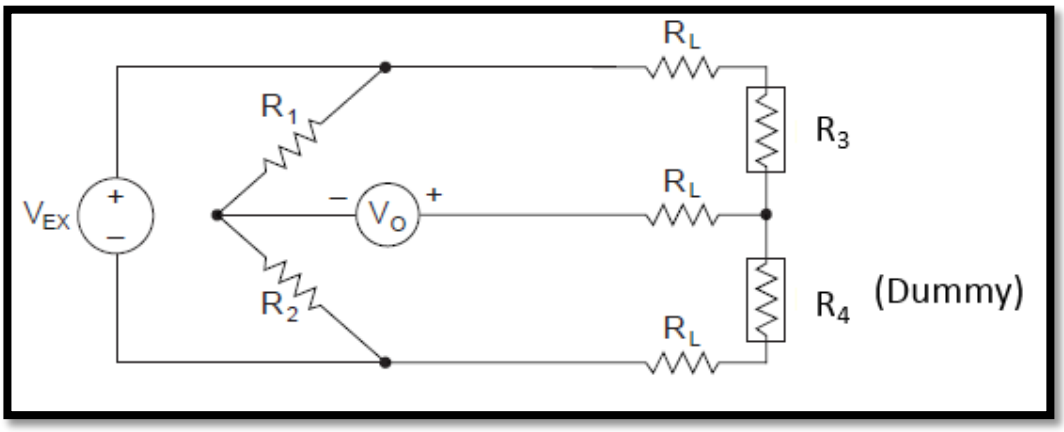

Figure 3.19. Quarter Wheatstone bridge configuration. (Source: National Instrument– Measuring strain with strain gauges, 2014).

The temperature effect further was minimized using two dummy strain gauges replacing the resistance arm on Wheatstone bridge configuration. Any changes in temperature affects both

the gauges equally such that the ratio of the resistors remains same and the effect of temperature change is minimised.

3.5.7.2 Instrumentation – (Dummy gauge concept to eliminate thermal strain)

Eight strain gauges were mounted on the chalk block, five aligned vertically on face B and one on vertical faces A, C and D (Figures 3.12 and 3.14). In addition, four gauges were aligned vertically on vertical face B of both sandstone blocks (Figures 3.12 and 3.13). Strain gauges mounted on different parts of the chalk and sandstone blocks to accomplish objective 3.1 (O3.1). The strain gauges had 120 Ω resistor values (RS Pro wire lead strain gauge, Part No. 632-124), with a gauge factor of two (which measures the sensitivity of the gauge). Before mounting the gauges on the rock face, the relevant parts of the rock were smoothed with sandpaper to ensure a good and lasting contact between the gauge and the rock. An epoxy of powder and liquid (X-60 two-component adhesive, HBM) was used to mount the gauges on the vertical rock faces. The same epoxy was also used to mount the dummy gauges on the plastic ruler (Figure 3.20).

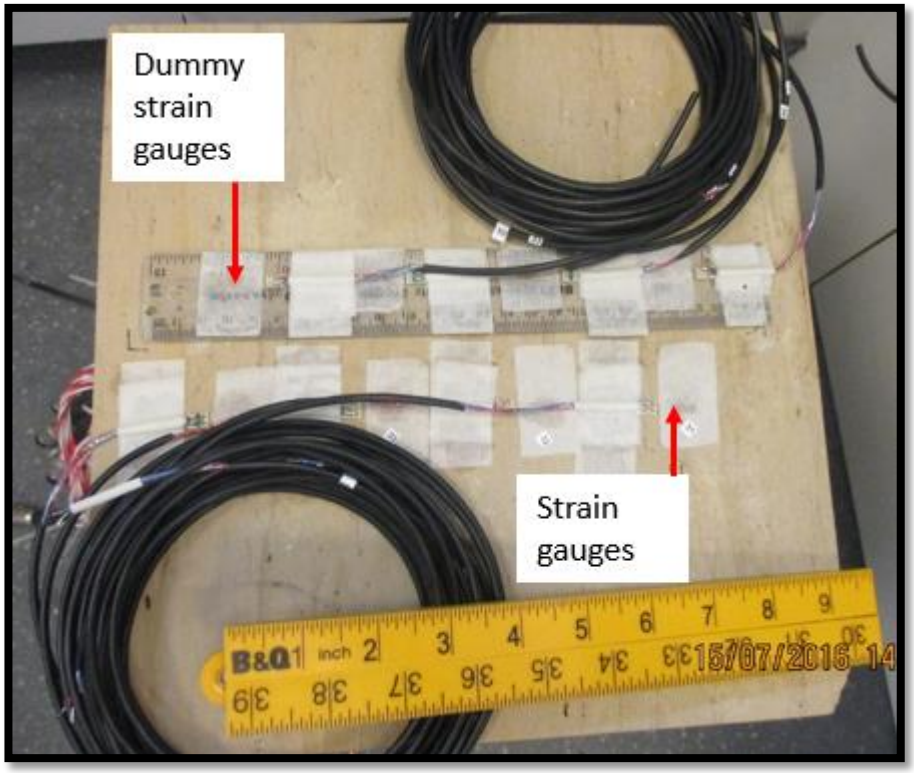

Figure 3.20. Strain gauges mounted on vertical face D of Ardingly Sandstone in a linear vertical array with their respective dummy gauges mounted on a ruler.

Dummy gauges were mounted on three plastic rulers, in the same layout as the real gauges on the rock surfaces. Two additional holes were made on the top and bottom of each scale to mount the dummy gauges adjacent to their real gauge counterpart.

The two-arm Wheatstone bridge circuit with 100 times gain (16-signal conditioning electrical circuit) was encased within a thermally insulated box inside the cold-room to minimise the noise it causes in long wire cables.

Prior to the experiment, the 16-signal conditioning electrical circuit was calibrated in both extension and compression regimes to obtain a similar gain value. The error range was then further minimised, repeating the test in different temperature regimes to simulate the freeze–thaw cycles and establish a calibration curve for each signal conditioning circuit. The temperature ranges used to calibrate the circuits are within the limits of the temperature window used in the experiment.

3.5.7.3 Data acquisition system and measurement protocol

Data were acquired using the similar NI Compact DAQ multiplexed USB data acquisition system used for temperature and heave acquisition. Ten minutes mean data were recorded into a text (.txt) format with a date and time stamp and generates an individual file at 24 hr intervals.

Chapter 4

Results–Image Analysis

4.1 Introduction

Chapter 4 presents the findings and analyses of repeated μ-CT scans of the small rock cylinders for 20 cycles of unidirectional freezing. The progressive development of the fracture phase after repeated scanning of the specimens was visualized using the rendering software called 'Drishti'. Following the objective 2.1 (O2.1) outlined in chapter one, the morphology of the visible cracks is compared with the growing cracks identified in the repeated images. Possible weak zones that initiated and developed cracking are identified. Strain induced during the course of freezing and thawing is measured based on the shift in pixels of identical spots used as marker pairs to address objective 2.2 (O2.2). Considering the heterogeneous nature of rock samples at small scale, the morphological development of cracks is assessed using three statistical functions that correlate the probability of finding points, clusters and linear movements in the fracture phase. The consistent linear growth of the crack phase is identified as informative and therefore analyzed in detail.

4.2 Micro-CT imaging of small core specimens

Two core cylinders (20 mm in diameter and 30 mm long) of tuffeau chalk and Ardingly Sandstone were scanned repeatedly after defined numbers of freeze–thaw cycles. Figure 4.1a–c shows the damage resulting in both specimens after 20 cycles. Figure 4.1a displays an inclined vertical crack in the middle of the chalk. Dark patches in the chalk indicate the regions where loose material fell off during freezing and thawing. Following the 3D visualization of the chalk core in Figure 4.2, it is apparent that the inclined vertical crack in the middle was partially developed after freeze–thaw cycle 15 and became distinct after the 20th cycle. Figure4.1b shows a concentric vertical crack developed near the top surface in chalk as well as some areas from which small chunks of chalks spalled off following the formation of the concentric vertical crack. From figure 4.2, it is evident that some vertical penetration of the fracture phase took place during freeze–thaw cycles 10–15 and the concentric morphology developed during cycle 20. The sandstone, on the other hand, remained relatively intact after 20 freeze–thaw cycles (Figure 4.1c).

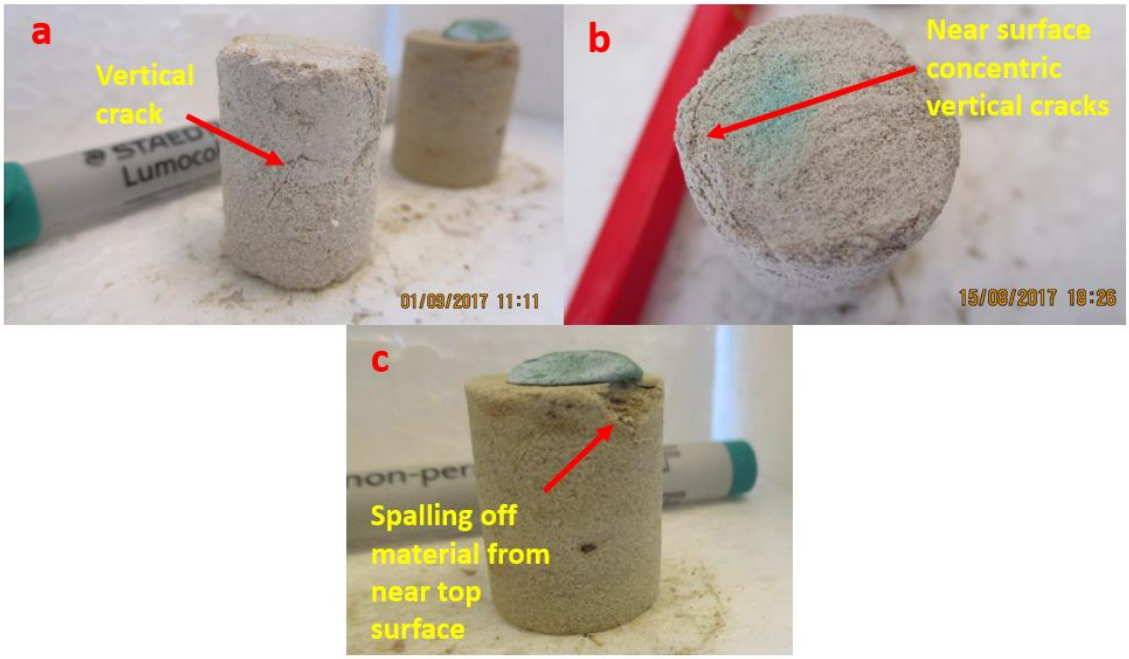

Figure 4.1. Photographs of core cylinders (20 mm in diameter and 30 mm long) after 20 freeze–thaw cycles (a) and (b) chalk, (c) sandstone.

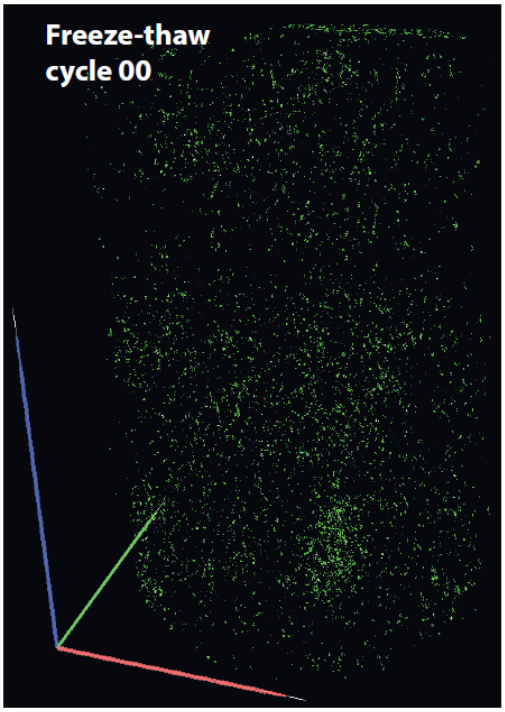

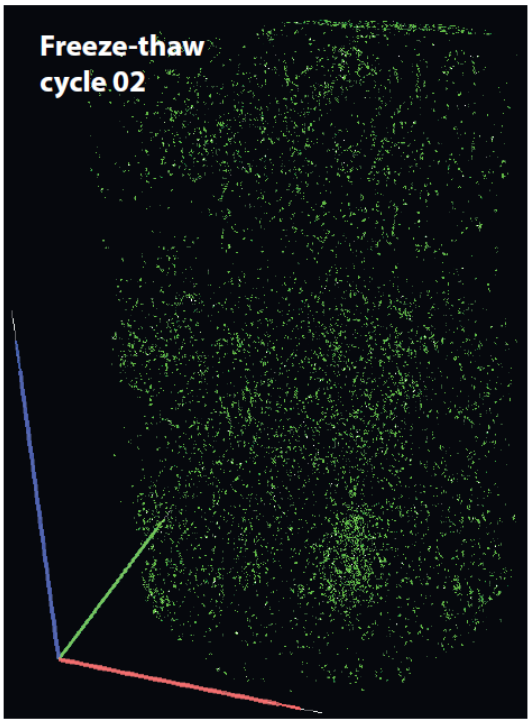

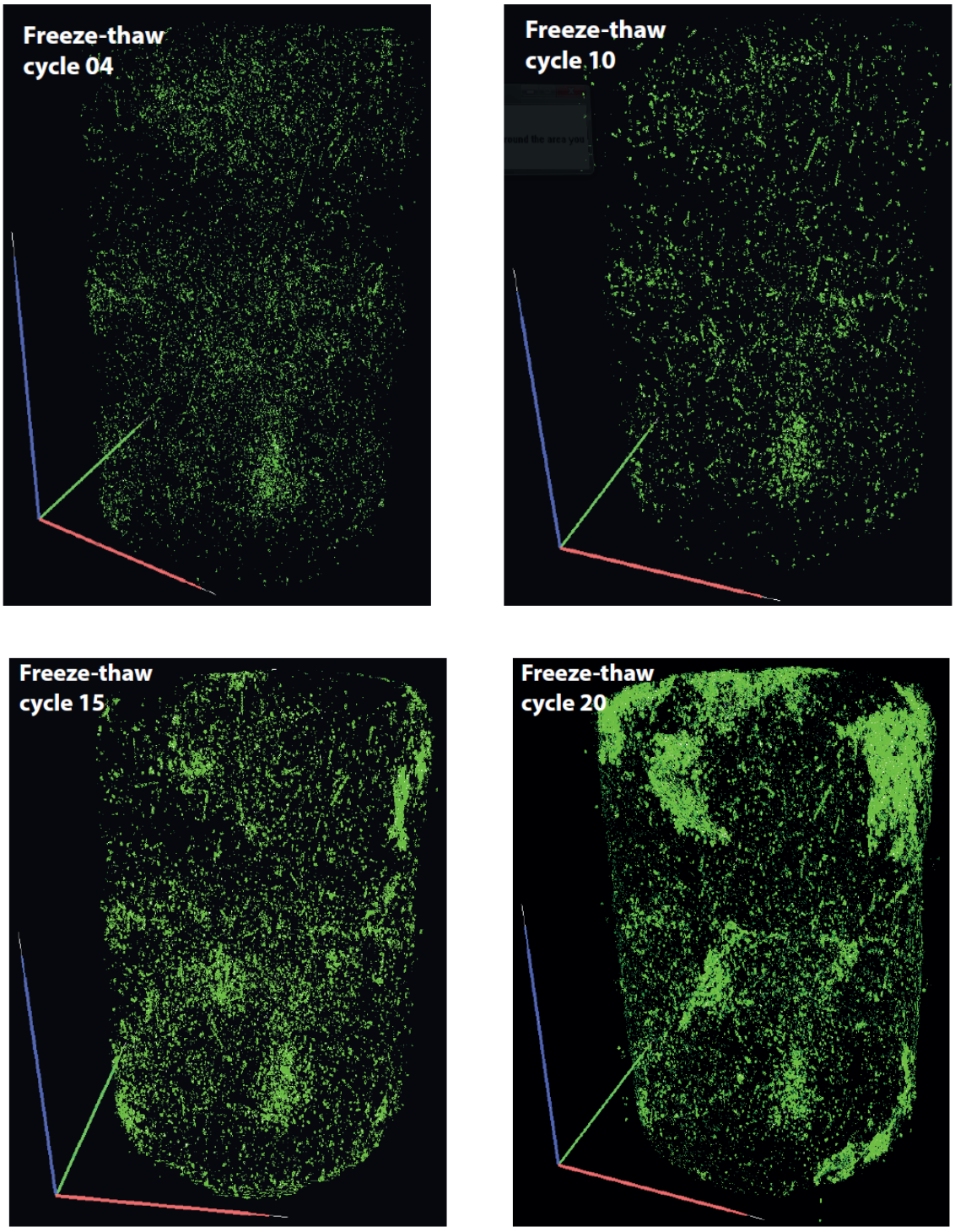

Figure 4.2. 3D visualization of the chalk cylinder (20 mm in diameter and 30 mm in length) showing the progressive development of the fracture phase after different numbers of freeze-thaw cycles.

The progressive development of concentric microcracks captured in the scanned images is shown in Figure 4.3a–c for freeze–thaw cycles 0, 10 and 20, respectively. The cracks developed near the upper boundary of the specimen (Figure 4.2). A crack visible near the bottom of Figure

4.3a–c was partially developed in the 10th freeze–thaw cycle along the grain boundary of a fossil fragment that was released in the 20th cycle. Measurement of transverse strain determined from marker points on repeated scans of the circular cross section of the specimen revealed mostly dilation (but some contraction in the middle of the core) during the first 10 freeze–thaw cycles, followed by widespread dilation during cycles 10–20 (see discussion in section 4.3).

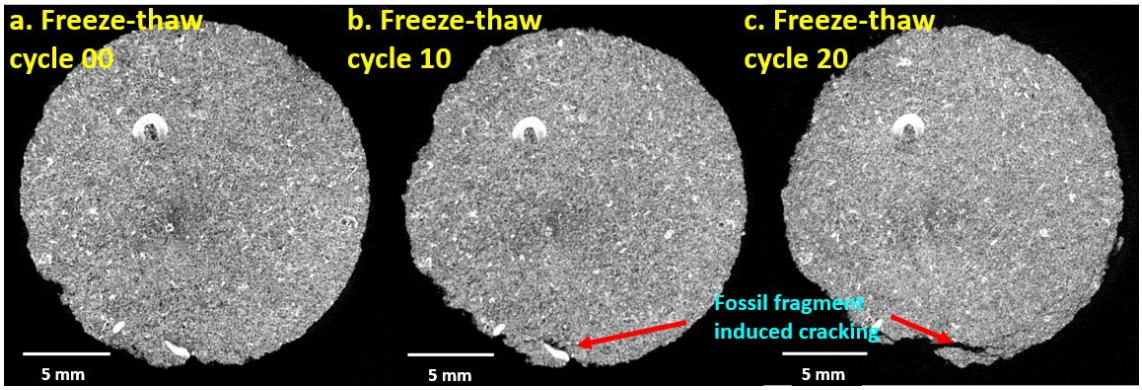

Figure 4.3. Micro-CT image slices showing the progressive development of near-surface concentric cracks in chalk after 0, 10 and 20 freeze–thaw cycles.

Figure 4.4a–c shows the development of a steeply inclined crack formed in the middle of the chalk core specimen. A faint crack is visible after10 freeze–thaw cycles, and a prominent crack is seen after 20 cycles. The aperture is greatest near the boundary and gradually decreases inward into the specimen. Strain measured following the protocol used for Figure 4.4a–c indicates dilation. Figure 4.5a–c illustrates the development of a concentric vertical crack at the bottom of the specimen which is further visualized in figure 4.2 near the base. The lower part of the specimen was enclosed within polystyrene, allowing limited heat transfer compared to the upper part. Therefore, the chalk is more damaged near the top compared to the base of the specimen.

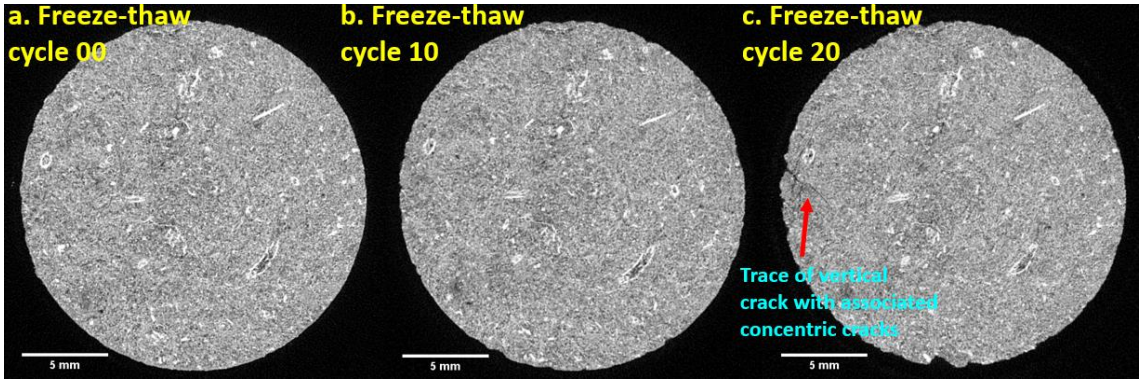

Figure 4.4. Micro-CT image slices showing a vertical crack developed in the middle of the chalk specimen after 0, 10 and 20 freeze–thaw cycles.

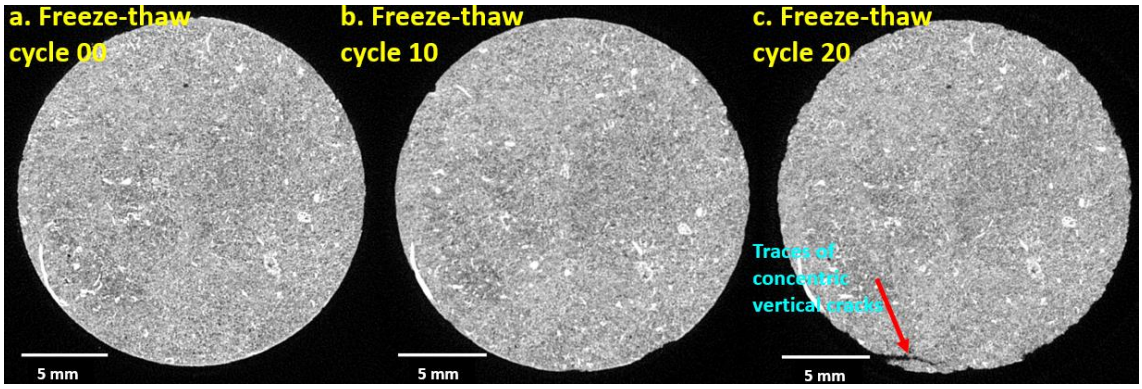

Figure 4.5. Micro-CT image slices showing a concentric vertical crack at the bottom of the chalk specimen after 0, 10 and 20 freeze–thaw cycles.

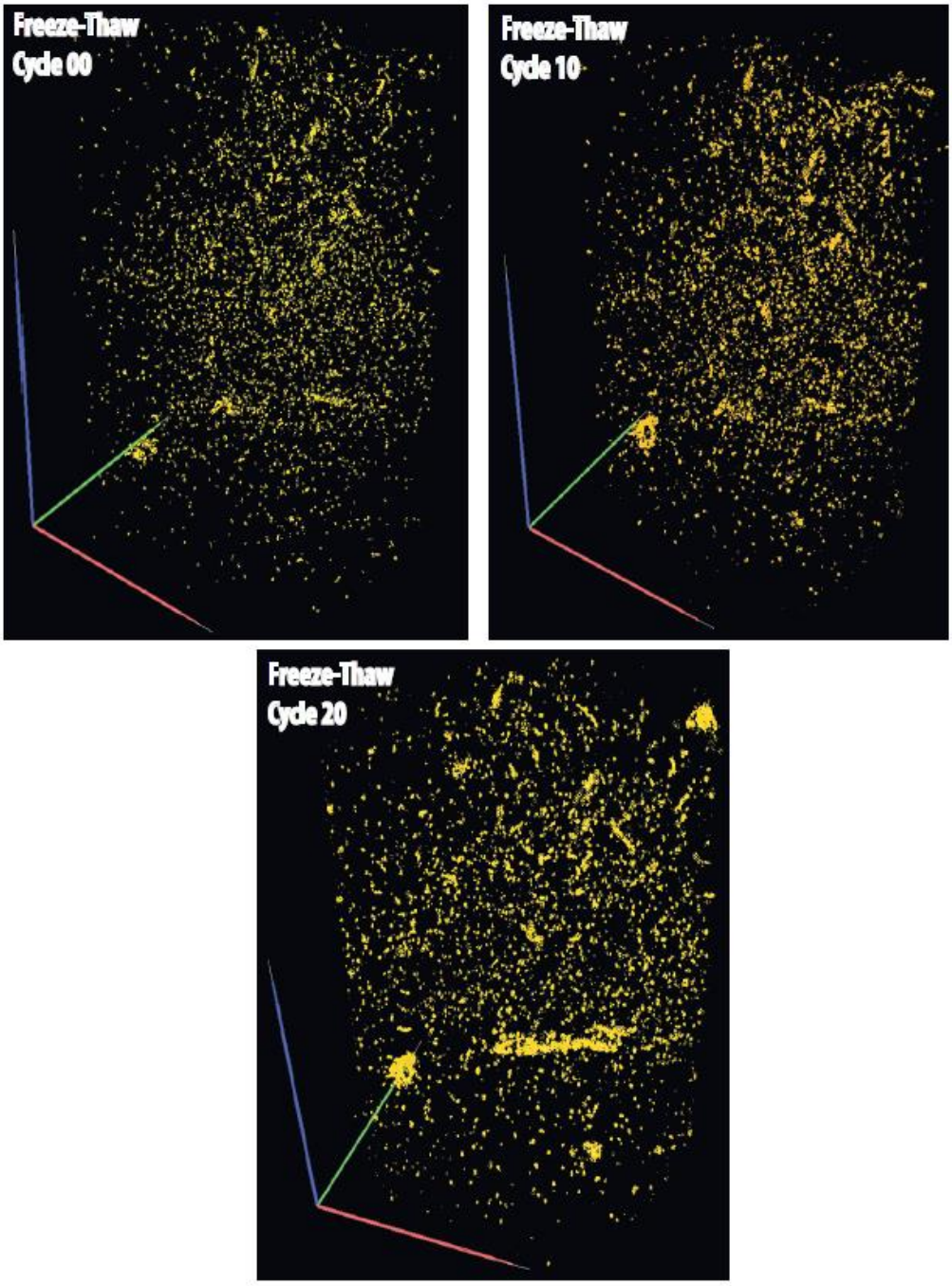

Figure 4.6. 3D visualization of the sandstone cylinder (20 mm in diameter and 30 mm in length) showing the progressive development of the fracture phase after different numbers of freeze-thaw cycles.

The spalling off of material from the top surface of the Ardingly Sandstone specimen induced by a pre-existing void is shown in Figure 4.6 and 4.7a–c. The shape of the crack observed after 20 freeze–thaw cycles followed the outline of the high-entropy material (white granular mass clustered in cone shape) seen after 0 and 10 cycles that formed a cone around the tabular void.

In addition, concentric cracks developed to the right of the principle void formed along the faint outline of the high-entropy material.

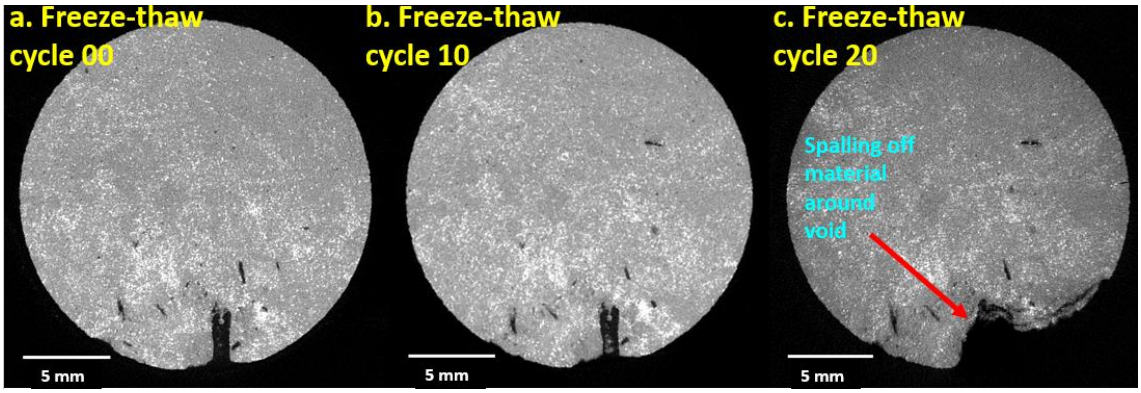

Figure 4.7. Micro-CT image slices showing cracks and material spalling off around a void and defect clustering (seen in white cluster) in the sandstone specimen after 0, 10 and 20 freeze–thaw cycles.

4.3 Estimation of strain (based on pixel method)

The small size of the specimen and experimental set-up prevented use of miniature strain gauges to measure strain. Therefore, digital information from fossil fragments, voids, grain boundaries and inherent structures was considered as identifying markers within the specimens. Any two markers of recognizable morphology within a particular depth slice of CT image were considered as marker pair (Figure 4.8) to estimate the pixel based strain. The changes in the number of pixels between two identical marker pairs in repeated scan were measured to estimate progressive strain. As the markers were selected on the circular cross sections perpendicular to the axial dimension, the transverse strains were estimated using the pixel-based method. The strain measured in freeze–thaw cycles 15 and 20 in chalk ranged between 0.05–0.07% and 0.14–1.2%, respectively (Figure 4.9). Strain before freeze–thaw cycle 10 was less than 0.04%. The markers located near the top parts of chalk experienced relatively higher strain compared to markers situated near the middle and base of the specimen. The sandstone core, on the other hand, experienced 0.01—0.02% strain and no such variations along the axial dimension were observed.

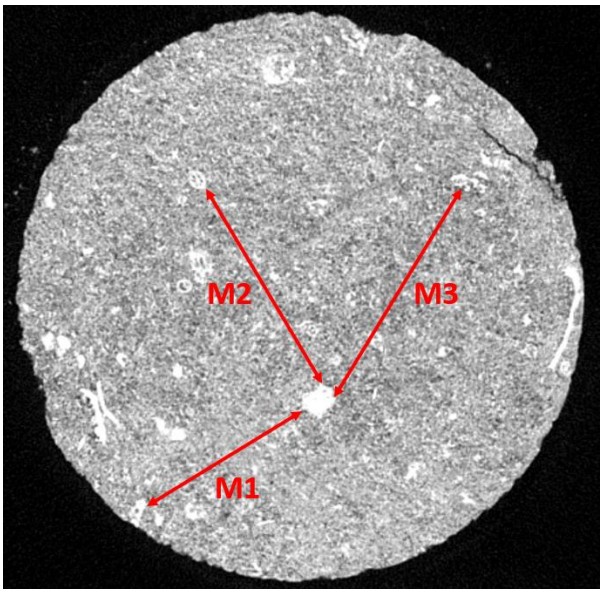

Figure 4.8. Micro-CT image slice illustrating selection of marker pairs (M1 to M3) for strain estimation. The distance between a marker pair is measured before any thermal treatment and the progressive changes in the distance between the marker pair is estimated from the later scanning of the specimen.

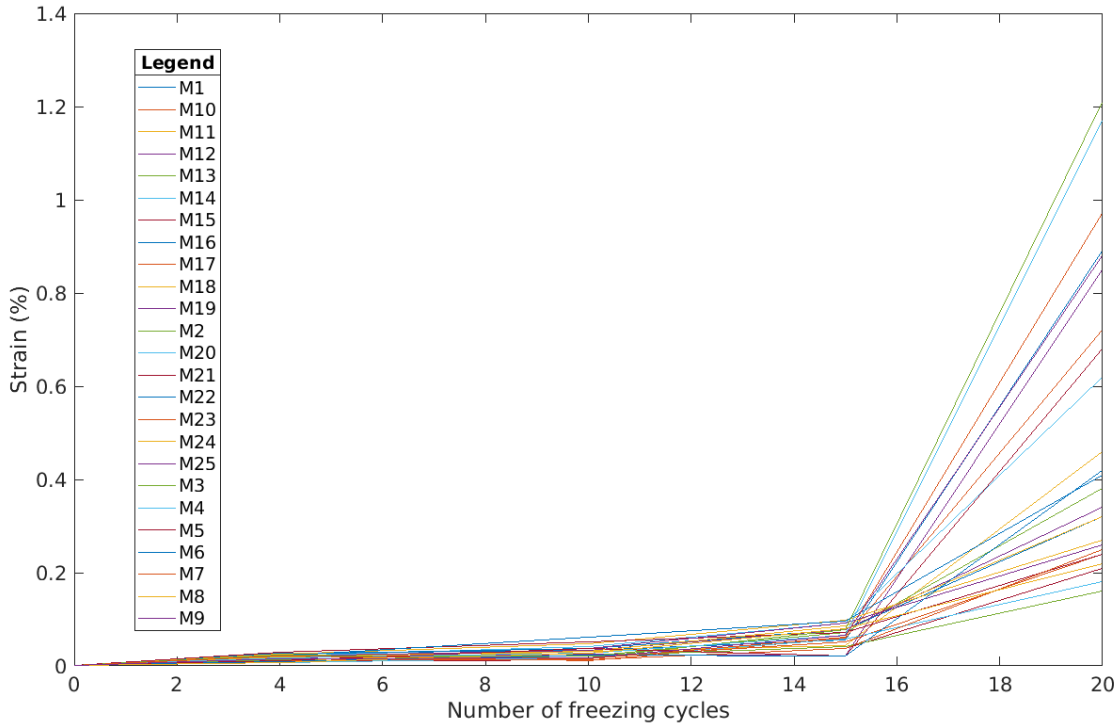

Figure 4.9. Transverse strain estimated in the chalk specimen following the pixel-based method. M in the figure indicates number of each marker pair.

4.4 Statistical correlation functions

Three low-order statistical correlation functions—(a) two-point probability function, (b) two-point cluster function and (c) lineal path function—were defined and described in section 3.3.5. Section 4.4.3 addressed objective 5.1 (O5.1) and objective 5.2 (O5.2) following the linear continuity of the fracture phase for both chalk and sandstone. Below, the results obtained at different stages of freezing and thawing using these correlation functions are presented to infer the changes in morphology of the fracture phase.

4.4.1 Two-point probability function

From Figures 4.8–4.10, it is evident that the two-point probability function is a useful method to detect progressive development of microcracks. When the r/D ratio (increment) is low, the probability of obtaining the fracture phase is high, while the probability approaches zero when the r/D ratio increases. Figures 4.10 and 4.11 show that crack propagation took place within the chalk along the X- and Y-directions that comprise the development of a horizontal plane. The development along the z-direction in Figure 4.12 indicates vertical growth of the fracture phase as the number of freeze–thaw cycles increases.

Along each of the three principle directions (XYZ), for < 0.05 r/D, the higher probability values for all repeated freeze–thaw cycles indicate the spread of inherent defects within the material along that principle orthogonal direction. Values of $S_f(r)$ > 0.4 for each principle direction describe the microinheritance of material flaws. Values of $S_f(r)$ < 0.4 and > 0 illustrate the development of progressive microcracking during freezing and thawing. When $S_f(r)$ approaches zero, the extent of microcracking dissipates beyond the associated value of r/D. The limit of intense microcracking activity varies along X-, Y- and Z-directions for $S_f(r)$=0.05 with r/D values of 0.25, 0.09 and 0.38, respectively.

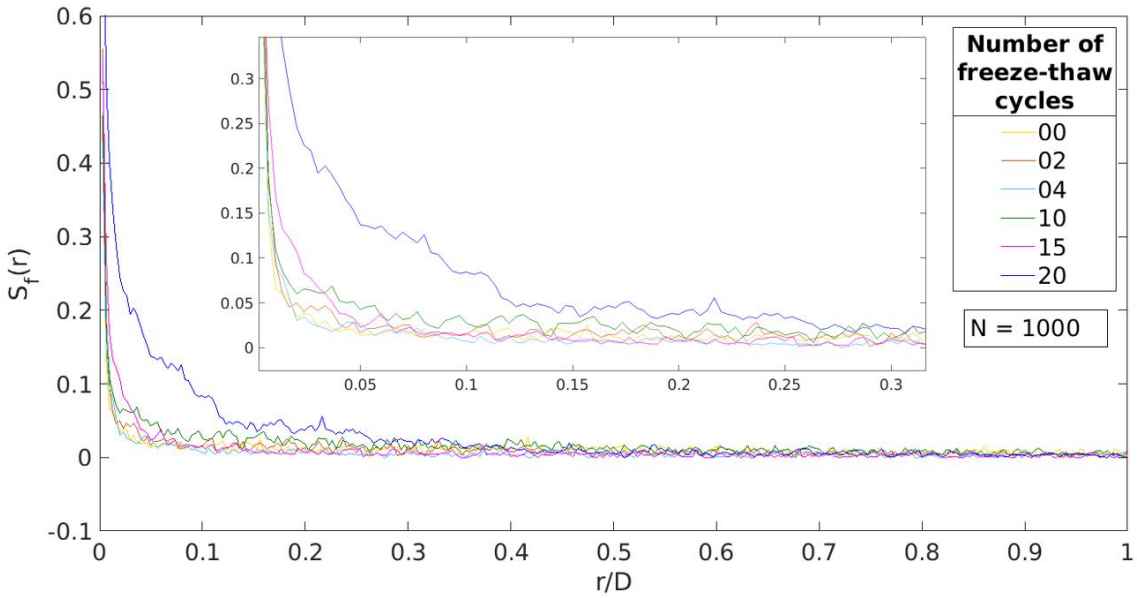

Figure 4.10. Two-point probability function for chalk along the X-direction.

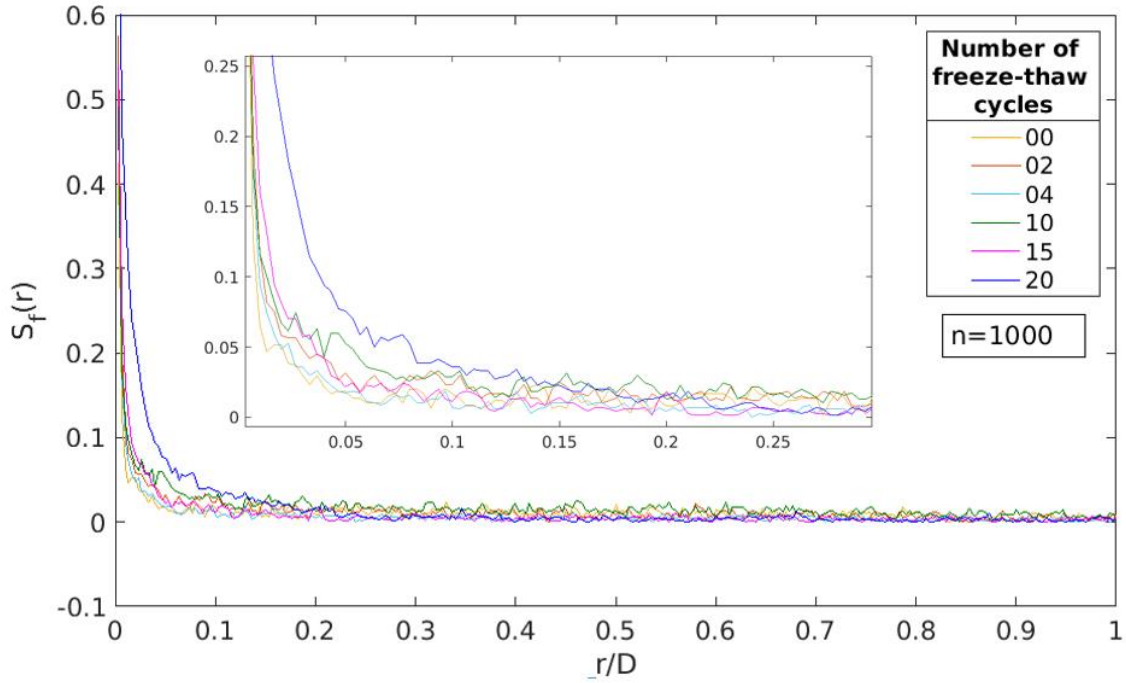

Figure 4.11. Two-point probability function for chalk along the Y-direction.

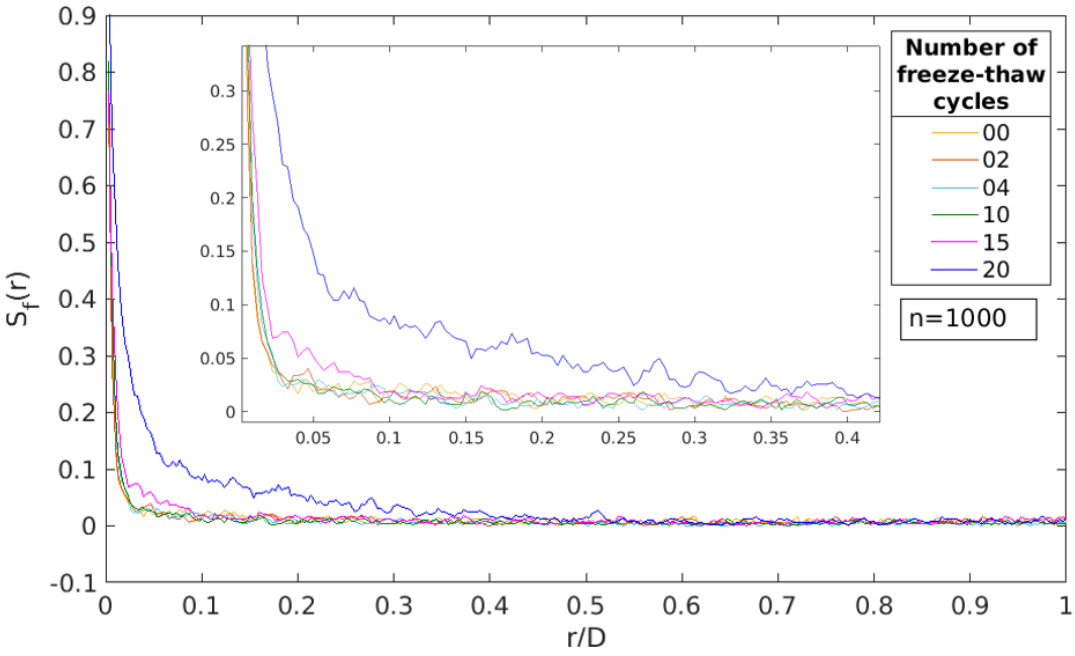

Figure 4.12. Two-point probability function for chalk along the Z-direction.

The results for the two-point probability function of Ardingly Sandstone are shown in Figure Figures 4.13–15. The developments of the fracture phase along the Y- and X-directions were high compared to that along the Z-direction as the lamination within the sandstone was horizontal. Higher $S_f(r)$ values (gentle slope) and a high r/D ratio (=0.25) in the Y-direction combining all the freeze–thaw cycles were compared with scanned images that reveal major inherited voids and flaws were oriented along the Y-direction (Figure 4.7).

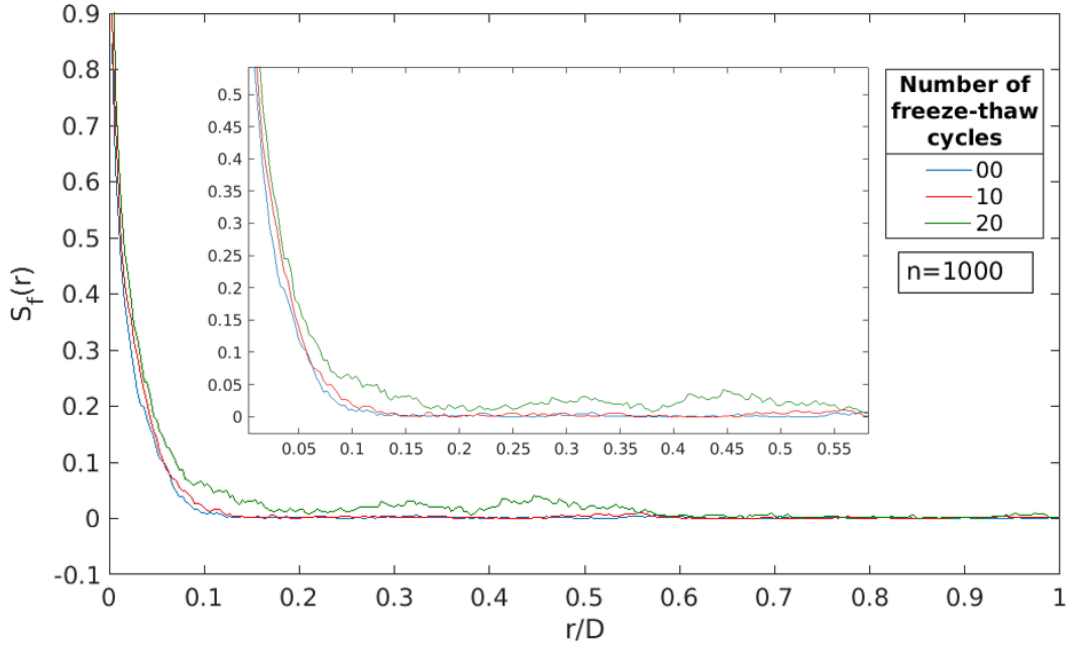

Figure 4.13. Two-point probability function for sandstone along the X-direction.

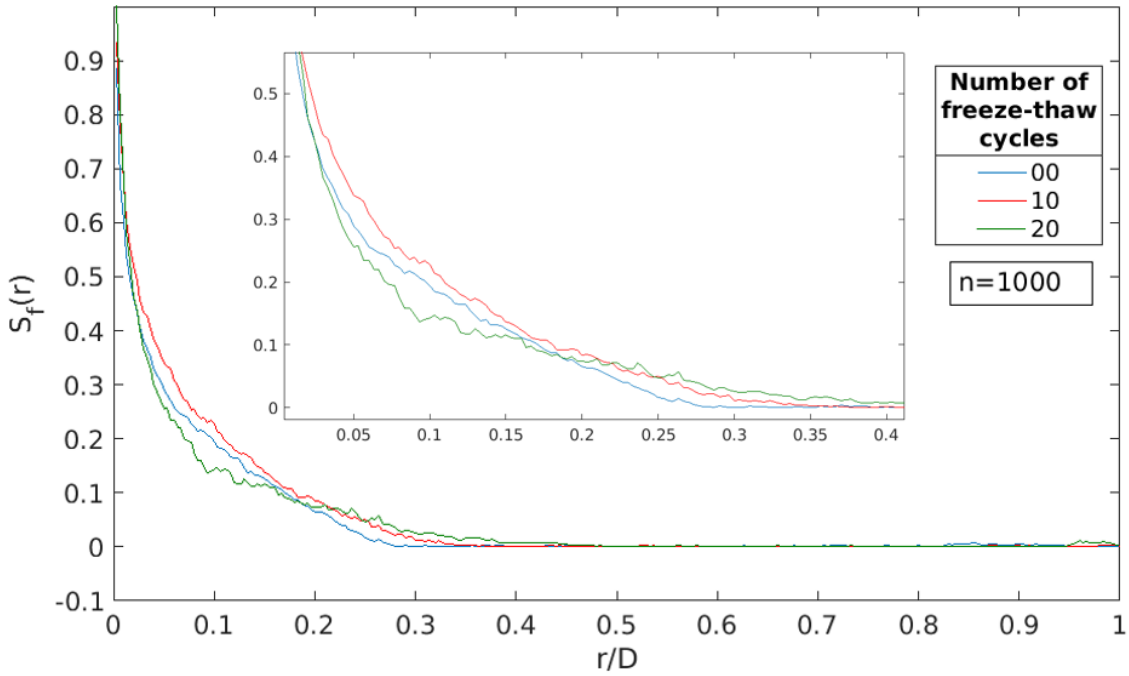

Figure 4.14. Two-point probability function for sandstone along the Y-direction.

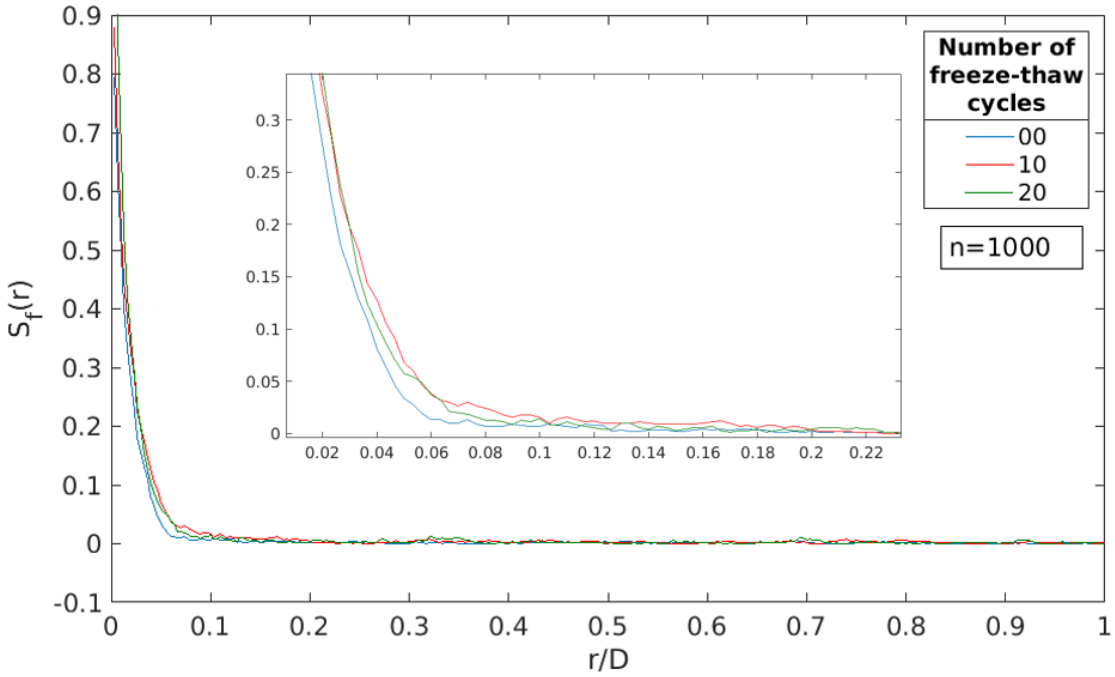

Figure 4.15. Two-point probability function for sandstone along the Z-direction.

4.4.2 Two-point cluster function

To describe the progressive development of the fracture phase, the two-point cluster function documents weak changes in probability (< 1%) compared to other statistical functions. Figures 4.16 and 4.17 illustrate the two-point cluster function for chalk and sandstone. They show that

the probability of finding two random points in the fracture phase irrespective of any directional constraint is less than 10%. As the number of freeze–thaw cycles increases, the changes in $C_f(r)$ is comparatively high when the r/D ratio is less than 0.1 (=2 mm), which decreases as the r/D ratio increases.

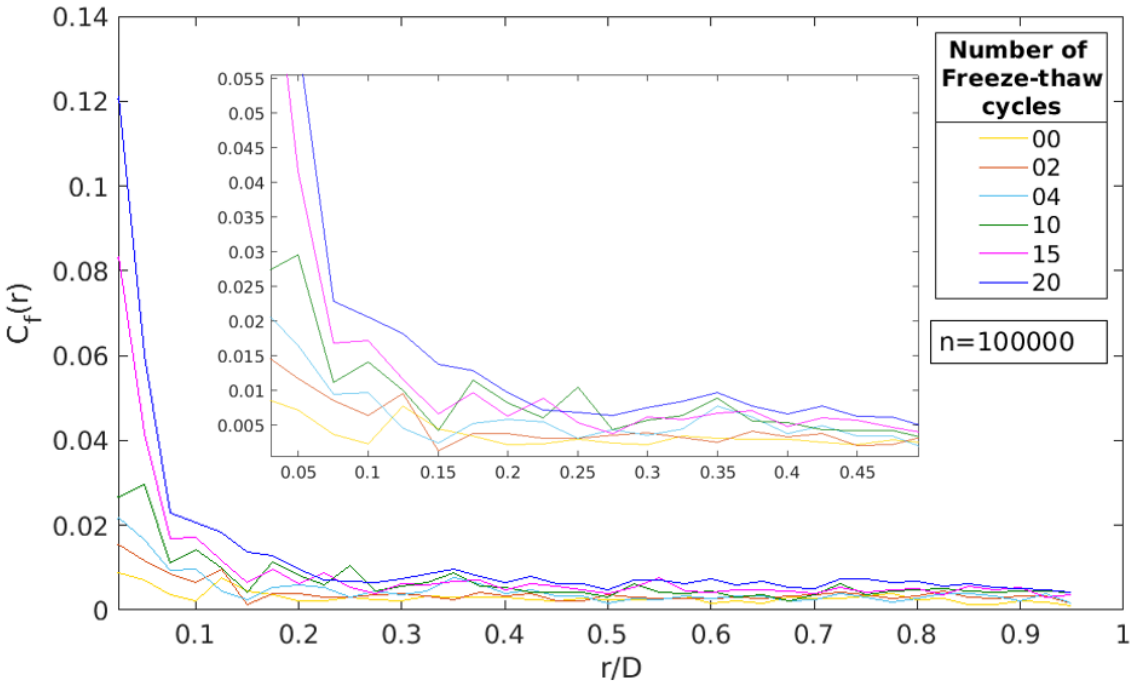

Figure 4.16. Two-point cluster function for chalk.

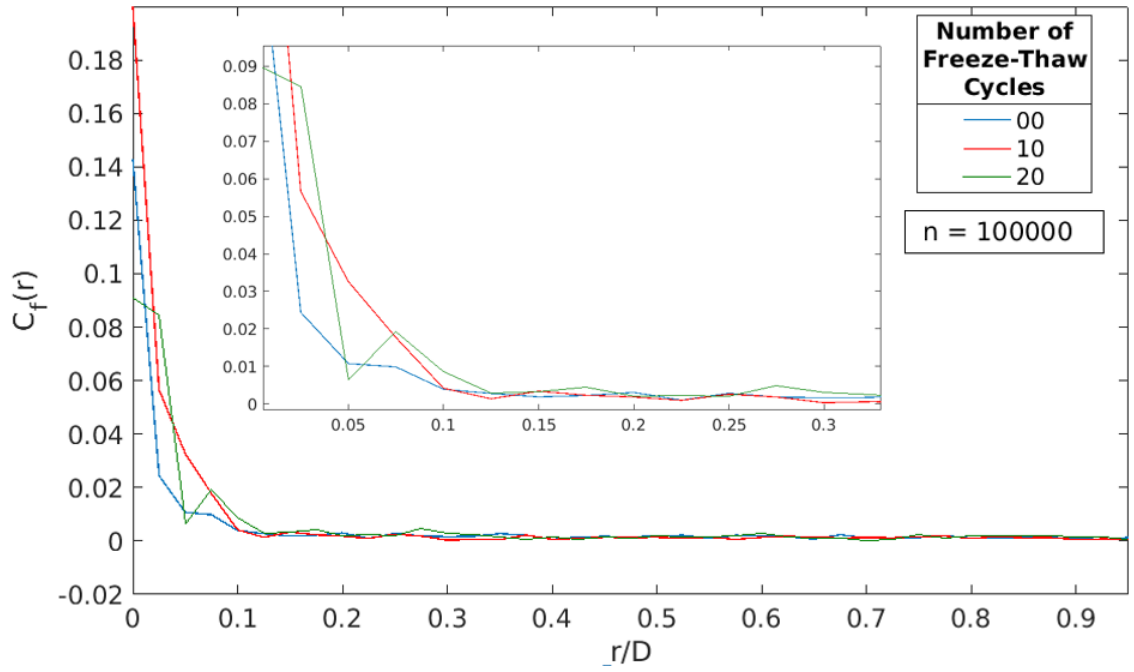

Figure 4.17. Two-point cluster function for sandstone.

4.4.3 Lineal path function

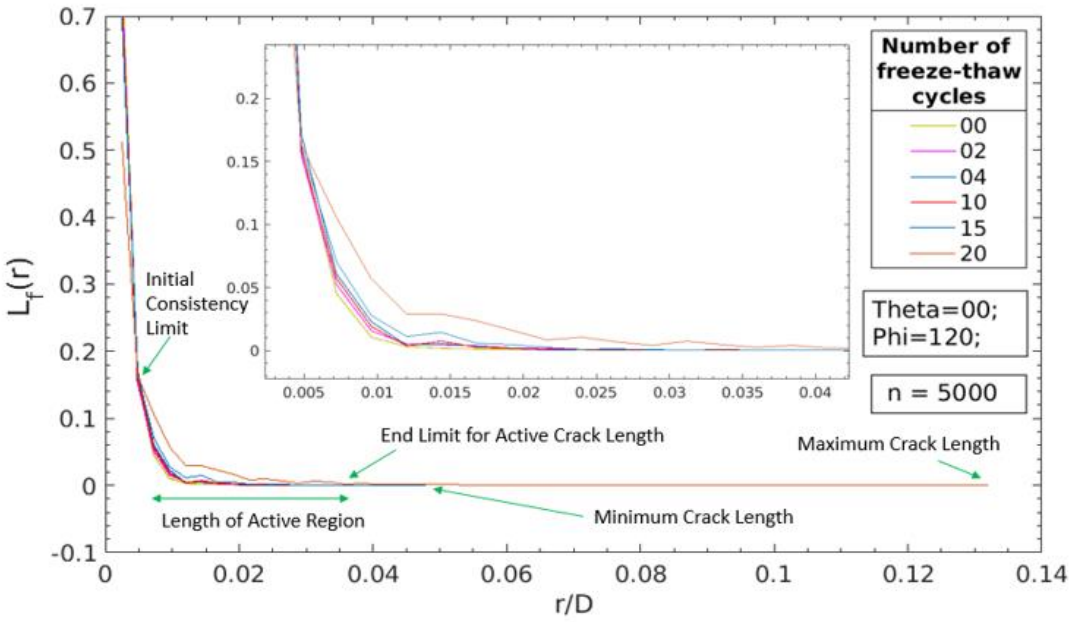

Figure 4.18. Description of various segments of the lineal path function.

Parameters that describe the different segments of the lineal path function are illustrated in Figure 4.18. The values of this function for different freeze–thaw cycles followed a similar trajectory at the very beginning, when the distance $r \rightarrow 0$. The maximum dimension (r/D) of length common to all the cycles defines the initial consistency limit. On the other hand, when the distance $r \rightarrow D$, the trajectory of the curves for different cycles again merges with each other, which is described by the *end limit for the active crack length*. The region between the initial consistency limit and the end limit for active crack length, where the trajectory of the curves for different freeze–thaw cycles developed progressive changes is termed the *length of active region*. Within this region the activity, expressed in terms of changes in $L_f(r)$, is high compared to that in the zones on either side. The r/D ratio in the lineal path function captures the information about the continuity of the fracture phase, whereas the other two functions assess the development of the fracture phase irrespective of continuity. The length of the continuous fracture phase increases progressively as the number of the freeze–thaw cycles increases. The length information (r/D ratio) at the initial stages of scanning is termed the *minimum crack length*, whereas the final length of the continuous fracture phase is termed the *maximum crack length* (Figure 4.18). To understand the progressive development of the continuous fracture phase along various linear directions, lineal path functions were compared for different freeze–thaw cycles along combinations of various θ & ϕ orientation (Figure 4.9). For each scan, a total 49 orientations was considered and compared with the further scanning

to detect the growth of a continuous line in the fracture phase. Figure 4.19 shows the lineal path function for chalk for different freeze–thaw cycles along the direction θ = 60° and ϕ = 60°. Figure 4.20 illustrates the lineal path function for sandstone oriented along θ = 60° and ϕ = 120°. Figures of lineal path function for various combination of θ and ϕ for chalk and sandstone are reported in Appendix A and B respectively.

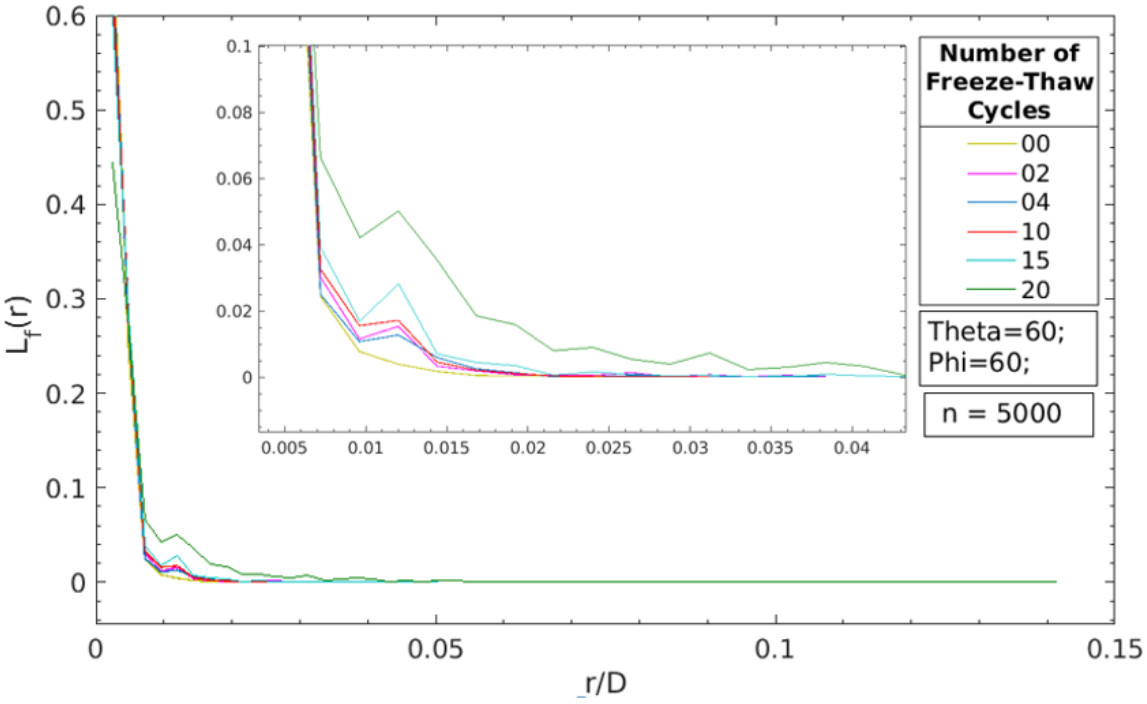

Figure 4.19. Description of the lineal path function for chalk along ϑ = 60° and ϕ = 60°.

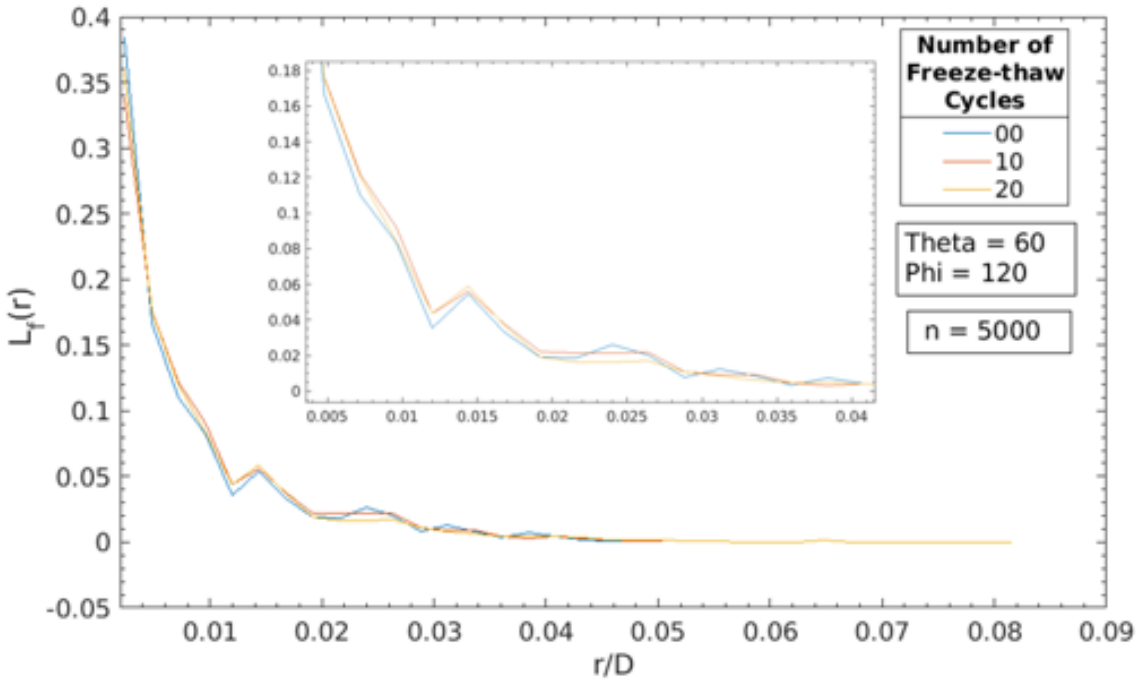

Figure 4.20. Description of the lineal path function for sandstone along ϑ = 60° and ϕ = 120°.

Figure 4.21a-g shows the results of changes in $L_f(r)$ values for different combination of θ and ϕ in chalk. The distance where the maximum changes identified were labelled in green in the boxplots for different θ and ϕ values. The average changes in probability for all the 49 directions is 6.49%. The maximum difference was 8.67% when the orientation was ϕ =0°, which suggests that growth of microfracture phase took place along the horizontal plane during freezing and thawing. The average distance where the maximum difference in $L_f(r)$ occurred is 0.1747 mm, combining all the projected directions.

The increment of continuous line length before any treatment with freezing temperature and after final scanning at the end of 20th freeze–thaw cycle for chalk is presented in Figure 4.22a-g (The difference between the parameter minimum crack length and maximum crack length is illustrated in Figure 4.18). The differences in minimum and maximum length labelled in green nest to their respective θ and ϕ values. The average length of increment combining all the various combinations of θ and ϕ values is 1.3842 mm. The maximum increment noted is 1.5766 mm when ϕ= 90°, which can explain the concentric vertical cracks visible by naked eye. In addition, significant growth of the continuous line segment in the fracture phase was noted in

the direction when ϕ = 30^o and 180^o with values of 1.5266 and 1.5466 mm, respectively. Values higher than average in these particular directions suggest horizontal and near-horizontal development of the fracture phase as a consequence of freezing and thawing.

The changes in $L_f(r)$ along the preset 49 directions within sandstone for various combinations of theta and phi were presented in Figure 4.23a-g. The average changes in $L_f(r)$ were estimated to 2.18% whereas in chalk the changes were 6.49%. The changes were consistent to ~2% along all the various directions unlike chalk where additional development along the vertical and horizontal directions were observed. The average distance interval where maximum probability change noted was 0.021 mm.

The gain in the consistent line length of fracture phase before and after treatment with 20 freeze-thaw cycles were shown in Figure 4.24a-g.The average length of increment was 0.255 mm combining the various 49 directions whereas the gain in chalk was 5 times higher (1.384 mm) relative to sandstone. The maximum (0.3257) and minimum (0.18) increment noted when phi = 60 and 90 respectively.

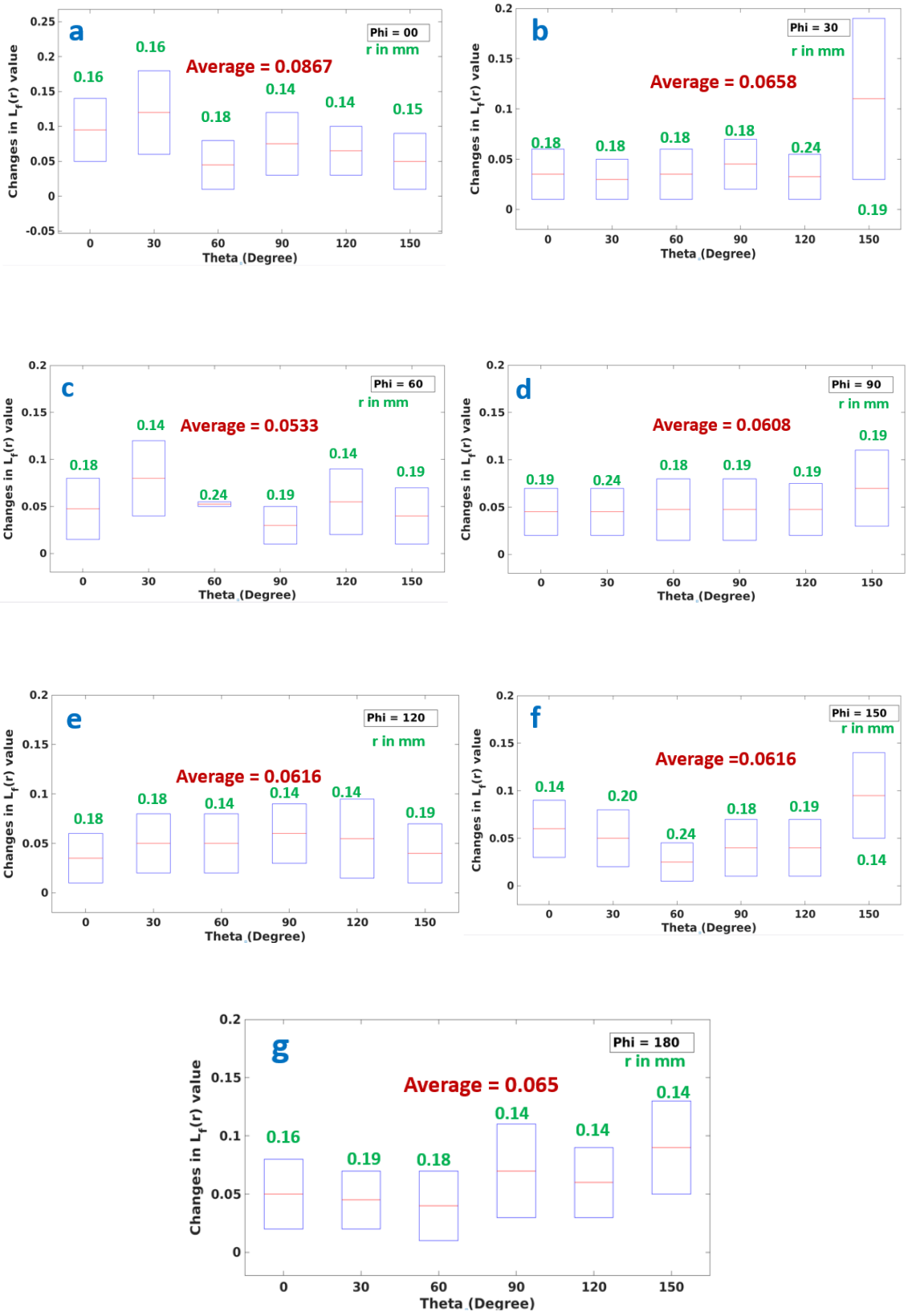

Figure 4.21. Changes in $L_f(r)$ along various directions in chalk.

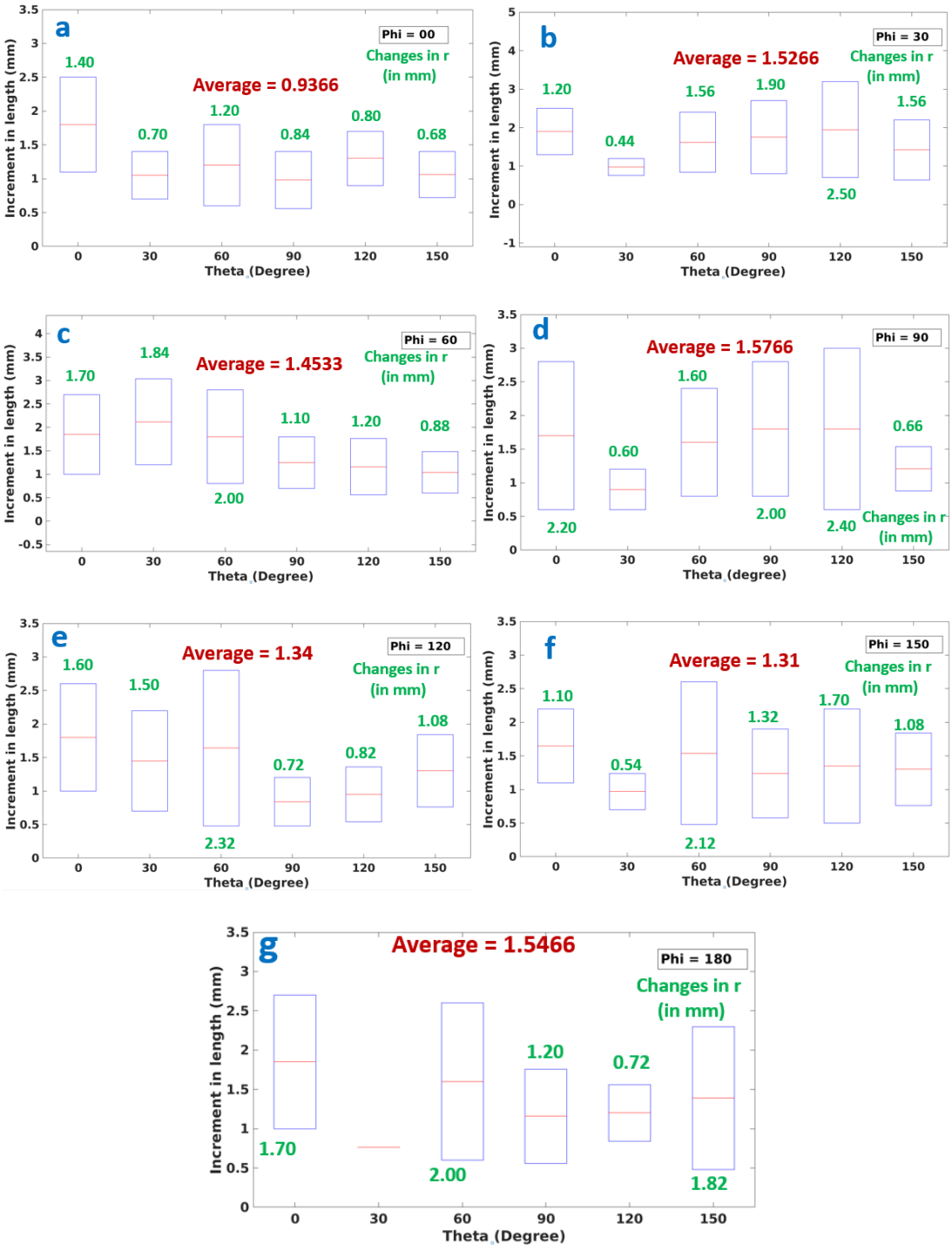

Figure 4.22. Incremental changes in line length along various directions in chalk.

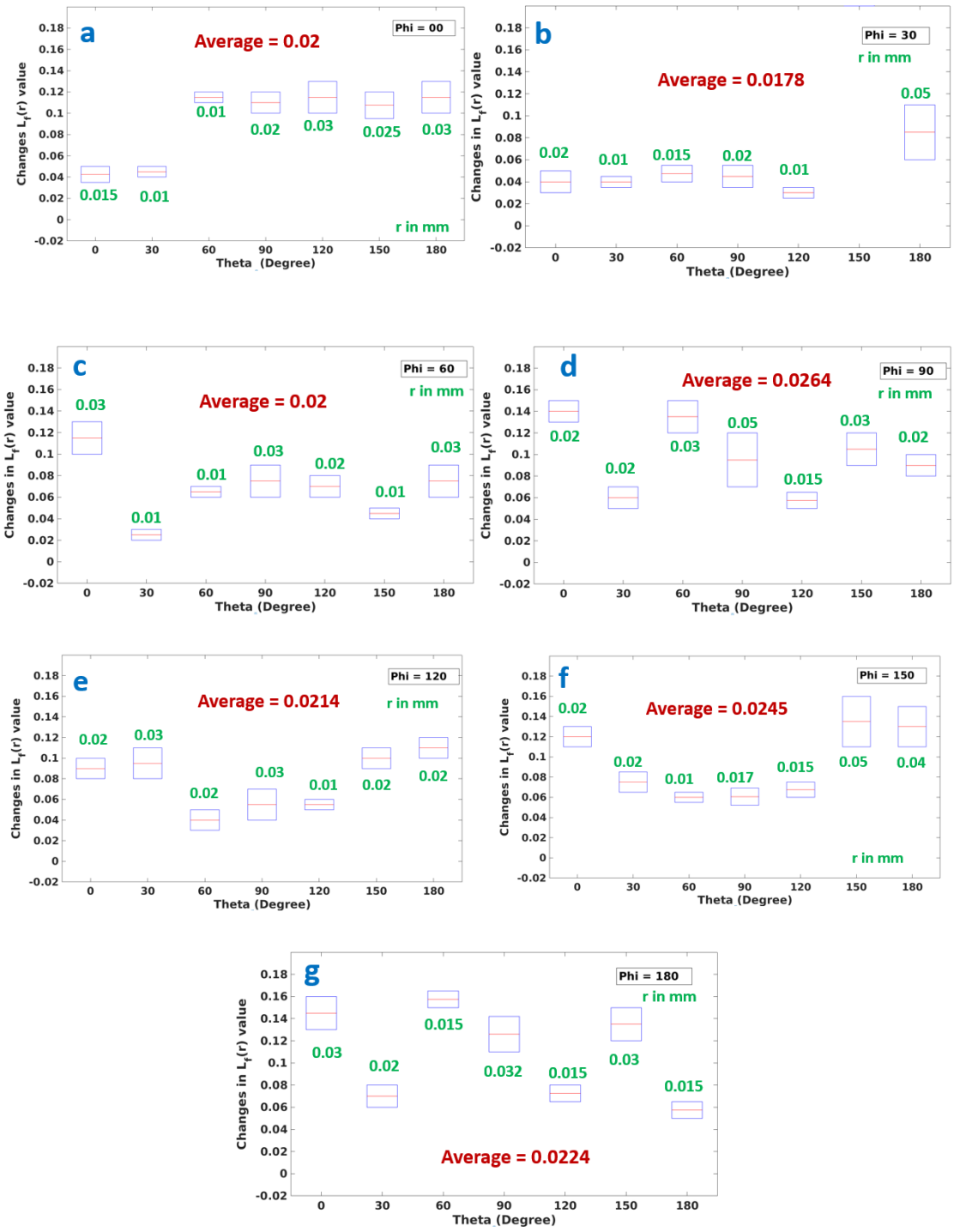

Figure 4.23. Changes in Lf(r) along various directions in sandstone.

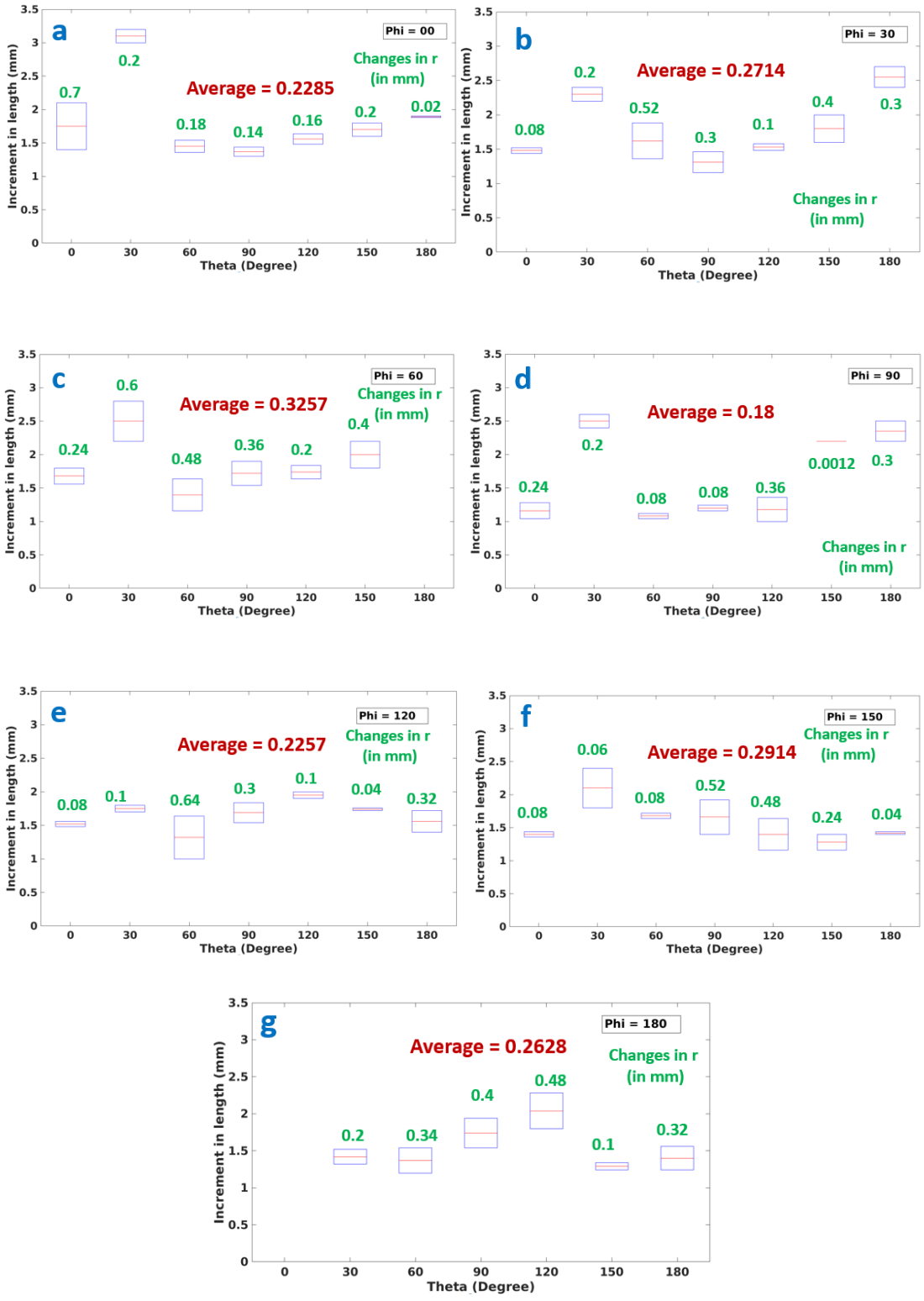

Figure 4.24. Incremental changes in line length along various directions in sandstone.

4.5 Conclusion

Two different methods of deformation analysis were implemented in the repeated micro-CT images of tuffeau chalk and Ardingly sandstone core plugs. Transverse strain estimated following the pixel-based method revealed that significant change took place within the chalk after freeze–thaw cycle 15 (Figure 4.9). Analysis of low-order probability functions, especially the two-point probability and lineal path functions, recorded similar behaviour after freeze–thaw cycle 15, where sharp changes in the probability index were identified (Figures 4.10–12 and 4.19). These different analyses together suggest that the degree of damage associated with chalk crossed a threshold after freeze–thaw cycle 15, where after the specimen started degrading faster than during the initial cycles.

Chapter 5

Results – Compression Test

5.1 Introduction

Chapter 5 reports the pattern and details of cracking of unfrozen chalk and sandstone specimens under compressive loading. The development of fractures between the initial stages of cracking and the final stages of failure are identified, and the effect of contrasting lithologies on the main crack path is analyzed. The visible macrocomponent of alternative and/ or repetitive tension and shear forming a well-developed failure plane is identified. Axial and transverse strains measured at various locations in the specimens are presented.

5.2 Mechanism of fracture in sandstone

Figures 5.1 and 5.2 indicate that the cracks initiated at the two bounding surfaces (where the separation of the cracked faces was greatest) and propagated towards the centre of each specimen. A maximum separation of 5 mm between the cracked faces was observed on the upper part of the crack on the right side (marked as 1A in Figure 5.1b). The crack initiated at the lower left corner of the specimen has a similar separation to the crack on the upper right corner (marked as 1B in Figure 5.1b). The prominent crack on the right consisted of three tension cracks (marked as 2A, 2B and 2C in Figure 5.1b) and three coplanar shear cracks (marked as 3A, 3B and 3C). The shear cracks were curved, whereas the tension cracks were straight. As the loading increased, the tension cracks lengthened while the shear cracks shortened.

The crack on the lower left of the specimen propagated following the same mechanism as the crack on the upper right by the development of consecutive tension and shear cracks. However, at the bottom left of the specimen, a bifurcation angle of 17^{o} was observed 5.2 mm above the bottom face just after the initiation of the crack, with the path of the main crack following the right-hand branch. Four slip surfaces were identified along the main crack (marked as 4A, 4B, 4C and 4D in Figure 5.1b). The initial three shear faces (marked as 4A, 4B and 4C in Figure 5.1b) shortened as the loading progressed, while the fourth (marked as 4D in Figure 4.2b) developed near the boundary of the low-density material and was longer than the initial three shear cracks.

In addition to the main cracks, stress concentrated on two opposite points near the boundary of low- and high-density material. This led to the initiation of cracks that were similar to cracks

developed in an empty hole. The cracks initiated from this boundary between rock of contrasting mineralogy, density and strength and propagated along the direction of axial loading (marked as 6A and 6B in Figure 5.1b).

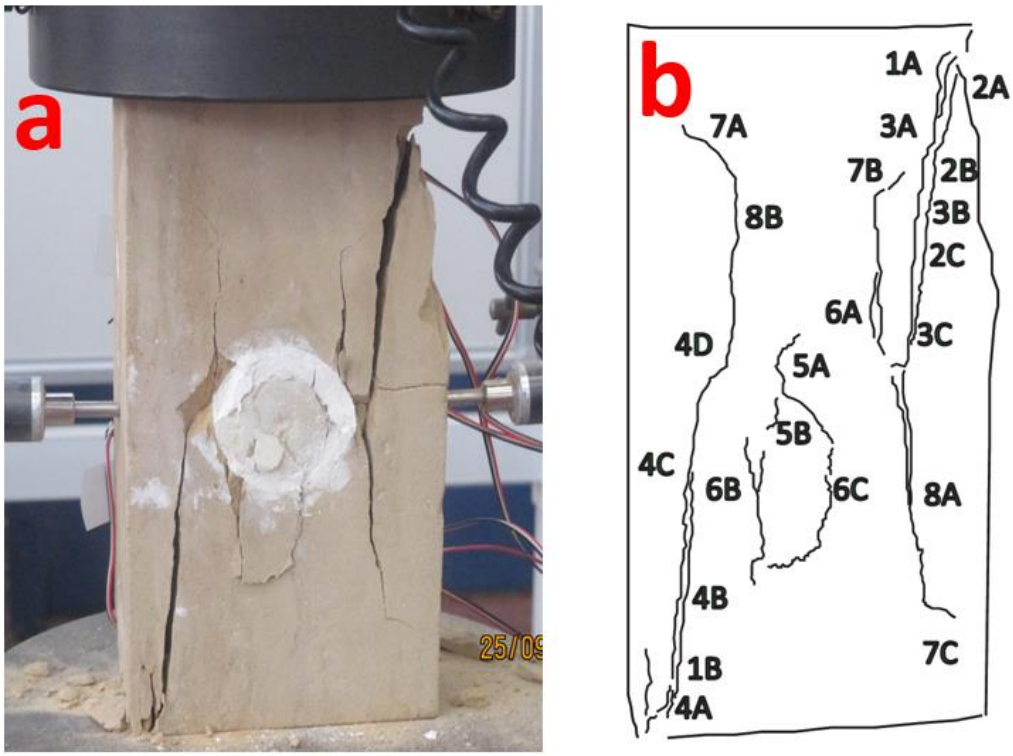

Figure 5.1. (a) Photograph showing the development of cracks within the sandstone specimen during axial loading. (b) Diagram tracing the trajectory of the propagating cracks.

At the point where the two main cracks (upper right and lower left) that propagated towards the central hole interacted with the chalk core close to the place where cracks 6a and 6B initiated, the cracks swung around the hole, as indicated by the longer slip surface.

During progressive loading the propagating cracks probably encountered the central chalk core from the lower left and upper right side. Surprisingly, however, the crack developed inside the chalk core trended from the top left to bottom right (Figure 5.1). But after ultimate failure occurred, the rock material spalling off from the surface indicates that the chalk core connected the two high stress concentrations on opposite points by two tension cracks (marked as 1A and 1B in Figure 5.2b) and a shear crack in between.

Three well-developed wing cracks formed at the end phase of the loading. All of the wing cracks protruded outward relative to the central vertical loading axis. The angle of the wing cracks ranged from 55^{o} to 70^{o} relative to the direction of crack propagation.

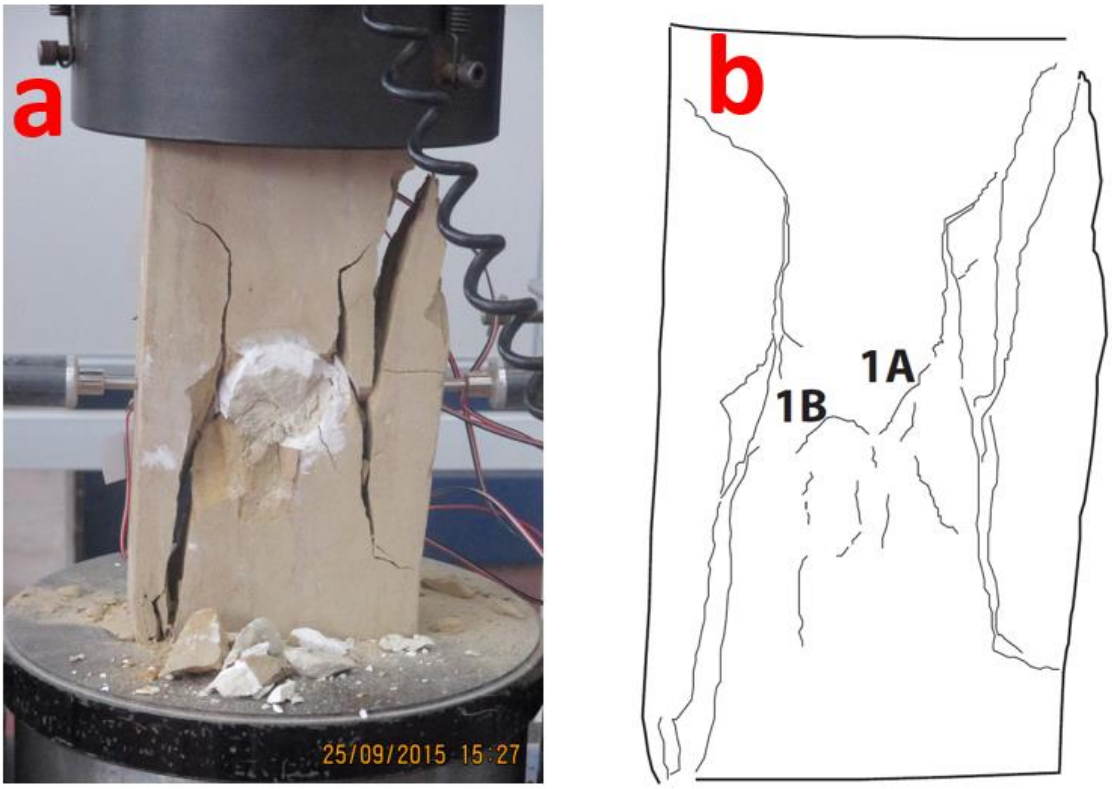

Figure 5.2. (a) Photograph showing the development of cracks within the sandstone specimen during axial loading. (b) Diagram tracing the trajectory of the propagating cracks.

5.3 Mechanism of fracture in chalk

Fracture of the chalk specimen initiated from the top face, close to the central vertical axis (marked as 1A and 2A in Figure 5.3b). The main crack was interrupted at two different locations by secondary cracks in the upper half of the specimen (marked as 2B and 3A in Figure 5.3b). From the sequential photographs captured during the compressive test, the crack from the left developed first; later, the crack from the right met with its trajectory 13 mm above the central high rigidity zone. The mechanism is evident from the aperture of the cracks, which is relatively wide for the crack on the left compared to the crack on the right side (Figures 5.3 and 5.4). As the loading progressed, the secondary cracks (marked as 2B and 3A) coalesced with the main crack trajectory on the shear planes.

The main crack trajectory consisted of successive tensile and shear cracks. The tension cracks developed initially later merged with each other following the formation of shear cracks, as

evident from the initial and final phase of loading (Figures 5.3 and 5.4). The tension cracks 1E, 4A, 5A in Figure 5.3b coalesced with each other by the development of shear cracks marked as 3A, 3B and 3C in Figure 5.4. Unlike sandstone, the final slip surfaces were long compared to the slip surfaces developed during the initial phase of loading. But the length of the tensile cracks surface increased as the crack continued to grow, as in the sandstone specimen. The region where crack 3A meets 1D (Figure 5.3b) is a bit disturbed (in terms of slip surface length and crack length), where the crack from the right side merges with the crack from the left and material spalling off from the surface.

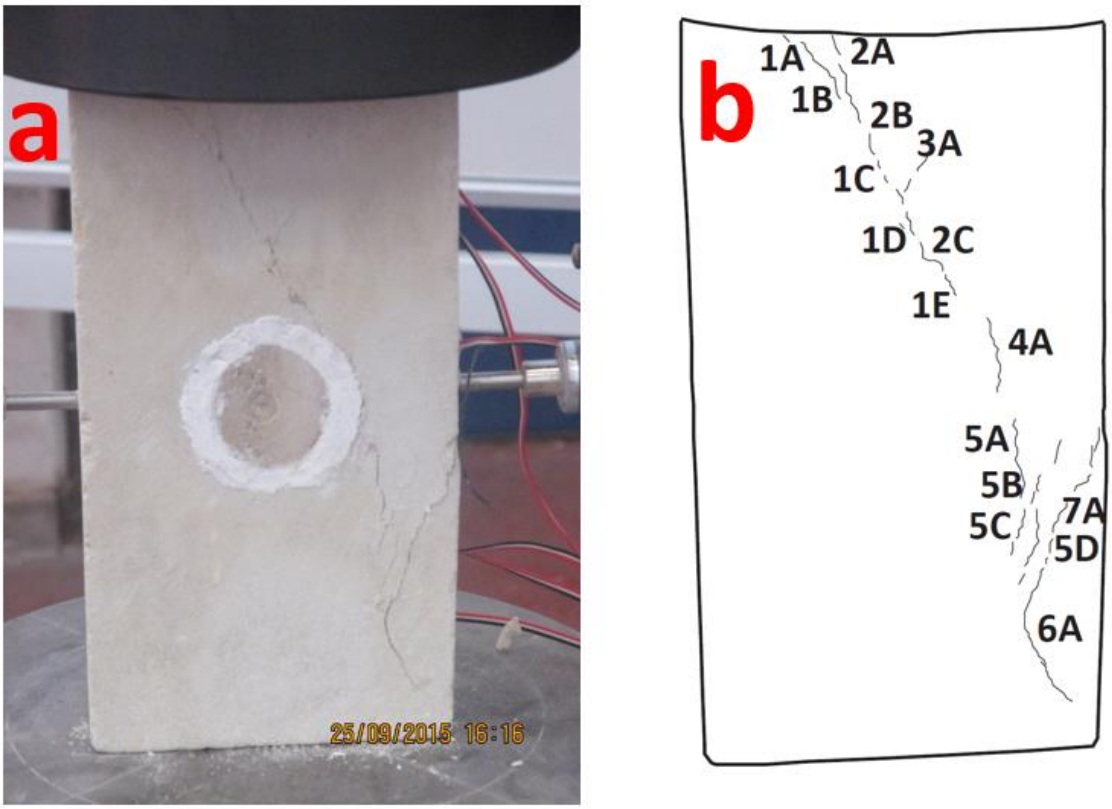

Figure 5.3. (a) Photograph showing the development of cracks within the chalk specimen during axial loading. (b) Diagram tracing the trajectory of the propagating cracks.

The region where crack 3A meets 1D (Figure 5.3b) is a bit disturbed (in terms of slip surface length and crack length), where the crack from the right side merges with the crack from the left and material spalling off from the surface.

The trajectory of the main crack skirts around the sandstone core and propagates through their boundary face. The slip surface (marked as 3A, 3B and 3C in Figure 5.4b) and the propagating

crack can be distinguished by their wide aperture. Like sandstone, wing cracks developed at the tail of the main crack in an outward direction from the central vertical axis.

Bifurcation from the main crack trajectory was observed at two different locations (marked as 5C and 5D in Figure 5.3b) in the lower half of the specimen. In the lower half of the main crack trajectory the bifurcation and slip surface developed very close to each other.

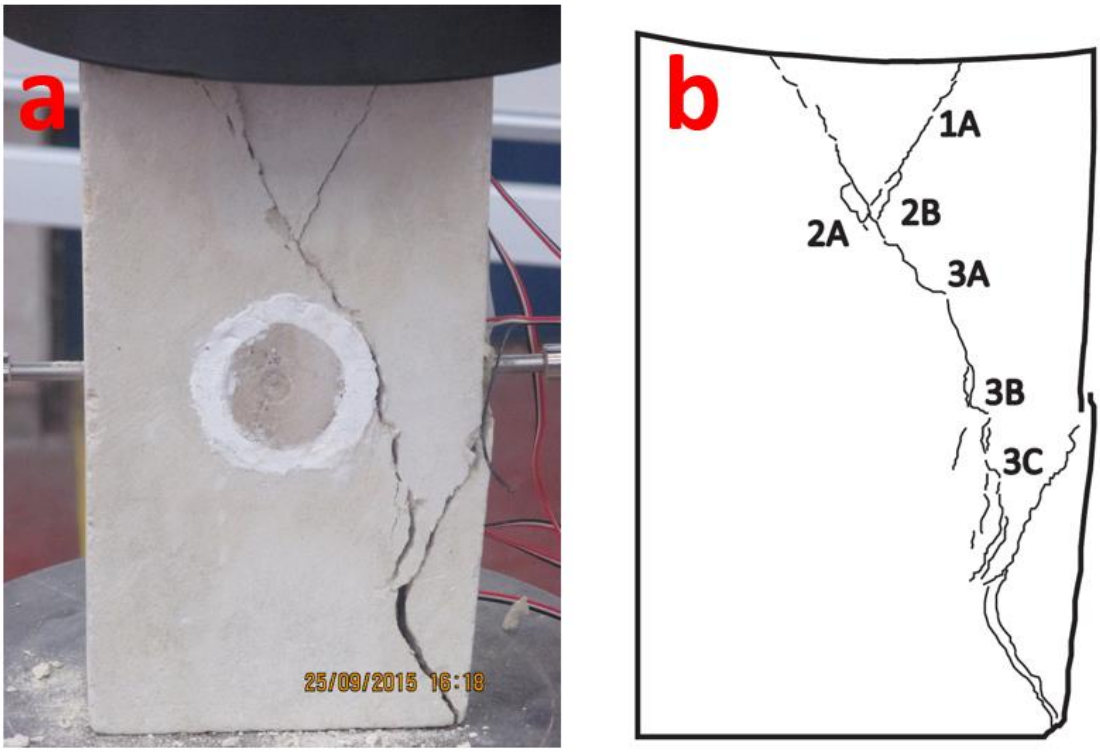

Figure 5.4. (a) Photograph of the chalk specimen at the end of the experiment, after failure. (b) Diagram tracing the ultimate fracture path.

5.4 Stress–strain curve for sandstone under compression

Strain gauge two (SG2) was mounted on the chalk core along the direction of axial loading. The gradient of the stress–strain curve lies in between the gradient of the strain gauges mounted axially above (SG5) and below (SG4) of SG2 (Figure 5.5).

Strain gauge three (SG3) was placed on the inner chalk core perpendicular to the direction of axial loading. The strain retained within the chalk inner core exceeded the strain retained within the sandstone, which was evident by substantial difference in gradient of their respective stress–strain curve.

Strain gauge four (SG4) was mounted on sandstone along the direction of axial loading near the central chalk core. The stress–strain curve of SG4 had a minimum gentle slope compared to other gauges mounted axially.

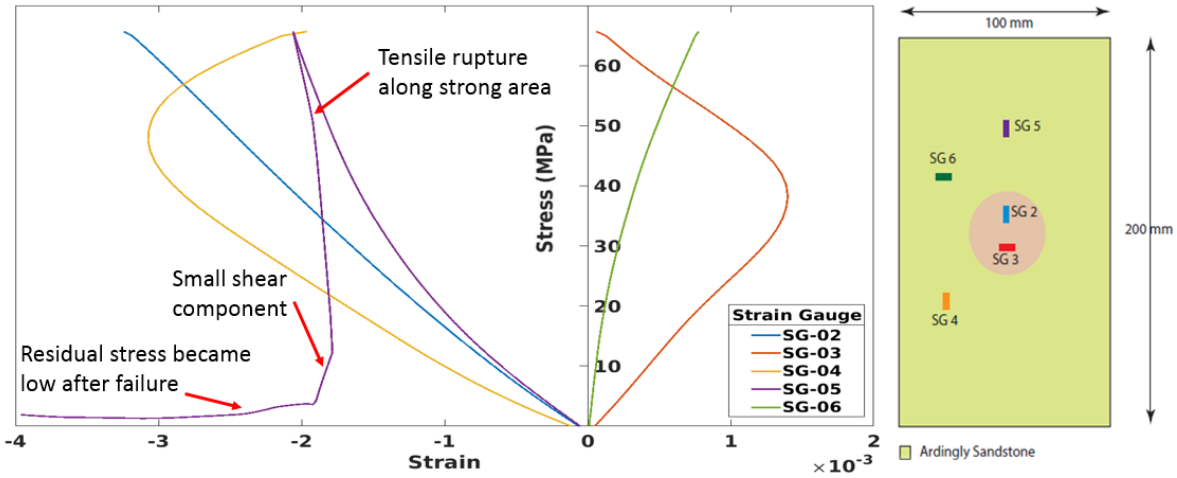

Figure 5.5. The stress–strain curve of the sandstone specimens during axial compressive loading. The diagram on the right shows the location and colour code of the strain gauges mounted on the sandstone.

Strain gauge five (SG5) was attached on the upper part of the sandstone specimen along the direction of axial loading. The stress–strain curve initially started with a gentle slope that became steeper as the loading continued, followed by a sharp rupturing event. After the failure had taken place, the residual strength of the material became low, which was evident by the lower value of stress at the tail of the stress–strain path. The sharp linear changes of the stress–strain curve after it reached its peak strength indicates a prominent tensile rupture event.

Strain gauge six (SG6) was mounted on the sandstone near the central chalk core, perpendicular to the direction of axial loading. The deformation retained within the strain gauge was low, as indicated by the steep slope of the stress–strain curve.

5.5 Stress–strain curve for chalk under compression

Strain gauge one (SG1) was oriented along the axial direction of loading and mounted on the upper half of the specimen, where the secondary crack from the upper right coalesced with the main crack trajectory from the left. The stress–strain curve was not linear within the elastic limit of the material but contained evidence of tensile and shear cracks that was evident by the non-linear trajectory (Figure 5.6). The material did not rupture after the load reached its peak. Instead, it retained the signature of large shearing event along the boundary between two

contrasting materials, which is evident by the gentle slope of the stress–strain curve. The shearing event was followed by rupture along the strong part of the material.

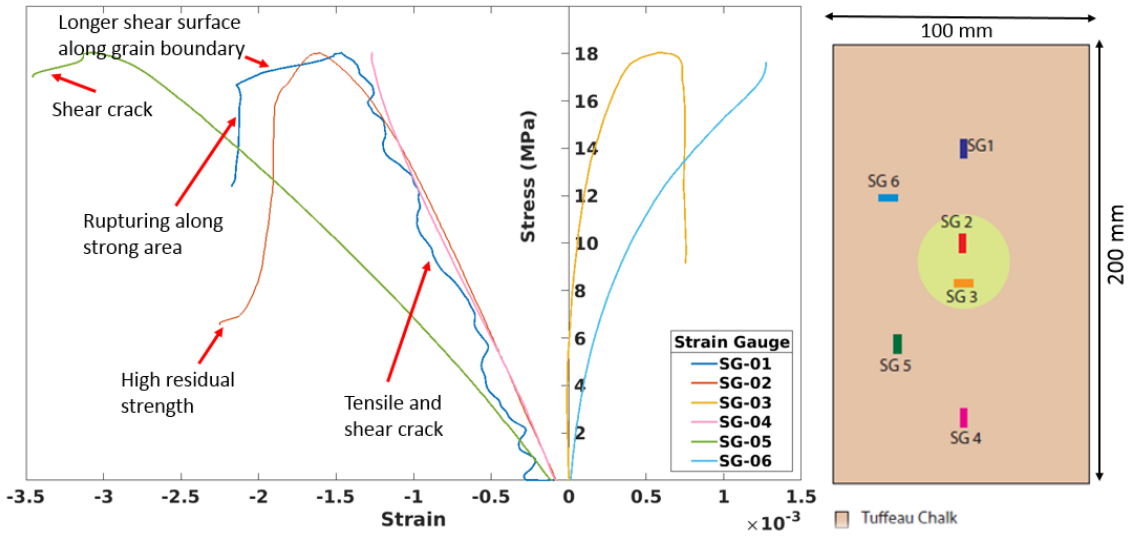

Figure 5.6. The stress–strain curve of the chalk specimen during axial compressive loading. The diagram on the right shows the location and colour code of the strain gauges mounted on the chalk block.

Strain gauge two (SG2) was mounted on the inner sandstone core along the direction of axial loading. The stress–strain curve was linear and had the steepest slope of all the strain gauges on this specimen. The slope became slightly gentler before the specimen reached its peak load, followed by a gentle bending. The comparatively gentle trajectory before and after the material experienced its peak load indicates microshearing activity rather than rupture. Finally, the residual strength of the sandstone core became high while the specimen developed fractures, leading the failure.

Strain gauge three (SG3) was attached to the sandstone core perpendicular to the direction of axial loading. The stress–strain curve recorded a maximum value of slope during compressive loading. The slope became very gentle before the material experienced maximum loading. Although the curve retained signatures of rupture after the load reached its maximum, no macrocracks were visible on the sandstone core.

Strain gauge four (SG4) was mounted on the lower part of the specimen along the direction of axial loading. The slope of the stress–strain curve was linear and similar to that of mounted longitudinally on the sandstone core.

Strain gauge five (SG5) was placed on the chalk along the direction of axial loading just below the sandstone core. The stress–strain curve had a gentle slope compared to other strain gauges

on the specimen. After the material reached its peak load, the slope became gentler, which denoted an unstable shear crack that swung around the sandstone core.

Strain gauge six (SG6) was mounted on the chalk perpendicular to the direction of axial loading. The slope of the stress–strain curve was gentler compared to SG3 and as the loading continued, the slope became gentler.

5.6 Measurement of lateral displacement

The two LVDTs attached to either side of the specimen measured the lateral movement during axial loading. Combining the total displacement on either side of the specimens showed (Figure 5.7–8) that the sandstone (23 mm) experienced higher lateral movement compared to the chalk (14 mm). For sandstone, the movement initiated before the peak load is reached while in chalk the movement began at the end of maximum loading.

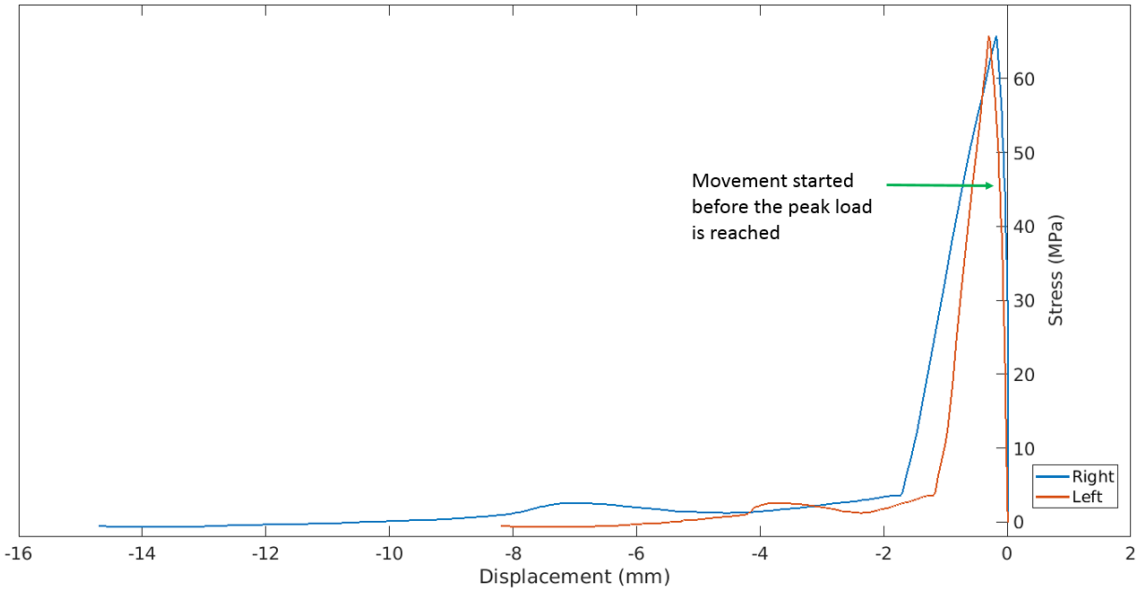

Figure 5.7. Displacement of LVDTs on either side of the sandstone specimen with increasing load.

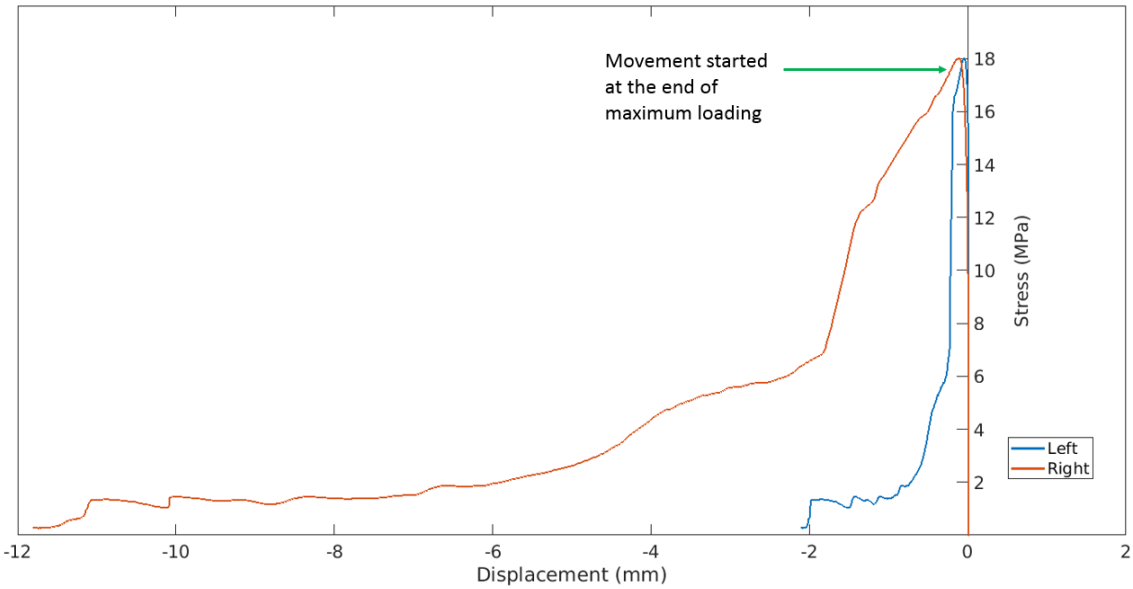

Figure 5.8. Displacement of LVDTs on either side of the chalk specimen with increasing load.

Chapter 6

Results - Macroscale experiment

6.1 Introduction

Chapter 6 presents the outcomes of the macroscale experiment on bidirectional freezing conducted in the Permafrost Laboratory over the course of 315 days. The effects of changing the depth of a simulated active layer above permafrost on cracking and brecciation in the chalk are illustrated. Heave and settlement time series data of the rock top at various stages of freezing and thawing are presented, along with changes in strain at different depths estimated using a dummy gauge protocol. The formation and growth of brecciated zones and vertical cracks developed at different depths within a chalk block are identified, and the morphology of the cracks is described. AE activity due to microcracking at different depths within the block is filtered for different numbers and phases of freezing and thawing to correlate with the development of visible cracks. Tensile and shear modes of cracking are distinguished based on the analysis of AE waveform parameters. Using the 3-dimensional locations of the acoustic events, a statistical function is introduced to assess the mechanism of cracking following the spatial relationship of hypocenters arranged in their temporal order of occurrence.

6.2 Temperature and active-layer thickness (ALT)

The three blocks were initially frozen from the top downward to simulate natural downward freezing of rock beneath a horizontal surface. Thereafter, the lower half of the chalk block and the sandstone block with laminae oriented horizontally (block SH) was generally at subzero temperature (to simulate permafrost) while the upper half froze bidirectionally and thawed unidirectionally (to simulate an active layer during winter and summer). In contrast, the upper half of the sandstone block with laminae oriented vertically (block SV) did not thaw during thawing periods because it is thought to have had a high permeability and thermal conductivity in this orientation. The mean air temperatures during the initial (P1, FT cycles 1–4), intermediate (P2, FT cycles 5–8) and final (P3, FT cycles 9–12) phase of freezing cycle were –15, –10 and –5°C, respectively. In thawing (T) cycle, the mean air temperatures were 22, 18 and 26°C for three different phases. Time series of vertical temperature profiles of the three blocks for the first eight cycles (P1 and P2, days 0–207) are shown in Figure 6.1a–c. The freezing cycles 2–5 were the coldest of all the cycles.

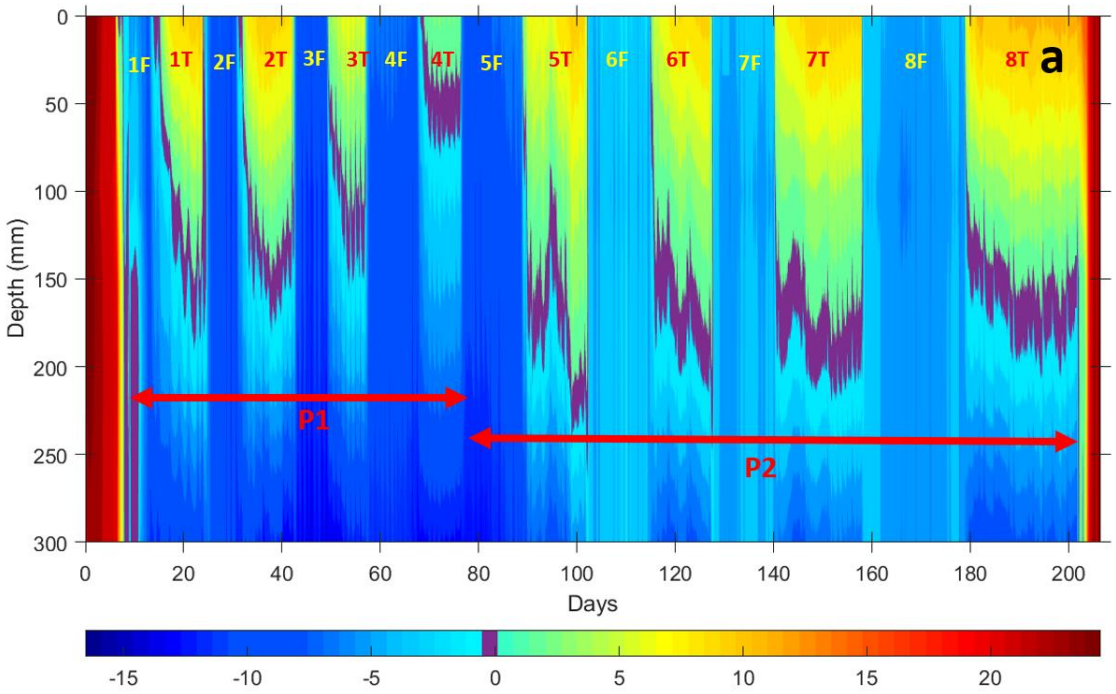
1F
1T
2F
2T
3F
3T
4F
4T
5F
5T
6F
6T
7F
7T
8F
8T
a
P1
P2
Depth (mm)
Days
0
50
100
150
200
250
300
0
20
40
60
80
100
120
140
160
180
200
-15
-10
-5
0
5
10
15
20

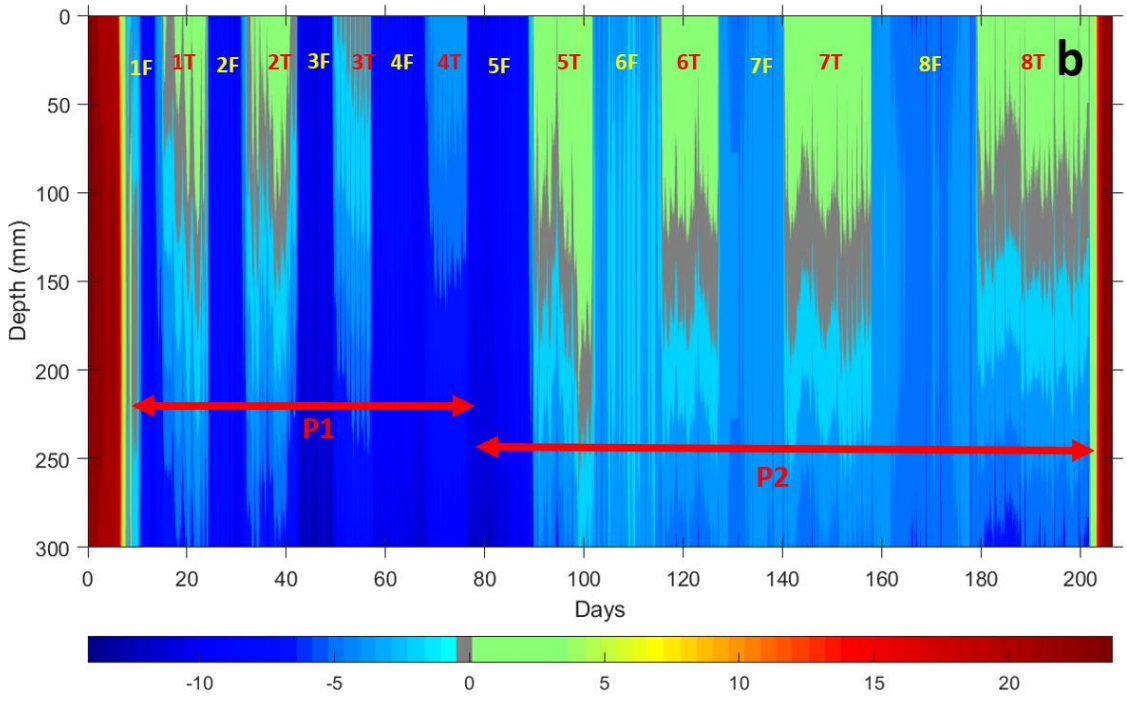
1F
1T
2F
2T
3F
3T
4F
4T
5F
5T
6F
6T
7F
7T
8F
8T
b
P1
P2
Depth (mm)
Days
0
50
100
150
200
250
300
0
20
40
60
80
100
120
140
160
180
200
-10
-5
0
5
10
15
20

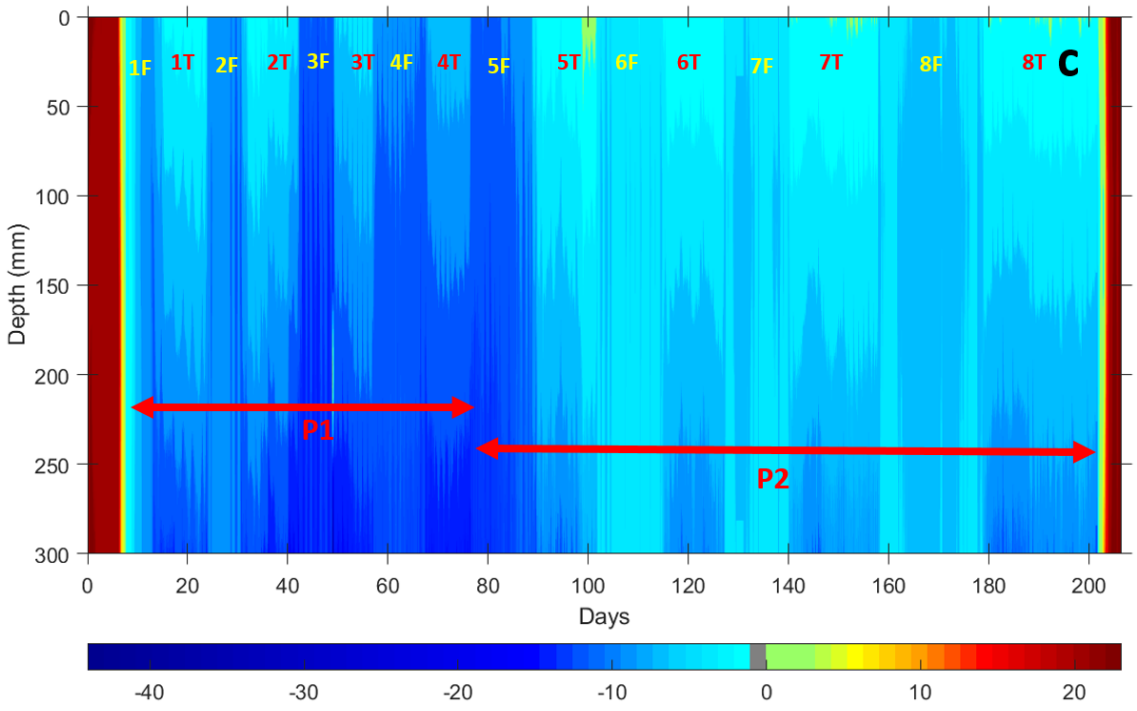

Figure 6.1. Time series of temperature profiles of the three blocks during P1 and P2 (freeze–thaw cycles 1–8). (a) Chalk, (b) sandstone with lamination horizontally oriented and (c) sandstone with lamination vertically oriented.

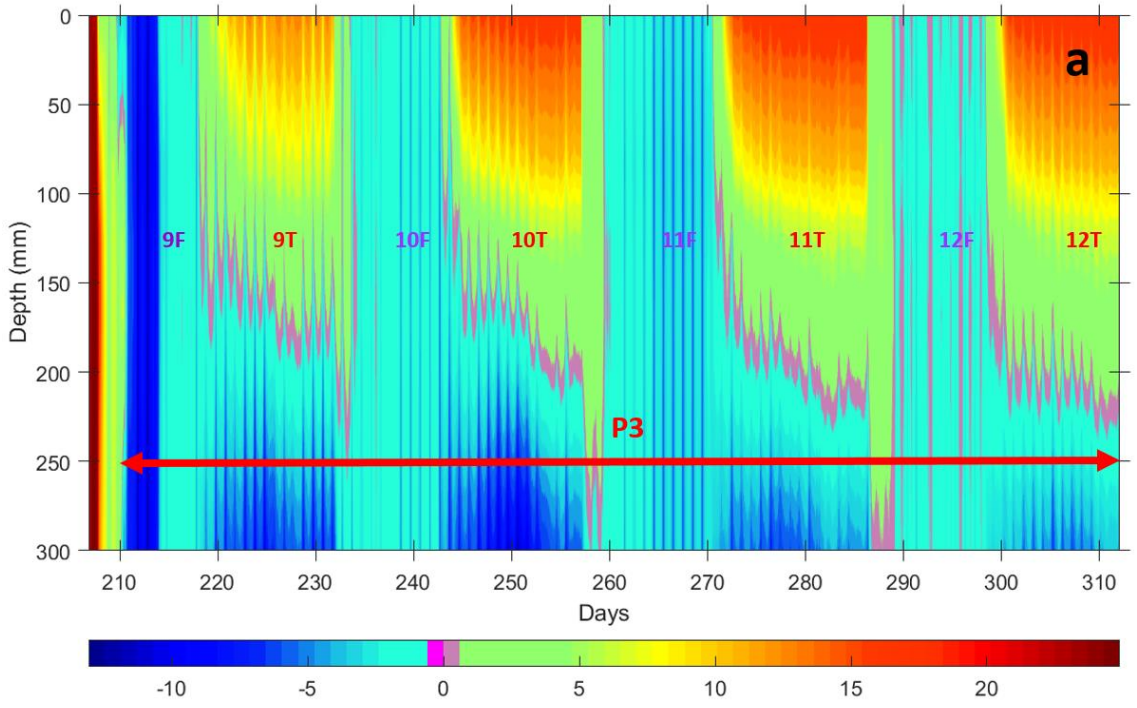

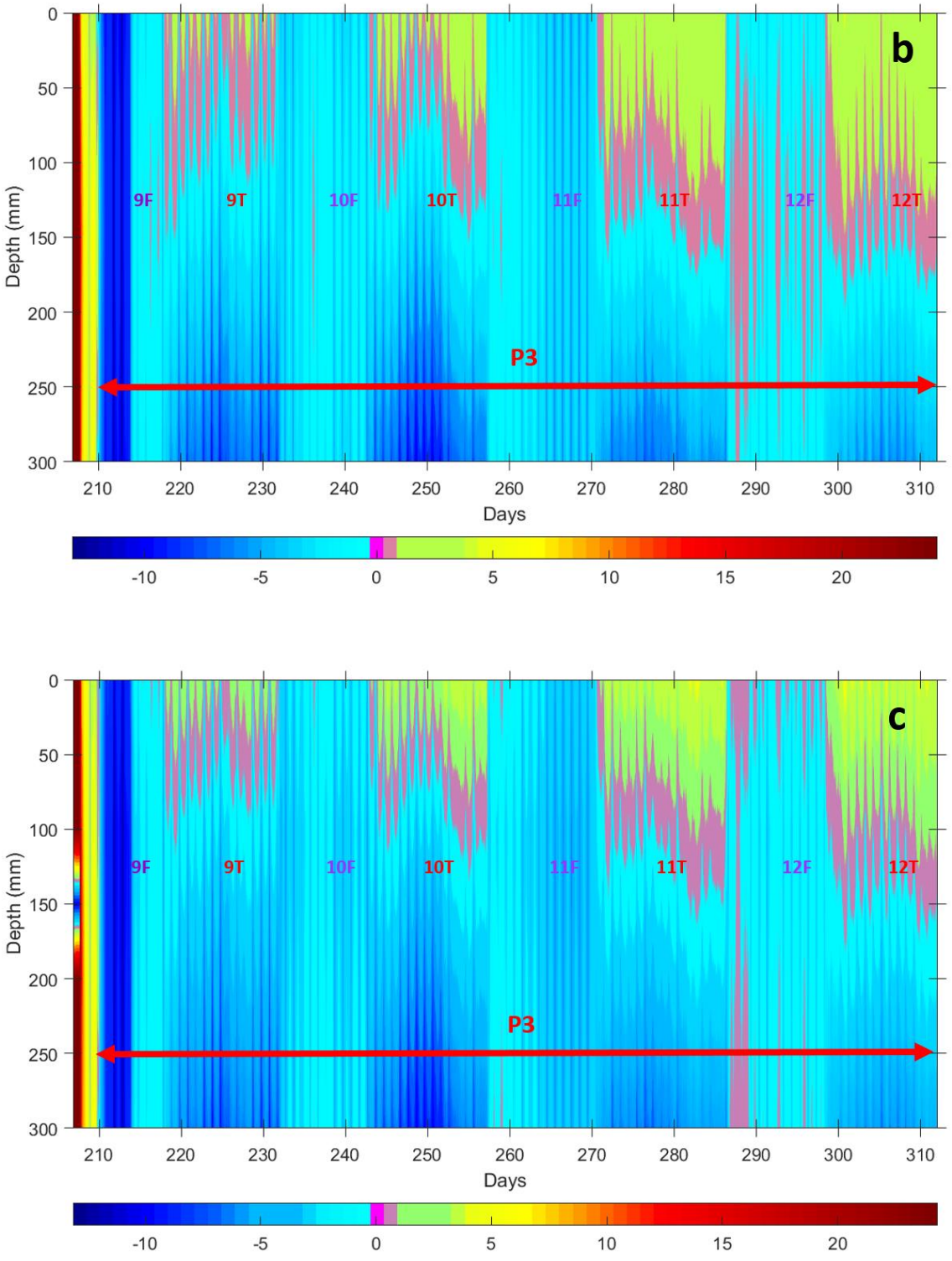

Figure 6.2. Time series of temperature profiles of the three blocks during P3 (freeze–thaw cycles 9–12). (a) Chalk, (b) sandstone with lamination horizontally oriented and (c) sandstone with lamination vertically oriented.

6.3 Heave and settlement

After day 8, the blocks cooled and froze from the top downwards. The three blocks experienced settlement equal to 2.1, 1.8 and 3.7 mm for CM, SH and SV blocks, respectively (Figure 6.3a). Both sandstone blocks retained accumulated heave during freeze cycles 1, 3 and 4, while no significant heave was recorded in CM block at that time. The amount of heave recorded in SH block was 2–2.5 times higher than that of SV block in freeze cycle 3. During thaw cycles 6 and 7, all three blocks heaved substantially to varying amounts and retained the accumulated heave until the next thaw cycle.

The first noticeable settlement was observed in both sandstone blocks during 5T, when the cooling plate temperature was lowered compared to previous thaw cycles (Figure 6.3a). The accumulated heave (4 and 2 mm) restored within SH and SV settled down completely. Due to intense cooling during P1 when the active layer hardy developed within the sandstone blocks (SV completely frozen and SH ~90% frozen), ice crystals developed within the pores caused noticeable accumulated heave until thaw cycle 5. The SH block heaved 2.5 times that of SV block, while there is no significant heave in the chalk block during P1. The chalk block experienced significant heave of 6, 3 and 5 mm, respectively, during thaw cycles 6–8.

At the beginning of freezing cycle 9, thermal contraction occurred but less than that at the beginning of first freeze cycle. The ambient freezing temperature was lower in freezing cycle 9 than freezing cycle 1.

During thaw cycles 10–12, the chalk block heaved 0.5, 3.5 and 2 mm respectively when the thermal gradient was stable during the later stage of thawing periods. At the end of the experiment, 5.5 mm was heave retained in CM block, while the heave developed in the sandstone blocks was less.

Small bursts of heave were abundant during the initial phase of freezing, although similar bursts, of varying magnitude, occurred throughout the experiment.

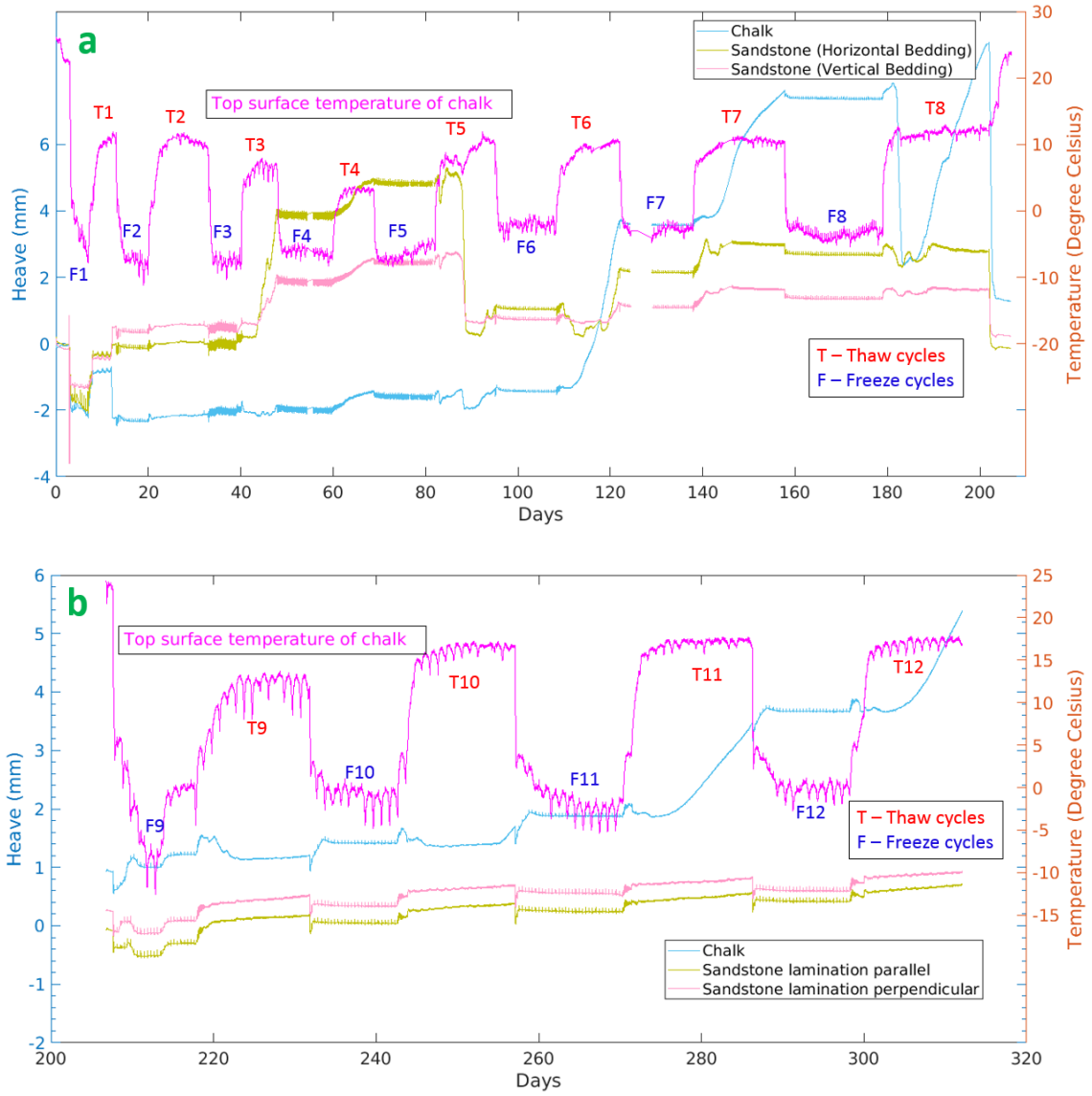

Figure 6.3. Heave time series for the three rock blocks during (a) P1 and P2, (b) P3.

6.4 Strain measurement

Overall a trend of contraction was observed in strain gauges mounted on the chalk block, as shown by the decreasing trend in Figure 6.4a–b. The decreasing trend observed in the SH block (Figure 6.5a) was much less inclined than that in the chalk block.

A mean value of 300–400 microstrain (με) was observed during transitions between freezing and thawing in the chalk block (Figure 6.4b). The largest fluctuations were observed in the strain gauge located at 150 mm depth from the top (in the middle of the chalk block, B face, Figure 6.4a), which had values around 1500 με. The other strain gauges behaved similarly (except for A240). During early thaw cycles these gauges initially had ranges of ~100 με, but by thaw cycle 8 the range had reduced to ~25με (Figure 6.4b). In contrast, the separation during the freeze cycles (50 με at the beginning) increased (~180 με) as the number of cycles increased (similar to

the case of SV between 60 and 180 mm depth). The developments between the middle to late stage of thawing period when the temperature gradient stabilized were around 50 με.

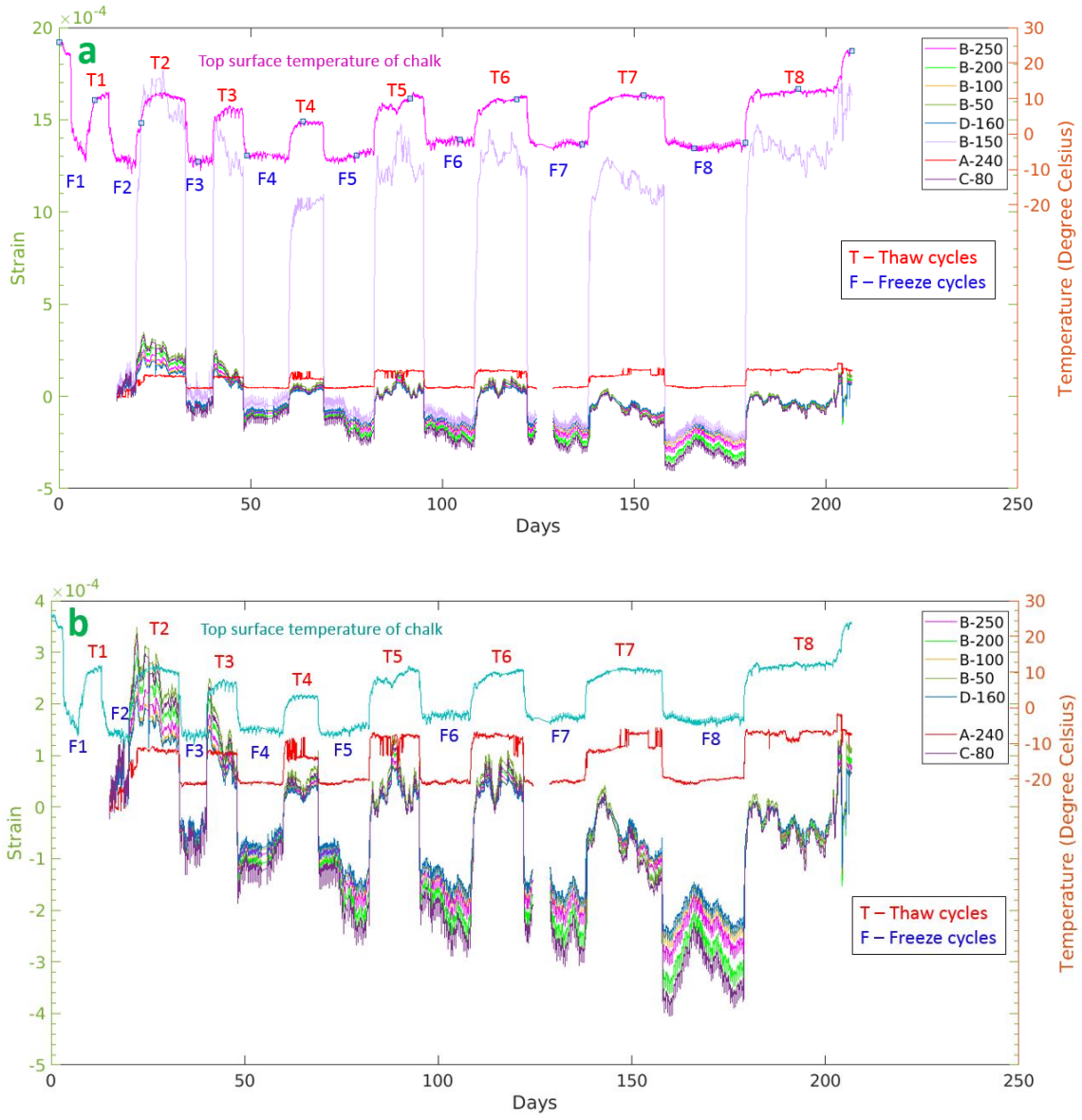

Figure 6.4. Strain time series of the chalk block during P1 and P2 (a). Letters in legend indicate vertical face; number indicates depth (mm). B-150 is omitted in (b).

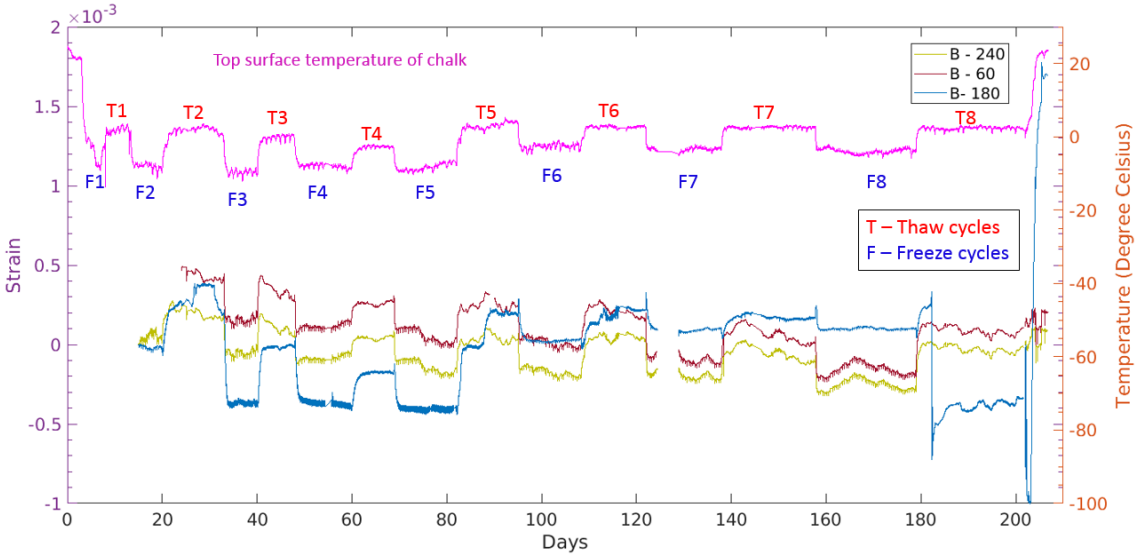

Figure 6.5. Strain time series of the sandstone block with lamination horizontally oriented during P1 and P2. Letters in legend indicate vertical face; number indicates depth (mm).

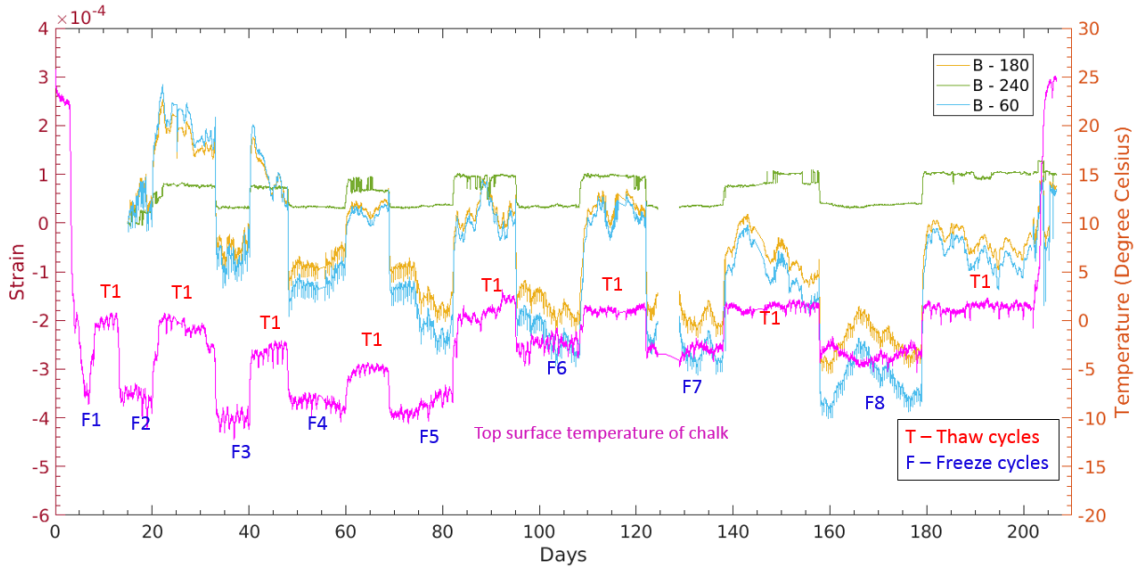

Figure 6.6. Strain time series of the sandstone block with lamination vertically oriented during P1 and P2. Letters in legend indicates vertical face; number indicates depth (mm).

6.5 Cracking during freezing

A horizontal to sub-horizontal brecciated layer developed at 80–110 mm depth from the top surface of the chalk block. The fractures were clearly visible at the end of freeze–thaw cycle 8 (Figure 6.7a). A network of macrocracks visible on the top surface of the block suggests that near-surface vertical cracks (not visible on vertical face B) had also developed. In addition, faint outlines of cracks were visible near depths of 50 mm and 120–150 mm.

By the end of freeze–thaw cycle 12, another horizontal to sub-horizontal brecciated layer had developed at a depth of 200–220 mm in the chalk (Figure 6.7b). The network of macrocracks observed after freeze–thaw cycle 8 on the top face had developed near-surface vertical cracks visible on face B. Another vertical crack had formed on the left part of this face at 100–180 mm depth. A network of several horizontal cracks observed around the vertical cracks developed at 100–180 mm depth and near the surface.

No macrocracks were observed in either block of sandstone after 12 freeze–thaw cycles.

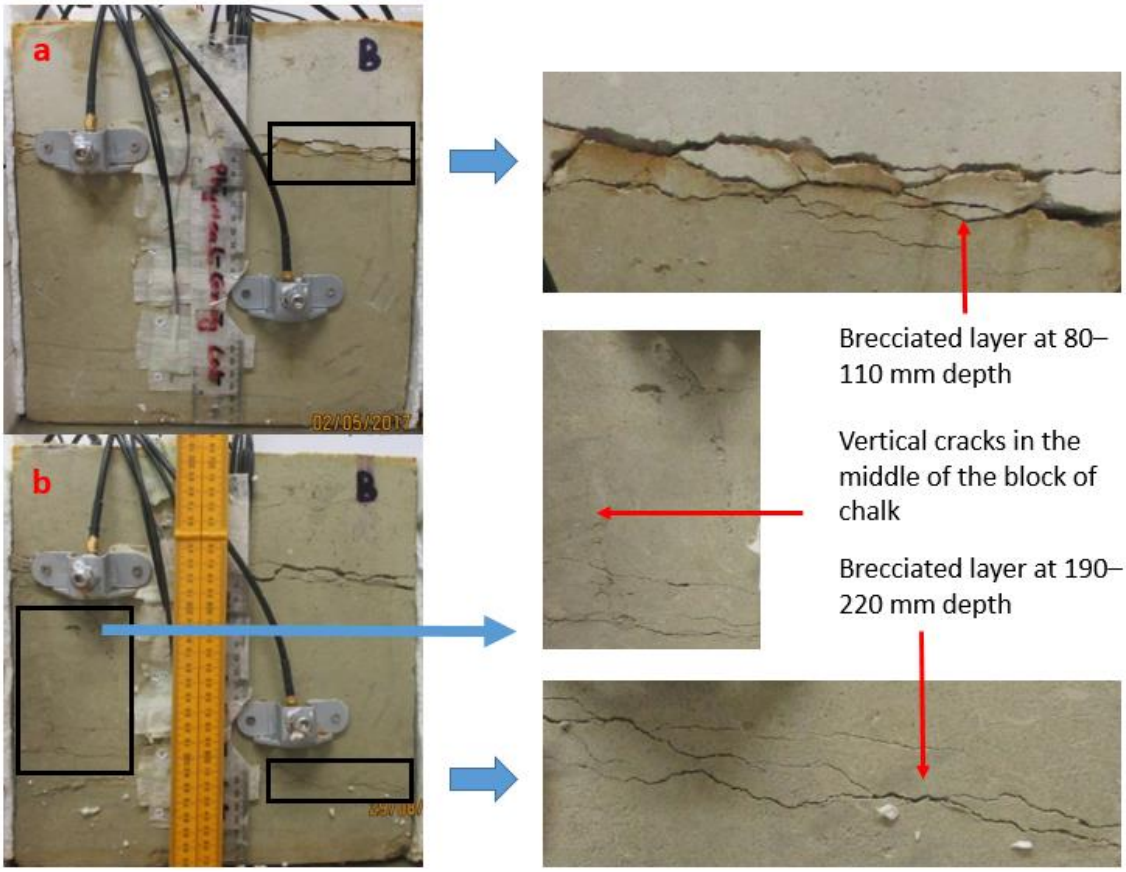

Figure 6.7. Photographs of vertical face B of chalk block after 8 (a) and 12 (b) freeze–thaw cycles.

6.6 Acoustic emissions and cracking

Eight AE sensors mounted on the chalk block captured the acoustic energy released as a result of the mechanical instability during microcracking events. The 3D locations of the events were determined based on the arrival time of acoustic waveforms at the sensors. An event is defined if at least four of the eight sensors captured the pulses of energy released. The objective 3.3 and

objective 3.4 (O3.4) outlined in the chapter one are address in this section. Histograms showing the depths of events during individual periods of freezing (F), freeze–thaw transition (FT), thawing (T) and thaw–freeze transition (TF) are plotted in Figure 6.8a–d. The 3D location of the AE events are illustrated in Figure 6.9a–d. The strength of each event in the 3D plot in Figure 6.9a–d was classified based on the amplitude of the source. The tensile and shear events based on average frequency and RA value are shown in Figure 6.11a–d. Figure 6.12a–d segments out the strength of the amplitude and the corresponding number of hits that define an event.

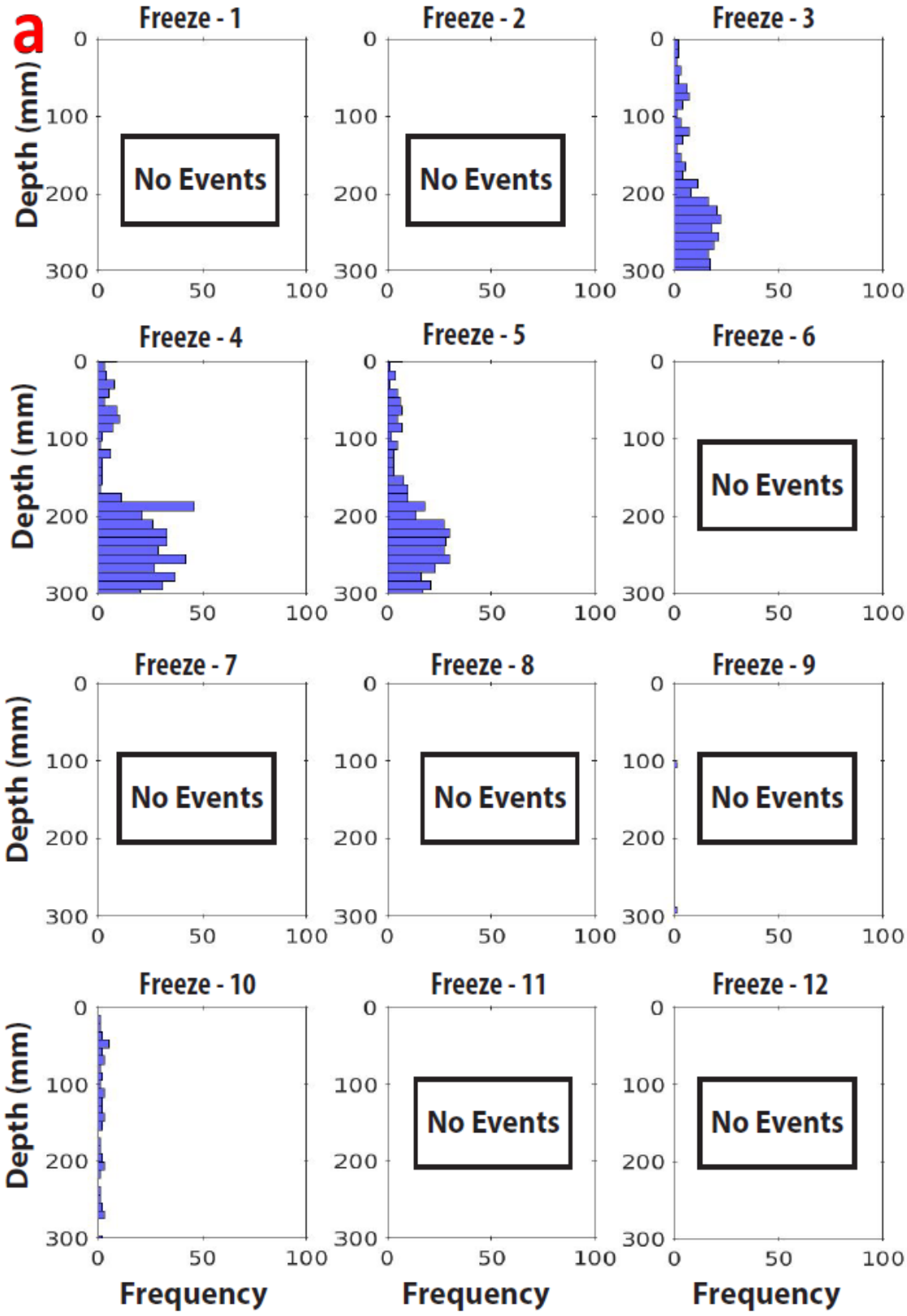
a
Freeze - 1
Freeze - 2
Freeze - 3
Freeze - 4
Freeze - 5
Freeze - 6
Freeze - 7
Freeze - 8
Freeze - 9
Freeze - 10
Freeze - 11
Freeze - 12
No Events
Depth (mm)
Frequency
0
100
200
300
0
50
100

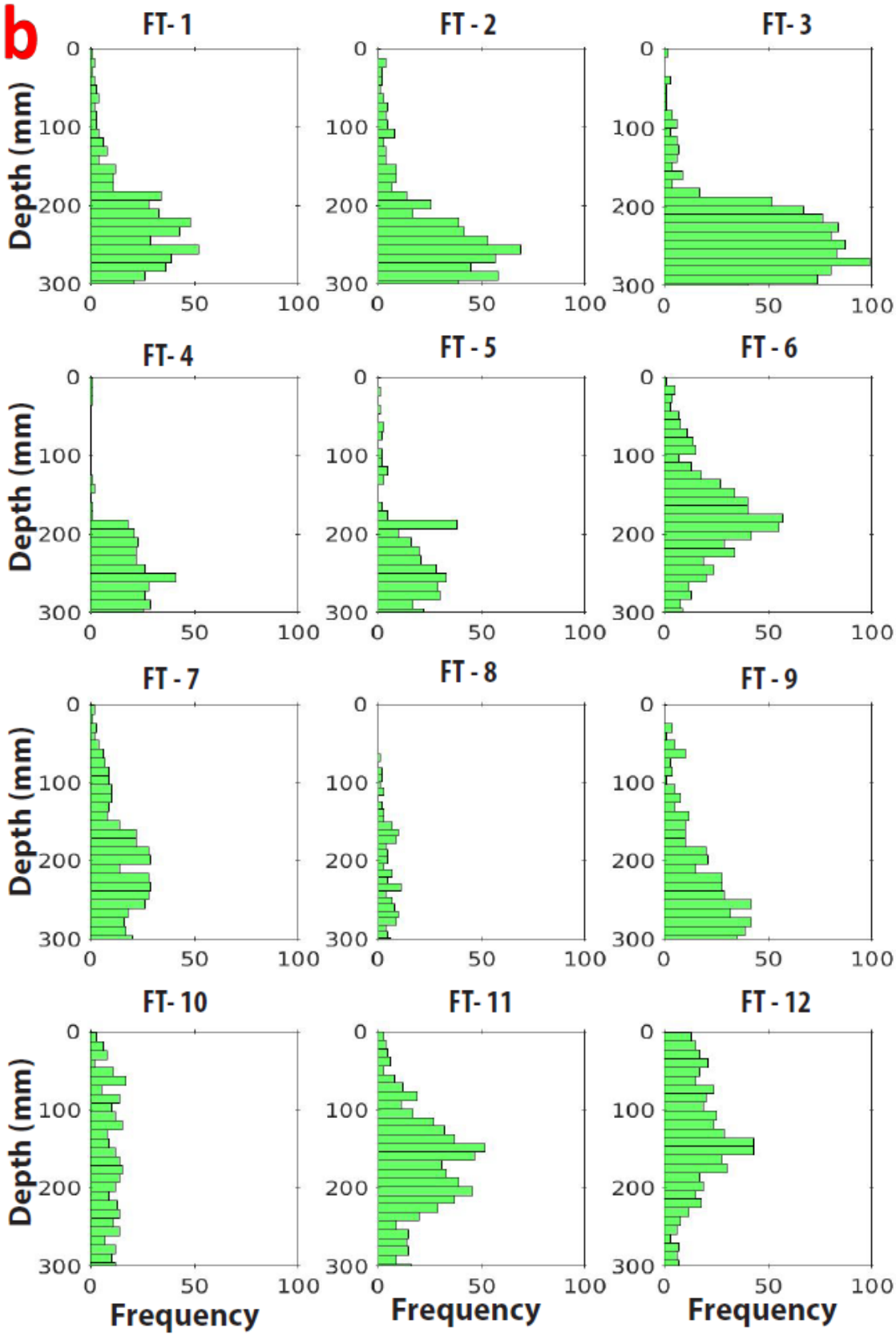
b
FT- 1
FT - 2
FT- 3
FT- 4
FT - 5
FT - 6
FT - 7
FT - 8
FT - 9
FT- 10
FT- 11
FT - 12
Depth (mm)
0
100
200
300
0
50
100
Frequency

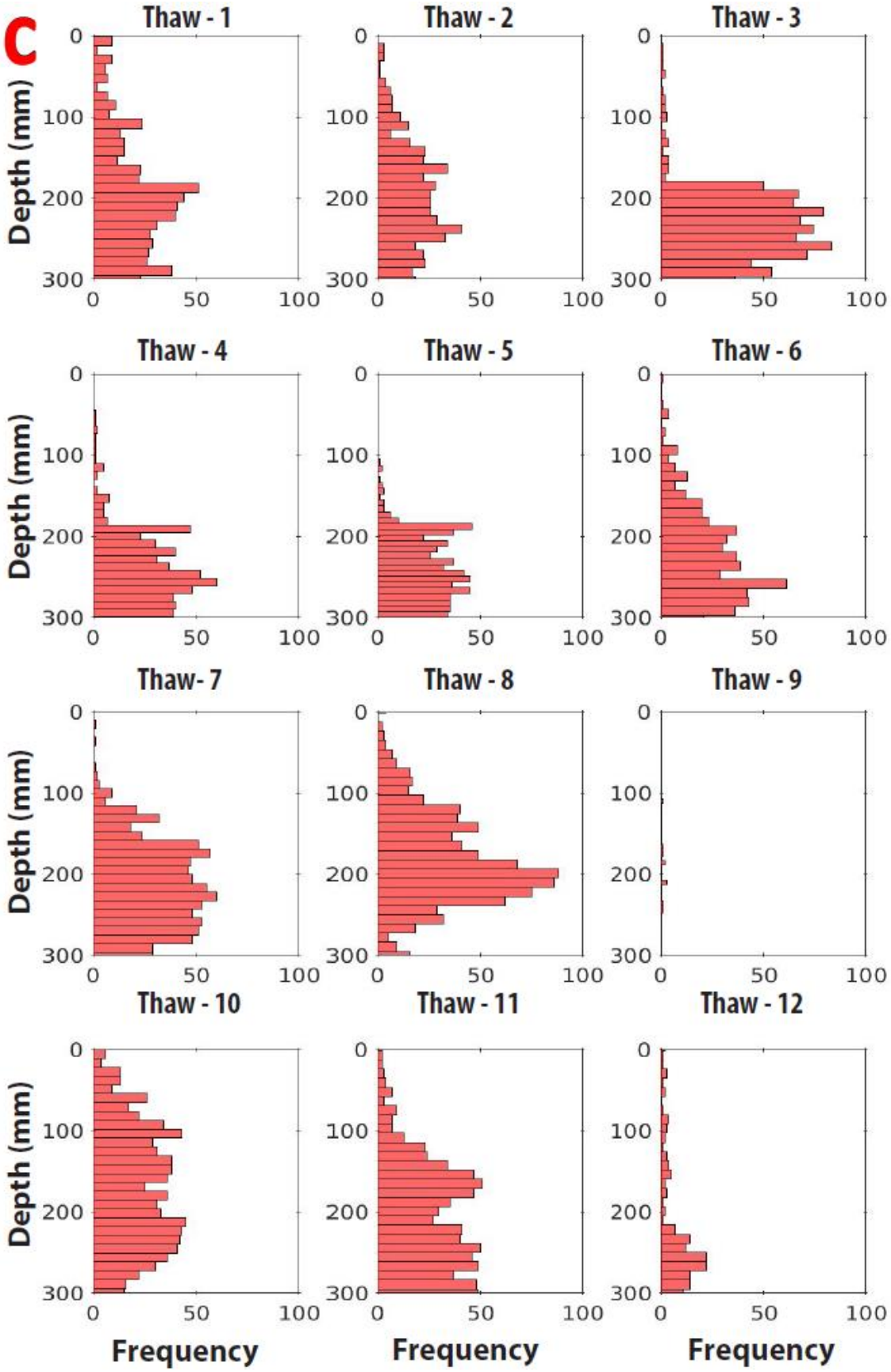
C
Thaw - 1
Thaw - 2
Thaw - 3
Thaw - 4
Thaw - 5
Thaw - 6
Thaw- 7
Thaw - 8
Thaw - 9
Thaw - 10
Thaw - 11
Thaw - 12
Depth (mm)
Frequency
0
100
200
300
0
50
100

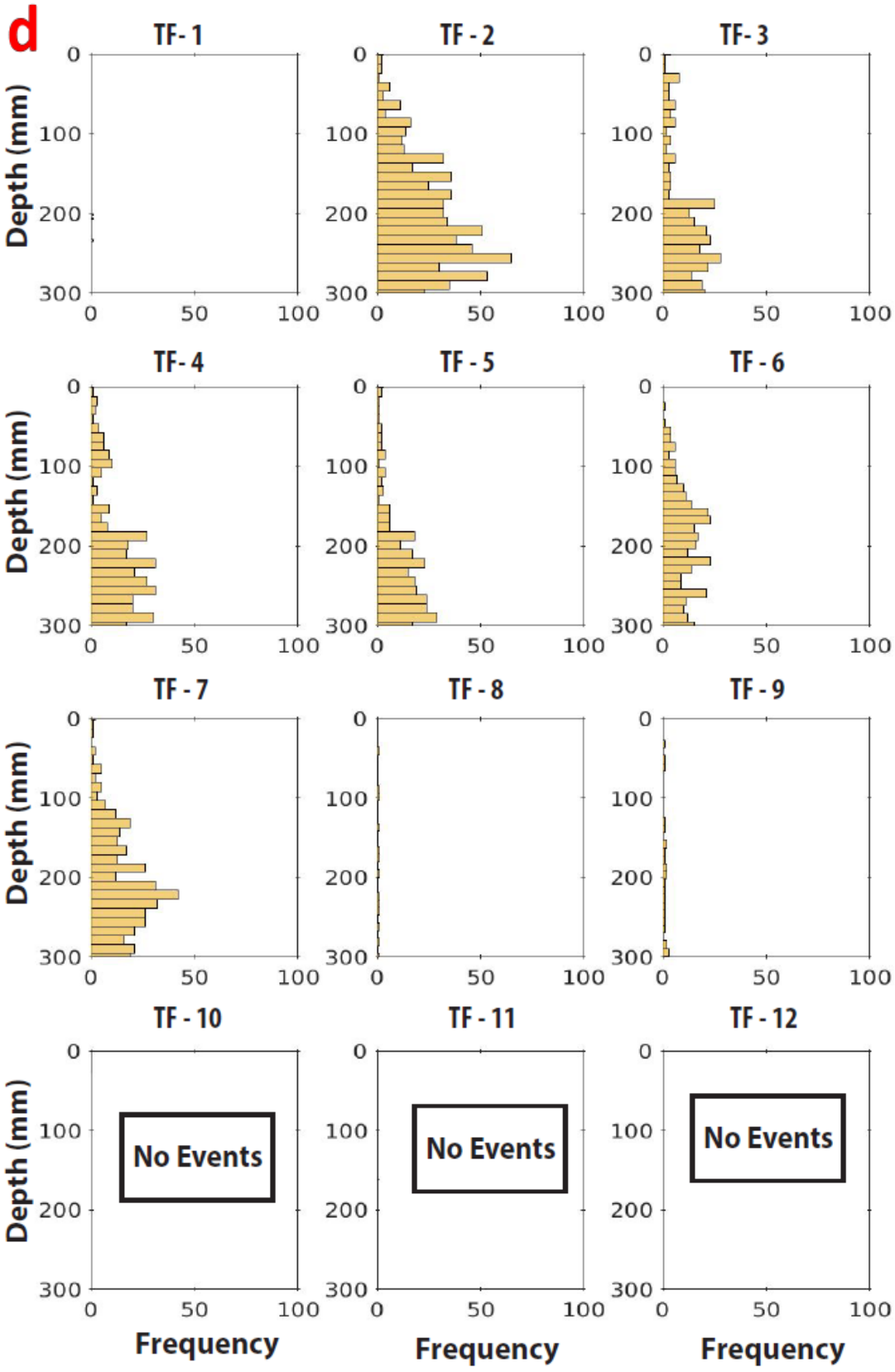

Figure 6.8. Histograms showing the depth of acoustic events during individual periods of (a) freezing, (b) freeze–thaw transition, (c) thawing and (d) thaw–freeze transition.

a

Freeze - 1

No Events

Freeze - 2

No Events

Freeze - 3

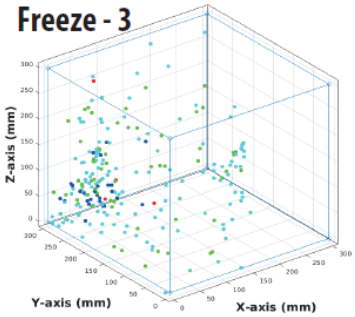

Freeze - 4

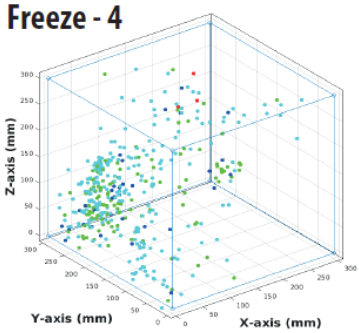

Freeze - 5

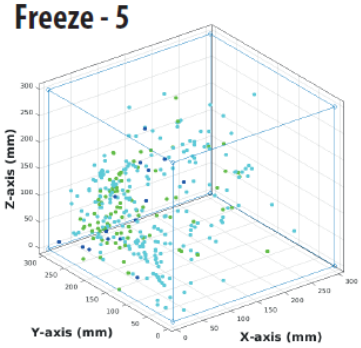

Freeze - 6

No Events

Freeze - 7

No Events

Freeze - 8

No Events

Freeze - 9

No Events

Freeze - 10

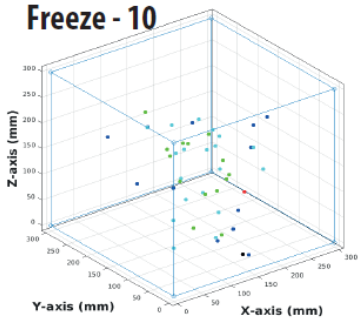

Freeze - 11

No Events

Freeze - 12

No Events

Legend	Amplitude (dB)
●	> 40 and < 50
●	> 50 and < 60
●	> 60 and < 70
●	> 70 and < 80
●	> 80

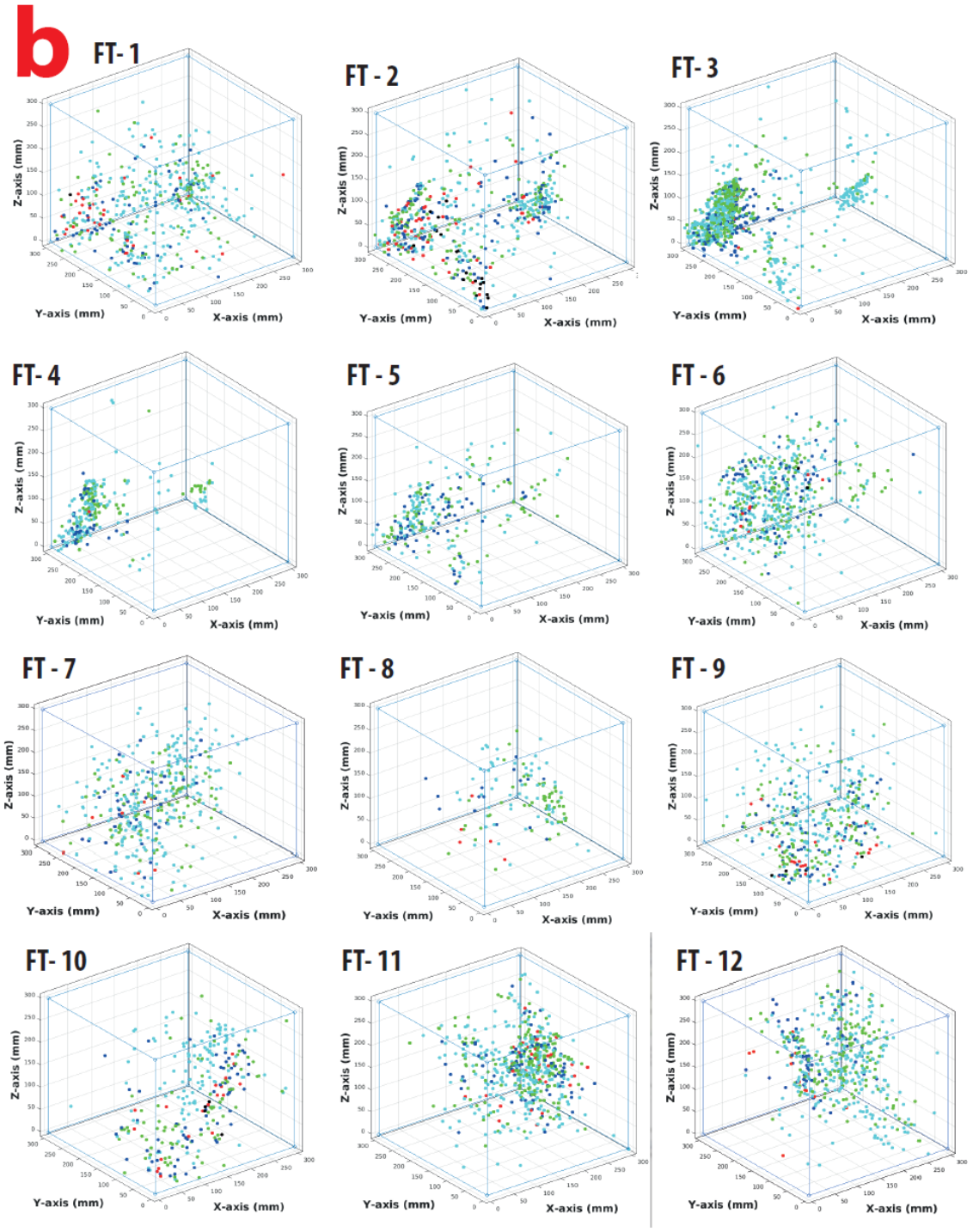

Legend	Amplitude (dB)
●	> 40 and < 50
●	> 50 and < 60
●	> 60 and < 70
●	> 70 and < 80
●	> 80

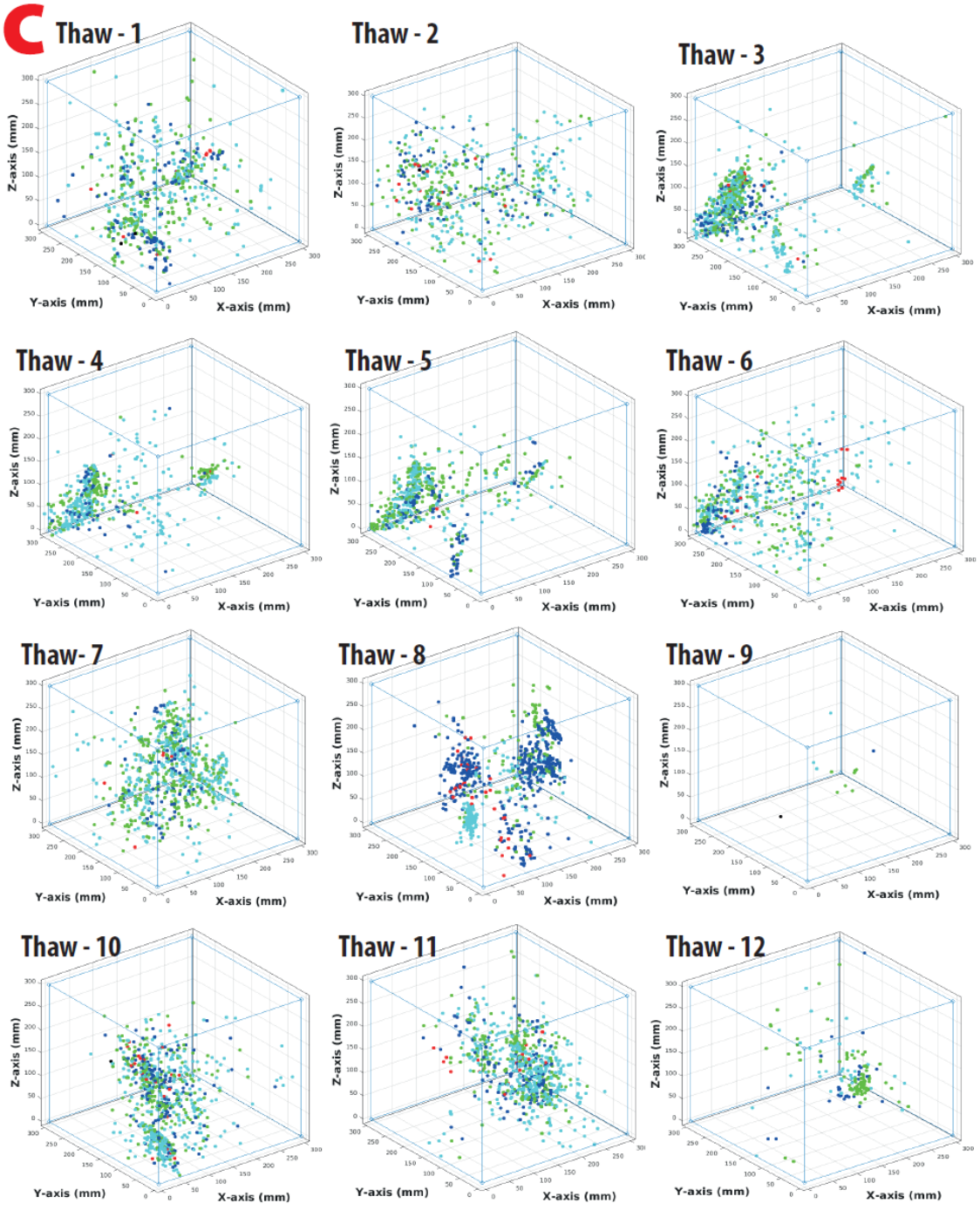

Legend	Amplitude (dB)
●	> 40 and < 50
●	> 50 and < 60
●	> 60 and < 70
●	> 70 and < 80
●	> 80

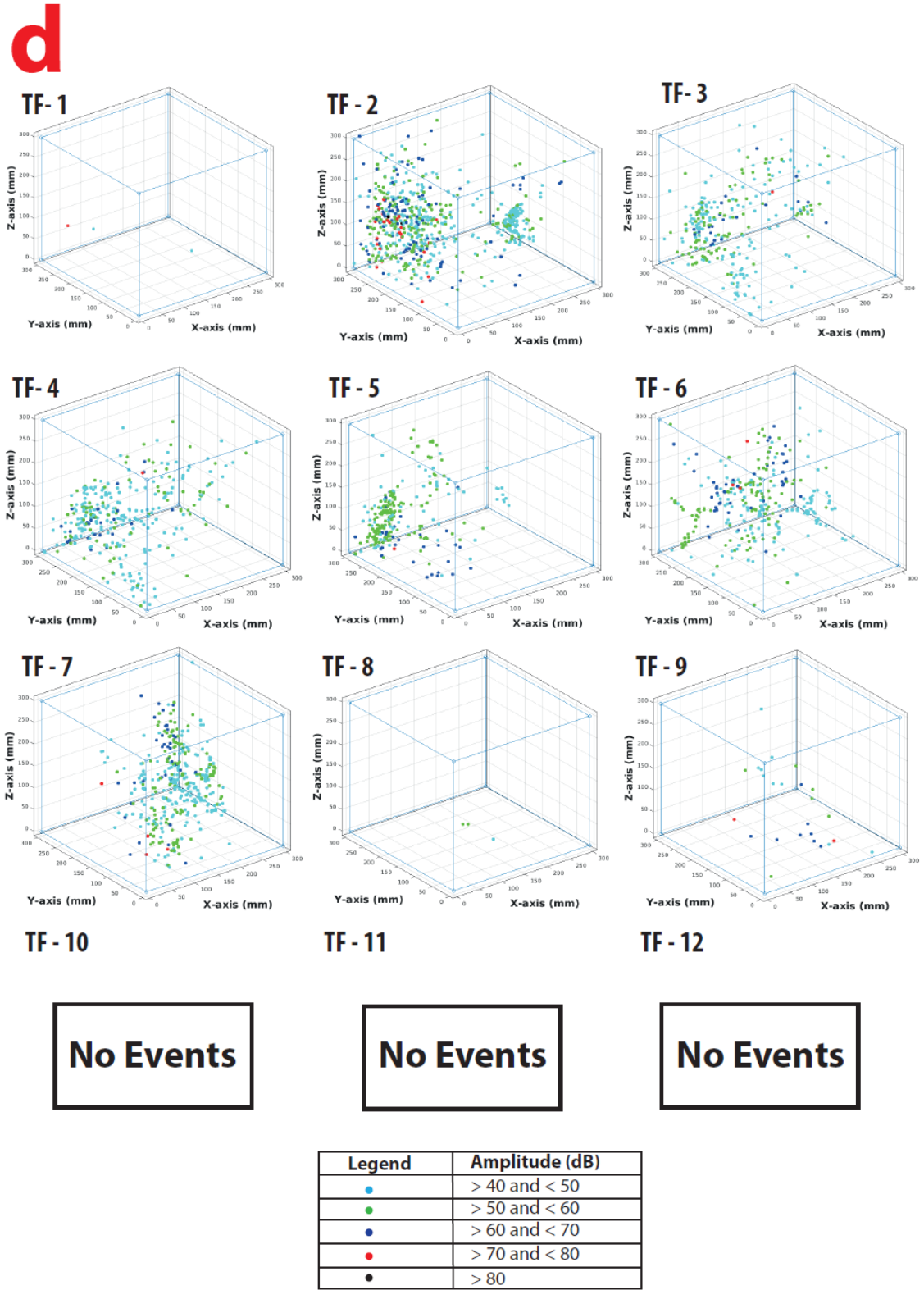

Figure 6.9. 3D plot showing the locations of the AE events based on the amplitude level during individual periods of (a) freezing, (b) freeze–thaw transition, (c) thawing and (d) thaw–freeze transition.

During the experiment, the AE sensors captured the waveform characteristics of the acoustic waves, including the number of hits, duration of the signals, number of counts above a preset threshold (= 40 dB), rise time, amplitude, and energy released (Figure 6.10a). In order to classify the nature of cracking, the RA value and average frequency were calculated from the waveform characteristics as follows,

$$\text{RA value} = \text{rise time}/\ \text{maximum amplitude}$$

$$\text{Average frequency} = \text{AE counts}/\ \text{duration time}$$

Based on these two parameters cracks were classified as mode-I (tension) and mode-II (shear) crack (Figure 6.10b; JCMS-IIIB5706, 2003). The RA value versus AF plots for all the freezing, freeze–thaw transition, thawing and thaw–freeze transition cycles are shown in Figure 6.11a–d. Different waveform characteristic of the AE events captured during the experiment were reported in Appendix C.

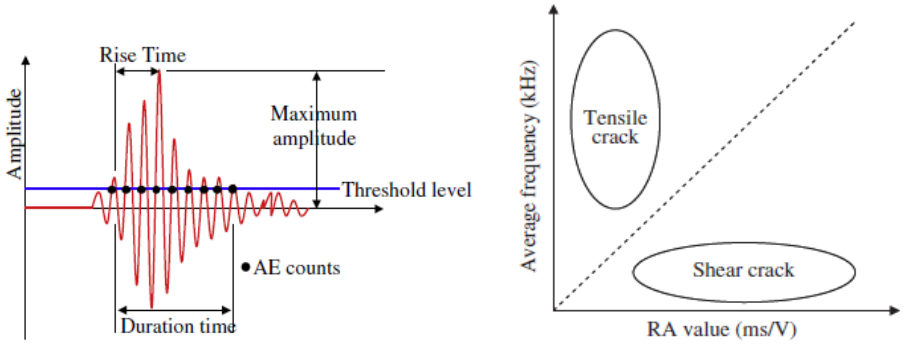

Figure 6.10. Schematic diagrams of (a) different waveform parameters of the acoustic waves, (b) RA vs average frequency plot to discriminate tension and shear fracture. Source: Ohno et al., 2010.

6.6.1 Freezing cycles

AE events were recorded during freezing cycles 3–5 (Figure 6.8a), while during the other freezing cycles no such significant events were captured above the pre-set threshold of 40dB. Cycle 10 witnessed relatively few events compared to cycles 3–5, which were distributed throughout the block, with high-amplitude events at 150–200 mm depth (near face A, Figure 6.9a). Comparatively steep freezing gradients during P1 initiated AE activity at the beginning of the experiment. As the intensity of freezing fell in later cycles, the frequency AE activity reduced. The AE events during freezing are classified mostly in terms of tensional activity, though a few shearing events were inferred during F3 and 4 (Figure 6.11a). Most of the events originated

within the lower half of the block (Figure 6.8a), but some were observed within 100 mm from top surface (Figure 6.9a). In F4, some high-amplitude events were recorded that follow the trace of the near-surface vertical crack. The details of the source amplitude of AE events and the duration of each freezing cycle are summarised in Table 6.1.

Freezing Cycles	Amplitude (dB)					Total Number of Events	Duration (Days)
	40-49	50-59	60-69	70-79	>80		
1	0	0	0	0	0	0	4
2	0	0	0	0	0	0	5
3	145	66	26	4	0	241	6
4	269	124	34	3	0	430	10
5	230	91	17	0	0	338	11
6	0	0	0	0	0	0	10
7	0	0	0	0	0	0	14
8	0	0	0	0	0	0	18
9	0	0	0	0	0	0	7
10	19	14	12	1	1	47	10
11	0	0	0	0	0	0	10
12	0	0	0	0	0	0	9

Table 6.1. The value and frequency of source amplitude of the AE events during 12 freezing cycles.

6.6.2 Freeze–thaw transitions

The period between turning off the chilled air supply and development of a stable vertical thermal gradient in the simulated active layer was considered as a freeze–thaw (FT) transition (mean duration = 1.5 days). During this period the 0°C isotherm descended into the block and stabilized at a certain depth. 34% of the total AE events were captured during these short transitions. During FT 1–4, AE events originated mostly within the lower ~110 mm of the chalk block (Figure 6.8b), mostly near face D (Figure 6.9b). AE events were noticeable around two separate vertical clusters near faces D and B. The vertical clustering near face D was more intense compared to that near face B (B face of the block was photographed at different intervals of freezing and thawing). During FT6, the distribution of significant AE activity expanded into the upper 150 mm of the block. During the first four FT transitions, high-amplitude events (>70 dB) were recorded mostly in FT1-2, near the base of the block. Some high-amplitude events were observed near the top during FT6. The events recorded during FT 6–7 were dispersed throughout the block compared to the vertical concentration of AE activity in previous FT transitions. During FT9–10, more high-amplitude events recurred as the cooling system restarted in P3 and repeated what happened during the beginning of P1. The events were dispersed within the block during FT 9–10 but concentrated into two vertical clusters in the middle of the block and near face B during FT 11–12. A tendency of vertical clustering of events

was observed followed by dispersed events within the block. The higher thermal gradient in P3 was associated with more high-amplitude events than in P1–2.

Up to FT5, 1 mm heave of the top of the chalk block was recorded after initial consolidation (Figure 6.3a). AE events were observed within the lower 150 mm of chalk during FT1–5. During FT6, significant heave of 5 mm in the chalk block occurred when microcracking events extended into the upper 150 mm of the block. These events may have started to form the brecciated layer at 80-110 mm depth. The heave retained in FT6 recorded more shearing activity than in FT4 and 5 (Figure 6.11b). FT9 showed even more shearing activity, possibly due to the reactivation of cracks developed during P1 and P2.

In FT4, AE activity was strongly concentrated within the lower 100 mm, unlike events that occurred at depths above 150 mm during and after FT6. During FT4, the 0^{o}C isotherm (thawing front) only reached ~50 mm depth in the chalk, much shallower than in the other cycles (Figure 6.1a) and the number of AE events reduced compared to previous cycles. In FT6 and 7, accumulated heave attributed to the development of segregated ice at ~100 mm depth coincided with a small number of inferred shearing events that were absent in FT8. This also explains the dispersed distribution of AE hypocentres within the block in FT 6–7 relative to the vertical clustering of in FT 1–5. The concentration of AE hypocentres in vertical arrays at different locations within the block suggests the migration of water induced AE activity on its transportation path. Super cooled water could have originated as the thawing process started. The magnitude of the source amplitude of AE events are summarised in Table 6.2.

Freeze-thaw Transition	Amplitude (dB)					Total Number of Events	Duration (Days)
	40-49	50-59	60-69	70-79	> 80		
1	254	112	67	33	1	467	1.5
2	190	143	126	52	19	530	1.5
3	451	317	112	16	0	896	1.5
4	156	90	43	1	0	290	1.5
5	129	95	67	0	0	291	1.5
6	321	153	84	9	2	569	1.5
7	242	101	41	8	0	392	1.5
8	63	53	15	5	0	136	1.5
9	198	125	69	24	4	420	1.5
10	122	82	63	19	4	290	1.5
11	282	196	84	34	0	596	1.5
12	276	160	64	13	0	513	1.5

Table 6.2. The value and frequency of source amplitude of the AE events during 12 freeze-thaw transition periods.

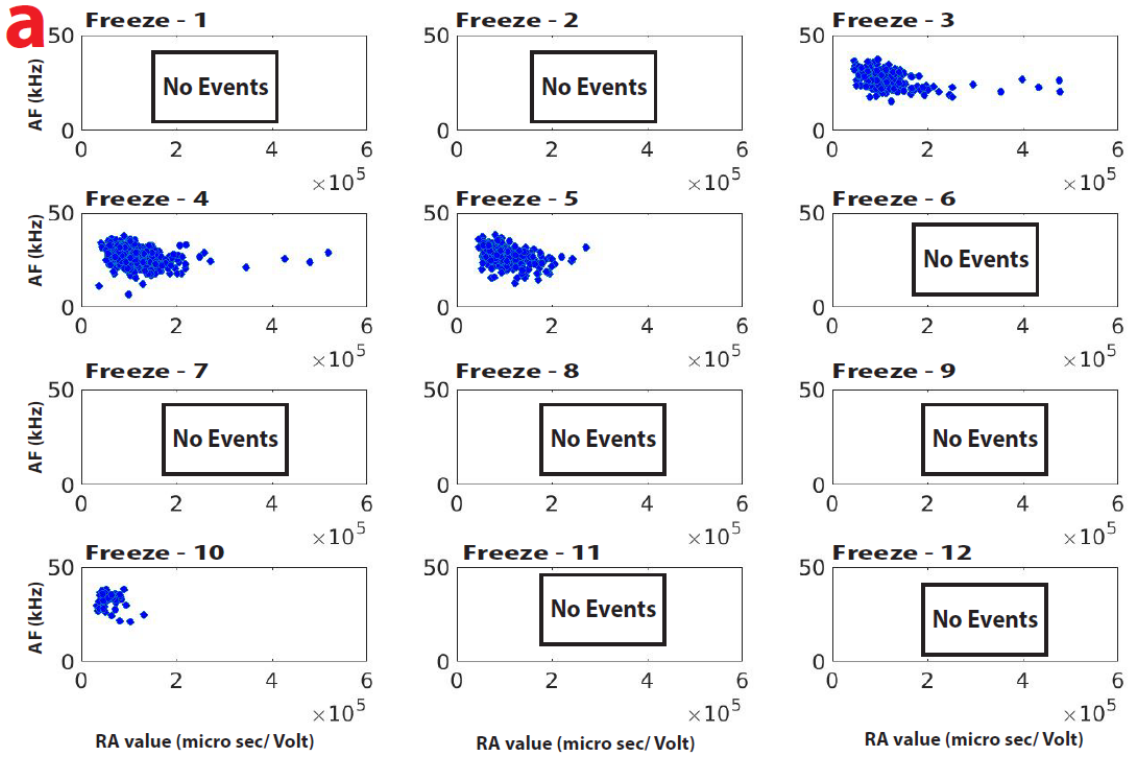
a
Freeze - 1
Freeze - 2
Freeze - 3
Freeze - 4
Freeze - 5
Freeze - 6
Freeze - 7
Freeze - 8
Freeze - 9
Freeze - 10
Freeze - 11
Freeze - 12
No Events
AF (kHz)
RA value (micro sec/ Volt)
×10^5

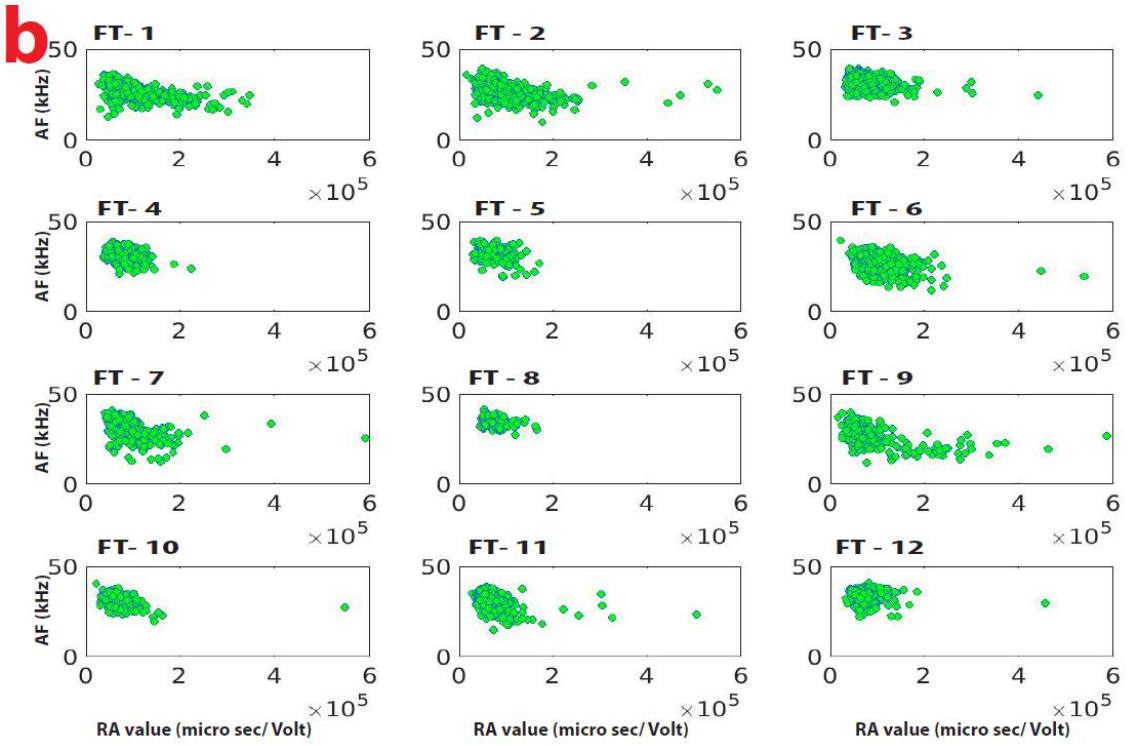
b
FT- 1
FT - 2
FT- 3
FT- 4
FT - 5
FT - 6
FT - 7
FT - 8
FT - 9
FT- 10
FT- 11
FT - 12
AF (kHz)
RA value (micro sec/ Volt)
×10^5

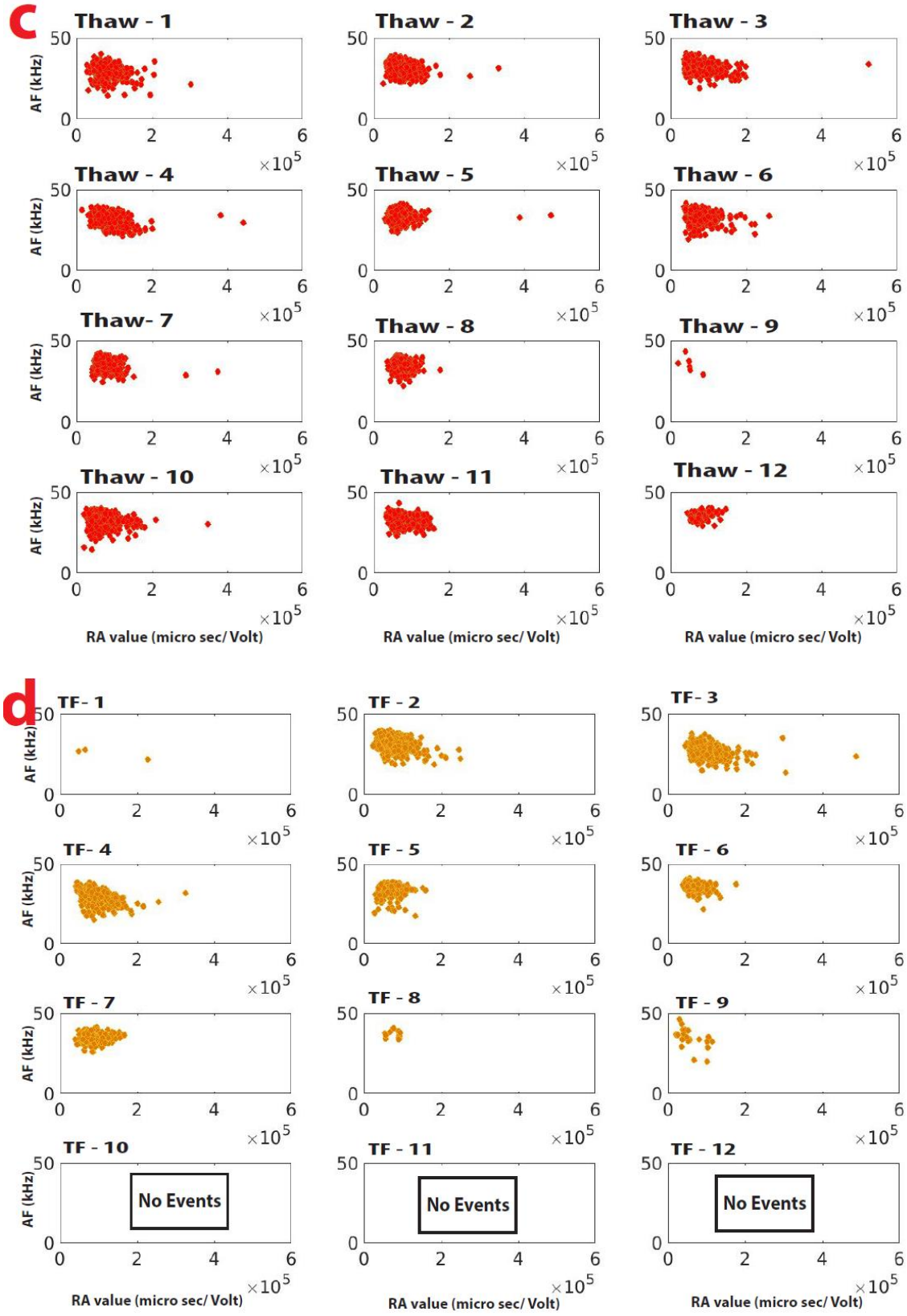

Figure 6.11. Abundance of tension and shearing activity during periods of (a) freezing, (b) freeze–thaw transition, (c) thawing and (d) thaw–freeze transition.

6.6.3 Thawing cycles

More of the AE activity occurred in thawing cycles (~44%) relative to the freezing cycles and other transition phases. The shearing components of microcracking were fewer in the thawing (T) cycles than those in the freeze–thaw transitions (Figure 6.11b–c). The depth range of AE events during T1 and 2 extended more or less to the top of the chalk block (Figure 6.8c and 6.9c). By contrast, the depth of AE events during T3–5 was limited mostly to the lower half of the block and was similar to the vertical clusters recorded during FT3–5 (Figure 6.8b–c). From T6 onwards, AE activity extended into the upper half of the block, possibly due to the development of new microcracking at 100–150 mm depth during P2 and 100–150 and 150–200 mm depth during P3. During T6, dispersed activity was observed within the chalk, as in FT6–7. In T7 and in T8, the events clustered around two distinct vertical shapes around the central vertical axis, with abundant high-amplitude events between 60 and 70 dB (blue). AE events were also distributed in vertical arrays around the central vertical axis in T10 and 11, following the two similar vertical patches developed in T8. The distribution of hypocentres of AE events expanded upward above a depth of 150 mm during and after T6 (following the similar pattern in FT6), suggesting the development of brecciated layer at ~100 mm depth. The broad depth ranges of AE activity during T6–8 and 11–12 coincide with significant heave observed in the chalk block (Figure 6.3a–b). The strength of the source amplitude of AE events and the duration of each thawing cycle are summarised in Table 6.3.

Thawing Cycles	Amplitude (dB)					Total Number of Events	Duration (Days)
	40-49	50-59	60-69	70-79	> 80		
1	195	241	118	10	2	566	5
2	199	189	86	13	1	488	12
3	389	283	94	21	0	787	6
4	326	173	64	4	0	567	7
5	273	243	110	2	0	628	11
6	287	149	80	14	0	530	12
7	371	337	79	6	0	793	18
8	163	119	524	35	0	841	22
9	3	7	1	0	1	12	12
10	354	241	153	25	1	774	13
11	353	230	136	18	0	737	13
12	36	91	31	0	0	158	13

Table 6.3. The value and frequency of source amplitude of the AE events during 12 thawing cycles.

6.6.4 Thaw–freeze transitions

The period between imposing a sub-zero air temperature and the onset of more or less isothermal conditions in the frozen chalk block is termed the thaw–freeze (TF) transition (mean duration = 1.5 days). Around 14% of AE events occurred during such transitions. TF transitions 1–5 showed AE activity across a broad range of depth and reached near the top of the block, though most events were located within the lower 150 mm (Figure 6.8d and 6.9d). As in FT6 and T6, AE activity during TF6 extended upwards to depths shallower than 150 mm, interpreted as the initiation of cracking at ~100 mm depth. In TF6, the events were dispersed throughout the block, favouring the development of a horizontal brecciated layer, while the hypocentres in TF7 clustered in a vertical fashion, contributing to the development of vertical cracks. When the temperature gradient declined from TF9 onwards, hardly any AE events were recorded. The magnitude of the source amplitude of AE events and the duration of each thaw–freeze transition period are summarised in Table 6.2.

Thaw-freeze Transition	Amplitude (dB)					Total Number of Events	Duration (Days)
	40-49	50-59	60-69	70-79	> 80		
1	2	0	0	1	0	3	1
2	313	229	104	24	2	672	1
3	162	96	23	1	0	282	1.5
4	222	84	27	1	0	334	1.5
5	72	159	30	1	0	262	2
6	132	120	47	3	0	302	2
7	221	129	35	4	0	389	2
8	1	2	0	0	0	3	1.5
9	9	6	8	2	0	25	1.5
10	0	0	0	0	0	0	1.5
11	0	0	0	0	0	0	1.5
12	0	0	0	0	0	0	-

Table 6.4. The value and frequency of source amplitude of the AE events during 12 thaw-freeze transition periods.

a

Freeze - 1

No Events

Freeze - 2

No Events

Freeze - 3

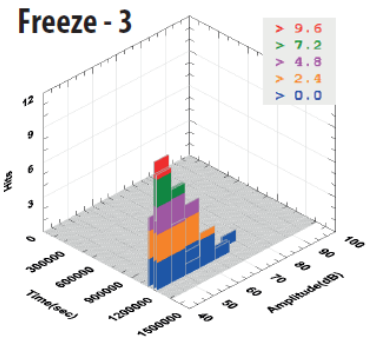

Freeze - 4

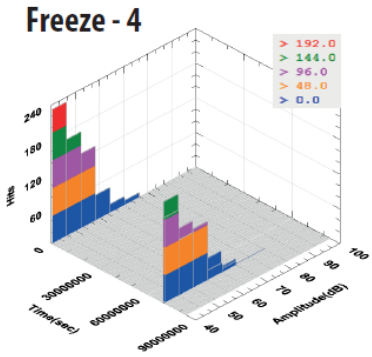

Freeze - 5

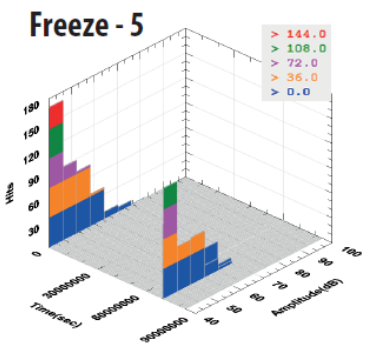

Freeze - 6

No Events

Freeze - 7

No Events

Freeze - 8

No Events

Freeze - 9

No Events

Freeze - 10

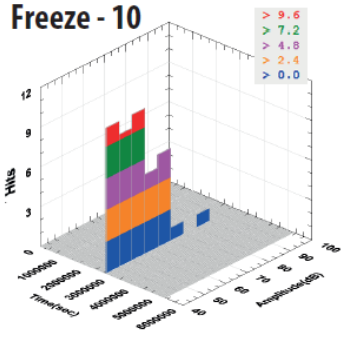

Freeze - 11

No Events

Freeze - 12

No Events

b

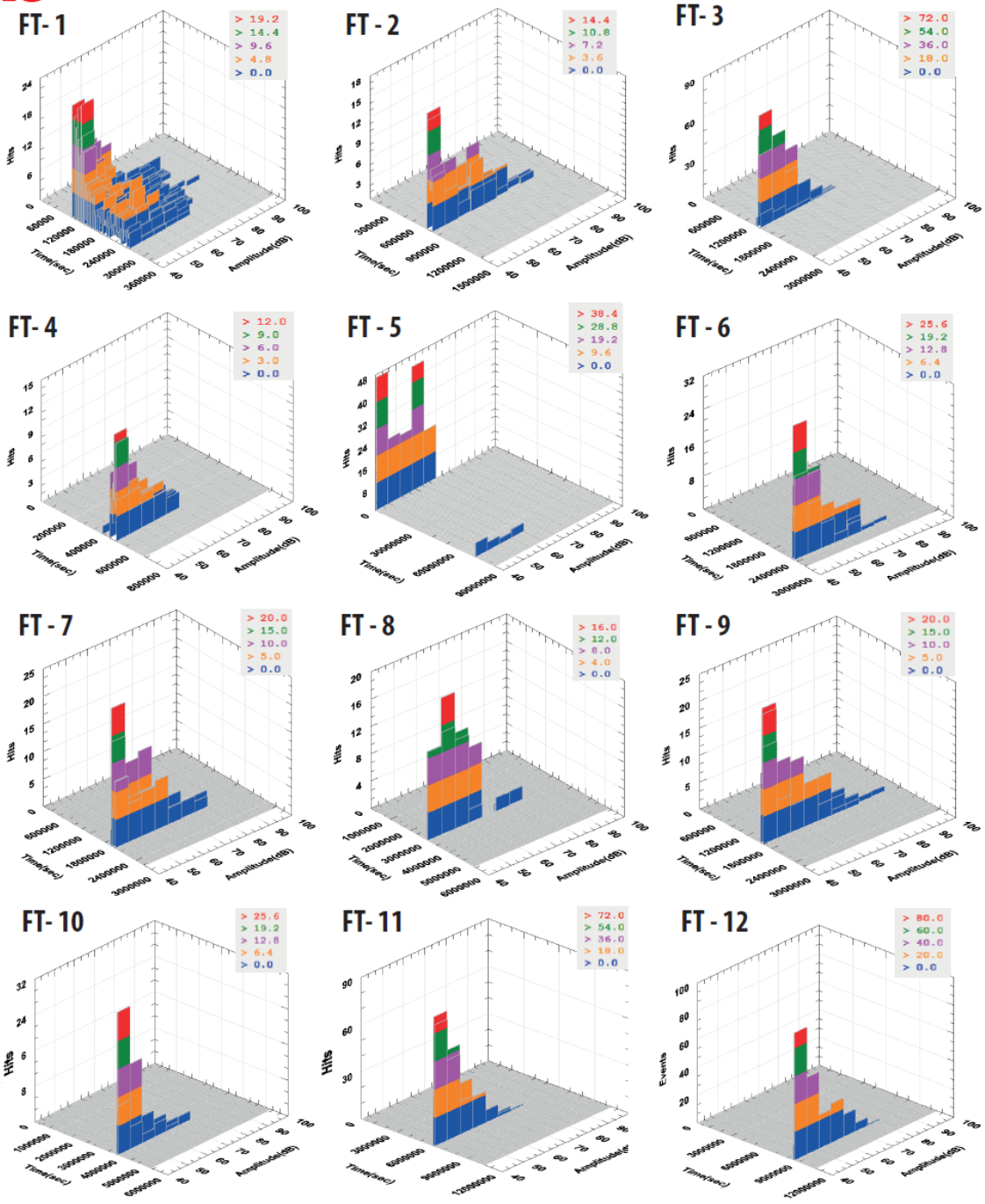
FT- 1
> 19.2
> 14.4
> 9.6
> 4.8
> 0.0
Hits
Time(sec)
Amplitude(dB)
FT - 2
> 14.4
> 10.8
> 7.2
> 3.6
> 0.0
Hits
Time(sec)
Amplitude(dB)
FT- 3
> 72.0
> 54.0
> 36.0
> 18.0
> 0.0
Hits
Time(sec)
Amplitude(dB)
FT- 4
> 12.0
> 9.0
> 6.0
> 3.0
> 0.0
Hits
Time(sec)
Amplitude(dB)
FT - 5
> 38.4
> 28.8
> 19.2
> 9.6
> 0.0
Hits
Time(sec)
Amplitude(dB)
FT - 6
> 25.6
> 19.2
> 12.8
> 6.4
> 0.0
Hits
Time(sec)
Amplitude(dB)
FT - 7
> 20.0
> 15.0
> 10.0
> 5.0
> 0.0
Hits
Time(sec)
Amplitude(dB)
FT - 8
> 16.0
> 12.0
> 8.0
> 4.0
> 0.0
Hits
Time(sec)
Amplitude(dB)
FT - 9
> 20.0
> 15.0
> 10.0
> 5.0
> 0.0
Hits
Time(sec)
Amplitude(dB)
FT- 10
> 25.6
> 19.2
> 12.8
> 6.4
> 0.0
Hits
Time(sec)
Amplitude(dB)
FT- 11
> 72.0
> 54.0
> 36.0
> 18.0
> 0.0
Hits
Time(sec)
Amplitude(dB)
FT - 12
> 80.0
> 60.0
> 40.0
> 20.0
> 0.0
Events
Time(sec)
Amplitude(dB)

C

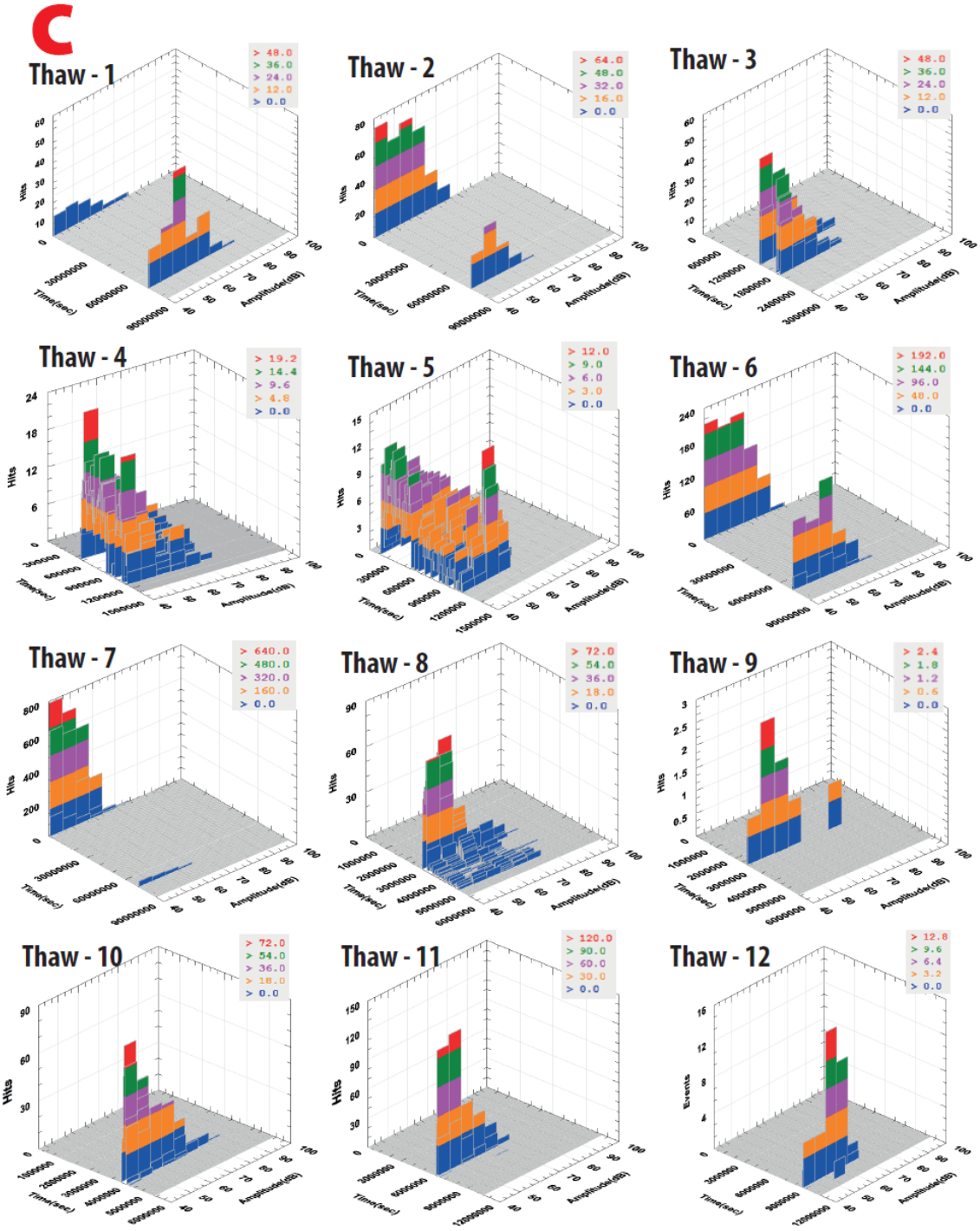
Thaw - 1
> 48.0
> 36.0
> 24.0
> 12.0
> 0.0
Hits
Time(sec)
Amplitude(dB)
Thaw - 2
> 64.0
> 48.0
> 32.0
> 16.0
> 0.0
Thaw - 3
> 48.0
> 36.0
> 24.0
> 12.0
> 0.0
Thaw - 4
> 19.2
> 14.4
> 9.6
> 4.8
> 0.0
Thaw - 5
> 12.0
> 9.0
> 6.0
> 3.0
> 0.0
Thaw - 6
> 192.0
> 144.0
> 96.0
> 48.0
> 0.0
Thaw - 7
> 640.0
> 480.0
> 320.0
> 160.0
> 0.0
Thaw - 8
> 72.0
> 54.0
> 36.0
> 18.0
> 0.0
Thaw - 9
> 2.4
> 1.8
> 1.2
> 0.6
> 0.0
Thaw - 10
> 72.0
> 54.0
> 36.0
> 18.0
> 0.0
Thaw - 11
> 120.0
> 90.0
> 60.0
> 30.0
> 0.0
Thaw - 12
> 12.8
> 9.6
> 6.4
> 3.2
> 0.0
Events

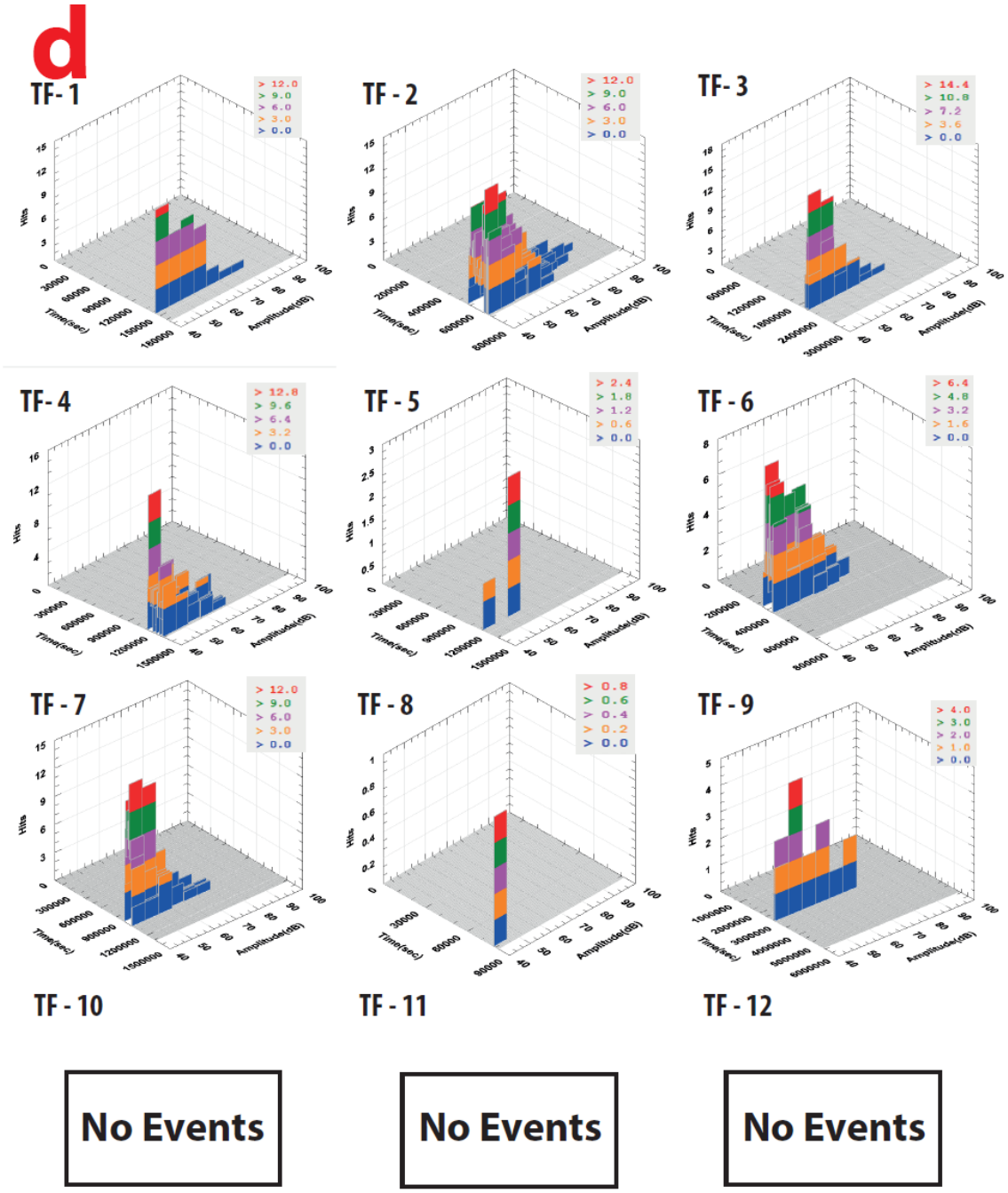

Figure 6.12. 3D plot showing the amplitude and number of hits of AE events during periods of (a) freezing, (b) freeze–thaw transition, (c) thawing and (d) thaw–freeze transition.

6.7 Mechanism of crack propagation

6.7.1 Theory and mathematical explanation

The AE sensors mounted on the block of chalk captured the 3D locations of microcracking events in their temporal order of occurrence during the freeze–thaw cycles. This section simulates three boundary condition for crack propagation to address objective 6.1 (O6.1) set out in chapter one. To understand the mechanism of crack propagation following objective 6.2 (O6.2), a statistical

function is proposed to assess the distance and angular relationships among the temporal order of events. It is assumed that the locations of cracking events arranged through time during the experiment relate to the crack initiation and propagation history observed in the chalk block. The function measures the distance and angular relationship of the next N (=3, 5 and 10) events relative to each event. The model is based on three principle cases of fracture propagation (discussed below) and then correlated with the results obtained by the AE technique during the 12 freeze–thaw cycles. As the well-developed cracks observed in the block after 8 and 12 freeze–thaw cycles were horizontal, the model considers the mechanism of crack propagation along the horizontal direction only.

Three cases of fracture propagation underpin the model: (1) unidirectional propagation of cracks from one side of the block to another side, (2) propagation of cracks from inside the block to the outside, and (3) propagation of cracks from the surface of the block to the inside. The three cases produced three different sets of 3D points containing the locations of the events arranged according to their time of occurrence. The fracture propagation function was then tested on the 3D location matrices to discriminate the patterns in three different scenarios. Testing of the function with varying numbers of next events (N=3, 5 and 10) on the three scenarios of crack propagation showed a good agreement when N=10 with minimum dispersion (standard deviation) in both the distance and angular relationship.

$\mathbb{E}_n$ is the set containing the location information of events arranged in their temporal order during any sequence of cracking and is defined as

$$\mathbb{E}_n = \{\xi_1, \xi_2, \dots\dots\dots\dots, \xi_n\}$$

where $\xi_1, \xi_2, \dots., \xi_n$ are the locations of cracking events. The fracture propagation function $\mathbb{FP}$ has two aspects that assess the distance (r) and angular (θ) relationship of events and is defined as

$$\mathbb{FP}\ (r) = f(\mathbb{E}_n)$$

$$\mathbb{FP}\ (\theta) = f(\mathbb{E}_n)$$

Higher values of $\mathbb{FP}$ indicate successive cracking events occurring at different locations within the specimen and can be interpreted as individual cracking events with no definite relationship to each other. Lower values of $\mathbb{FP}$ suggest localized events, possibly relating a sequence of cracking. $\mathbb{FP}\ (\theta)$ was estimated by converting the location information $\xi_1, \xi_2, \dots., \xi_n$into a vector by joining them to the origin, and the angular relationship of events was derived using the dot product of location vectors.

6.7.1.1 Unidirectional propagation

The unidirectional propagation mechanism assumes that a crack propagates from one side of the specimen to another side. To evaluate this mechanism with that of the brecciated layer developed in the macroscale experiment, a definite zone at depth was considered that generated a random set of 3D numbers representing each AE event. The numbers were generated in an order to simulate the propagation of a crack from one side of the specimen to another side (Figure 6.13). As the crack lengthened, the spatial boundary condition of random number generation expanded. The 3D random numbers simulating AE events were restored in a set ($\mathbb{E}_{UD}$) according to their directional order of occurrence. The results of the fracture propagation function on unidirectional movement ($\mathbb{FP}_{UD}$) are shown in Figure 6.14. The figure indicates that with the directional development of the crack, the distance and angular relationship of successive events increases. In other words, as the number of AE events increases, the crack becomes mature and the separation of the neighbouring events increases.

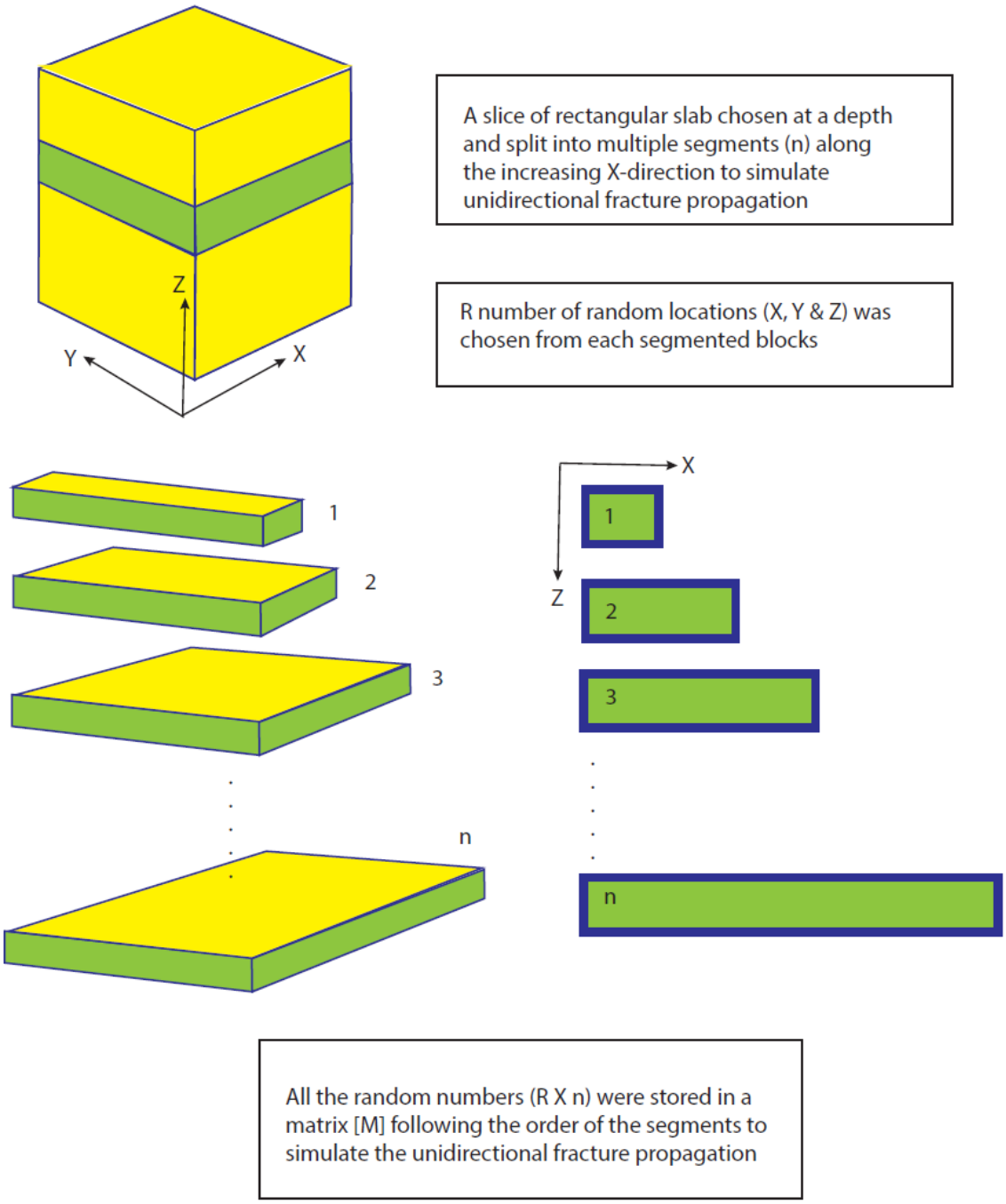

Figure 6.13. Schematic diagram explaining the creation of event locations to simulate the unidirectional propagation of a crack.

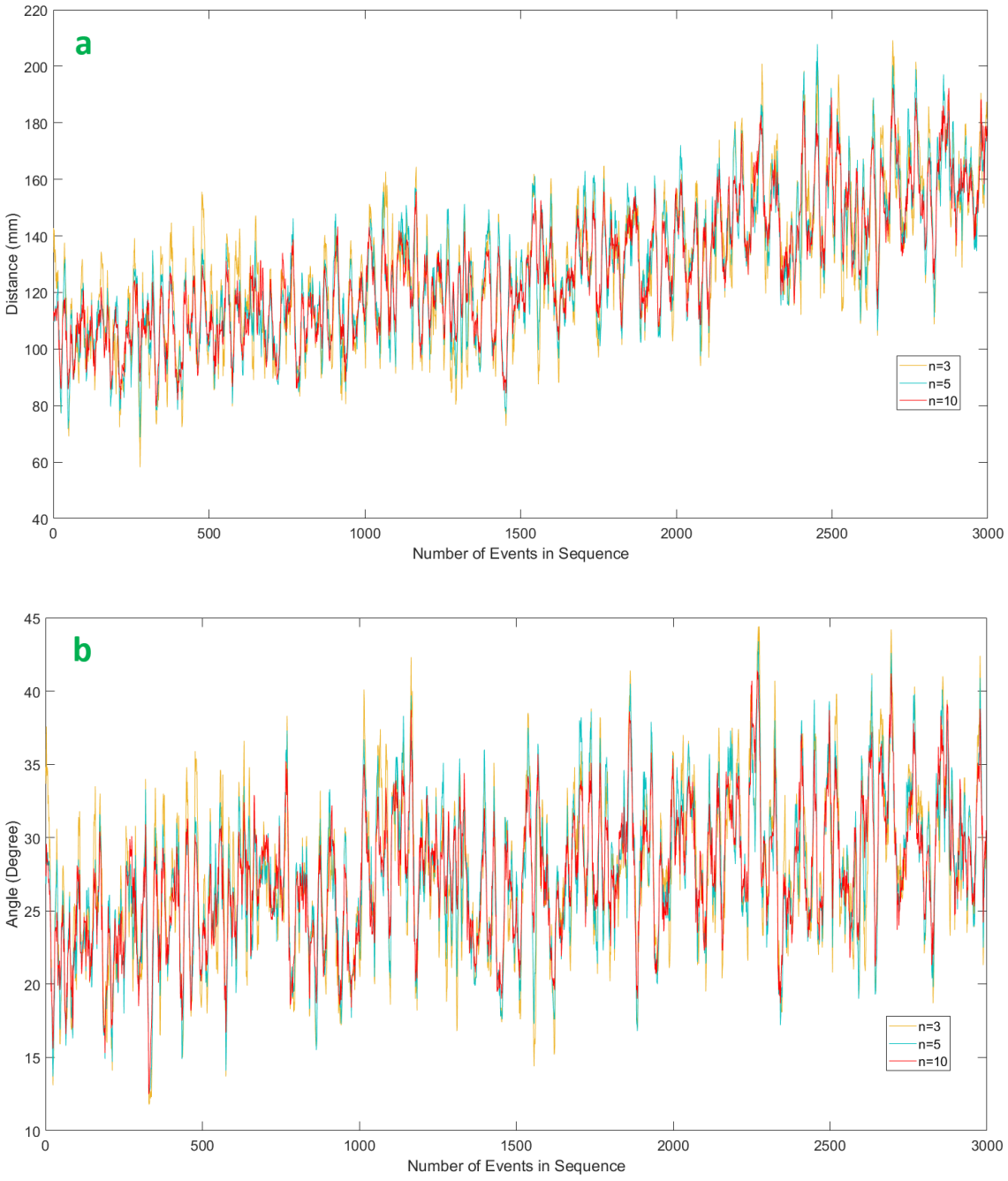

Figure 6.14. Unidirectional propagation of AE events in the chalk block from one side of the specimen to another side according to the unidirectional movement function in terms of (a) distance and (b) angular relationships.

6.7.1.2 Inside–out propagation

The inside–out propagation mechanism replicates the case where a crack initiated inside the block and propagated outward towards either side as cracking progressed. To arrange the set of events simulating the inside–out propagation mechanism ($\mathbb{E}_{IO}$), a definite depth range within the specimen was considered and the 3D random points were generated in a sequence that

expanded its spatial extent from inside to outward (Figure 6.15). The results for inside–out fracture propagation ($\mathbb{FP}_{IO}$) are illustrated in Figure 6.16. The distance and angular relationship of events increases with the development of the fracture. The slope of the distribution curve for inside–out propagation is steeper than that for unidirectional propagation.

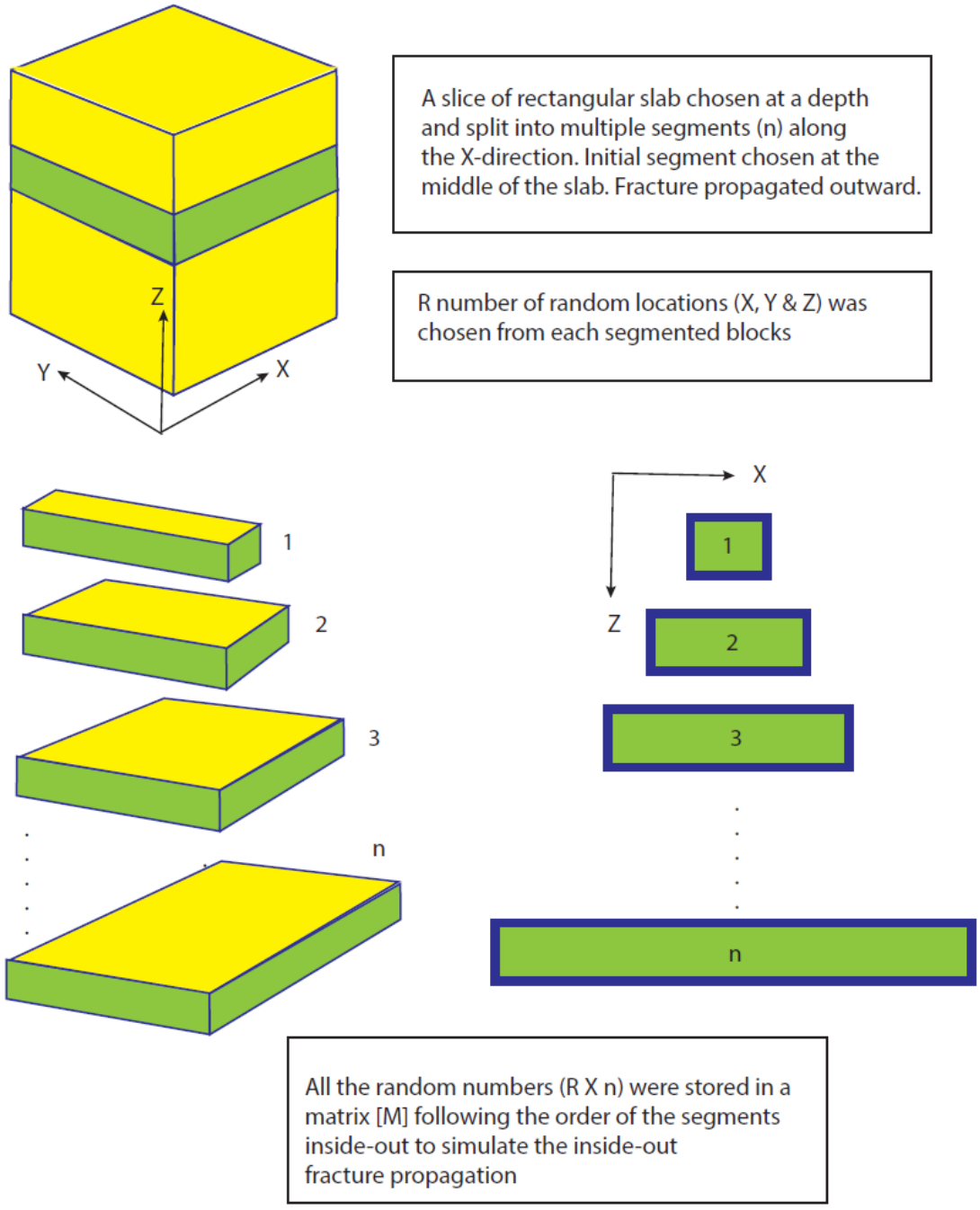

Figure 6.15. Schematic diagram explaining the creation of event locations to simulate the inside-out propagation of a crack.

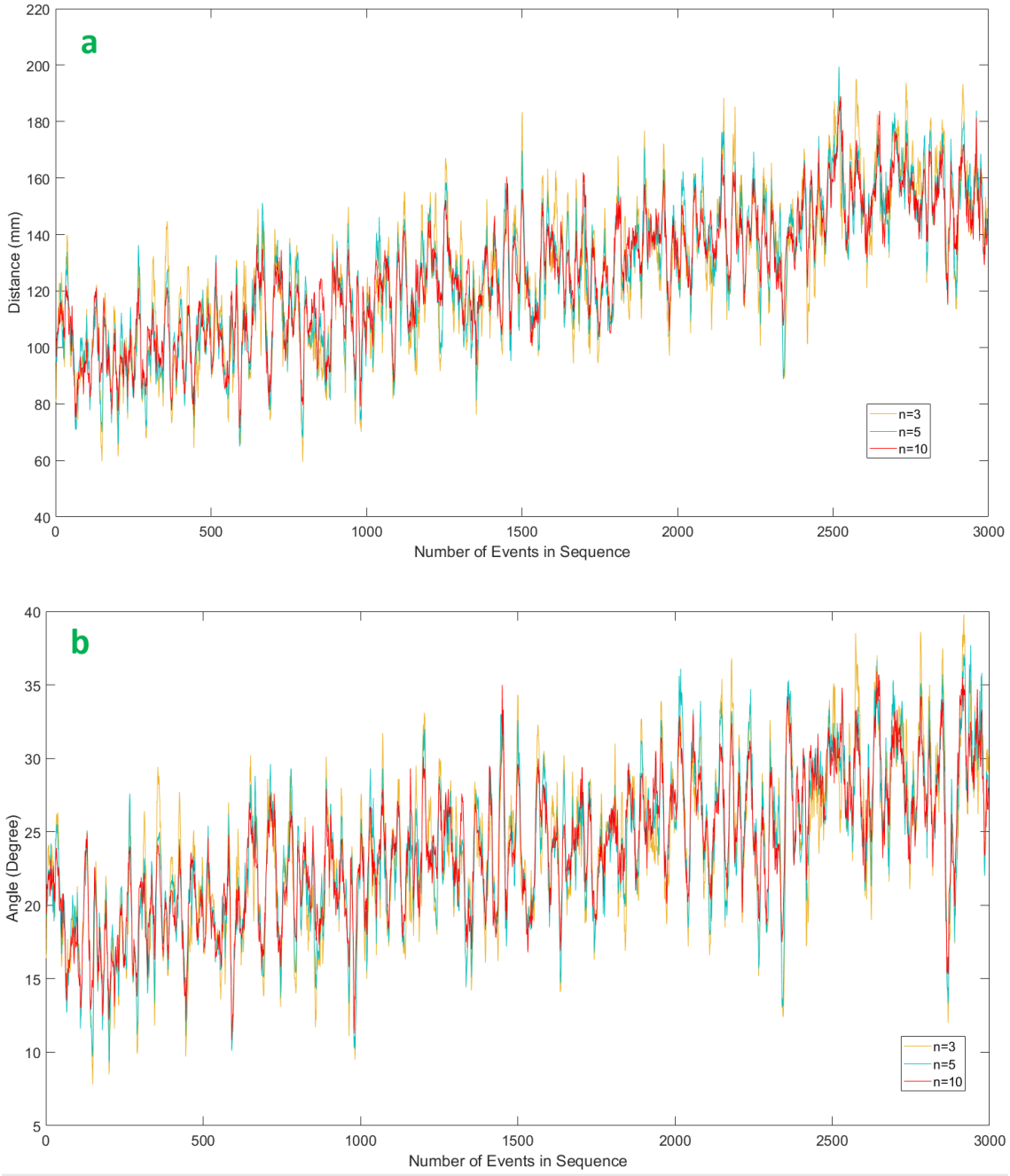

Figure 6.16. Propagation of AE events in the chalk block from inside the specimen to outside according to the inside–out fracture propagation function in terms of (a) distance and (b) angular relationships.

6.7.1.3 Outside–in propagation

The outside–in propagation mechanism simulates the situation where a crack originated on either side of the block within a definite depth interval and propagated inward towards the middle of the block. A similar protocol was applied to create the set ($\mathbb{E}_{OI}$) of location of events that replicates the outside–in propagation of cracking (Figure 6.17). The results are illustrated in

Figure 6.18.Unlike the first two cases, the distance and angular relationship of events decreased for outside–in fracture propagation ($\mathbb{FP}_{OI}$) as the crack propagated.

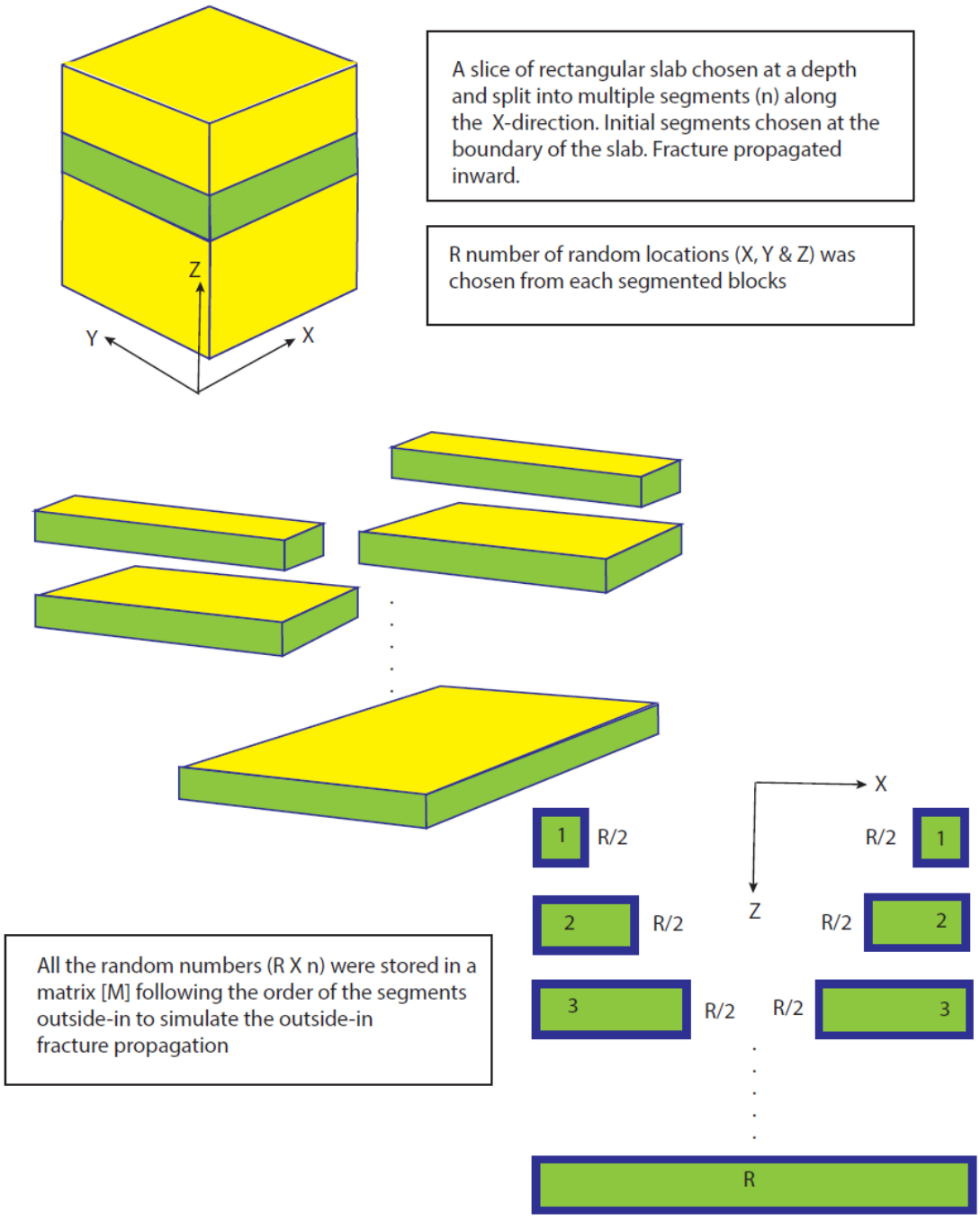

Figure 6.17. Schematic diagram explaining the creation of event locations to simulate the outside-in propagation of a crack.

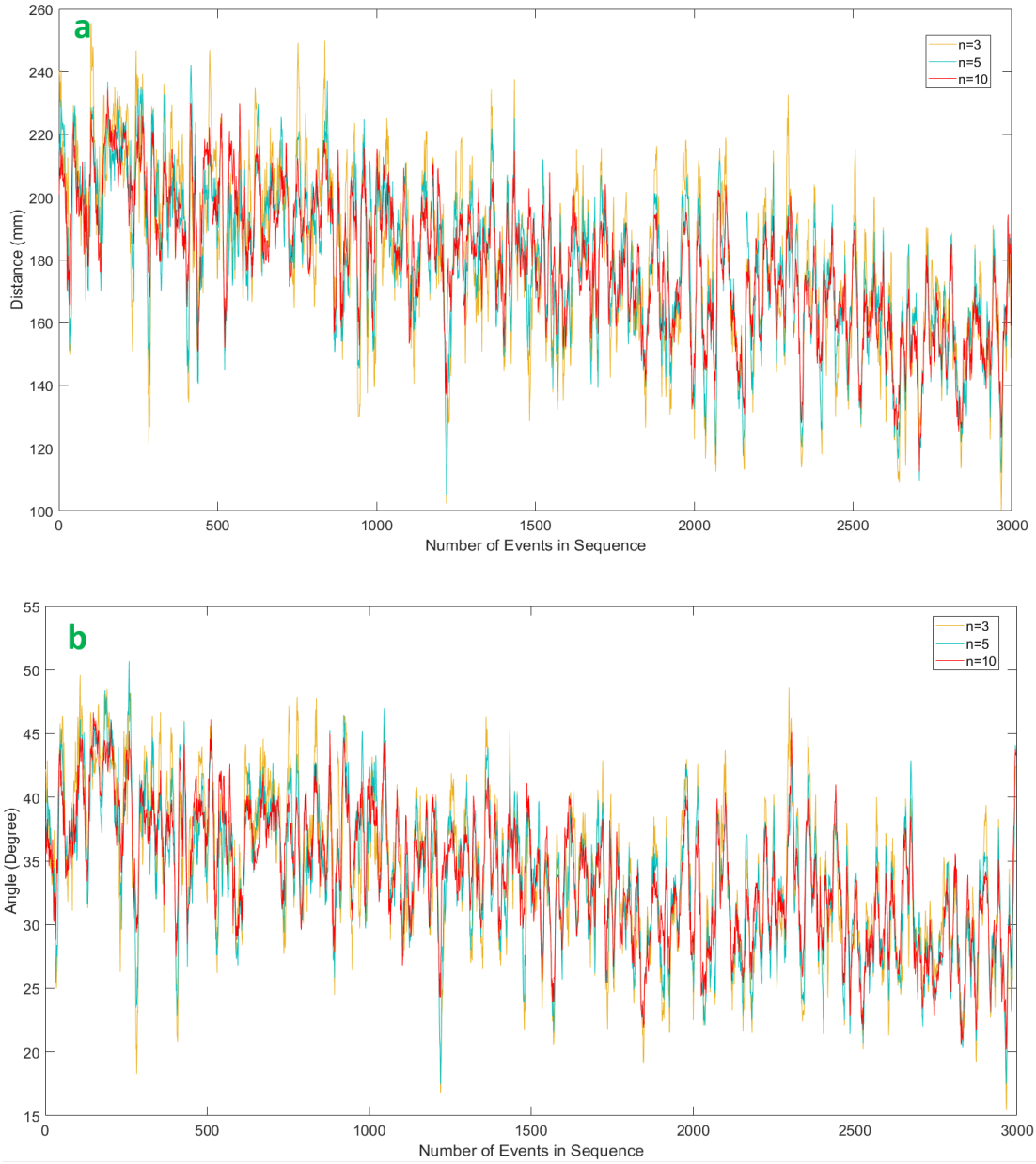

Figure 6.18. Propagation of AE events in the chalk block from outside the specimen to inside according to the outside–in fracture propagation function in terms of (a) distance and (b) angular relationship.

6.7.2 Analysis of cracks developed in macroscale freezing experiment

The macroscale freezing experiment formed visible macrocracks at four different depths in the block of chalk. The events that occurred at a particular depth were filtered and arranged in their order of temporal occurrence following the time stamp recorded during acquisition. The step processing structure of the fracture propagation function is schematically illustrated in Figure 6.19. The process was repeated for the four different depths that contained visible brecciation and vertical cracks. The fracture propagation functions $\mathbb{FP}\ (r)$ and $\mathbb{FP}\ (\theta)$) operate separately

on the hypocentres of events at four different spatial locations in the block to accomplish objective 6.3 (O6.3).

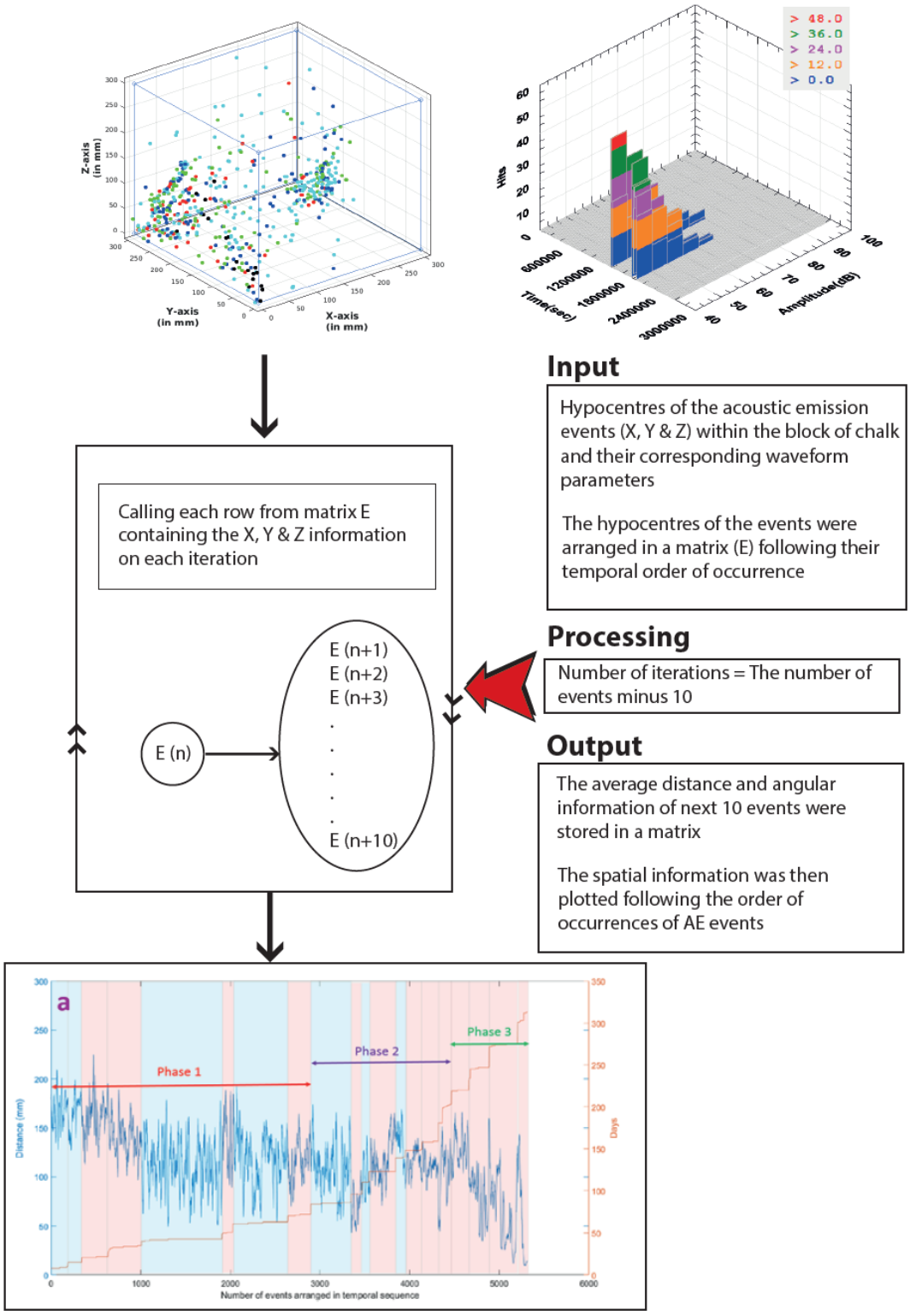

Figure 6.19. Schematic diagram explaining the input of 3D AE locations following their temporal occurrence, subsequent processing and final output of crack propagation hypothesis.

6.7.2.1 Horizontal brecciated layer

The macroscale experiment developed two horizontal to subhorizontal brecciated layers at 80–110 and 190–220 mm depth. The fractured zone at 80–110 mm was well developed compared to the layer at 190–220 mm. The proportion of AE events recorded at these depths were 5 and 19% of the total number of AE events, respectively.

In the case of $\mathbb{FP}_{80-110}(r)$and $\mathbb{FP}_{80-110}(\theta)$ a gradual decreasing trend followed in P1 and P2, which became almost consistent in P3 (Figure 6.20). At the beginning of freezing cycles, a sharp increase was noted, followed by a decreasing trend, while initiation of thawing cycles was marked with a sharp decline followed by an increase. The spatial and angular relationships were relatively high among events that occurred at 80–110 mm depth compared to 190–220 mm. The frequency of events were nearly evenly distributed for P1, P2 and P3.

A decreasing trend in $\mathbb{FP}_{190-220}(r)$ and $\mathbb{FP}_{190-220}(\theta)$ was observed (Figure 6.21) during P1, which is similar to the trend formed in outside–in propagation. The distribution followed an increasing trend in P2 and remained constant in P3. Out of the total events at 190–220 mm depth, only 11% occurred in P3, while 44% of the events at 190–220 mm depth were recorded during P3. $\mathbb{FP}_{190-220}(r)$ fell to a value of almost zero during freeze–thaw cycle 5.

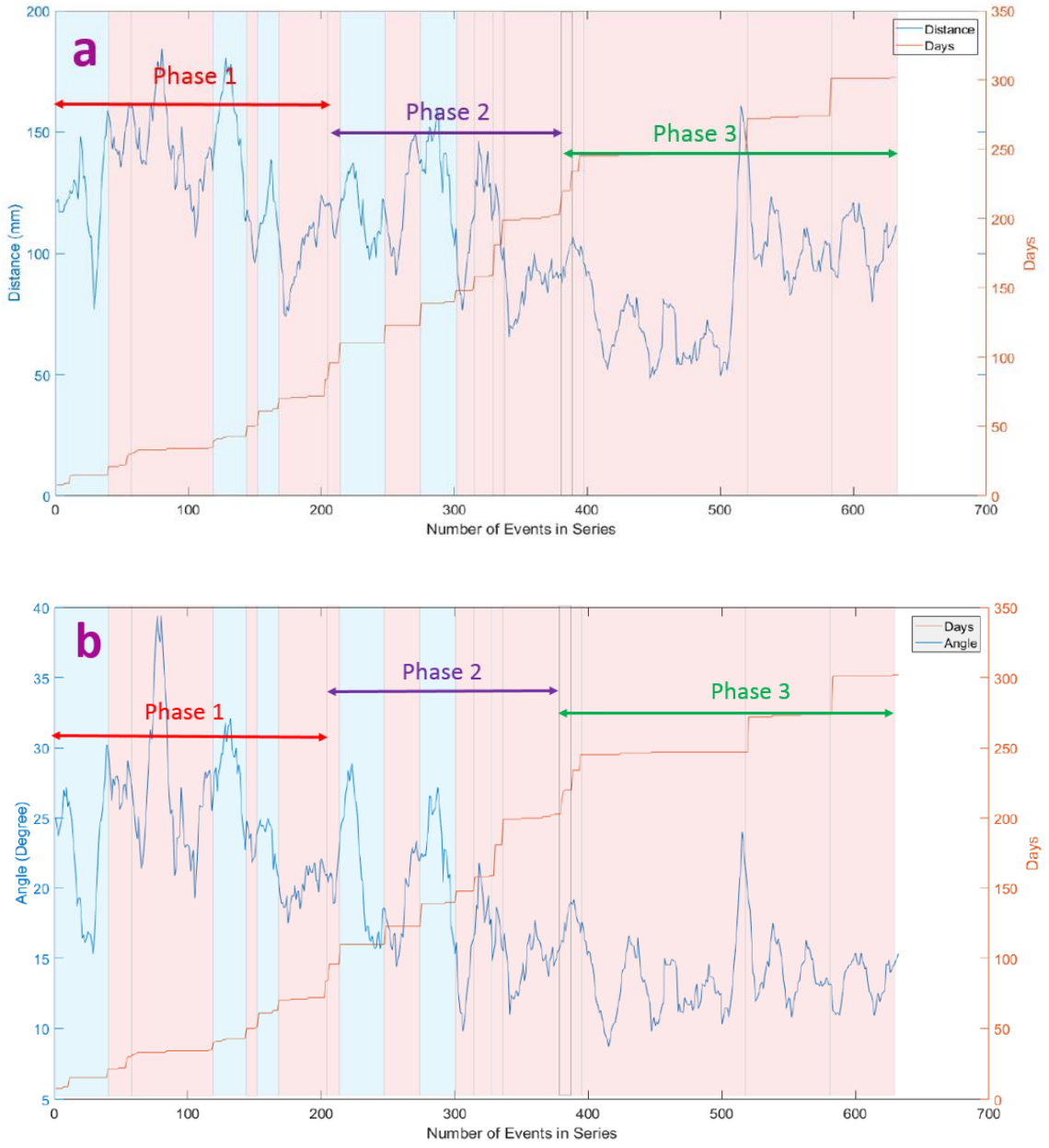

Figure 6.20. Fracture propagation function for distance (a) and angular (b) relationships at 80–110 mm depth in the chalk block. Blue shading represents freezing periods, and the red shading represents thawing periods.

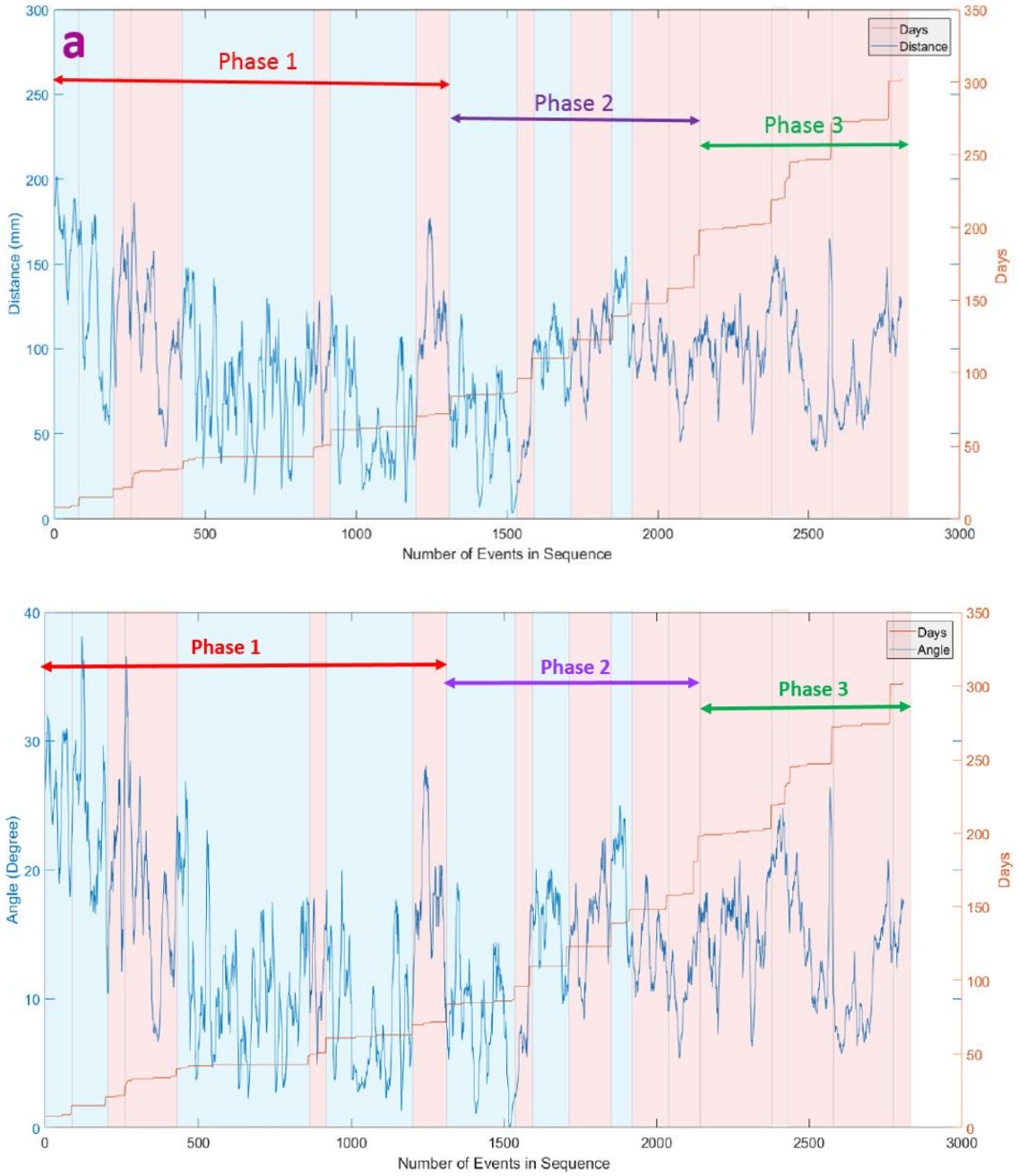

Figure 6.21. Fracture propagation function for distance (a) and angular (b) relationships at 190–220 mm depth in the chalk block. Blue shading represents freezing periods, and the red shading represents thawing periods.

6.7.2.2 Vertical cracks

Two vertical to subvertical cracks developed at depths of 0-60 and 140-180 mm in the chalk. Most of the AE activity was recorded near the base (~34%) compared to the activities at other depths.

The trend fluctuated around the average value of ~100 mm and 20° during P1 for $\mathbb{FP}_{00-60}(r)$ and $\mathbb{FP}_{00-60}(\theta)$, followed by a sharp decline and gradual increasing trend in P2 and P3 respectively (Figure 6.22). In the case of $\mathbb{FP}_{140-180}(r)$ and $\mathbb{FP}_{140-180}(\theta)$, a gradual decreasing trend at the beginning of P1 became consistent later in P1 for $\mathbb{FP}_{00-60}(r)$ and $\mathbb{FP}_{00-60}(\theta)$. The distribution sharply increased in P2, followed by a sharp decline in P3 (Figure 6.23).

In both cases, a sharp decrease at the beginning of thaw cycles was followed by a sharp increase, which is similar to the trend noted for horizontal fracture in thaw cycles. The higher value of $\mathbb{FP}_{140-180}(r)$ compared to the $\mathbb{FP}_{00-60}(r)$ suggests the AE events were more localised at 00–60 mm depth compared to the AE activity at 140–180 mm depth. In both cases of vertical fractures, the spatial and angular distribution progressively declined from P1 to P2 and P3. The spatial and angular relationships of acoustic hypocentres were relatively high in cases of vertical cracks compared to horizontal fractures.

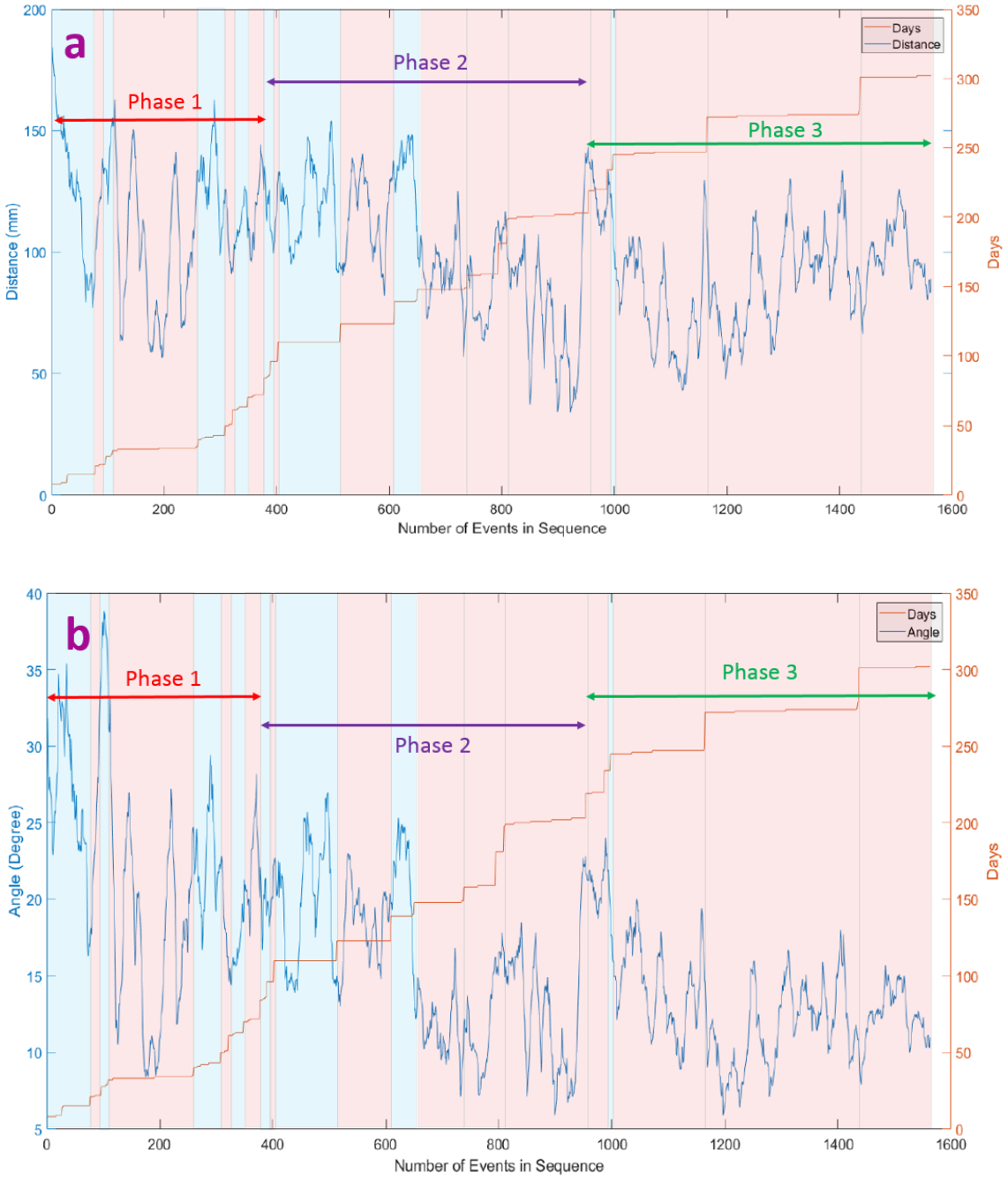

Figure 6.22. Fracture propagation function for distance (a) and angular (b) relationships at 00–60 mm depth in the chalk block. Blue shading represents freezing periods, and the red shading represents thawing periods.

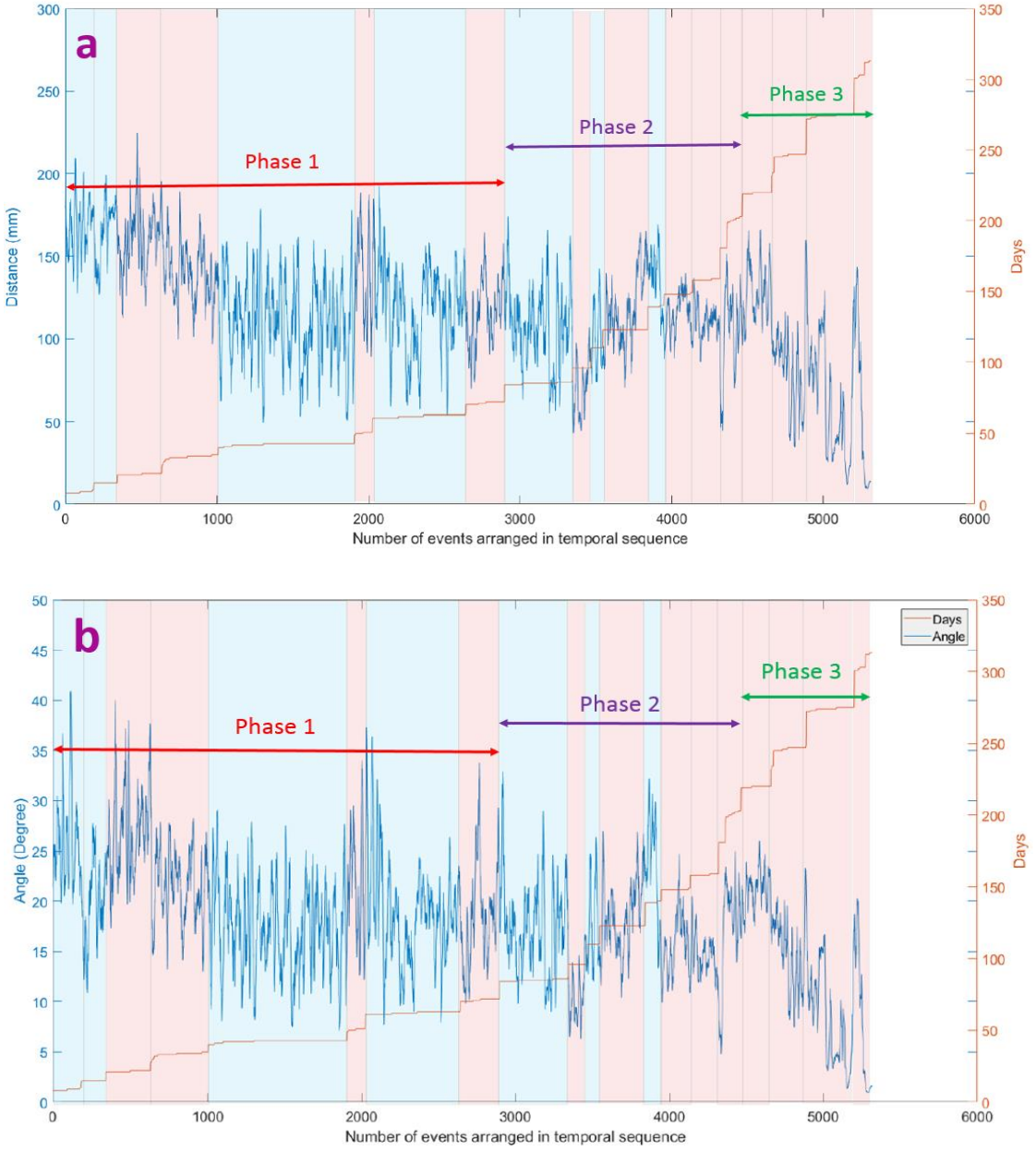

Figure 6.23. Fracture propagation function for distance (a) and angular (b) relationships at 140–180 mm depth in the chalk block. Blue shading represents freezing periods, and the red shading represents thawing periods.

Chapter 7

Discussion

7.1 Introduction

Chapter 7 summarises the findings of the micro- and macroscale experiments described in chapters 4, 5 and 6 within the context of the aims (A1–6) and objectives set out in chapter 1. The nature and types of cracks developed in chalk and sandstone are compared with those identified in the field and in previous experiments. Morphological growth of microcracks and continuity of the fracture phase in small cylinders of rocks are discussed using three probability functions. The progressive development of macrocracks is correlated with the response captured by sensors mounted at various locations within the blocks of rock during different phases of freezing and thawing. Various internal and external factors that initiated and promoted frost-induced cracking are summarized. Different active and inactive zones of microcracks are classified and the damage zones around inherent flaws within chalk and sandstone are compared. Based on the spatial relationships of the hypocentres of microcracking, the mechanisms of crack propagation during freezing and thawing are compared.

7.2 Experimentally-formed cracks

7.2.1 Outcome from objective 1.1

The microscale experiment successfully allowed quantification of structural changes within the chalk and sandstone cylinders, and caused cracking in the chalk visible to the naked eye. The experiment demonstrates a proof-of-concept approach to investigating such changes under freezing conditions because the application of μ-CT in frost weathering experiments on rock is new. A similar experiment conducted on 20 mm cubic blocks of tuffeau developed mostly horizontal cracks (Murton et al., 2001) near the base of the specimens, but did not quantify them. The contrast in morphology of the concentric vertical cracks and basal horizontal cracks (Murton et al., 2001) may be explained by the availability of the simulated ground water table for cubic specimens, while the rock cylinders were wetted by capillary action before the beginning of each freeze cycle. High-resolution digital images (Xia et al., 2005; Xia, 2006) and particle image velocimetry (Azmatch et al., 2008) of frost-susceptible Devon silt captured vertical ice veins reaching up to horizontal ice lenses, whereas discrete vertical cracks formed at different depths in the tuffeau(Figure 4.1a–b). The near-surface concentric vertical cracks

developed in the microscale experiment have some similarities to field observations of hexagonal network of vertical cracks in lake and marine clays, tills and mudflow deposits in northern Canada (Mackay 1974). This similarity suggests there is some spatial control (apart from imposing a vertical thermal gradient) that connects the freezing-induced vertical cracks in some geometric arrangement. Cheng (1983) has pointed out that the ‘‘law of unequal migration of unfrozen water’’ controlled by gravity and the thermal gradient contributes to the formation of hexagonal or nearly hexagonal patterns of cracks. Alternatively, the geometry of the core cylinders in the microscale experiment may have induced near-surface vertical cracking, if some degree of inward freezing occurred, causing water to migrate outward toward the sides of the cylinder and supply vertical ice lenses. The influences of varying sample sizes on the morphology of the cracks were evaluated by Murton et al. (2001) but the consequences of varying shapes were not investigated under laboratory freezing experiments. A final possibility is that the concentric vertical cracks might be attributed to thermal fatigue observed near the surface of rocks, which can play a significant role in weathering (Jia et al., 2015; Hall, 1999).

7.2.2 Outcome from objective 1.2

The macroscale freezing experiment successfully developed horizontal to sub-horizontal brecciated layers at different depths in the block of chalk. The results were consistent with a similar experiment conducted on the same type of chalk by Murton et al. (2001, 2005, 2016b). In addition to the brecciated zones, vertical macrocracks formed within the top 60 mm and in the middle of the chalk specimen. The characteristics of the experimentally formed vertical cracks differ from those of the horizontal cracks in terms of prominence, aperture, number of associated cracks forming the horizontal or vertical fracture surface, bifurcation angle and bifurcation distance (Figure 6.7). Vertical cracks developed during freezing are thought to act as routes for water migration at various depths within the blocks, in similar fashion to vertical cracks observed in some frost-susceptible soils (Arenson et al., 2008). Following the experiment it is apparent that near-surface vertical cracks supplied water to the brecciated layer at 80–110 mm depth, while vertical cracks in the middle formed at a later stage of freezing, connecting the two brecciated layers (Figure 6.7). It is also observed that near-surface vertical macrocracks formed in the early cycles of freezing but did not widen further (i.e. their aperture did not increase through time), unlike horizontal to subhorizontal macrocracks in the brecciated zone. Their constant aperture suggests that the vertical cracks functioned as conduits for migration of unfrozen water during freezing rather than accommodating initiation and growth of ice veins within them. No visible cracks were observed in the two blocks of sandstone. As the sandstone is stronger than the chalk (as evident from the compression test discussed below in outcome

from objective 1.3), it may require additional freeze–thaw cycles to develop cracks than are required for chalk. But the orientation of the lamination with respect to the imposed thermal gradient plays an important role in the migration of unfrozen water, with vertical lamination allowing ice to accumulate on the top surface of block SV.

7.2.3 Outcome from objective 1.3

To understand the mechanical characteristics of the specimens used in the freezing experiment, compression tests were carried out. They indicated that the compressive strength of Ardingly Sandstone is three to four times higher than that of the tuffeau chalk. The cracks developed in sandstone had sharp faces compared to those formed in chalk (Figure 5.1–4). The sharp crack surfaces are attributed to the high ejection velocity (splitting velocity) measured by the LVDTs attached to the two sides of the specimens to capture the linear movement. Movement recorded in the sandstone occurred *before* the peak load was reached, while that in the chalk occurred *after* it (Figures 5.7 and 5.8). Wing cracks developed in sandstone near the contrasting rock boundary with the central plug of chalk. Similar cracks have been observed in experiments with a single hole and multiple holes in blocks of Hong Kong granite (Wong et al., 2006; Lin et al., 2015), which is explained in terms of stress release (concentration) near both the empty and filled hole (low-density material in hole compared to material under compression). The main macrocrack developed in the chalk consisted of small macrocracks (low bifurcation distance) linked together and more or less aligned in the direction of the main macrocrack trajectory.

Macrocracks in the brecciated zone developed in the macroscale freezing experiment branched out at various distances, forming a network of small lens-shaped irregular cracks on the vertical surface of the block of chalk. The distance at which a propagating macrocrack bifurcates in chalk was greater in the freezing experiment than in the compression test, suggesting slow degradation of rock during freezing. Jia et al. (2016) attributed the slow degradation of sandstone during freezing cycles to fatigue. In the compression test, the bifurcation direction was strongly guided by the direction of compression, and the small bifurcation distance was also controlled by the higher magnitude of stress under compression relative to tensile stress in the macroscale freezing experiment, which induced a higher bifurcation distance. The branching out of macrocracks at higher intervals favoured the development of a brecciated zone in the chalk freezing experiment.

7.3 Microcracking development

7.3.1 Outcome from objective 2.1

The repetitive scanning of the small cylinders of chalk and sandstone was undertaken when the specimens were completely thawed and dried to avoid any error in the grey-scale range due to moisture content variations. Time-lapse digital photographs of saturated and frozen Devon silt (Xia et al., 2005) distinguished the ice and soil phases, but detection of the fracture phase enhances the grey-scale range in dry samples relative to wet ones. The fracture and non-fracture (material) phases in the μ-CT images were separated following the Otsu method (1979) of thresholding and the binary masked stack of images used for further processing (see objectives 2.2 and 2.3). The 3D locations of binary masked images that highlight the fracture phase are thought to quantify the progressive development of cracks by comparing the repeatedly scanned images.

7.3.2 Outcome from objective 2.2

One-dimensional freezing tests conducted on 100 mm diameter cores of frost-susceptible Devon silt (Xia, 2006) developed a regular network of vertical ice veins throughout the frozen zone (Arenson et al., 2008). In the present study, by contrast, regular concentric vertical cracks formed near the top surface of a small core cylinder of chalk. Assessment of transverse strain suggests dilation of material perpendicular to the axial dimension due to the formation of vertical cracks which push material outward. Until freeze–thaw cycle 15, the transverse strain measured at various depths of the chalk specimen was limited to 0.07% and in cycle 20, there is noticeable change occurred that ranges between 0.14–1.2%. The top of the specimen containing the concentric vertical cracks experienced higher stain compared to the bottom of the specimen. Azmatch et al. (2008) noted similar horizontal strain in Devon silt as a consequence of formation of vertical tension cracks. The higher tensile strength of rocks compared to soils is thought to delay the onset of cracking.

7.3.3 Outcome from objective 2.3

The measurement of correlation functions from images of natural and synthetic materials has evolved considerably since the work of Corson (1974). The present study assessed three probabilistic correlation functions to predict the development of microcracking during freezing in anisotropic sedimentary rock.

The two-point probability function measures the growth of the fracture phase along the X-, Y- and Z-directions even if the fracture phase is not continuous (i.e., it is interrupted by the non-fracture phase). The results showed that development of cracking took place along all three

orthogonal directions as the number of freeze–thaw cycles increased, both in chalk and sandstone. The higher r/D value for S_f (r) = 0.05 along the Z-direction (r/D = 0.35) relative to X- (r/D = 0.25) and Y- directions (r/D = 0.1) in chalk indicates vertical development of the fracture phase, which was observed as the concentric vertical macrocracks near the top of the specimen.

Applying the two-point probability function alone is not sufficient to reconstruct the internal morphology of anisotropic material, and incorporating the lineal path function improves the accuracy (Yeong and Torquato, 1998). To assess the continuity of the fracture phase along various 3D-directions, the lineal path function was applied to the specimens of chalk and sandstone. Following the consistency of probability across various r/D ratios, the plot (Figure 4.18) combining all the $L_f(r)$ for different freeze-thaw cycles along a definite direction was classified into several parameters such as minimum crack length and maximum crack length. Comparative assessment of these newly classified parameters helped to distinguish directional growth above the average threshold. The maximum changes in $L_f(r)$ of 8.67% were noted in chalk (average =6.49%) when $\phi=0^o$ (Figure 4.21), which indicates growth in the horizontal direction. The formation of concentric vertical cracks followed by dilation (noted in pixel-based strain measurement) increases the probability of linear growth in the horizontal direction relative to other directions (radial expansion near the specimen boundary) as no visible development was observed in the horizontal direction. The maximum increment in the length of continuous fracture phase was observed in the vertical direction ($\phi=90^o$) followed by the horizontal orientation ($\phi=0^o$) (Figure 4.22). The increase in continuous length along the vertical direction suggests the vertical veins developed maximum continuity on retaining fracture phase.

For sandstone, the average change in $L_f(r)$ =2.17% compared to 6.49% for chalk, which indicates that the sandstone was less damaged than the chalk (Figures 4.23 and 4.21) after 20 freeze–thaw cycles. This result is also consistent with the compressive strength of sandstone (3–4 times higher than that of the chalk) and with the linear development of the fracture phase (three times lower than that of the chalk). The average linear growth after 20 freeze–thaw cycles for chalk and sandstone was 1.38 and 0.26 mm, respectively (Figures 4.24 and 4.22). Increase in $L_f(r)$ and increment in continuous line length of the fracture phase weakens material as the number of freeze–thaw cycles increases. A similar phenomenon was described by Jia et al. (2015) as a fatigue effect as the number of freeze–thaw cycles increases. The results from the present study suggest that the lineal path function along with the newly proposed parameters defining various segments of the curve can be used as a method to quantify the retention of directional damage (non-reversible) in anisotropic rock along various directions during freezing.

The two-point cluster function permits assessment of the progressive changes in the fracture phase between two random points irrespective of morphology or direction. Development of the fracture phase around the dimension of inherent flaws was noticeably high ($r/D < 0.05$), which suggests the cluster of the fracture phase around inherent flaws may be due to the effect of stress concentration.

7.4 Mechanisms of cracking

7.4.1 Outcome from objective 3.1

After initial calibration of sensors (between the beginning of the experiment and day 8) as the freezing temperature was imposed, the three blocks froze from the top downward and thermally contracted. The initial thermal contraction in SH block (~1.5 mm) exceeded that in SV block (~1.2 mm), which is attributed to the variation in mechanical properties along directional discontinuities. If the arrangement of flaky mica minerals is different in SH and SV, then a similar temperature change might cause various degrees of expansion or contraction. The initial thermal contraction was within the range of 1–2 mm for both rock types and the maximum contraction was noted in chalk (~2mm), which did not contract beyond the 2 mm limit throughout the experiment. Heave measured (Figure 6.3a) in the sandstone blocks during P1 (freeze–thaw cycles 1–4) can be attributed to volumetric expansion as 90 and 100%, respectively, of SH and SV blocks experienced sub-zero temperature (Figure 6.1b–c) but a minimal thermal gradient. In addition, small bursts of heave observed in the two sandstone and one chalk block during P1 were attributed to volumetric expansion. The magnitude of the bursts was higher in freezing cycles 2, 3 and 4 compared to that in other freezing cycles, indicating volumetric expansion related to higher sub-zero temperature (Figure 7.1). Similar small bursts noted by Prick (1995) and Murton et al. (2016b) were attributed by these authors to volumetric expansion.

At the beginning of P2 (freeze–thaw cycles 5–8), substantial settlement of the sandstone blocks (SH heaved and settled twice the amount of SV) is explained by the melt of ice accumulated during intense freezing cycles 1–4. During P2, substantial heave in the block of chalk can be attributed to ice segregation. A higher thermal gradient (associated with lower temperature at the base of the blocks) in P2 favours ice segregation compared to volumetric expansion during a lower thermal gradient. Heave developed in chalk during P2 and late P3 (freeze–thaw cycles 9–12) can be explained by the formation of well-developed horizontal to sub-horizontal fractures near 100 and 200 mm depth that allow ice crystals to form and expand. The imposed thermal gradient changed the depth of the 0°C isotherm from ~100 to ~200 mm during P2 and P3. The presence of the 0°C isotherm initiated microcracking at these depths and substantial

heave occurred as the microcracks coalesced with each other to develop macrocracks (brecciated zone). Similar heave was noted in the wettest blocks B1 and B2 of tuffeau by Murton et al. (2016b) followed by crossing over a threshold.

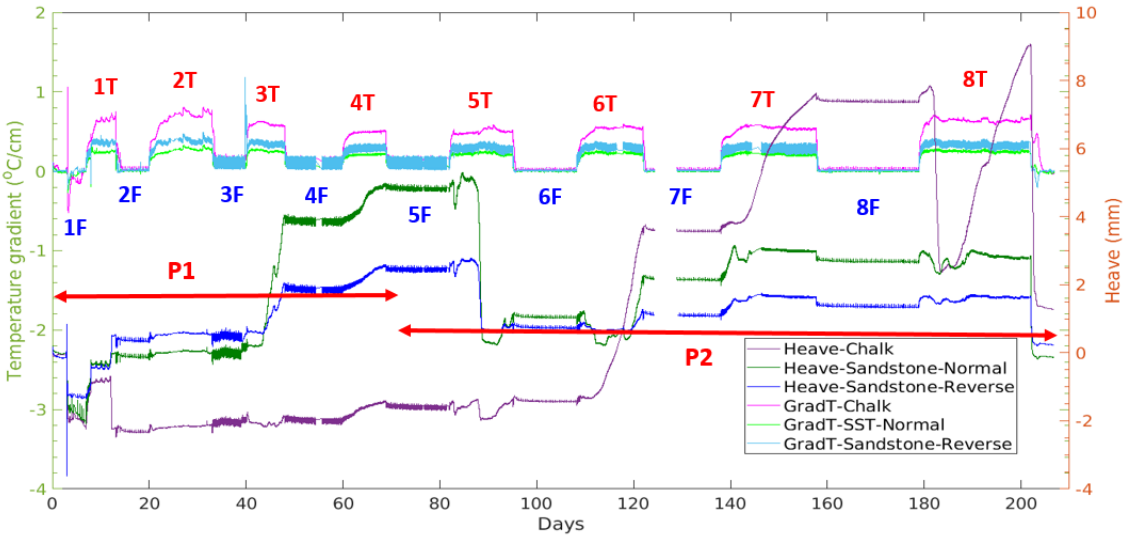

Figure 7.1. Heave of the three blocks with their respective thermal gradient along the time series during P1 and P2.

At the beginning of P3, all the three blocks contracted, but the amount of contraction was less than that at the beginning of the experiment, possibly because the thermal gradients in P3 were greater than in P1. Any settlement was followed by a small burst of heave noted in all three blocks prior to contraction.

Miniature strain gauges detected a variation of 300–400 microstrain due to changes in freezing and thawing temperature, while no correlation was established that explains the temperature gradient and strain (both thermal and mechanical) at various depths of the blocks. The strain gauge mounted at 150 mm depth on vertical face B recorded a maximum of 1500 microstrain, consistent with the abundant AE activity at the middle of the block. But the strain gauge located at 160 mm depth on vertical face D did not record such high strain.

7.4.2 Outcome from objective 3.2

Well-developed brecciated layers formed at depths of 80–110 mm and 200–220 mm in the block of chalk along with vertical to sub-vertical cracks at 0–60 mm and 140–180 mm depth. Abundant AE activity during P1 occurred within the lower ~100 mm, although some was observed throughout the chalk (Figure 6.8). The abundant low-amplitude events in the lower half of the block was associated with imposing lower freezing temperature at the base and correlated to

the initial thermal contraction and heave observed. Clustering of AE events near the central vertical axis of the block was associated with the development of a near-surface vertical crack and associated horizontal cracks visible after cycle 8 on vertical face B (Figure 6.9). During and after cycle 6, abundant AE activity extended upwards into the upper 150 mm, followed by significant heave. Both the sustained heave and peak in microcracking activity in the upper 150 mm suggest the dominance of ice segregation over volumetric expansion that eventually developed a prominent brecciated zone seen at 80–110 mm depth after freeze–thaw cycle 8. Similar observations of heave and the first appearance of macrocracking were noted by Murton et al. (2016b) in bidirectional freezing of tuffeau during thawing cycle 10 (B1) at 250 mm depth. The source amplitude segmented 3D AE responses along with heave data provide a useful combination in filtering out the macrocracking AE characteristics from the abundant and dispersed microcracking activity within the block. After freeze–thaw cycle 6, noticeable AE activity in the upper half of the block indicated the development of new microcracks marked by crossing a threshold of the depth of AE activity.

In P2, gentler thermal gradients were imposed compared to those in P1, favouring ice segregation, as indicated by significant heave. Microcracks formed at 80–110 mm depth coalesced with each other, forming a well-developed brecciated layer which set a condition for newer microcracks to develop at greater depth even if the imposed thermal gradient was consistent during P2. The effective stress at the furthest extent of pore ice, the temperature gradient and the temperature to which ice extends were identified by Rempel (2011) as principle controls on ice-lens spacing in the THM modelling of freezing soil. The temperature gradient in the macroscale experiment was effective in developing a new ice lens at depth. The macrocrack developed at 200—220 mm depth was not visible after freeze–thaw cycle 8 but was seen at the end of freeze–thaw cycle 12, which suggests the brecciated layer formed during P3, at greater depth. During cycles 5–6, AE events were dispersed throughout the block, but during cycles 7–8 thaw and thaw—freeze transition, events were clustered around the central vertical axis. Such vertical alignment of AE hypocentres can be attributed to the water migration mechanism once a stable thermal gradient is established, as thaw cycles 7–8 (~20 days) were of longer duration than thaw cycles 5—6 (~11.5 days).

The thermal gradient imposed during P3 was higher than that in P2, which caused the 0^{o}C isotherm to penetrate deeper in chalk and form cracks at greater depth. During P3, the AE events were located at various depths within the block, but in some cases the activity recorded was bimodally distributed, with peaks at ~100 and ~200 mm depth, suggesting the synchronous growth of two well-developed brecciated layers (Figure 6.8). Two vertical cracks developed, one

within 60 mm of the top and the other at 100–180 mm depth. Partially developed horizontal cracks formed around the two vertical cracks. Near-surface AE events were recorded throughout the experiment, including some of high amplitude (Figure 6.9). Minimal changes were observed in aperture relative to that of the horizontal cracks. Similar vertical cracks observed in frozen silt by Arenson et al. (2008) were thought to explain the transport of water to the freezing front and the nature of the thin film of water around these vertical veins is different from that around horizontal ice lenses. Vertical veins are thought to develop as a consequence of reduced permeability due to accumulation of segregated ice (Chamberlain and Gow, 1979; Konrad and Samson, 2000a, 2000b). Possibly the vertical crack at 100–180 mm depth formed during the later stage of the experiment (freeze–thaw cycles 6–12), connecting the two well-developed brecciated layers such that water supply was maintained to form ice lenses at depth due to ice segregation. Such evidence is observed during longer thaw cycles 7–8, where AE events were vertically clustered around the central vertical axis, suggesting migration of water.

7.4.3 Outcome from objective 3.3

The average frequency of AE waveforms recorded during freezing and thawing cycles ranged from 35 to 40 kHz, respectively, while some thaw cycles exceeded 40 kHz, which is interpreted as thermal dilation of cracks (Amitrano et al., 2012). The abundance of microcracking during periods of (a) freezing, (b) freezing to thawing transition, (c) thawing and (d) thawing to freezing transition was 7.09, 34.52, 44.07 and 4.63%, respectively, while the average duration was 9.5, 1.5, 12 and 1.5 days accordingly. Higher negative temperature at the base lead to increased AE activity as evident in freeze cycles 3–5 which is absent in later freeze cycles with relatively low sub-zero temperature. During freezing cycles, the entire blocks experienced almost the same sub-zero temperature and hence a negligible vertical thermal gradient existed (Figure 6.1a–c). Therefore, the events that occurred during the freezing cycles can be attributed to volumetric expansion, as Walder and Hallet (1985) noted that a stable thermal gradient maintains the supply of water to a developed segregated ice lens in Berea sandstone. Thaw cycles 7–8 were of longer duration and imparted a stable thermal gradient compared to other thaw cycles. The AE activities recorded during thaw cycles 7–8 were clustered around the central vertical axis, suggesting the water migration mechanism noted by Walder and Hallet (1985). The depth of abundant microcracking became shallower than 150 mm from freeze-thaw transition 6 onwards (Figure 6.8), which suggests the initiation of new microcracks within the upper half of the block forming a brecciated layer at 80–110 mm depth. Although of relatively short duration (1.5 days) compared to freezing or thawing cycles, freeze-thaw transitions were characterized by abundant AE events (34.52 %). This suggests that freeze–thaw transitions associated with degrading

permafrost regions may promote bedrock fracture. Changes in AE activity from a unimodal distribution during P1 and P2 to a bimodal distribution during P3 signify synchronous development of reactivated and newly formed cracks at 80–110 mm and 200–220 mm depth during freeze–thaw transitions. At the onset of freeze–thaw transitions melting of ice developed weak slip surfaces containing pre-melted water, which caused settlement of the block.

7.4.4 Outcome from objective 3.4

Maximum AE activity took place during thawing periods (44.07%) followed by freeze–thaw transitions (34.52%). The intense microcracking activity during thawing explains the development of the prominent brecciated layer developed as a result of the dominance of ice segregation over volumetric expansion, as the number of AE events during freezing was less than during thawing.

Experimental studies on concrete generate higher frequency characteristics and lower RA values of AE waveforms during tensile cracking than shearing (JCMS-IIIB5706, 2003; Aggelis, 2011, 2013). A similar protocol adopted in the macroscale freezing experiment revealed a limited number of shearing events but abundant tensional ones. Crack opening is accompanied by tensile stress, while crack closing can also generate AE events (Moradian et al., 2010). A threshold of 40 dB was applied to eliminate such crack closure AE activity, but further studies are required to set up a definite threshold. Daily thermal cycling can cause shearing along existing fractures (Gunzburger et al., 2005), even in the absence of freeze–thaw cycles. One possible reason could be the block of chalk was insulated around the sides, therefore allowing little or no space left for shearing events. Most shearing is thought to have occurred during freeze–thaw transitions (based on average frequency and RA values, Figure 6.11) as partial melting of ice lenses acted as a plane of weakness that favoured shearing. Relatively high shearing activity was noted in P3 (freeze–thaw transitions 9 and 11), suggesting that tensile cracks formed earlier became unstable and generated the signature of shearing.

7.5 Influences on cracking

7.5.1 Outcome from objective 4.1

The thermal gradient imposed during P2 resulted in the 0°C isotherm being located near 100 mm depth, with AE activity at this depth peaking during freeze–thaw cycle 6 (Figure 6.8). The photographs taken after freeze–thaw cycle 8 captured a well-developed brecciated layer at ~100 mm depth. The stable thermal gradient during P2 (thawing) crossed the threshold induced by volumetric expansion and favoured the dominance of ice segregation, forming a prominent brecciated surface at 100 mm depth. The gentler thermal gradient in P3 shifted the 0°C isotherm

to ~200 mm depth and initiated cracking at 200–220 mm depth observed after freeze–thaw cycle 12. The observation made in P2 and P3 suggests that the presence of the 0°C isotherm induced localised microcracking and any changes in the depth of this isotherm initiate microcracking at corresponding depth. Significantly, this observation suggests that degrading permafrost may pose a serious threat in terms of bedrock integrity.

7.5.2 Outcome from objective 4.2

Tensile failure is initiated at the tip of minute defects that locally concentrate stress (Griffith, 1921). The growth of a concentric vertical crack formed along the boundary of a fossil fragment is illustrated in Figure 4.3. In addition, some spalling off of material from sandstone occurred around a void (Figure 4.7). Careful observation revealed that concentrations of contrasting material (white material in Figure 4.7) around a void formed a plane of failure and favoured cracking. The contrasting boundary of fossil fragments and voids act as a weak plane if encountered by propagating cracks, as seen in both the chalk and sandstone.

7.5.3 Outcome from objective 4.3

No visible cracks developed in the sandstone blocks oriented with their lamination either horizontal or vertical in the macroscale experiment. Clearly, the higher strength of the Ardingly Sandstone relative to the tuffeau chalk requires further freeze–thaw cycles to develop cracks. Some changes in the hydraulic and thermal properties were observed in the different orientations of the sandstone blocks. First, the permeability was greater when the lamination was vertical, as indicated by the faster capillary rise front in SV than SH when blocks were being saturated prior to the experiment (Figure 3.15). Second, the thermal conductivity of the thawed sandstone also differed, as indicated by the differences in active-layer depth for SV and SH under the same imposed thermal conditions (Figure 6.1b–c and 6.2b–c).

7.5.4 Outcome from objective 4.4

In the same way as stress concentrates near the two opposite sides of an empty hole (Wong et al., 2006), stress also concentrates near the filled hole with low-strength material encased within high-strength material. Whether it is low-density material encased within high-density material or vice versa, the trajectory of the main cracks under compressive loading tends to swing around the boundary of material (rock) contrast. Therefore, the rock boundaries are the preferred path for crack propagation rather than penetration through the boundary itself. The penetration through the low-density material is high compared to penetration through the high-density material, as shown by the sandstone specimen in the compression test. As with other geologic materials, most of the cracks are filled rather than empty (Hoek and Brown, 1997) and the present study assessed the consequence of filled crack in two contrasting cases.

7.6 Classification of microcracking zones

7.6.1 Outcome from objective 5.1

As noted (section 4.4.3), the lineal path function is particularly significant in quantifying the fracture phase compared to other probability functions as it contains information about the continuous fracture phase. The continuity of the fracture phase along 49 directions was assessed for both chalk and sandstone for different freeze–thaw cycles (Appendix A and B). The results were combined (Figure 4.21–24) to discriminate different zones of microcracking following the fracture mechanics theory. The changes in $L_f(r)$ and increments of line length in chalk are substantially higher than those in sandstone, which accounts for the extensive damage to the chalk.

7.6.2 Outcome from objective 5.2

Three zones are distinguished based on the probabilistic occurrence and extent of the fracture phase during freezing and thawing: (a) *zone of inherent flaws*, (b) *active zone of microcracking* and (c) *weak zone of influence during microcracking* (Figure 7.2). The zone of inherent flaws in both the chalk and sandstone was nearly the same (0.116 and 0.128 mm, respectively), while the active zone of microcracking was of broader extent in chalk than sandstone (1.004 and 0.71 mm, respectively). This signifies that the damage-influenced zone in chalk was more extensive than in sandstone. The active zone of microcracking ahead of the zone of inherent flaws can be considered as the plastic zone ahead of crack tips, following the theoretical models of fracture mechanics (e.g. Irwin, 1948; Von Mises et al., 1960). The progressive growth of this active zone during the course of 20 freeze–thaw cycles may be consistent with the growing plastic zone ahead of crack tips. As the macroscopic property of interest of a material is a function of appropriate local fields weighted with definite correlation functions (Torquato, 2002), a new approach in the present study was undertaken using the lineal path function to quantify different zones of microcracking during freeze–thaw cycling of anisotropic rock. The comparative assessment of these zones along various directions can quantify damage based on the extent of the active zone of microcracking. A detailed investigation is required to check if there is a relationship between the extent of the active zone of microcracking and that of the weak zone of influence due to stress concentration near inherent flaws.

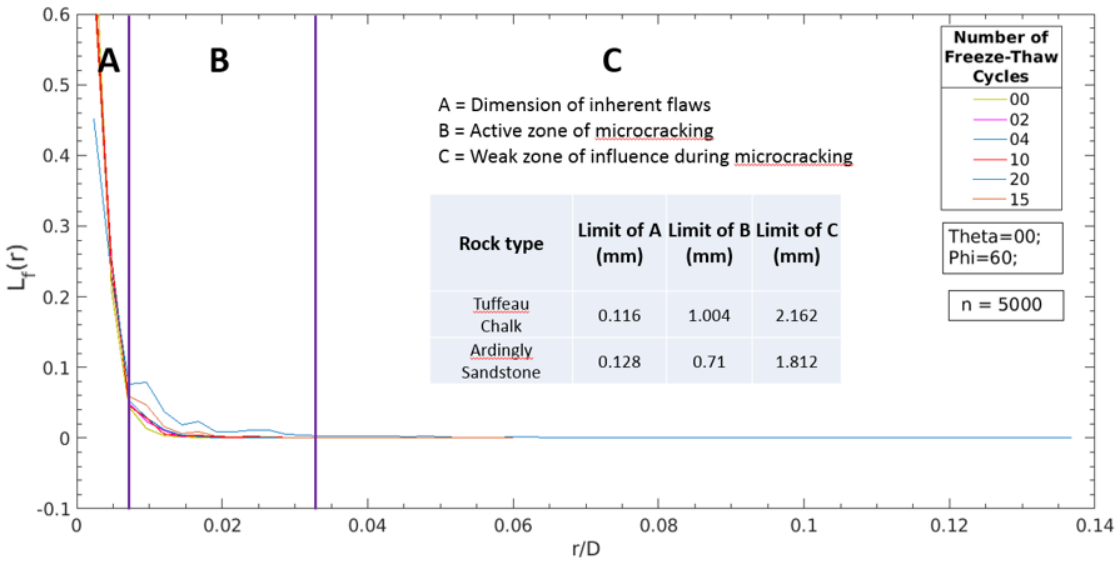

Figure 7.2. Zones of microcracking assessed after testing the probabilistic occurrence in various directions. Zone A indicates the average extent of inherent flaws, zone B (plastic zone) indicates the dimension of microcracking activity ahead of crack tip and zone C indicates weak zone of microcracking activity ahead of the plastic zone.

7.7 Mechanisms of crack propagation

7.7.1 Outcome from objectives 6.1 and 6.2

The framework of the proposed boundary conditions and the analysis fracture propagation function were explained in section 6.7 following the research objectives 6.1 and 6.2.

7.7.2 Outcome from objective 6.3

The rate of fracture propagation directly relates to the frequency of AE events (Costin, 1987). Hirata et al. (1987) introduced a correlation function for a set of number of hypocentres to estimate the spatial relationship of AEs. The present study introduced a statistical function that correlates the distance and angular relationship of the next ten hypocentres for each event arranged in their temporal order of occurrence (Figure 6.19). The model also considers three boundary conditions of crack propagation following the fracture surface developed in the macroscale experiment: (a) unidirectional, (b) inside–outward and (c) outside–inward (Figures 6.13, 6.15 and 6.17). The results show a higher distance and angular distribution during P1, which gradually decreased in P2 and P3 as the 0°C isotherm penetrated deeper into the rock. During freezing cycles a greater distance and angular relationship was maintained among events, while during thawing a downward trend in distribution was observed. During freezing, events occurred at various dispersed locations due to volumetric expansion, while during

thawing, accumulation of segregated ice spatially concentrated AE activity. Only in the case of the well-developed brecciated zone at 190–220 mm depth did the spatial distribution curve reach near zero values during freeze–thaw cycle 5. The clustering of AE events during cycle 5 is possibly connected to cycle 6, which recorded significant heave along with extended AE activity followed by crossing over a depth threshold.

Lower values of the fracture propagation function or a steeply decreasing trend in the spatial distribution of AE hypocentres might explain the crack coalescence (or crack bridging) phenomenon that involves abundant AE activity in a localized place within a short span of time or along a weak plane or zone. If the decreasing trend after a threshold is explained by crack coalescence, then it raises a new question. Did coalescence of horizontal microcracks (as in cycle 5) mark the threshold to initiate accumulation of ice in a vertical direction (as in cycle 6)? It was observed that greater AE activity peaked at the middle of the block in freeze–thaw cycle 6 and crossed the threshold of ~100 mm depth afterward (Figure 6.8b–d), generating AE events in the upper half of the chalk. Prior to that in freeze–thaw cycle 5, the spatial distribution of AE events descended deepest into the block, reaching 190-220 mm depth (Figure 6.21a–b).

Chapter 8

Conclusions and recommendations

8.1 Introduction

This chapter concludes the outcome of the research under the context of the four hypotheses described in chapter 1 and tested in the following chapters. Vertical cracks formed during freezing are identified as passages to transport unfrozen water towards growing ice lenses. The consequences of changing the active-layer depth on the depth of brecciation are discussed in the context of slope stability and global temperature rise. Mostly tensional modes of cracking are identified during freezing, although a limited amount of shearing occurs at the onset of thawing. The separation distance at which a growing crack bifurcates varies for compressive and tensile loading. The damage-influenced zone around inherent flaws is identified for chalk and sandstone. Variations in the mechanisms of crack propagation during freezing and thawing are highlighted. Lastly, the limitations encountered on conducting the experiments and recommendations for future research are presented.

8.2 Vertical cracks and water migration

Both the micro- and macroscale experiments successfully developed cracks during repeated freezing and thawing. Vertical cracks were identified as important controls of the dynamics of the system, both in one-sided freezing (simulating seasonal frost) and bidirectional freezing (simulating an active layer above permafrost). In one-sided freezing of small cylinders of tuffeau chalk, near-surface vertical cracks formed a concentric pattern comparable to hexagonal networks of cracks developed in permafrost. The lateral migration of unfrozen water together with the unequal distribution of water in different parts of the specimen function to connect the near-surface vertical cracks into such a regular geometric pattern. In bidirectional freezing of chalk, the shape and function of vertical cracks differ from those of horizontal to subhorizontal cracks as the aperture of the vertical cracks remained consistent after they formed during the early cycles, while the horizontal cracks coalesced with each other, forming a prominent brecciated zone. The intervening ice-poor zone in bidirectional freezing is the favoured region for vertical cracks to develop as a connecting passage to maintain the bidirectional migration of water. Some water was drawn upward towards the freezing front descending from the top surface of the rock, and some drawn downward towards freezing front rising from the

permafrost table to form segregated ice lenses that accumulate incrementally in macrocracks. Vertical cracks developed near the top surface of the chalk core in the unidirectional microscale freezing experiment, but it is not clear whether these cracks facilitated vertical transport of water. Rather, it contains the signature of lateral water migration as the vertical cracks coalesced, forming a concentric pattern. The macroscale bidirectional freezing experiment, on the other hand, formed vertical cracks near the top surface and in the middle of the chalk block. This suggests a connecting passage developed to transport water to form segregated ice at different depths. During the longer thaw cycles 7–8, AE events were clustered in a vertical array around the central vertical axis, providing evidence for water migration through these vertical vents. Overall, the macroscale experiment supported hypothesis 1, whereas the microscale experiment provided only partial support to it.

8.3 Changing active-layer depth

The base of the active layer and the top of the permafrost is the zone in which cracking was most active and damage was greatest in the macroscale experiment on wet chalk. Thus, any variation in the depth of the active layer, for example triggered by climate or local environmental change, can develop a new brecciated zone at different depth. Multiple or amalgamated zones of brecciation pose a serious threat to slope stability for steep and fractured rock walls as the shear strength is reduced significantly at the ice–rock interface when the temperature is just below the melting point of ice or during the onset of thawing, allowing the rock mass to move downslope.

The bidirectional freezing experiment simulated the consequence of changing active-layer depth by controlling the basal cooling plate temperature. The experiment successfully formed brecciated layers at different depths following a change in active-layer depth. Thus it supports hypothesis 2.

8.4 Tension and shear mode of cracking

The microcracks developed in chalk during bidirectional freezing were mostly tensional in origin, as opposed to shear-related. Of the limited number of shearing events identified, most occurred during periods of freeze–thaw transition rather than during thawing periods, as the ice lenses started melting, forming weak potential slip surfaces. Significant amounts of settlement at the beginning of thawing marked the initiation of melt of ice lenses, while large increments of heave during the later stage of thawing resulted from ice segregation within the macrocracks. In both volumetric expansion and ice segregation, the tensional stress regime dominated the microcracking activity.

The abundant tensional events relative to the shearing activity during freezing suggests that hypothesis 3 is partially supported. But further investigation is needed to elucidate shearing events during freeze–thaw transitions.

8.5 Bifurcation distance and local stress regime

The cracks developed in chalk and sandstone during the present experiments were not perfectly linear and continuous, but rather a combination of small tensional and shearing fractions that bifurcate and converge at various intervals of distance. The failure plane developed in chalk under compressive loading (~15 to 18 MPa) consisted of small cracks that branched out at short intervals, whereas the tension cracks formed under freezing (0.07 to 1.07 MPa tensile strength of tuffeau; Murton et al., 2000) with a relatively high separation distance. The weighted interval at which the trajectory of the crack path bifurcates can be used as a proxy to estimate the local stress regime.

Cracks developed during freezing and under compressive load were compared for the same rock types. The results show that the crack propagation during the experimental freezing conditions was slower and the distance at which cracks bifurcate was greater than under compressive loading. This supports hypothesis 4.

8.6 Damage and microchanges in inherent flaws

The macroscale property of interest in heterogeneous rock is a function of suitable local factors weighted with an appropriate correlation function. Classification of microcharacteristics of the fracture phase based on the lineal path probability function showed that the weighted extent of the damage zone around inherent flaws varies with rock types (1.004 and 0.71 mm for chalk and sandstone respectively), under identical thermal conditions.

The microscale freezing experiment assessed the linear continuity of the fracture phase based on the randomness and probabilistic occurrence of line segments of various length following Aim 5. Further detailed investigation is required to classify the damage influenced zone around inherent flaws and interpret it in terms of fracture mechanics (LEFM) theory.

8.7 Mechanism of crack propagation during freezing and thawing

A new approach is introduced in the present study to correlate the distance and angular relationship of hypocentres of AE events generated during microcracking following Aim 6. The arrangement of events according to their temporal order of occurrence elucidates the mechanism of crack propagation. At the beginning of freezing cycles, a sharp increase in the distance and angular relationship was observed, followed by a gradual decreasing trend. This is

interpreted as indicating a widespread distribution of pore-ice nuclei at the onset of volumetric expansion. The lower value later in the freezing cycles indicates some fraction of the pore-ice nuclei were inactive, possibly due to a shortage of available water. In contrast, thaw cycles start with a sharp decline in the relationship of events, followed by an increase, suggesting melting of pore ice in well-developed localized cracks as the thawing front penetrates deeper into the rock. Later during the thawing cycles, when the thermal gradient was stable, ice segregation dominates at various locations in macrocracks, increasing the distance and angular distribution of neighbouring events. The fracture propagation function identified relatively higher values of distribution for vertical cracks compared to horizontal to subhorizontal cracks.

8.8 Limitations

A dummy gauge concept was applied into the present study to estimate strain during freezing, but the reversible changes during freezing and thawing were captured. It is therefore challenging to filter the reversible (thermal strain) and irreversible (mechanical strain) component of strain when a temperature change is involved.

Micro-CT scans of small core cylinders conducted after freeze–thaw cycles 6 and 8 were discarded in the present study as the specimens were not completely dried before scanning, unlike in other cycles of scanning. Partial moisture content significantly shifts the grey scale range and induces error.

It is assumed that the acoustic wave velocity of the block of chalk during freezing and thawing were identical in the scale of the experiment. But for large-scale measurement this will induce error as the mechanical properties (e.g. primary and secondary wave velocities) of the frozen and unfrozen part of the block vary.

The development of cracking in rocks due to freezing is a slow process and requires adequate intervals of time. Thus, the present study focussed on crack initiation and the early stages of crack propagation, rather than later stages of crack growth. Experiments longer than 315 days are needed to simulate more than 12 cycles of active-layer freezing and thawing.

Both the unidirectional microscale freezing experiment and bidirectional macroscale freezing experiment successfully developed cracks in chalk. However, cracking of the harder Ardingly Sandstone would require more freeze-thaw cycles. Future research should ensure greater repeatability of the experiments and test a wider range of rock types.

Repeated micro-CT scanning were conducted on two sedimentary rock types to correlate the progressive changes of fracture phase. The two rock types were undergone same freezing

experiment but the sandstone did not developed crack as it is more hard compared to the chalk and possibly require more freeze-thaw cycles. Due to limited number of rock types and samples, this does not confirm the repeatability of the freezing experiment on developing crack.

8.9 Recommendations

From the measurement of AEs, it is evident that during freeze–thaw cycle 6 a threshold was crossed and, thereafter, the location of events extended to the upper half of the block of chalk. Prior to cycle 6, from the analysis of the fracture propagation function, a contrasting decline in the distance distribution of events was noticed (near zero values) in freeze–thaw cycle 5, that might explain the crack coalescence mechanism. Further investigations are required to justify if the high-magnitude shift in the heave (expansion in the vertical direction) is accompanied by lateral coalescence of microcracks.

A new approach is introduced using the lineal path function to classify different zones of microcracking based on their probabilistic occurrence. It is identified that the damage zone ahead of the inherent flaws by resembles with the plastic zone ahead of the crack tip. More analysis is required to correlate the extent of these two zones.

The number of rock specimens used in the present study was limited by practical considerations. Future studies should ideally seek to replicate the results of such experiments in multiple specimens. The study requires further testing of different rock specimens such that a broad correlation can be established for various igneous, sedimentary and metamorphic rock types. The problem associated with such an operation is that it requires more freeze-thaw cycles to developed cracks in hard lithologies.

It is found that migration of water plays a significant role on crack development during freezing. Therefore a similar experiment is suggested in dry and moist atmospheric conditions to compare the fracture networks developed and to distinguish the respective contribution of volumetric expansion and ice segregation.

The influence of the size of the specimen on developing freezing-induced cracks is examined in the thesis but the influence of the shape of the specimen requires to be investigated further.

A statistical function is proposed in the thesis to understand the fracture propagation mechanism. Further study is required to apply the statistical function to other disciplines, for example to correlate the hypocentres of small-scale earthquakes for predicting large-scale earthquakes.

Bibliography

Aggelis, D.G., 2011. Classification of cracking mode in concrete by acoustic emission parameters. *Mechanical Research Community*, 38, pp.153–157.

Aggelis, D.G., Mpalaskas, A.C. and Matikas, T.E., 2013. Investigation of different fracture modes in cement-based materials by acoustic emission. *Cement and Concrete Research*, 48, pp.1–8.

Akagawa, S. 1988. Experimental study of frozen fringe characteristics. *Cold Regions Science and Technology*, 15, pp.209–223.

Akagawa, S. and Nishisato, K., 2009. Tensile strength of frozen soil in the temperature range of the frozen fringe. *Cold Regions Science and Technology*, 57(1), pp.13–22.

Amitrano, D., Gruber, S. and Girard, L., 2012. Evidence of frost-cracking inferred from acoustic emissions in a high-alpine rock-wall. *Earth and Planetary Science Letters*, 341–344, pp.86–93.

Anisimov, O.A. and Nelson, F.E., 1996. Permafrost distribution in the northern hemisphere under scenarios of climatic change. *Global and Planetary Change,* 14, pp.59–72.

Arenson, L.U., Azmatch, T.F. and Sego, D.C., 2008. A new hypothesis on ice lens formation in frost-susceptible soils. In: Kane, D.L. and Hinkel, K.M. (eds) *Proceedings of the 9th International Permafrost Conference*, 29 June–3 July, University of Alaska Fairbanks. Institute of Northern Engineering, University of Alaska Fairbanks, vol. 1, pp.59–64.

Azmatch, T.F. Arenson, L.U. and Sego, D.C., 2008. Measuring ice lens growth and development of soil strains during frost penetration using particle image velocimetry (GeoPIV). In: Kane, D.L. and Hinkel, K.M. (eds) *Proceedings of the 9th International Permafrost Conference*, 29 June–3 July, University of Alaska Fairbanks. Institute of Northern Engineering, University of Alaska Fairbanks, vol. 1, pp.89–93.

Azmatch, T.F., Sego, D.C., Arenson, L.U. and Biggar, K.W., 2011. Tensile strength and stress-strain behaviour of Devon silt under frozen fringe conditions. *Cold Regions Science and Technology*, 68(1–2), pp.85–90.

Beskow, G. 1935. *Soil freezing and frost heaving with special application to roads and railroads*. Swedish Geological Society, Ser. 3, No. 375, 26th year, Book 3. Translated by J.O. Osterberg, The Technological Institute, Northwestern University, Evanston, Illinois (1947).

Bhreasail, Á.N., Lee, P.D., O'Sullivan, C., Fenton, C.H. and Hamilton, R., 2012. In-Situ Observation of Cracks in Frozen Soil using Synchrotron Tomography. *Permafrost and Periglacial Processes*, 23, pp.170–176.

Black, P.B., 1995. Application of the Clapeyron equation to water and ice in porous media. *Cold Regions Research and Engineering Laboratory*, Hanover, NH.

Brace, W. F., and Byerlee, J. D., 1966. Stick-Slip as a Mechanism for Earthquakes. *Science*, 153(3739), pp.990–992.

Brown, J., Ferrians Jr., O.J., Heginbottom, J.A. and Melnikov, E.S., (Eds) 1997. *Circum-Arctic map of permafrost and ground ice conditions.* U.S. Geological Survey in Cooperation with the Circum-Pacific Council for Energy and Mineral Resources. Circum-Pacific Map Series CP-45, scale 1:10,000,000, 1 sheet, Washington, DC.

Chamberlain E.J. and Gow A.J., 1979. Effect of freezing and thawing on the permeability and structure of soils. *Engineering Geology*, 13, pp.73–92.

Chung, S.Y., Han, T.S. and Kim, Y.W., 2015. Spatial distribution of voids in insulating concrete analyzed by micro-CT images and probability functions. *Advances in Materials Science and Engineering*, vol. 2015, article ID 516169.

Coker, D.A. and Torquato, S., 1995. Extraction of morphological quantities from a digitized medium. *Journal of Applied Physics*, 77(12), pp.6087–6099.

Collins, B.D., Stock, G.M., Eppes, M.C., Lweis, S.W., Corbett, S.C. and Smith, J.B., 2018. Thermal influences on spontaneous rock dome exfoliation. *Nature Communications*, 9(1):762, pp. 1–12.

Colombo, S., Main, I.G. and Forde, M.C., 2003. Assessing damage of reinforced concrete beam using b-value analysis of acoustic emission signals. *Journal of Materials in Civil Engineering*, 15(3), pp. 280–286.

Corson, P.B., 1974. Correlation functions for predicting properties of heterogeneous materials. I. Experimental measurement of spatial correlation functions in multiphase solids. *Journal of Applied Physics*, 45(7), pp.3159–3164.

Costin, L.S., 1987. Time-dependent deformation and failure. In: Atkinson, B.K. (ed.), *Fracture Mechanics of Rock*, Academic Press, London, pp.167–215.

Cule, D. and Torquato, S., 1999. Generating random media from limited microstructural information via stochastic optimization. *Journal of Applied Physics*, 86(6), pp.3428.

Dash, J.G., Rempel, A. W. and Wettlaufer, J.S., 2006. The physics of premelted ice and its geophysical consequences. *Reviews of Modern Physics*, 78, pp.695–741.

Duca, S., Occhiena, C., Mattone, M, Sambuelli, L. and Scavia, C., 2014. Feasibility of Ice Segregation Location by Acoustic Emission Detection: A Laboratory Test in Gneiss. *Permafrost and Periglacial Processes*, 25(3), pp.208–219.

Everett, D.H., 1961. The thermodynamics of frost damage to porous solids. *Transactions of the Faraday Society*, 57, pp.1541–1551.

Erdogan, F. and Sih, G.C., 1963. On the crack extension in plates under plane loading and transverse shear. *Journal of Fluids Engineering*, 85(4), pp.519–25.

Farnam, Y., Geiker, M.R., Bentz, D. and Weiss, J., 2015. Acoustic emission waveform characterization of crack origin and mode in fractured and ASR damaged concrete. *Cement and Concrete Composites*, 60, pp.135–145.

Fukuda, M., 1983. The pore water pressure in porous rocks during freezing. *In Proceedings of the Fourth International Conference on Permafrost*, 17-22 July, Fairbanks, Alaska. National Academy of Sciences, Washington, D.C., pp. 322–337.

Gilpin, R.R. 1980. A model for the prediction of ice lensing and frost heave in soils. *Water Resources Research*, 16, pp.918–930.

Goszczyńska, B., 2014. Analysis of the process of crack initiation and evolution in concrete with acoustic emission testing. Archives of Civil and Mechanical Engineering, 14(1), pp.134–143.

Griffith, A.A., 1921. The phenomena of rupture and flow in solids. *Philosophical Transactions of the Royal Society of London, Series A, Containing Papers of a Mathematical or Physical Character*, 221, pp. 163–198.

Grosse, C. U., Ohtsu, M., 2008. Acoustic Emission Testing. Basics for Research – Applications in Civil Engineering, *Springer-Verlag Berlin Heidelberg*.

Grosse, G., Goetz, S., McGuire, A.D., Romanovsky, V.E., and Schuur, E.A.G., 2016. Changing permafrost in a warming world and feedbacks to the Earth system. *Environmental Research Letters*, 11(4).

Gunzburger, Y., Merrien-Soukatchoff, V. and Guglielmi, Y., 2005. Influence of daily surface temperature fluctuations on rock slope stability: case study of the rochers de valabres slope (France). *International Journal of Rock Mechanics and Mining Sciences*, 42, pp.331–349.

Hall, K., 1999. The role of thermal stress fatigue in the breakdown of rock in cold regions. *Geomorphology,* 31, pp.47–63.

Hallet, B., Walder, J.S. and Stubbs, C.W., 1991. Weathering by segregation ice growth in microcracks at sustained sub-zero temperatures: verification from an experimental study using acoustic emissions. *Permafrost and Periglacial Processes*, 2, pp.283–300.

Hansen, J., Sato, M., Ruedy, R., Lo, K., Lea, D.W. and Medina-Elizade, M., 2006. Global temperature change. *Proceedings of the National Academy of Sciences of the United States of America*, 103(39), pp.14288–14293.

Hardy, H. R., 2003. Acoustic Emission/ Microseismic Activity – Volume 1: Principles, Techniques and Geotechnical Applications. *A.A. Balkema Publisher*, Lisse, The Netherlands.

Harlan, R.L., 1973. Analysis of coupled heat–fluid transport in partially frozen soil. *Water Resources Research*, 9(5), pp.1314–1323.

Harris, C. (1996). Physical modelling of periglacial solifluction: review and future strategy. *Permafrost and Periglacial Processes*, 7(4), pp.349–360.

Harris, C., Luetschg, M., Davies, M.C.R., Smith, F., Christiansen, H.H. and Isaksen, K., 2007. Field instrumentation for real-time monitoring of periglacial solifluction. *Permafrost and Periglacial Processes,* 18, pp.105–114.

Harris, C., Kern-Luetschg M., Murton, J.B., Font, M., Davies, M. and Smith, F., 2008. Solifluction processes on permafrost and non-permafrost slopes: results of a large scale laboratory simulation. *Permafrost and Periglacial Processes*, 19, pp.359–378.

Hirata, T., Satoh, T. and Ito, K., 1987. Fractal structure of spatial distribution of micro-fracturing in rock. *Pure and Applied Geophysics*, 90, pp.369–374.

Hoek, E. and Bieniawski, Z.T., 1965. Brittle fracture propagation in rock under compression. *International Journal of Fracture Mechanics*, 1(3), pp.137–155.

Hoek, E. and Brown, E.T., 1997. Practical estimates of rock mass strength. *International Journal of Rock Mechanics and Mining Sciences*, 34(8), pp.1165–1186.

Jackson, K.A. and Chalmers, B., 1958. Freezing liquids in porous media with reference to frost heaving in soils. *Journal of Applied Physics*, 29, pp.1178–1181.

Jackson, K.A., Uhlmann, D.R. and Chalmers, B., 1966. Frost heave in soils. *Journal of Applied Physics*, 37, pp.848–852.

Jerz, U., 1999. Nacheiszeitliche Bergstürze in den Bayerischen Alpen. Relief, Boden, *Paläoklima*, 14, pp.31–40.

JCMS-IIIB5706, 2003. Monitoring method for active cracks in concrete by acoustic emission. Construction Materials Standard, Federation of Construction Materials Industries, Japan, pp.23–28.

Jia, H., Xiang, W., and Krautblatter, M., 2015. Quantifying Rock Fatigue and Decreasing Compressive and Tensile Strength after Repeated Freeze-Thaw Cycles. *Permafrost and Periglacial Processes*, 26(4), pp.368–377.

Kang, Y., Liu, Q., Liu, X. and Huang, S., 2014. Theoretical and numerical studies of crack initiation and propagation in rock masses under freezing pressure and far-field stress. *Journal of Rock Mechanics and Geotechnical Engineering*, 6, pp. 466–476.

Kong, B., Wang, E., Li, Z., Wang, X., Chen, L. and Kong, X., 2016. Nonlinear characteristics of acoustic emissions during the deformation and fracture of sandstone subjected to thermal treatment. *International Journal of Rock Mechanics and Mining Sciences*, 90, pp.43–52.

Konrad, J.M., 1989. Influence of cooling rate on the temperature of ice lens formation in clayey silts. *Cold Regions Science and Technology*, 16, pp.25–36.

Konrad, J.M., 2005. Estimation of the segregation potential of fine-grained soils using the frost heave response of two reference soils. *Canadian Geotechnical Journal*, 42, pp.38–50.

Krautblatter, M., Funk, D. and Gunzel, F.K., 2013. Why permafrost rocks become unstable: A rock-ice-mechanical model in time and space. *Earth Surface Processes and Landforms,* 38(8), pp.876–887.

Landis, E.N. and Baillon, L., 2002. Experiments to relate acoustic emission energy to fracture energy of concrete. *Journal of Engineering Mechanics*, 128, pp. 698–702.

Lee, S.B. and S. Torquato, 1989. Measure of clustering in continuum percolation: computer-simulation of the two-point cluster function. *The Journal of Chemical Physics*, 91(2), pp.1173– 1178.

Lei, X. L., Kusunose, K., Nishizawa, 0., Cho, A. and Satoh, T., 2000. On the spatiotemporal distribution of acoustic emissions in two granitic rocks under triaxial compression: the role of pre-existing cracks, *Geophysical Research Letters*, 27(13), 1997–2000.

L'Hermite, R.G., 1960. Volume change of concrete. Proceedings of the 4th International Symposium on Chemistry of Cement, V-3, NBS Monograph 43, NBS, Washington, DC, pp. 659–694.

Lin, P., Wong, R.H.C. and Tang, C.A., 2015. Experimental study of coalescence mechanisms and failure under uniaxial compression of granite containing multiple holes. *International Journal of Rock Mechanics and Mining Sciences*, 77, pp.313–327.

Loch, J.P.G. and Miller R.D., 1975. Tests of the concept of secondary heaving. *Soil Science Society of America, Proceedings*, 39, pp.1036–1041.

Lockner, D.A., 1993. The role of acoustic emission in the study of rock fracture. *International Journal of Rock Mechanics and Mining Sciences & Geomechanics Abstracts*, 30(7), pp.883–899.

Lockner, D. A., Byerlee, J. D., Kuksenko, V., Ponomarev, A. and Sidorin, A., 1991. Quasi–Static Fault Growth and Shear Fracture Energy in Granite, *Nature*, 350(6313), 39– 42.

Lu, B. and S. Torquato, 1992. Lineal-path function for random heterogeneous materials. *Physical Review*, 45(2), pp. 922–929.

Mackay, J.R. 1974. Reticulate ice veins in permafrost, Northern Canada. *Canadian Geotechnical Journal,* 11(2), pp.230-237.

Matsuoka, N., 1990. Mechanisms of rock breakdown by frost action: An experimental approach. *Cold Regions Science and Technology*, 17, pp.253–270.

Matsuoka, N., 2001. Microgelivation versus macrogelivation: Towards bridging the gap between laboratory and field frost weathering. *Permafrost and Periglacial Processes,* 12(3), pp.299–313.

Matsuoka, N., 2008. Frost weathering and rockwall erosion in the southeastern Swiss Alps: long-term (1994–2006) observations. *Geomorphology*, 99, pp.353–368.

Matsuoka, N. and Murton, J., 2008. Frost weathering: recent advances and future directions. *Permafrost and Periglacial Processes*, 19(2), pp.195–210.

Miller, R.D. 1972. Freezing and heaving of saturated and unsaturated soils. *Highway Research Record*, 393, pp.1–11.

Miller, R.D., 1977. Lens initiation in secondary heaving. *Proceedings of the International Symposium on Frost Action in Soils*, Luleå, Sweden, 2, pp.68–74.

Miller, R.D., 1978. Frost heaving in non-colloidal soils. *Proceedings of the 3rd International Conference on Permafrost, Edmonton, Canada*, 1, pp.708–713.

Miller, R.D., Baker, J.H. and Kolaian, J.H., 1960. Particle size, overburden pressure, pore water pressure and freezing temperature of ice lenses in soils. In: Van Beren, F.A. et al., (eds),

Transactions of the 7th International Congress of Soil Science, Madison, WI, Elsevier, Amsterdam, 1, pp.122–129.

Moradian, Z., Ballivy, G., Rivard, P., Gravel, C. and Rousseau, B., 2010. Evaluating damage during shear tests of rock joints using acoustic emissions. *International Journal of Rock Mechanics and Mining Sciences,* 47, 590–598.

Murton, J.B., Coutard, J.P., Lautridou, J.P., Ozouf, J.C., Robinson, D.A., Williams, G.G. and Simmons, P., 2000. Experimental design for a pilot study on bedrock weathering near the permafrost table. *Earth Surface Processes and Landforms*, 25, pp.1281–1294.

Murton, J.B., Coutard, J.P., Lautridou, J.P., Ozouf, J.C. and Robinson, D.A., 2001. Physical modelling of bedrock brecciation by ice segregation in permafrost. *Permafrost and Periglacial Processes*, 12, pp.255–266.

Murton, J.B., Kuras, O., Krautblatter, M., Cane, T., Tschofen, D., Uhlemann, S., Schober, S., and Watson, P., 2016a. Monitoring rock freezing and thawing by novel geoelectrical and acoustic techniques. *Journal of Geophysical Research: Earth Surface*, pp.1–24.

Murton, J.B., Ozouf, J.C., and Peterson, R., 2016b. Heave, settlement and fracture of chalk during physical modelling experiments with temperature cycling above and below 0°C. *Geomorphology*, 270, pp.71–87.

Murton, J.B., Peterson, R. and Ozouf, J.C., 2006. Bedrock fracture by ice segregation in cold regions. *Science*, 314, pp.1127–1129.

Ohtsu, M., 1988. Diagnostics of cracks in concrete based on acoustic emission. *Nondestructive Testing*, ACI SP-112, pp. 63–82.

Ohtsu, M., 1996. The history and development of acoustic emission in concrete engineering. *Magazine of Concrete Research*, 48(147), pp. 321–330.

Ohtsu, M. and Watanabe, H., 2001. Quantitative damage estimation of concrete by AE. *Construction Building Material,* 15(5–6), pp. 217–224.

Otsu, N., 1979. A threshold selection method from gray-level histograms. *IEEE Transactions on Systems, Man and Cybernetics*, 9(1), pp.62–66.

Penner, E., 1986. Aspects of ice lens growth in soils. *Cold Regions Science and Technology*, 13(1), pp.91–100.

Peppin, S.S.L. and Style, R.W., 2013. The Physics of Frost Heave and Ice-Lens Growth. *Vadose Zone Journal*, 12(1), vzj2012.0049.

Prager, C., Zangerl, C., Patzelt, G. and Brandner, R., 2008. Age distribution of fossil landslides in the Tyrol (Austria) and its surrounding areas. *Natural Hazards and Earth System Sciences*, 8(2), pp.377–407.

Radley, J.D. and Allen, P., 2012. The Wealden (non-marine Lower Cretaceous) of the Weald Sub-basin, southern England. *Proceedings of the Geologists' Association*, 123(2), pp.245–318.

Rao, M.V.M.S., and Prasanna Lakshmi, K.J., 2005. Analysis of b-value and improved b-value of acoustic emissions accompanying rock fracture, *Current Science,* 89 (9), pp. 1577–1582.

Rempel, A.W., 2007. Formation of ice lenses and frost heave. *Journal of Geophysical Research: Earth Surface*, 112(11), F02S21.

Rempel, A.W., 2010. Frost heave. *Journal of Glaciology*, 56(200), pp.1122–1128.

Rempel, A.W., 2011. Microscopic and environmental controls on the spacing and thickness of segregated ice lenses. *Quaternary Research*, 75(2), pp.316–324.

Rempel, A.W., Wettlaufer, J.S. and Worster, M.G., 2004. Premelting dynamics in a continuum model of frost heave. *Journal of Fluid Mechanics*, 498, pp.227–244.

Rempel, A.W. and Worster, M.G., 1999. The interaction between a particle and an advancing solidification front*, Journal of Crystal Growth*, (205), pp.427–440.

Robinson, D.A. and Williams, R.B.G., 1976. Aspects of the geomorphology of the sandstone cliffs of the central Weald. Report of an excursion to West Hoathly and Groombridge, Saturday 5 October 1974. *Proceedings of the Geologists' Association,* 87, pp.93–99.

Saliba, J., Matallah, M., Loukili, A., Regoin, J.P., Grégoire, D., Verdon L. and Pijaudier-Cabot G., 2015. Experimental and numerical analysis of crack evolution in concrete through

acoustic emission technique and mesoscale modelling. *Engineering Fracture Mechanics*, 167, pp.123–137.

Sammis, C.G. and Ashby, M.F., 1986. The failure of brittle porous solids under compressive stress states. *Acta Metallurgica*, 34(3), pp.511–526.

Scholz, C. H., 1968a. Microfracturing and the inelastic deformation of rock in compression, *Journal of Geophysical Research*, 73 (4), 1417–1432.

Scholz, C. H., 1968b. Experimental study of the microfracturing process in brittle rock, *Journal of Geophysical Research*, 73 (4), 1447–1454.

Shiotani, T., Yuyama, S., Li, Z.W. and Ohtsu, M., 2001. Application of the AE improved b-value to qualitative evaluation of fracture process in concrete materials. *Journal of Acoustic Emission*, 19, pp. 118–132.

Shiotani, T., Yuyama, S., Li, Z.W. and Ohtsu, M., 2000. Quantitative evaluation of fracture process in concrete by the use of improved b-value. 5th International Symposium on Non-Destructive Testing in Civil Engineering, T. Uohoto, ed., *Elsevier Science*, Amsterdam, pp. 293–302.

Smith, M.W., 1985. Models of soil freezing. In: Church, M. and Slaymaker, O. (eds), *Field and Theory: Lectures in Geocryology*. University of British Columbia Press, Vancouver, pp. 96–120.

Soldati, M., Corsini, A. and Pasuto, A., 2004. Landslides and climate change in the Italian Dolomites since the Late glacial. *Catena*, 55(2), pp.141–161.

Soulioti, D., Barkoula, D.N.M., Paipetis, A., Matikas, T.E., Shiotani, T. and Aggelis, D.G., 2009. Acoustic emission behaviour of steel fibre reinforced concrete under bending. *Construction Building Material,* 23, pp. 3532–3536.

Style, R.W., Peppin S.L., Cocks C.F. and Wettlaufer J.S., 2011. Ice-lens formation and geometrical supercooling in soils and other colloidal materials. *Physical Review E - Statistical, Nonlinear, and Soft Matter Physics*, 84, pp.1–12.

Style, R.W. and Peppin, S.S.L., 2012. The kinetics of ice-lens growth in porous media. *Journal of Fluid Mechanics*, 692, pp.482–498.

Taber, S., 1929. Frost heaving. *Journal of Geology*, 37, pp.428–461.

Taber, S., 1930. The mechanics of frost heaving. *Journal of Geology*, 38, pp.303–317.

Tanigawa, Y., Yamada, K. and Kiriyama, S., 1977. Frequency characteristics of AE in concrete. Japan Concrete Institute, Tokyo, JCI (2), pp. 129–132.

Thomas, H.R., Cleall, P.J., Li, Y., Harris, C. and Kern-Luetschg, M., 2009. Modelling of cryogenic processes in permafrost and seasonally frozen soils. *Géotechnique*, 59(3), pp.173–184.

Tinner, W., Kaltenrieder, P., Soom, M., Zwahlen, P., Schmidhalter, M., Boschetti, A. and Schluchter, C., 2005. The postglacial rockfall in the Kander valley (Switzerland): age and effects on palaeo-environments. *Eclogae Geologicae Helvetiae*, 98(1), pp.83–95.

Torquato, S., 1991. Random Heterogeneous Media: Microstructure and Improved Bounds on Effective Properties. *Applied Mechanics Reviews*, 44(2), p.37.

Torquato, S., 2002. Statistical Description of Microstructures. *Annual Review of Materials Research*, 32(1), pp.77–111.

Van Everdingen, R. (ed.) 1998, revised May 2005. Multi-language Glossary of Permafrost and Related Ground-ice Terms. National Snow and Ice Data Center/World Data Center for Glaciology, Boulder, Colorado.

Van Mier, J.G.M., 1997. Fracture process of concrete, assessment of material parameters for fracture models. *CRC Press*, ISBN: 0849391237.

Vidya Sagar, R., Raghu Prasad, B.K. and Karihaloo, B.L., 2010. Verification of the applicability of lattice model to concrete fracture by AE study. *International Journal of Fracture*, 161(2), pp. 121–129.

Vidya Sagar, R., 2010. Fracture mechanics of concrete – Experimental and numerical studies. VDM-Verlag Dr. Muller Aktiengesellschaft & Co.KG, Dudweiler Landstr. 99, 66123 Saarbruecken, Germany. ISBN 978-3-639-23724-5.

Vlahou, L. and Worster, M.G., 2010. Ice growth in a spherical cavity of a porous medium. *Journal of Glaciology*, 56, pp.271–277.

Walder, J. and Hallet, B. 1985. A theoretical model of the fracture of rock during freezing. *Geological Society of America Bulletin*, 96, pp.336–346.

Weiss, J., 1997. The role of attenuation on acoustic emission amplitude distributions and b-values. *Bulletin of Seismological Society America*, 87(5), pp. 1362–1367.

Wong, R.H.C., Lin, P. and Tang, C.A., 2006. Experimental and numerical study on splitting failure of brittle solids containing single pore under uniaxial compression. *Mechanics of Materials*, 38, pp.142–159.

Xia, D., Arenson, L.U., Biggar, K.W. and Sego, D.C., 2005. Freezing process in Devon silt – using time- lapse photography. In *Proceedings, 58th Canadian Geotechnical Conference and 6th Joint CGS and IAH-CNC Groundwater Specialty Conference.* Saskatoon, Saskatchewan, 18–21 September 2005, CD-ROM.

Xia, D., 2006. Frost Heave Studies Using Digital Photographic Technique. University of Alberta, Edmonton, AB, Canada, MSc Thesis. 165 pp.

Yang, Z.J. and Chen, J.F., 2004. Fully automatic modelling of cohesive discrete crack propagation in concrete beams using local arc-length methods. *International Journal of Solids and Structures*, 41(3–4), pp.801–826.

Yeong, C. L. Y., and Torquato, S., 1998.Reconstructing random media. II. Three-dimensional media from two-dimensional cuts. *Physical Review*, E58, pp.224–233.

Yoon, D.J., Weiss, W. and Shah, S.P., 2000. Assessing damage in corroded reinforced concrete using acoustic emission. *Journal of Engineering Mechanics*, 26(3), pp. 273–283.

Yuyama, S., Li, Z., Ito, Y. and Arazoe, M., 1999. Quantitative analysis of fracture process in RC column foundation by moment tensor analysis of acoustic emission. *Construction Building Material*, 13, pp.87–97.

Zang, A., Wagner, F. C., Stanchits, S., Janssen, C. and Dresen, G., 2000. Fracture process zone in granite, *Journal of Geophysical Research-Solid Earth,* 105, 23651–23661.

Zang, A., Wagner, F. C., Stanchits, S., Janssen, C., Dresen, G., Andresen, R. And Haidekker, M. A., 1998. Source analysis of acoustic emissions in Aue granite cores under symmetric and asymmetric compressive loads. *International Journal of Geophysics*, 135(3), pp. 1113–1130.

Appendices

A. Lineal Path Function (tuffeau chalk)

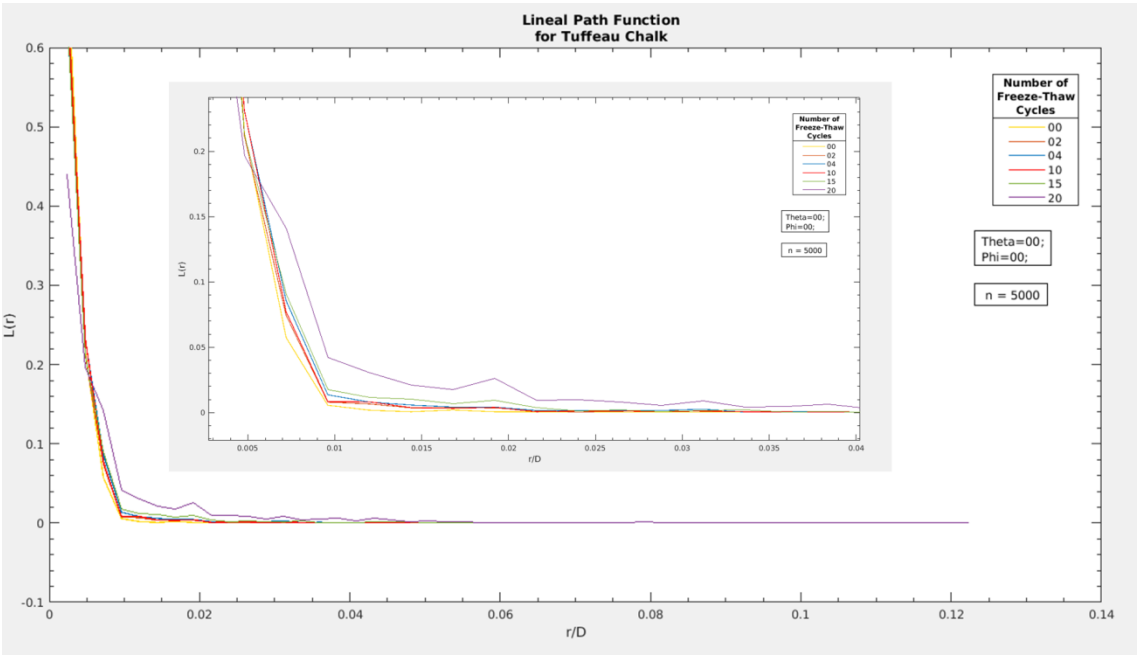

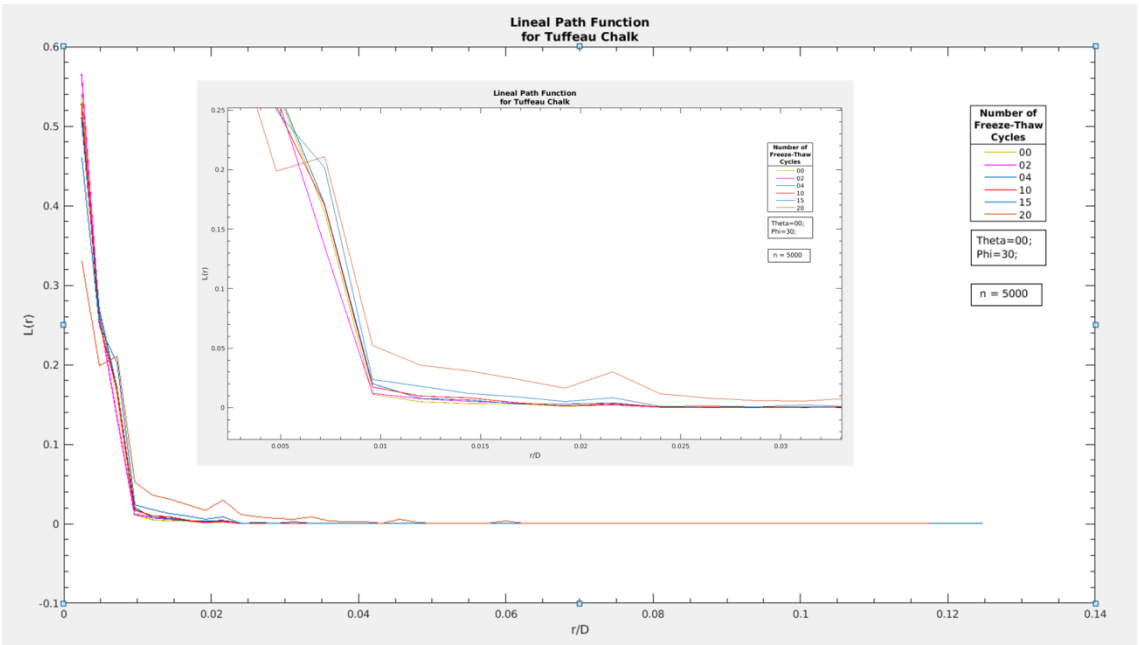

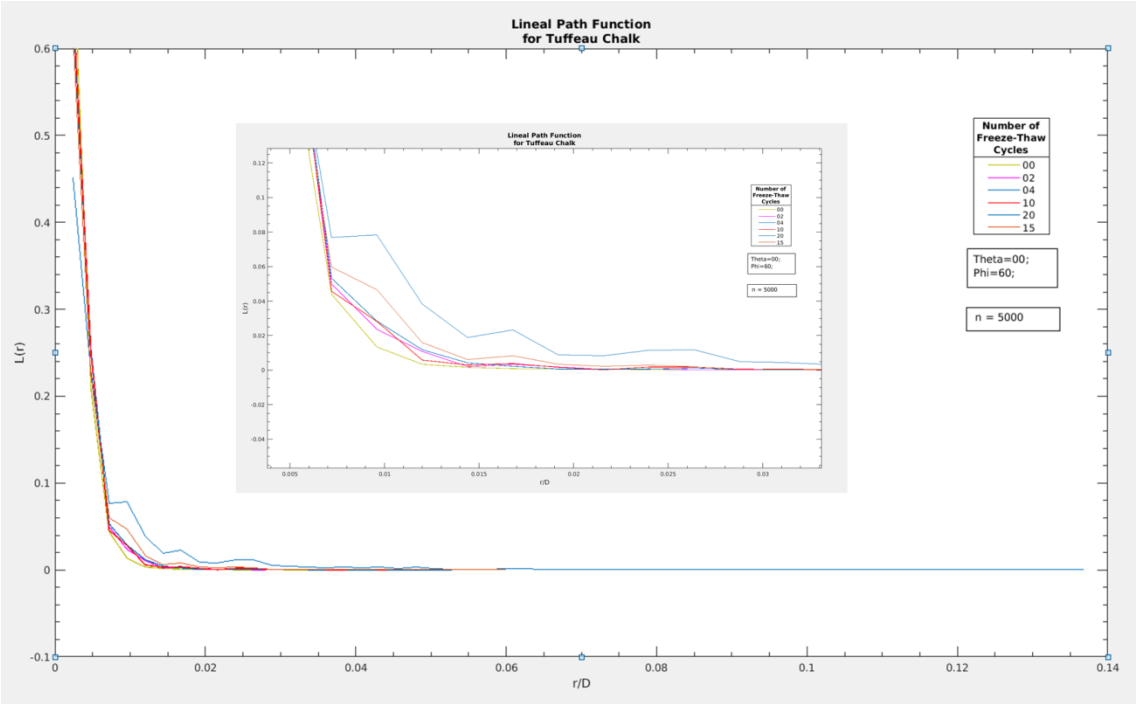
Lineal Path Function
for Tuffeau Chalk
L(r)
r/D
Number of Freeze-Thaw Cycles
00
02
04
10
20
15
Theta=00;
Phi=60;
n = 5000

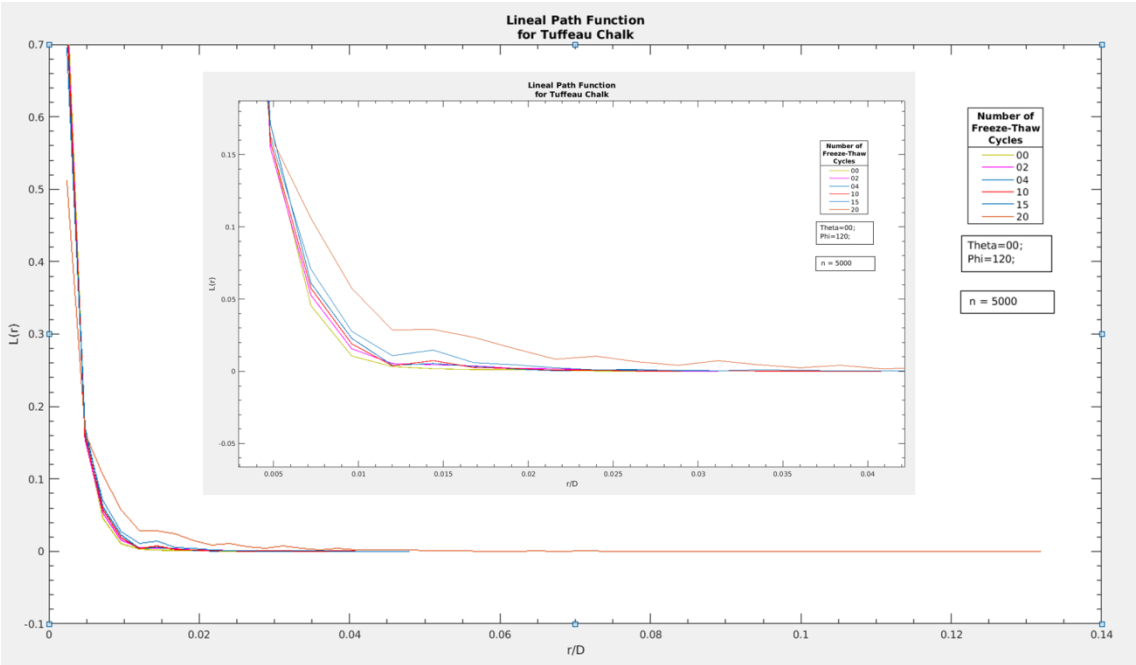
Lineal Path Function
for Tuffeau Chalk
L(r)
r/D
Number of Freeze-Thaw Cycles
00
02
04
10
15
20
Theta=00;
Phi=120;
n = 5000

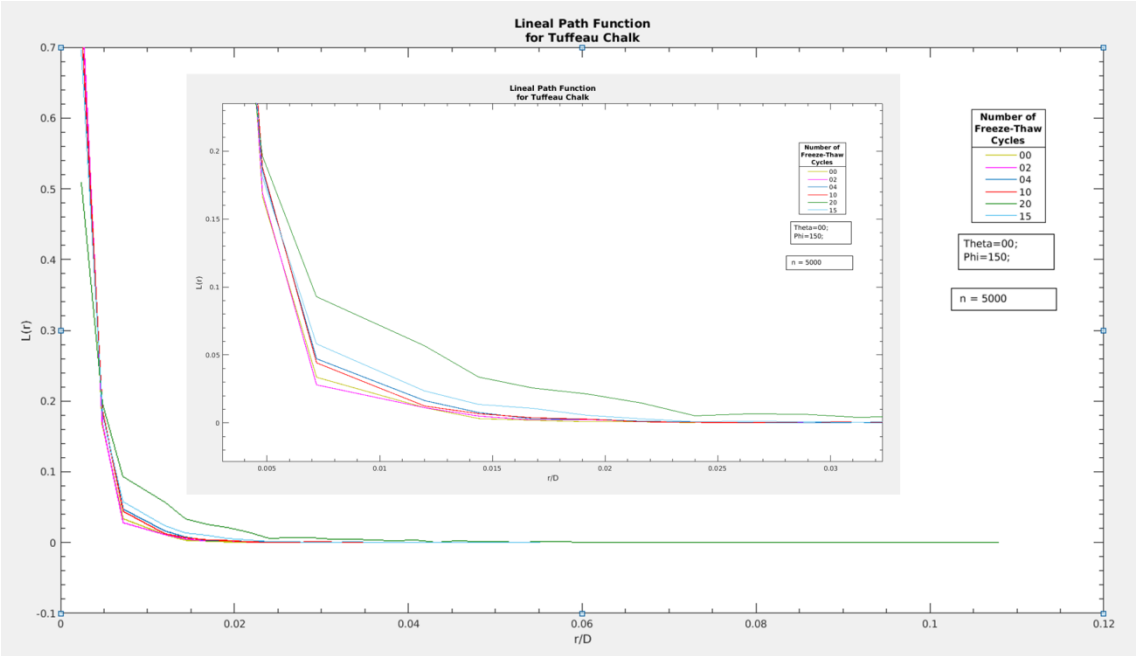
Lineal Path Function
for Tuffeau Chalk
L(r)
r/D
Number of
Freeze-Thaw
Cycles
00
02
04
10
20
15
Theta=00;
Phi=150;
n = 5000

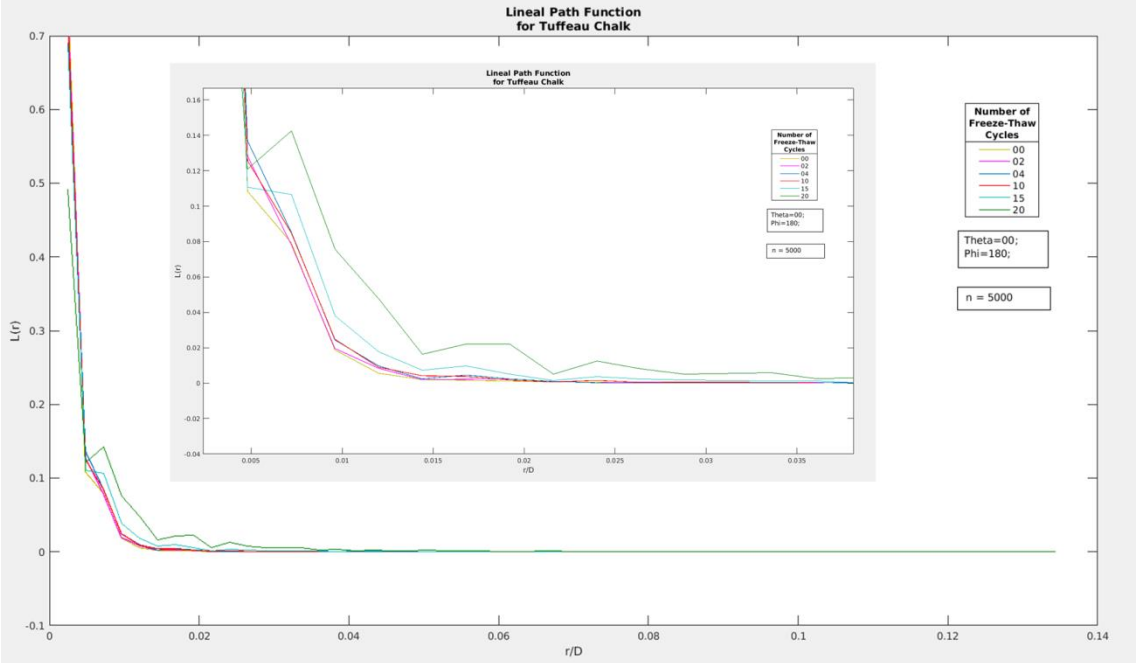
Lineal Path Function
for Tuffeau Chalk
L(r)
r/D
Number of
Freeze-Thaw
Cycles
00
02
04
10
15
20
Theta=00;
Phi=180;
n = 5000

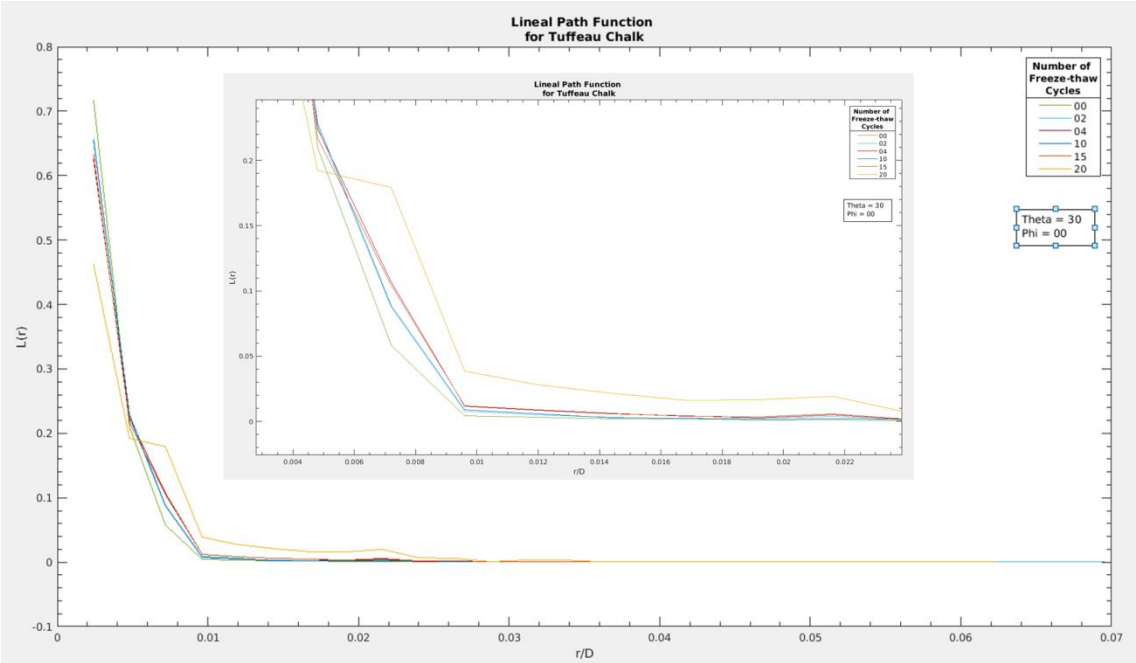
Lineal Path Function
for Tuffeau Chalk
L(r)
r/D
Number of
Freeze-thaw
Cycles
00
02
04
10
15
20
Theta = 30
Phi = 00

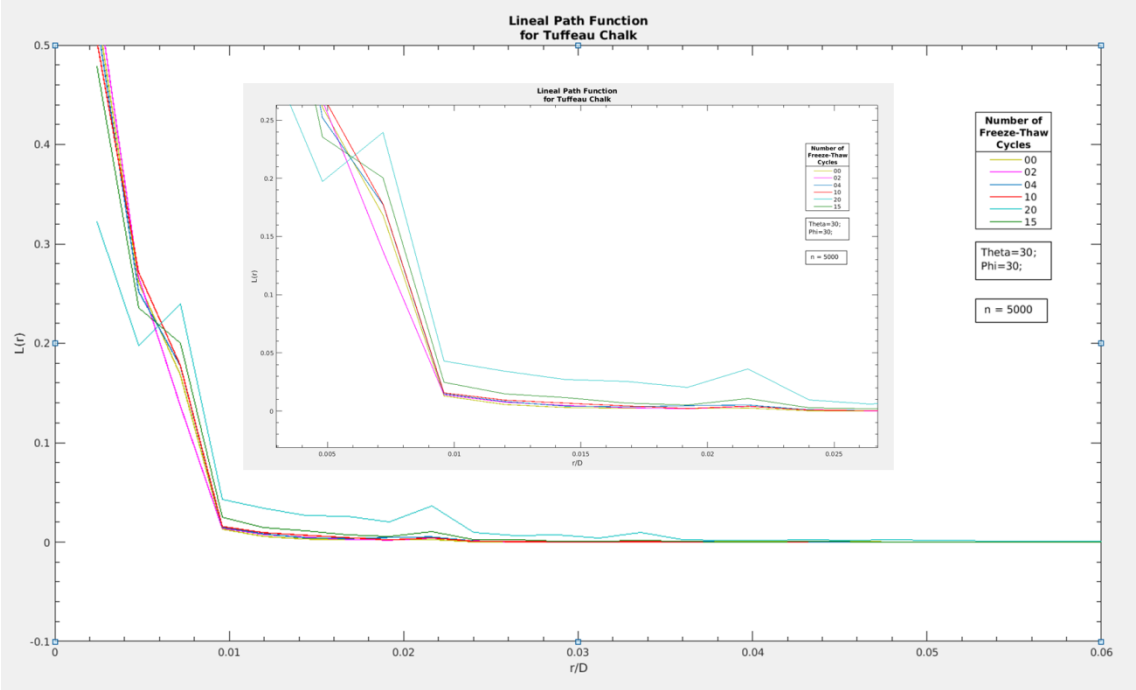
Lineal Path Function
for Tuffeau Chalk
L(r)
r/D
Number of
Freeze-Thaw
Cycles
00
02
04
10
20
15
Theta=30;
Phi=30;
n = 5000

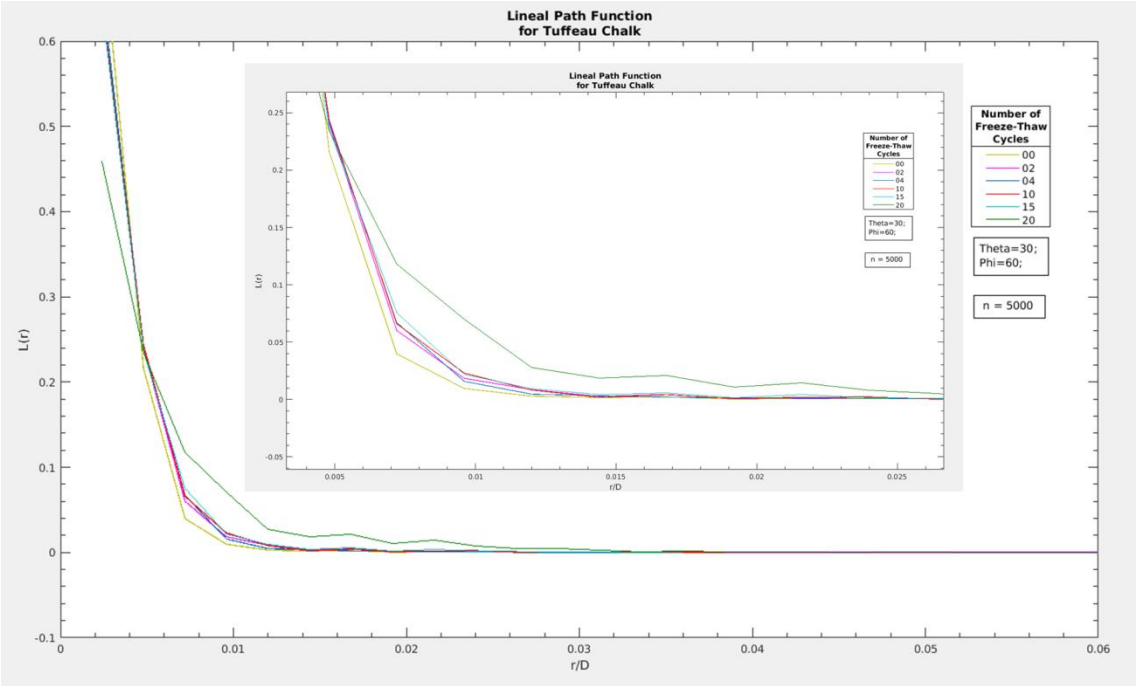
Lineal Path Function
for Tuffeau Chalk
L(r)
r/D
Number of
Freeze-Thaw
Cycles
00
02
04
10
15
20
Theta=30;
Phi=60;
n = 5000

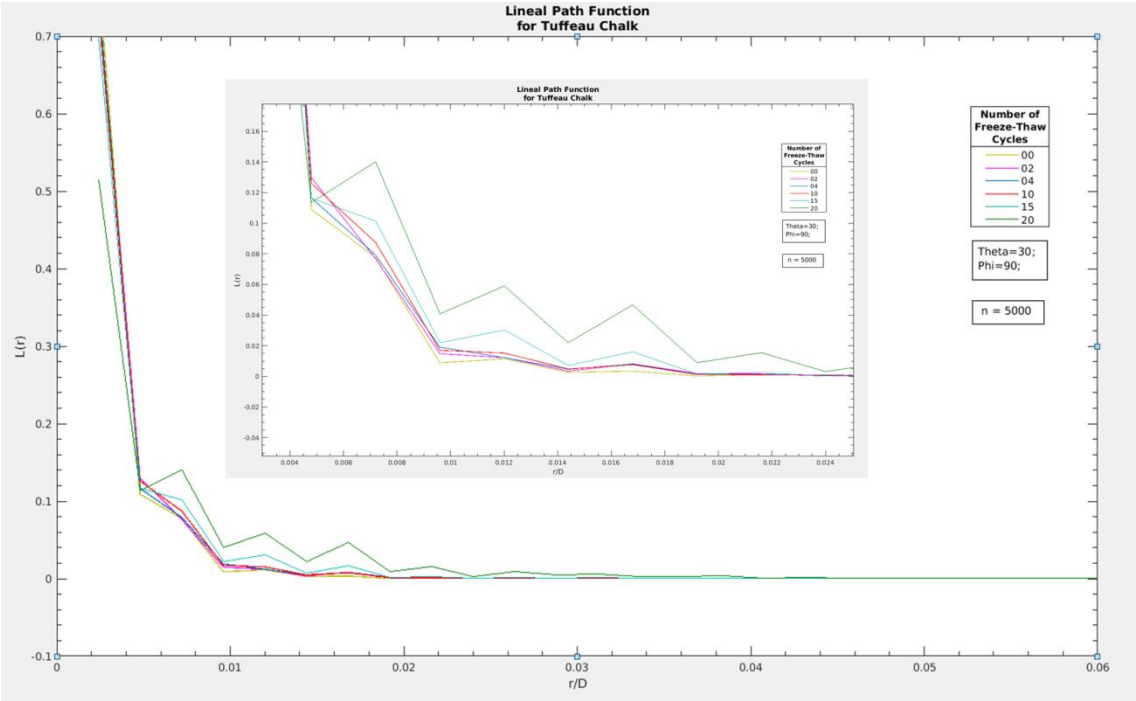
Lineal Path Function
for Tuffeau Chalk
L(r)
r/D
Number of
Freeze-Thaw
Cycles
00
02
04
10
15
20
Theta=30;
Phi=90;
n = 5000

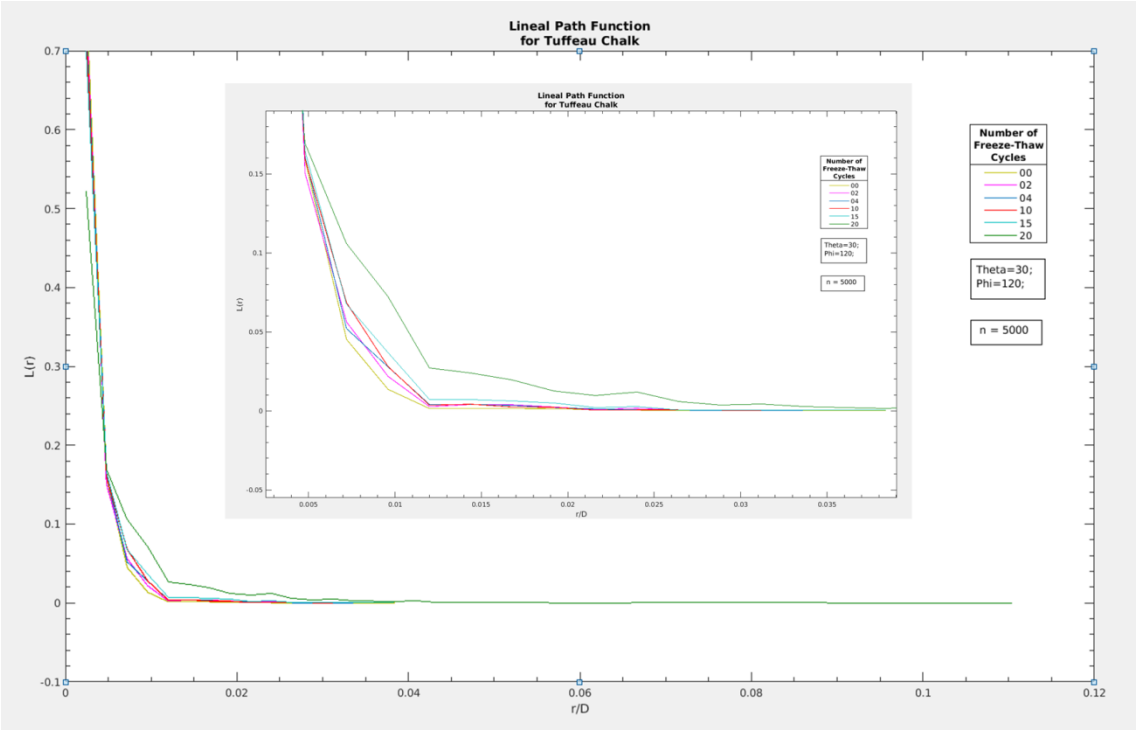
Lineal Path Function
for Tuffeau Chalk
L(r)
r/D
Number of
Freeze-Thaw
Cycles
00
02
04
10
15
20
Theta=30;
Phi=120;
n = 5000

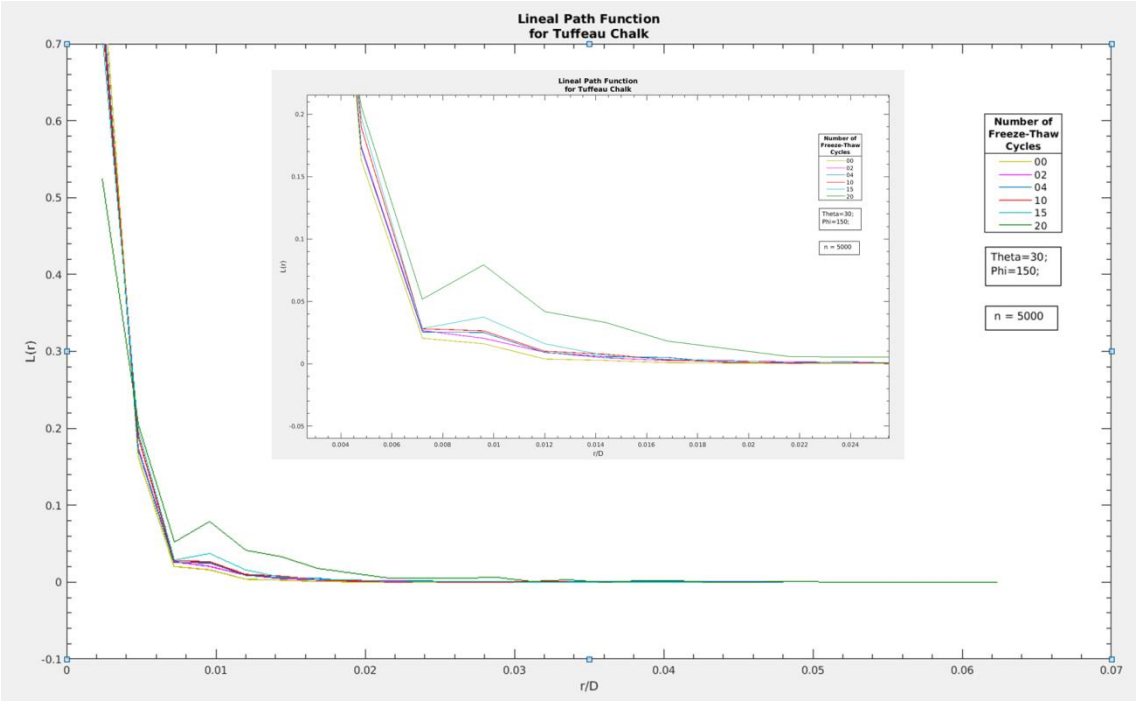
Lineal Path Function
for Tuffeau Chalk
L(r)
r/D
Number of
Freeze-Thaw
Cycles
00
02
04
10
15
20
Theta=30;
Phi=150;
n = 5000

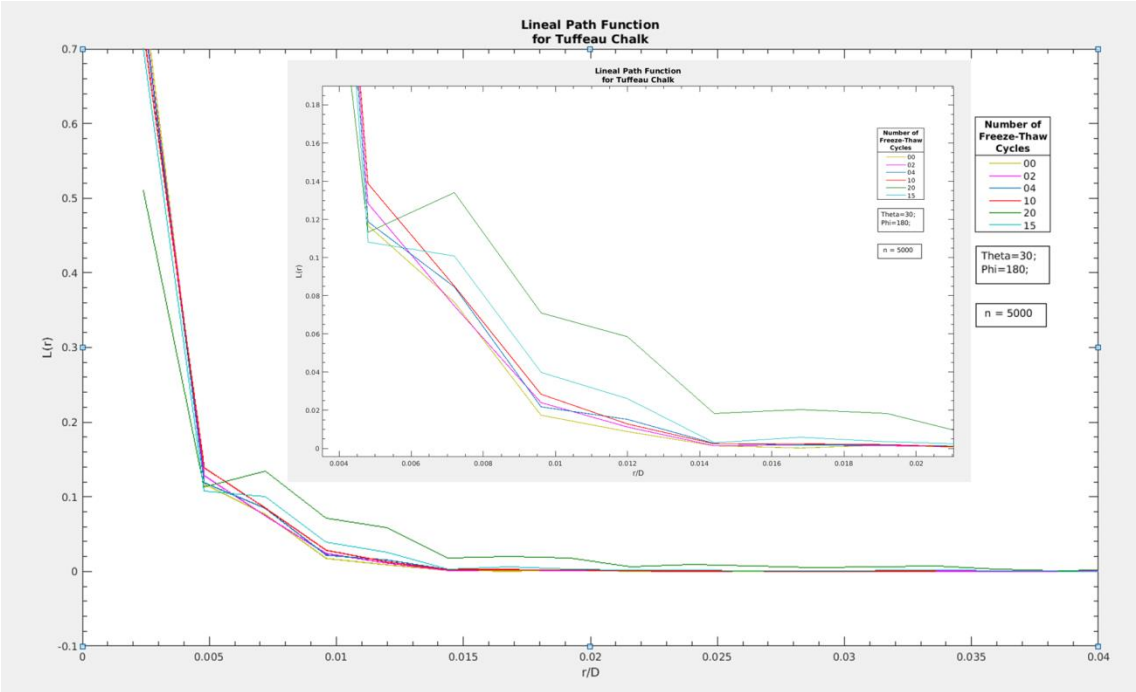
Lineal Path Function
for Tuffeau Chalk
L(r)
r/D
Number of
Freeze-Thaw
Cycles
00
02
04
10
20
15
Theta=30;
Phi=180;
n = 5000

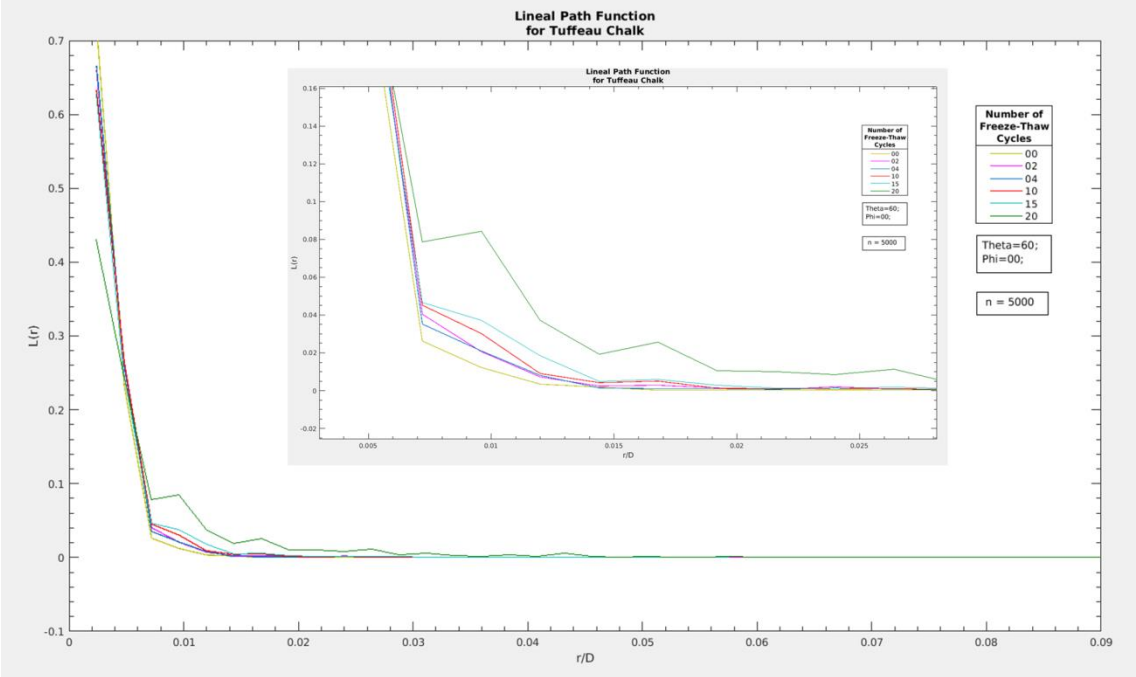
Lineal Path Function
for Tuffeau Chalk
L(r)
r/D
Number of
Freeze-Thaw
Cycles
00
02
04
10
15
20
Theta=60;
Phi=00;
n = 5000

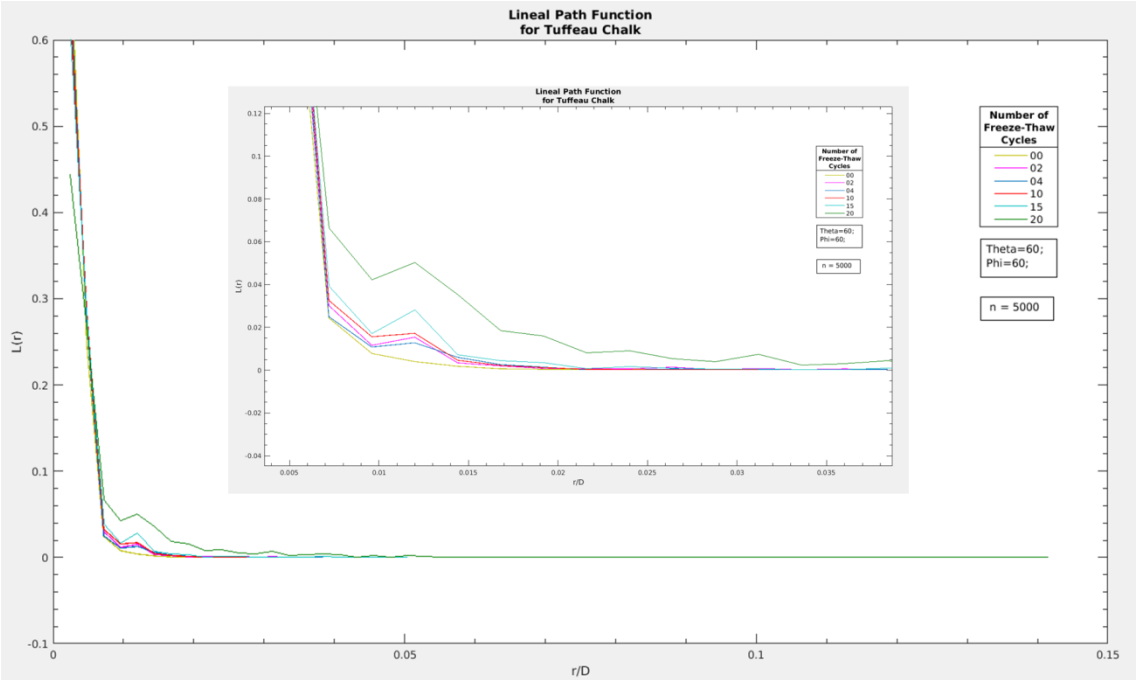
Lineal Path Function
for Tuffeau Chalk
L(r)
r/D
Number of Freeze-Thaw Cycles
00
02
04
10
15
20
Theta=60;
Phi=60;
n = 5000

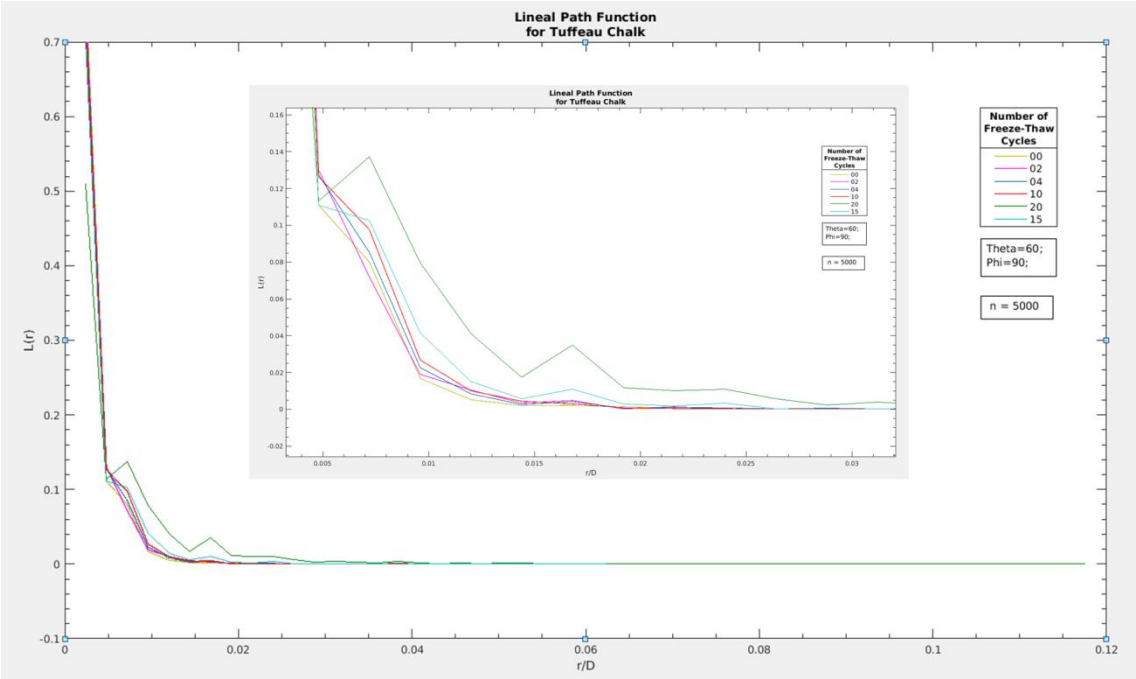
Lineal Path Function
for Tuffeau Chalk
L(r)
r/D
Number of Freeze-Thaw Cycles
00
02
04
10
20
15
Theta=60;
Phi=90;
n = 5000

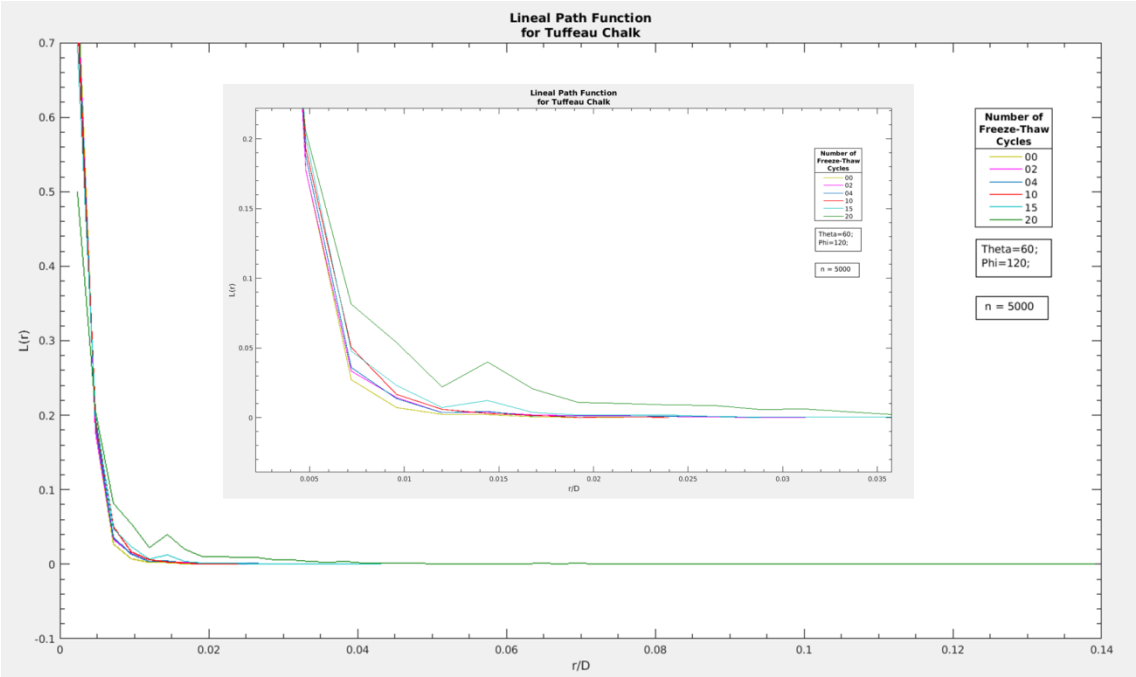
Lineal Path Function
for Tuffeau Chalk
L(r)
r/D
Number of Freeze-Thaw Cycles
00
02
04
10
15
20
Theta=60;
Phi=120;
n = 5000

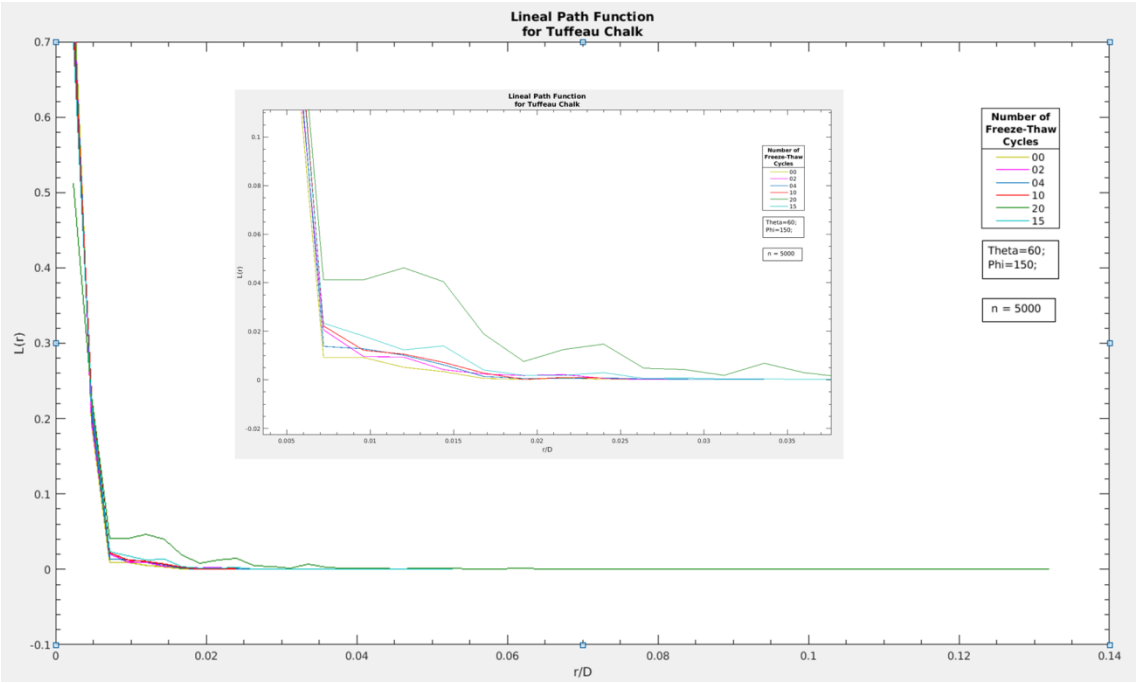
Lineal Path Function
for Tuffeau Chalk
L(r)
r/D
Number of Freeze-Thaw Cycles
00
02
04
10
20
15
Theta=60;
Phi=150;
n = 5000

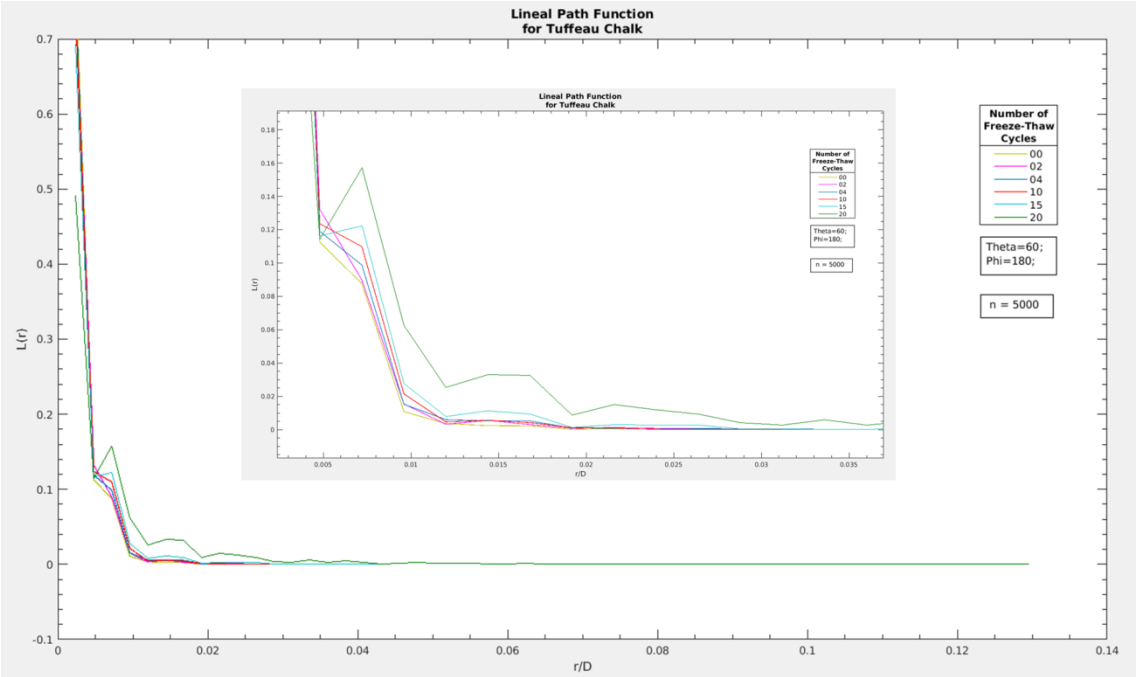
Lineal Path Function
for Tuffeau Chalk
L(r)
r/D
Number of
Freeze-Thaw
Cycles
00
02
04
10
15
20
Theta=60;
Phi=180;
n = 5000

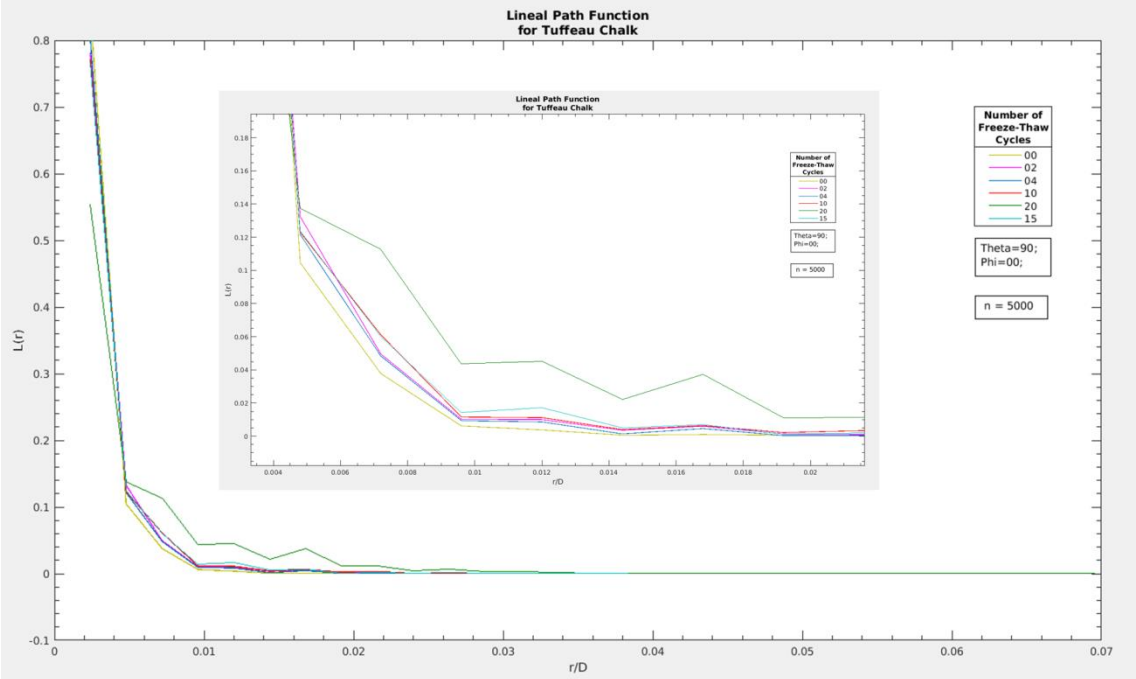
Lineal Path Function
for Tuffeau Chalk
L(r)
r/D
Number of
Freeze-Thaw
Cycles
00
02
04
10
20
15
Theta=90;
Phi=00;
n = 5000

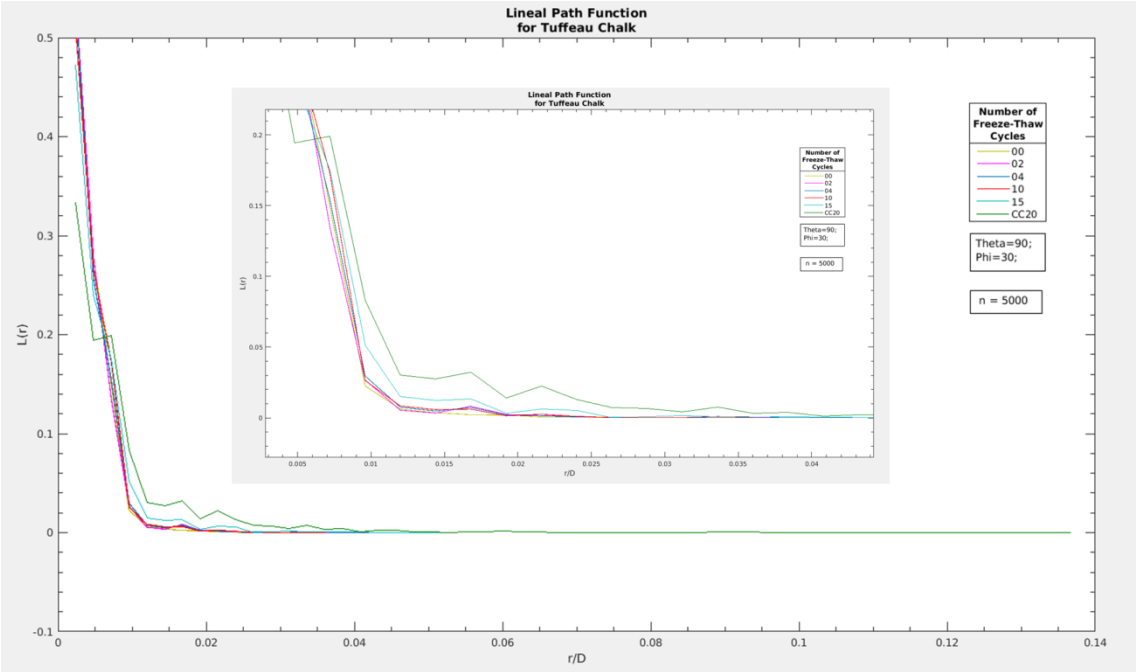
Lineal Path Function
for Tuffeau Chalk
L(r)
r/D
Number of
Freeze-Thaw
Cycles
00
02
04
10
15
CC20
Theta=90;
Phi=30;
n = 5000

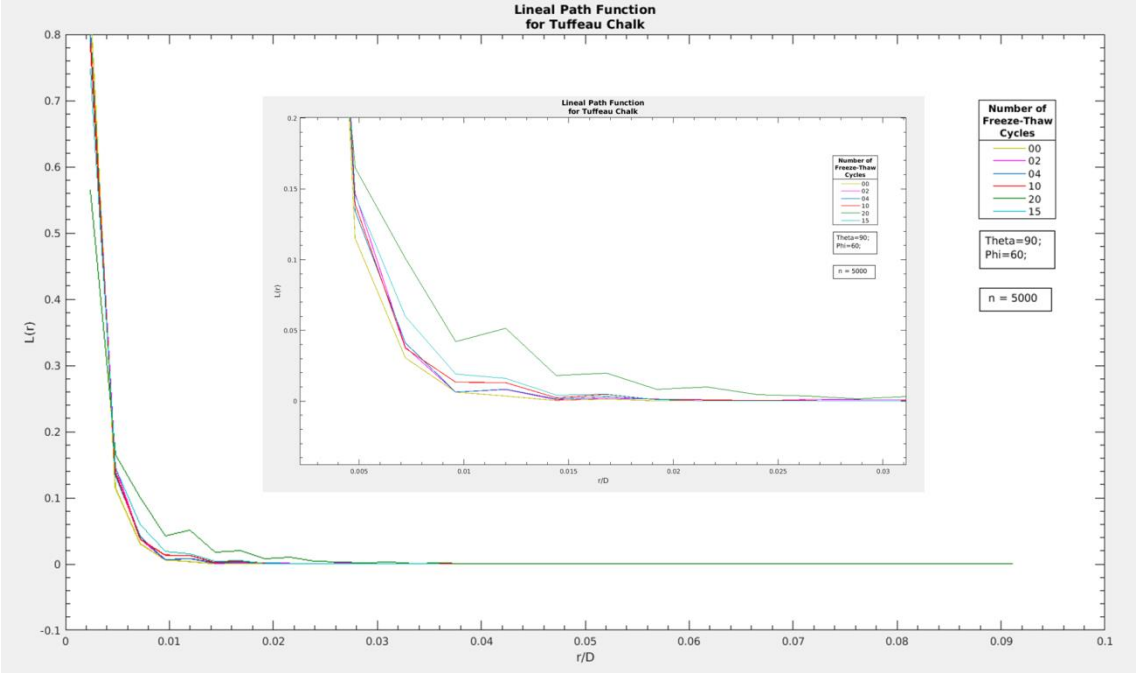
Lineal Path Function
for Tuffeau Chalk
L(r)
r/D
Number of
Freeze-Thaw
Cycles
00
02
04
10
20
15
Theta=90;
Phi=60;
n = 5000

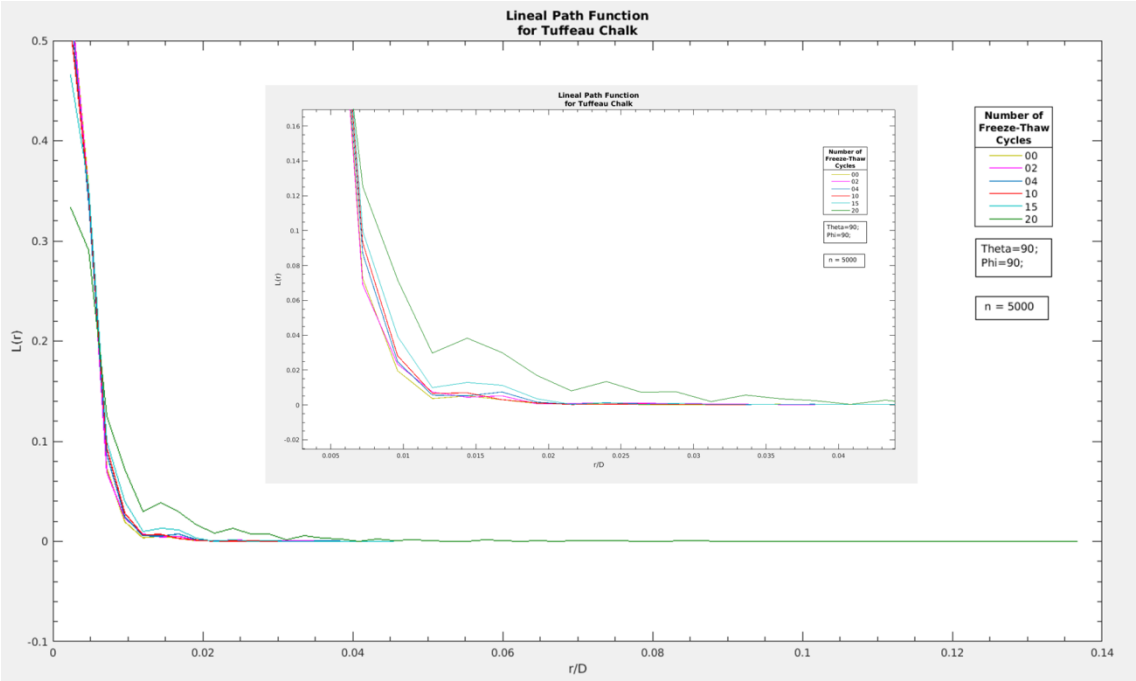
Lineal Path Function
for Tuffeau Chalk
L(r)
r/D
Number of Freeze-Thaw Cycles
00
02
04
10
15
20
Theta=90;
Phi=90;
n = 5000

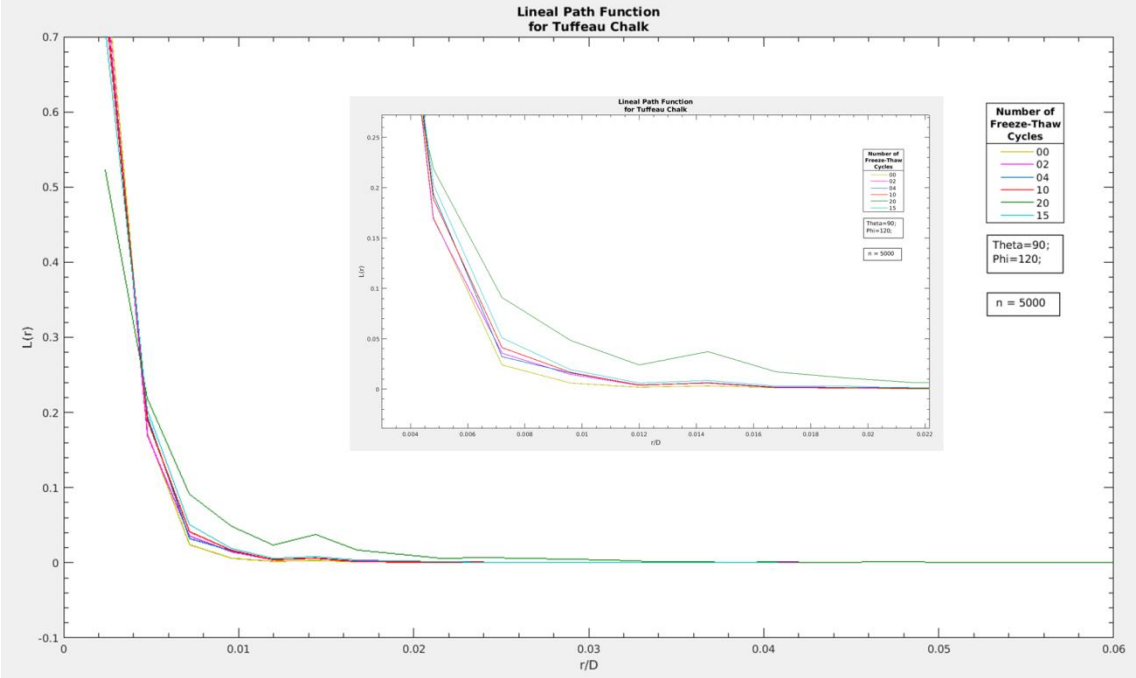
Lineal Path Function
for Tuffeau Chalk
L(r)
r/D
Number of Freeze-Thaw Cycles
00
02
04
10
20
15
Theta=90;
Phi=120;
n = 5000

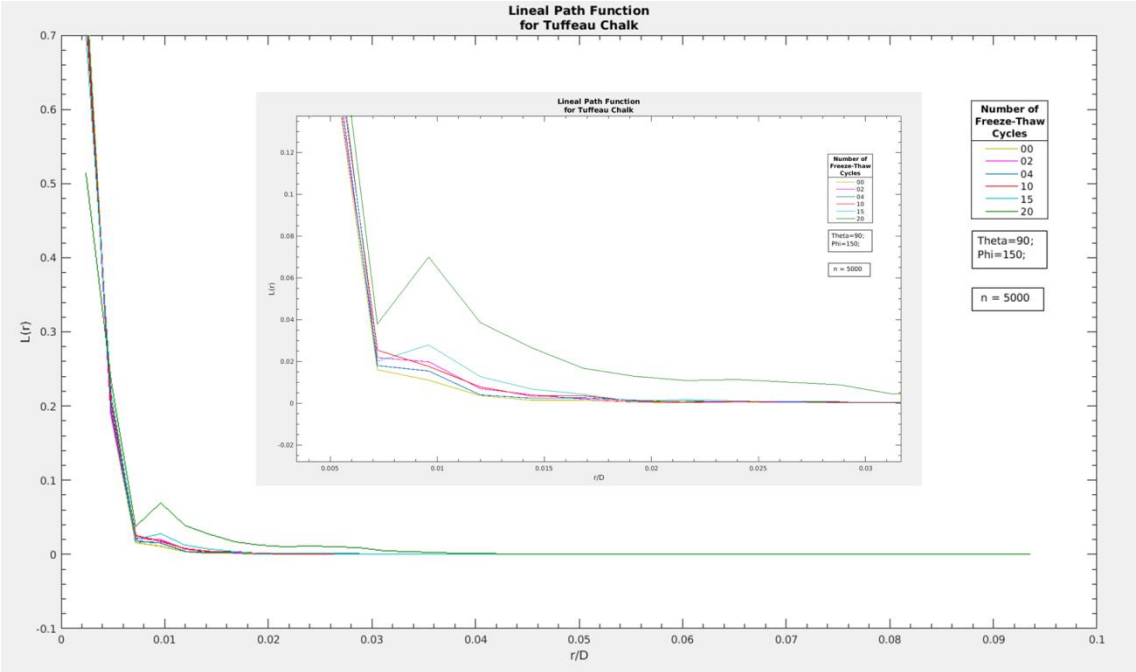
Lineal Path Function
for Tuffeau Chalk
L(r)
r/D
Number of Freeze-Thaw Cycles
00
02
04
10
15
20
Theta=90;
Phi=150;
n = 5000

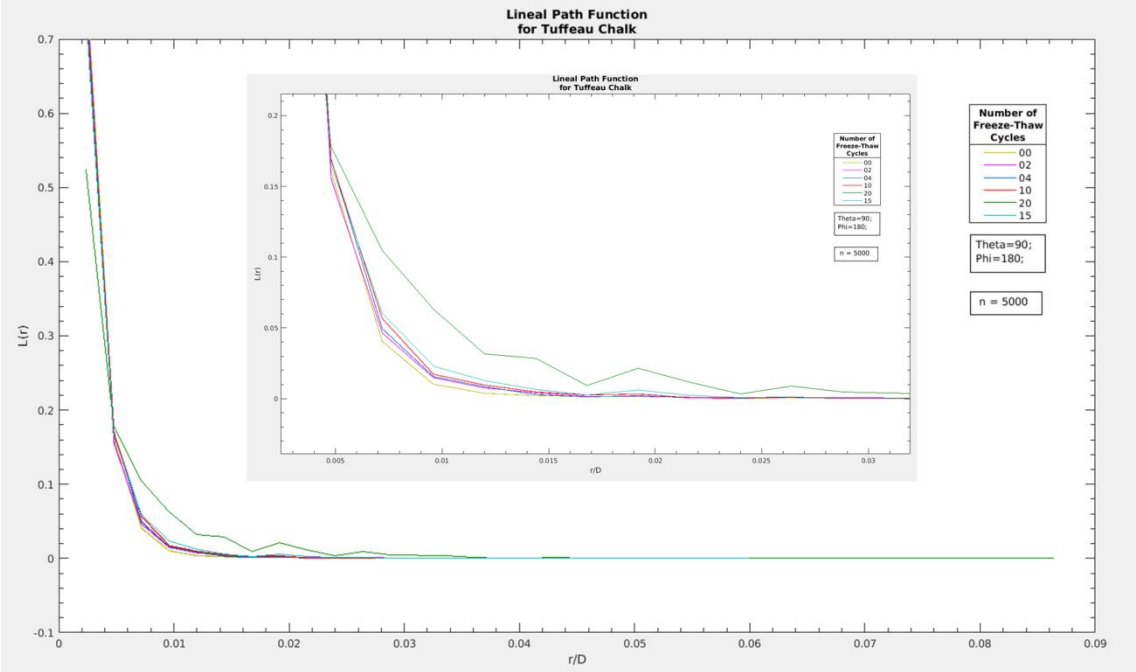
Lineal Path Function
for Tuffeau Chalk
L(r)
r/D
Number of Freeze-Thaw Cycles
00
02
04
10
20
15
Theta=90;
Phi=180;
n = 5000

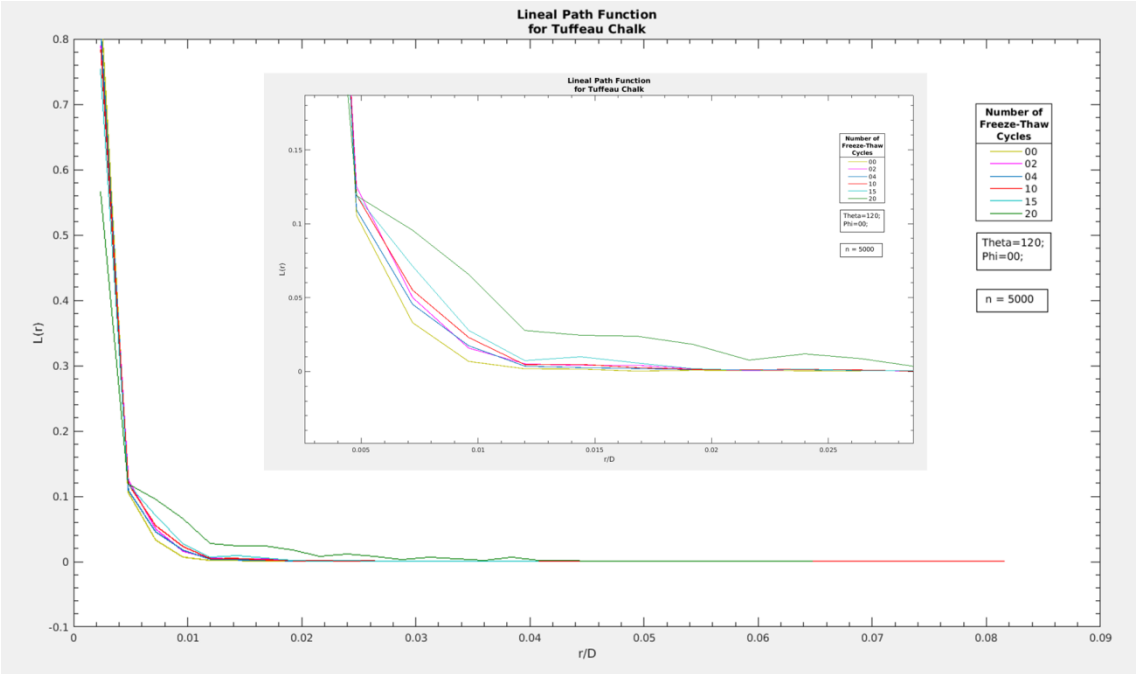
Lineal Path Function
for Tuffeau Chalk
L(r)
r/D
Number of
Freeze-Thaw
Cycles
00
02
04
10
15
20
Theta=120;
Phi=00;
n = 5000

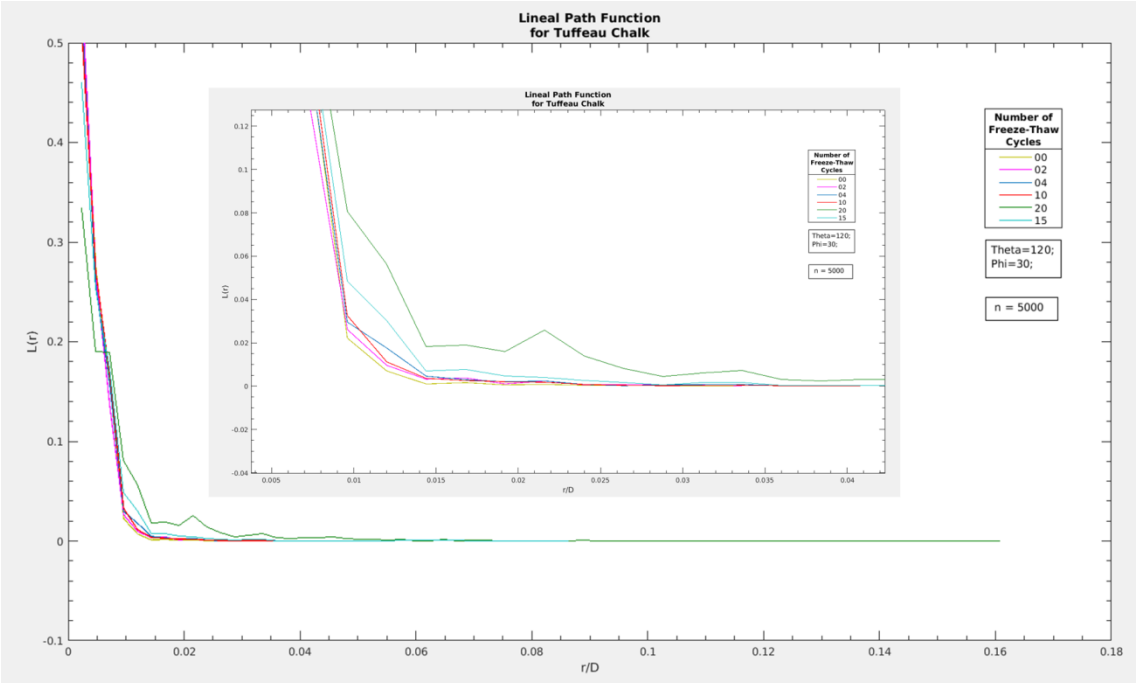
Lineal Path Function
for Tuffeau Chalk
L(r)
r/D
Number of
Freeze-Thaw
Cycles
00
02
04
10
20
15
Theta=120;
Phi=30;
n = 5000

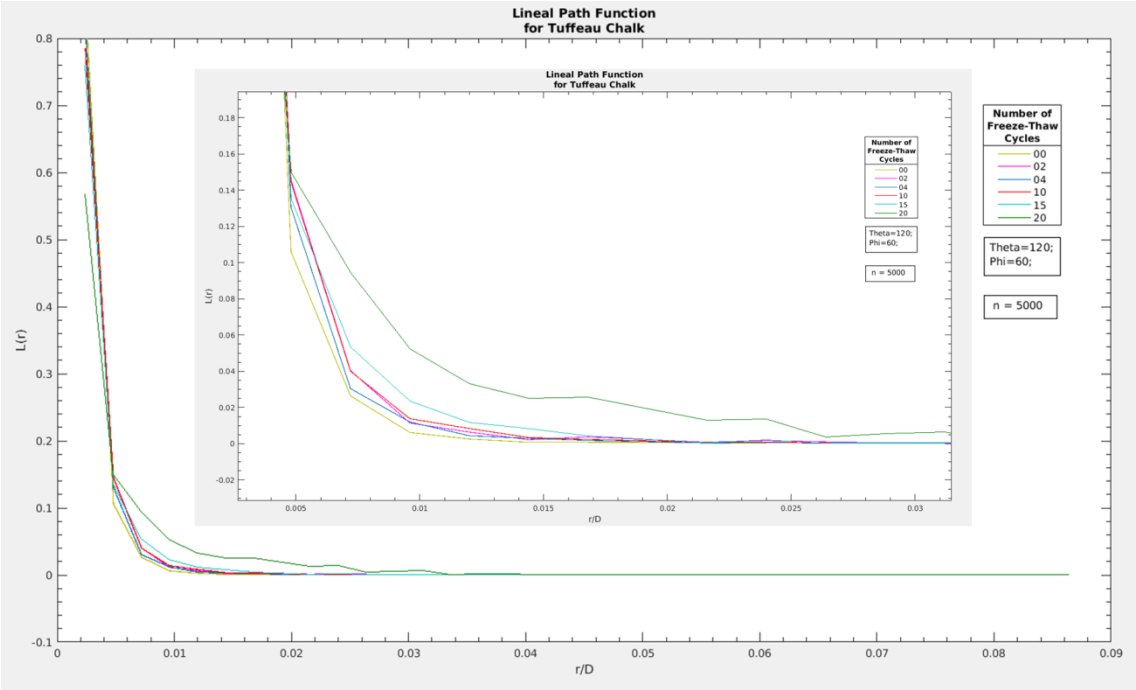
Lineal Path Function
for Tuffeau Chalk
L(r)
r/D
Number of Freeze-Thaw Cycles
00
02
04
10
15
20
Theta=120;
Phi=60;
n = 5000

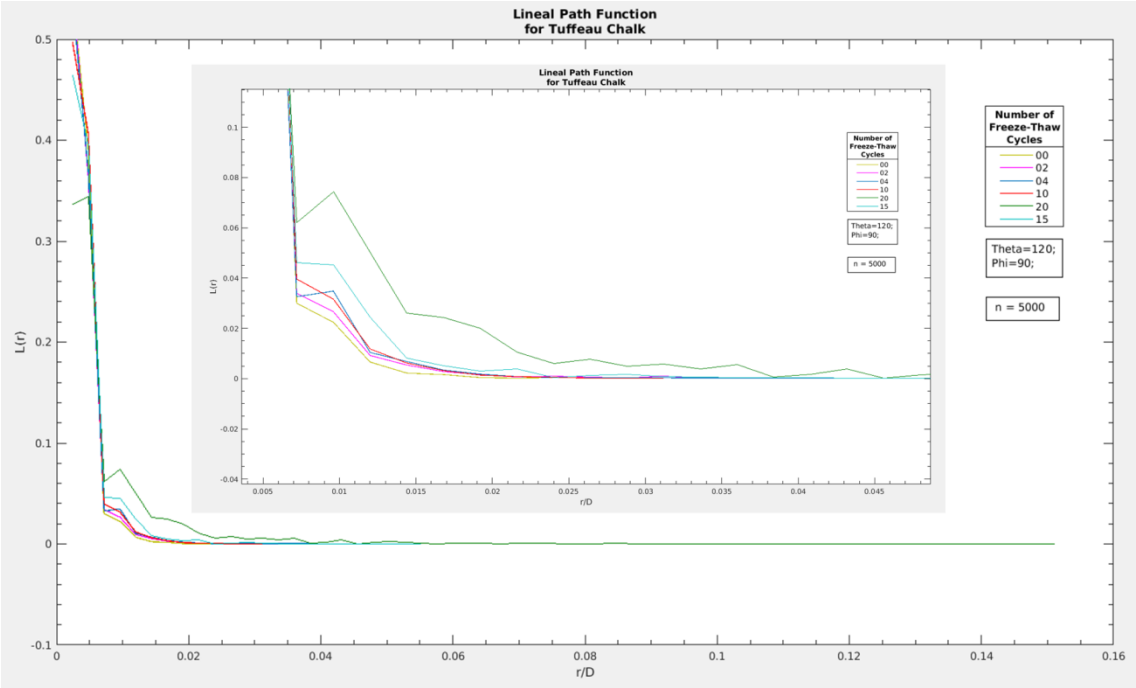
Lineal Path Function
for Tuffeau Chalk
L(r)
r/D
Number of Freeze-Thaw Cycles
00
02
04
10
20
15
Theta=120;
Phi=90;
n = 5000

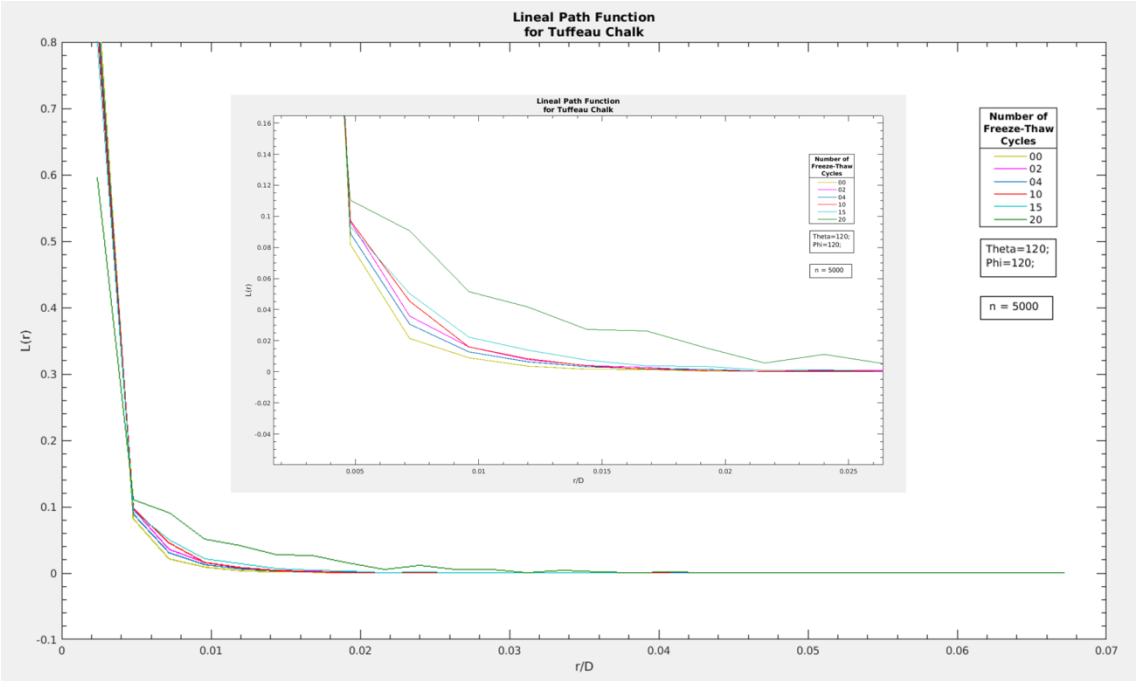
Lineal Path Function
for Tuffeau Chalk
L(r)
r/D
Number of Freeze-Thaw Cycles
00
02
04
10
15
20
Theta=120;
Phi=120;
n = 5000

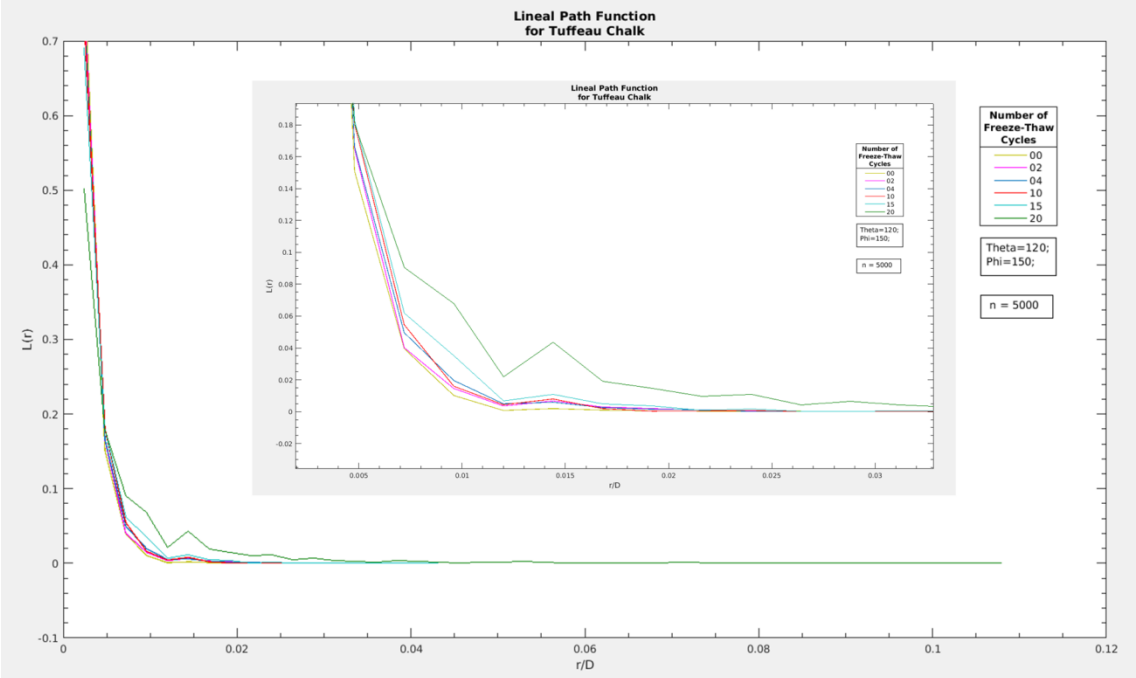
Lineal Path Function
for Tuffeau Chalk
L(r)
r/D
Number of Freeze-Thaw Cycles
00
02
04
10
15
20
Theta=120;
Phi=150;
n = 5000

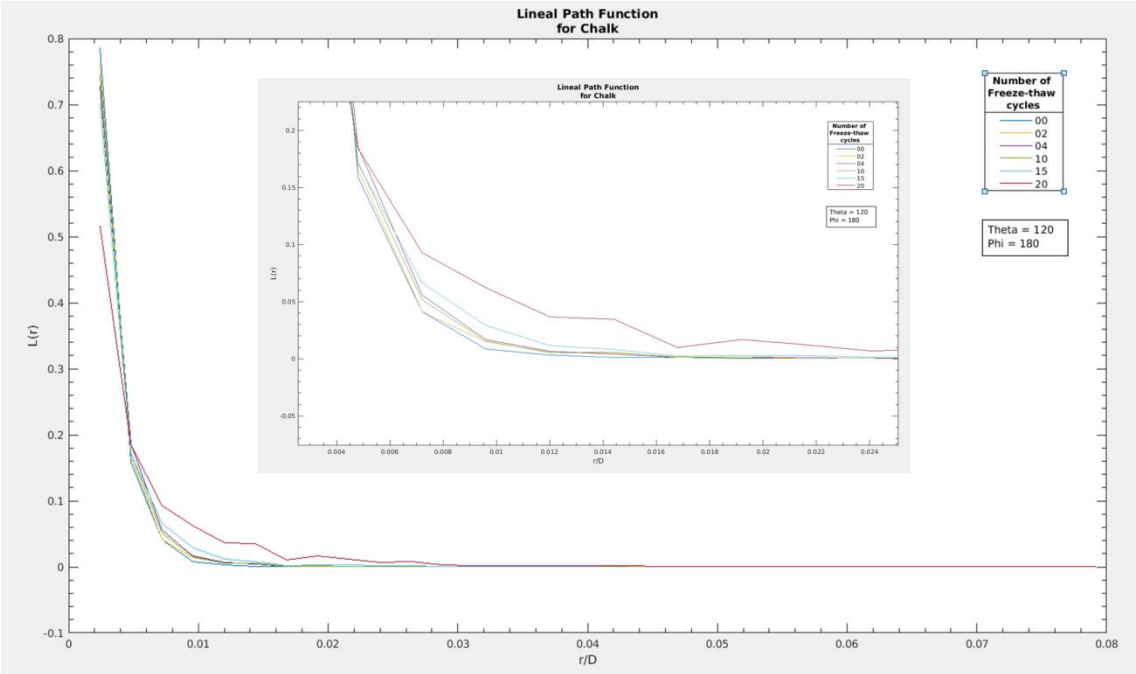
Lineal Path Function
for Chalk
L(r)
r/D
Number of
Freeze-thaw
cycles
00
02
04
10
15
20
Theta = 120
Phi = 180

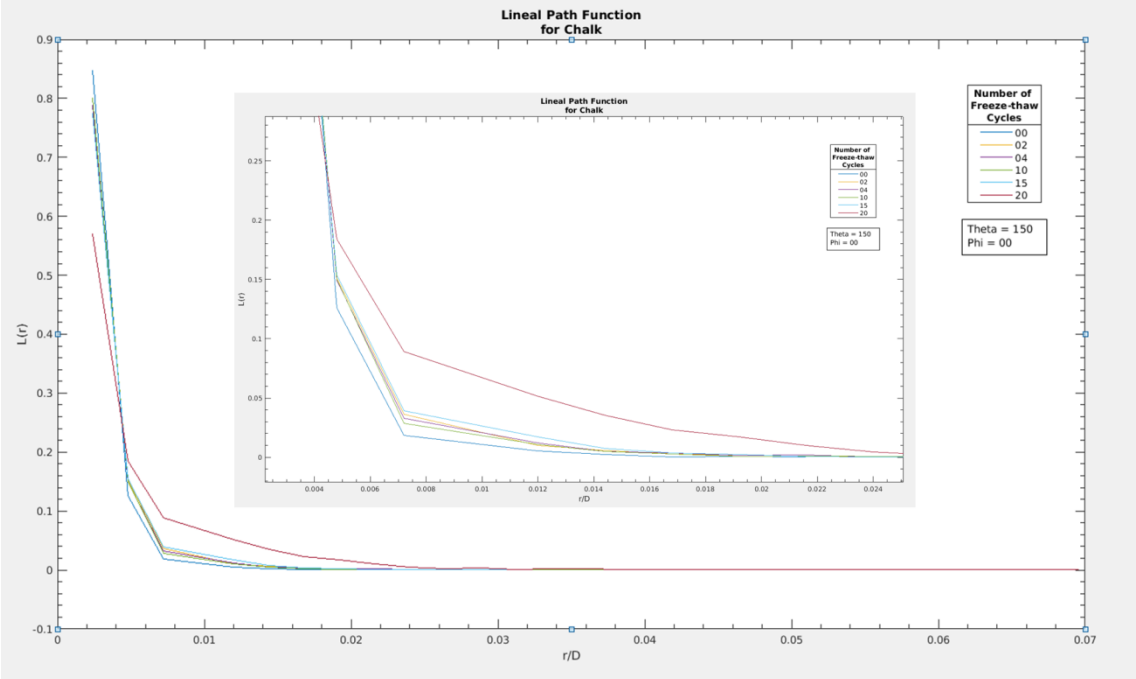
Lineal Path Function
for Chalk
L(r)
r/D
Number of
Freeze-thaw
Cycles
00
02
04
10
15
20
Theta = 150
Phi = 00

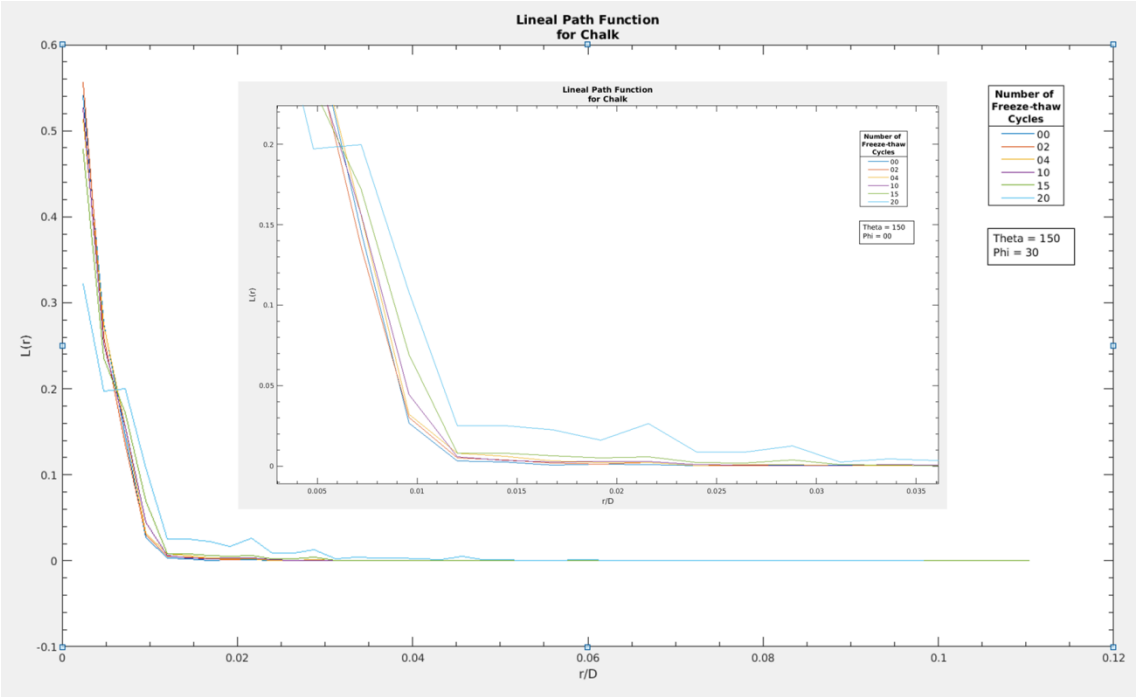
Lineal Path Function
for Chalk
L(r)
r/D
Number of
Freeze-thaw
Cycles
00
02
04
10
15
20
Theta = 150
Phi = 30

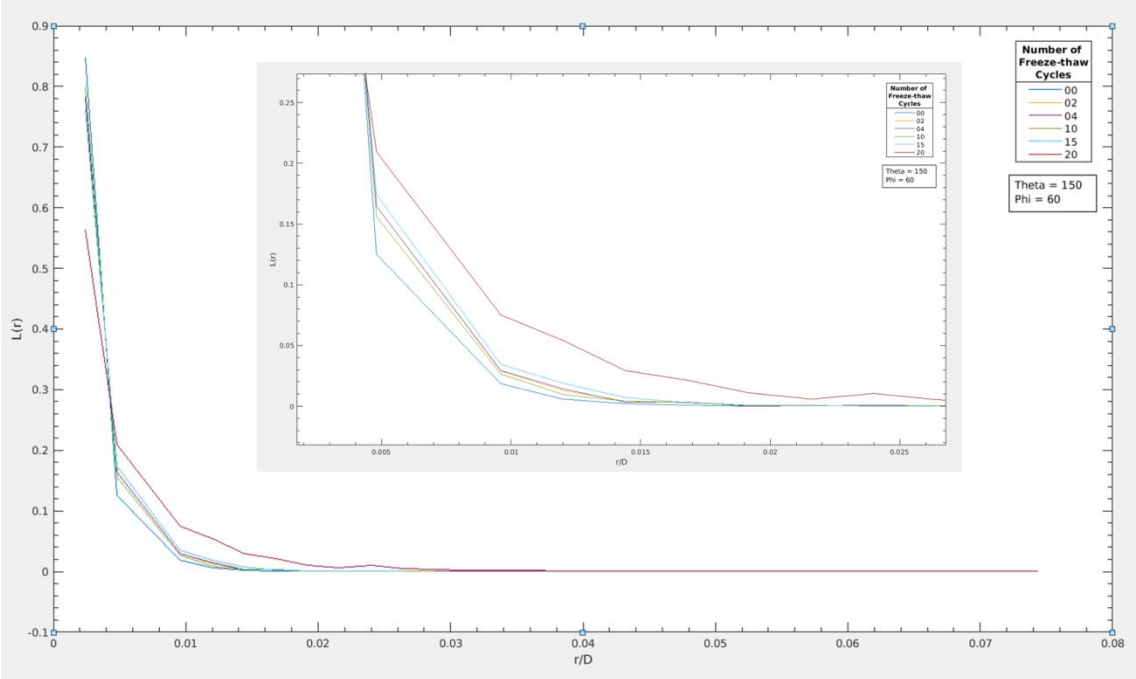
L(r)
r/D
Number of
Freeze-thaw
Cycles
00
02
04
10
15
20
Theta = 150
Phi = 60

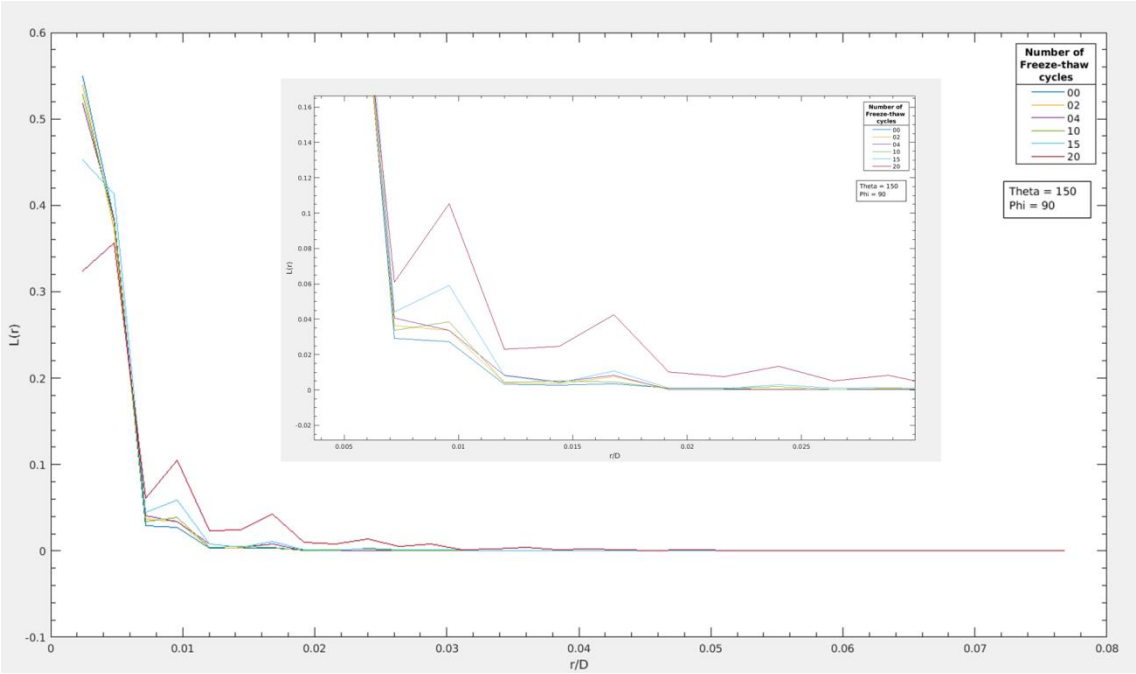
Number of Freeze-thaw cycles
00
02
04
10
15
20
Theta = 150
Phi = 90
L(r)
r/D

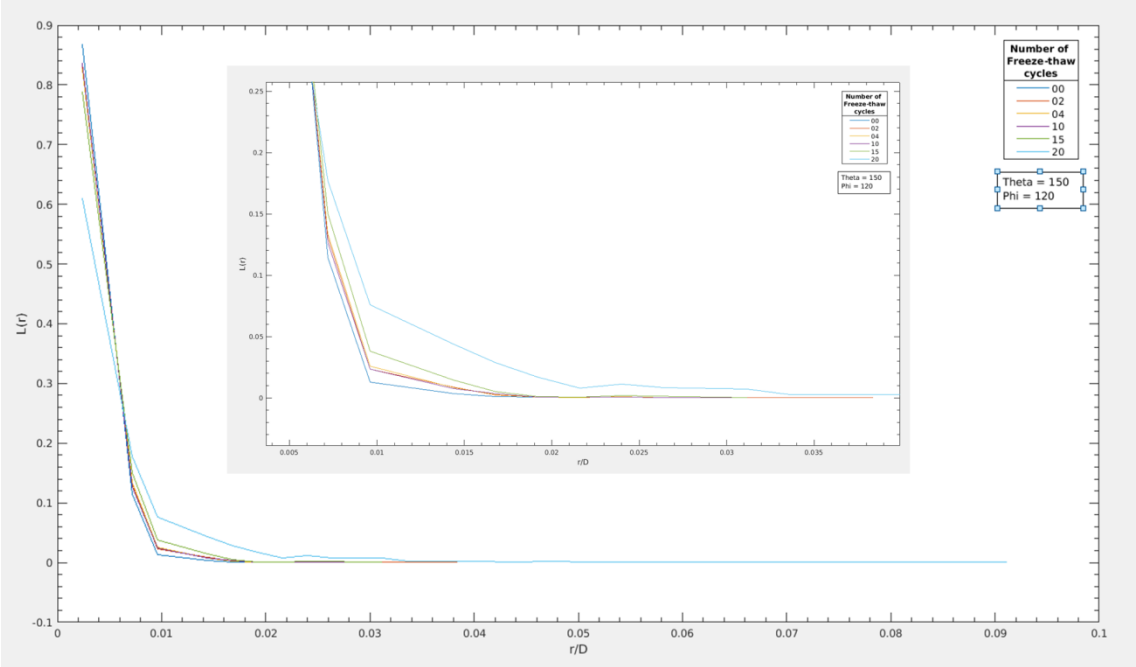
Number of Freeze-thaw cycles
00
02
04
10
15
20
Theta = 150
Phi = 120
L(r)
r/D

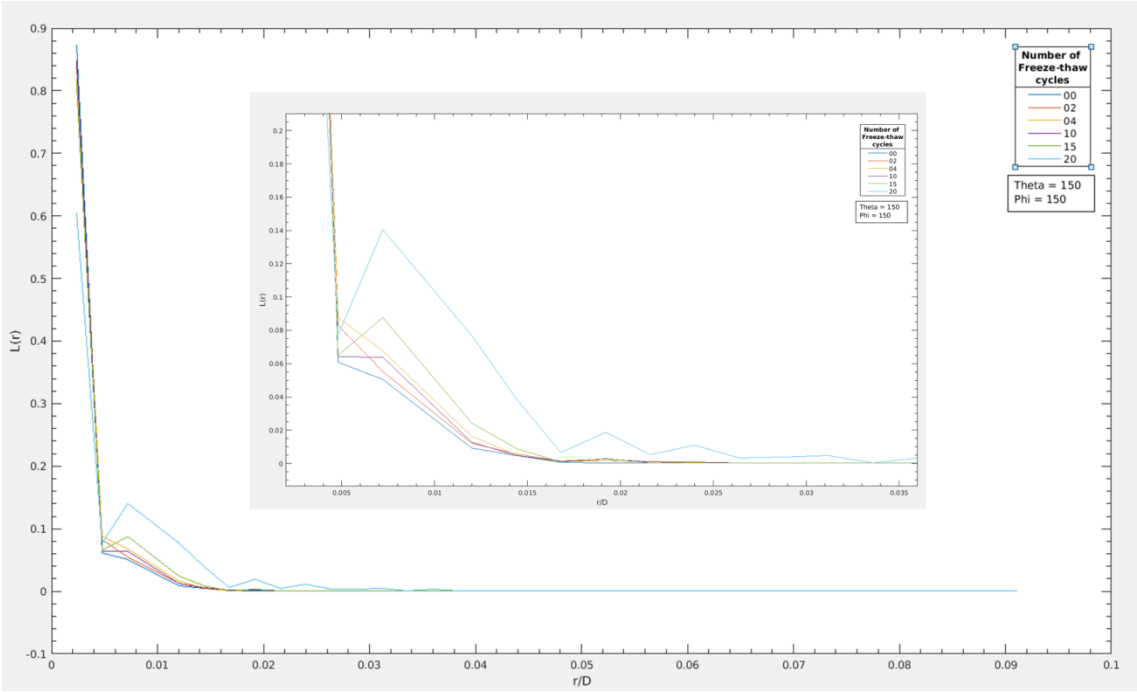
Number of Freeze-thaw cycles
00
02
04
10
15
20
Theta = 150
Phi = 150
L(r)
r/D

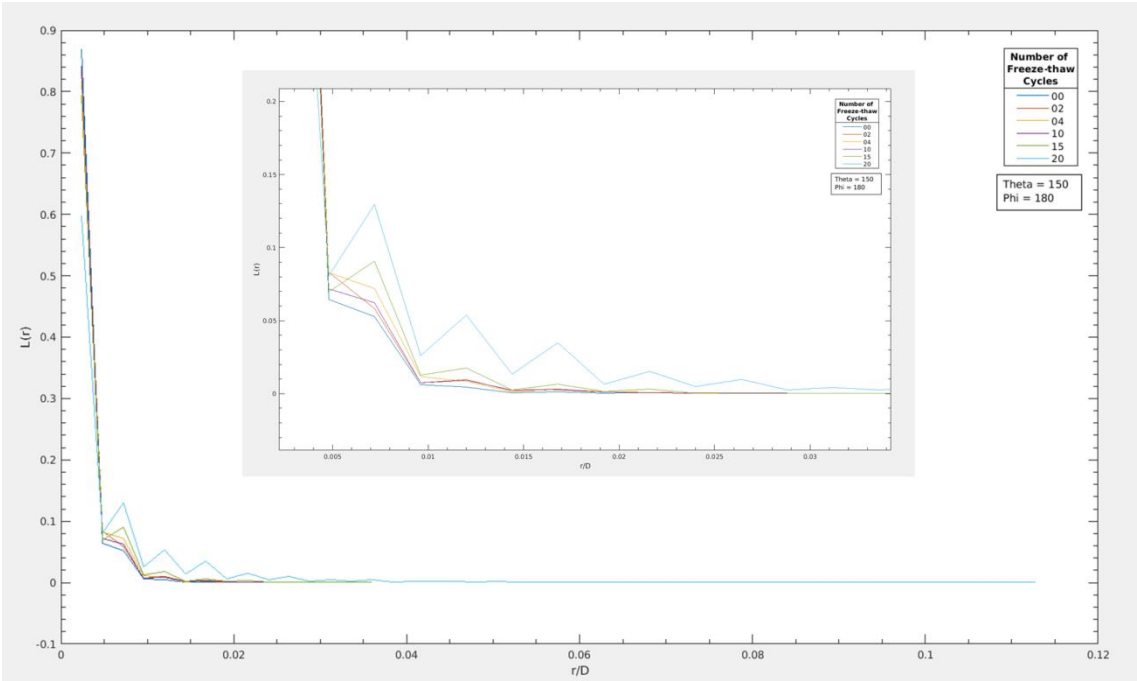
Number of Freeze-thaw Cycles
00
02
04
10
15
20
Theta = 150
Phi = 180
L(r)
r/D

B. Linear path function (Ardingly Sandstone)

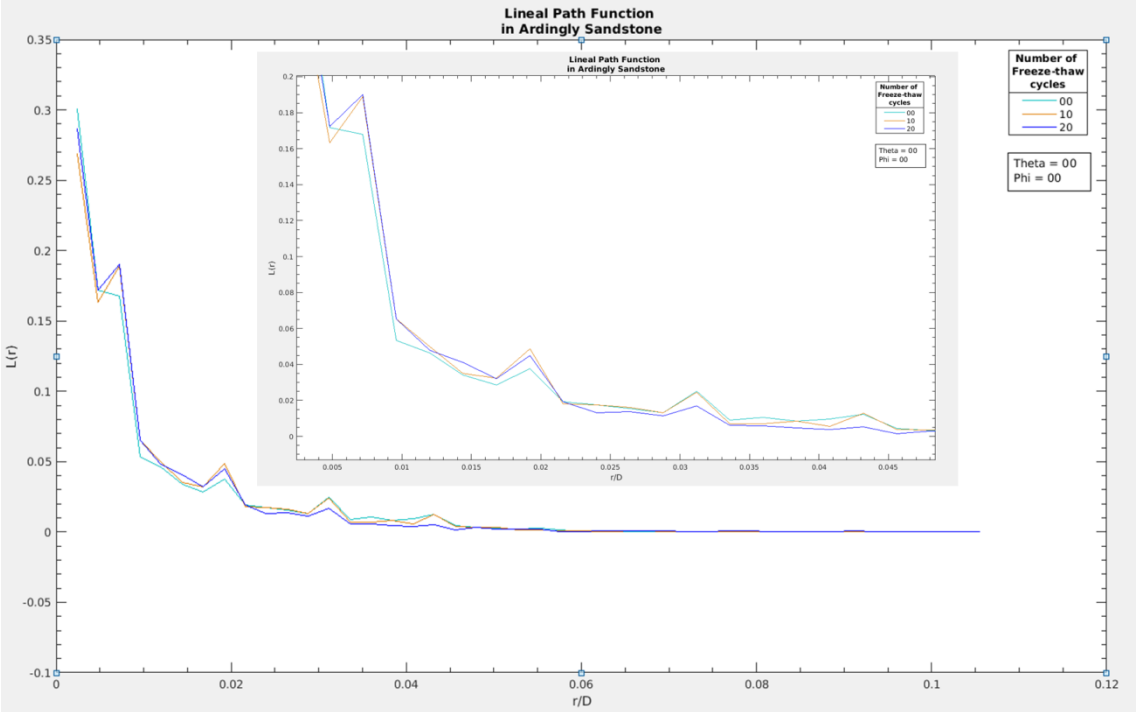

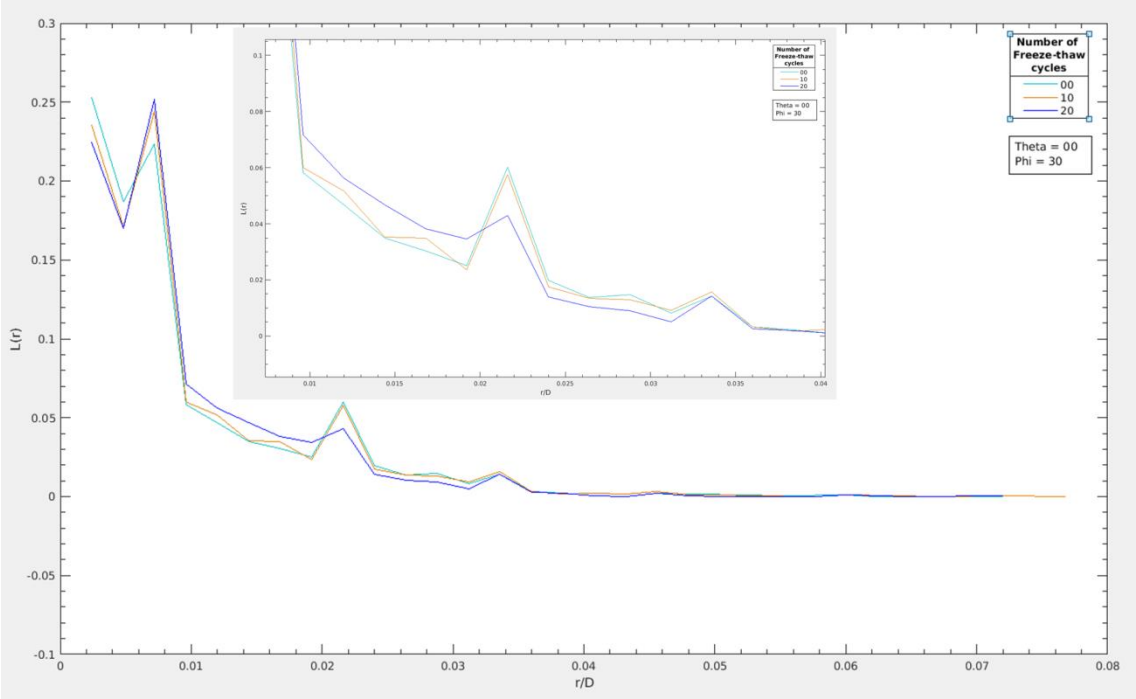

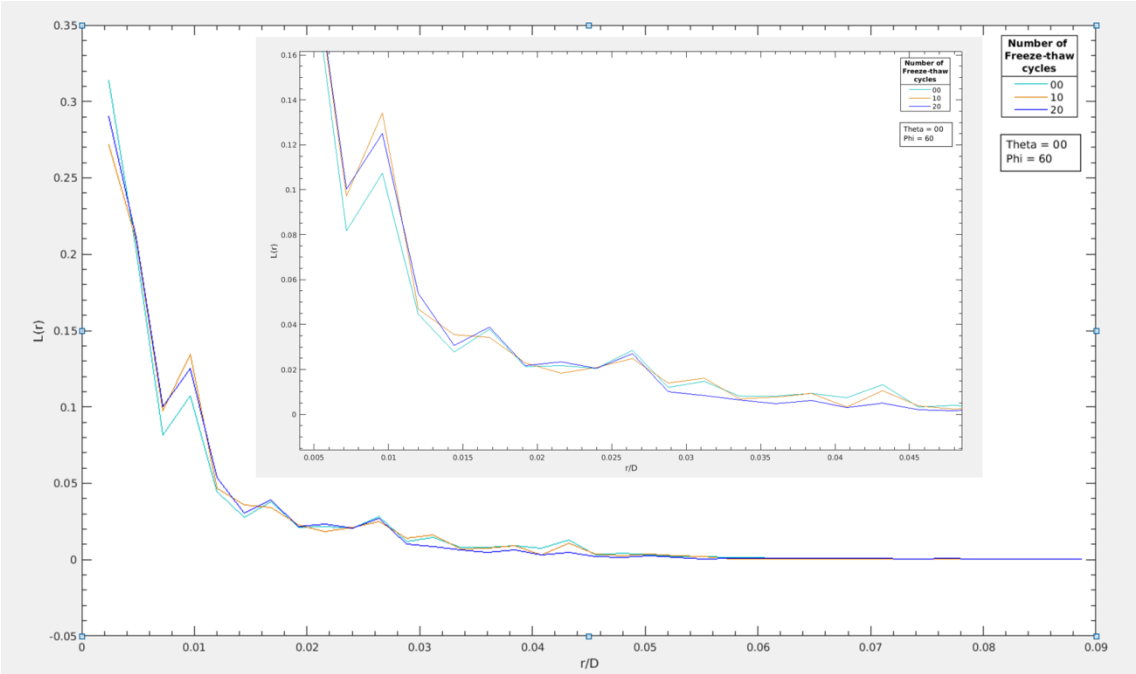
Number of Freeze-thaw cycles
00
10
20
Theta = 00
Phi = 60
L(r)
r/D

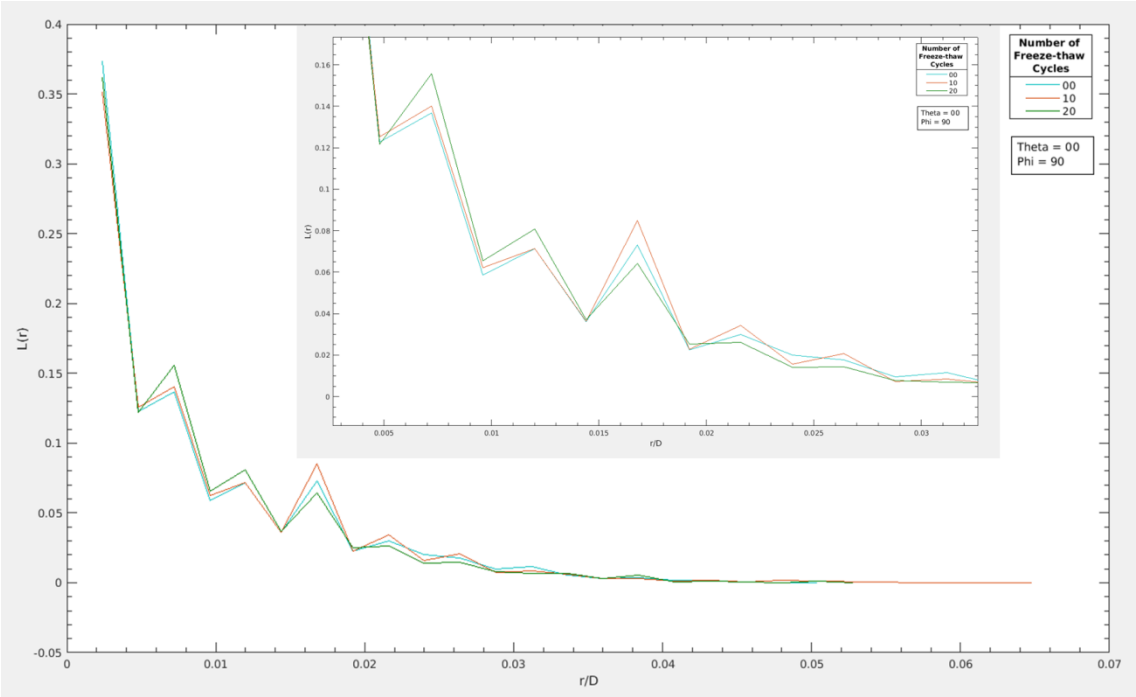
Number of Freeze-thaw Cycles
00
10
20
Theta = 00
Phi = 90
L(r)
r/D

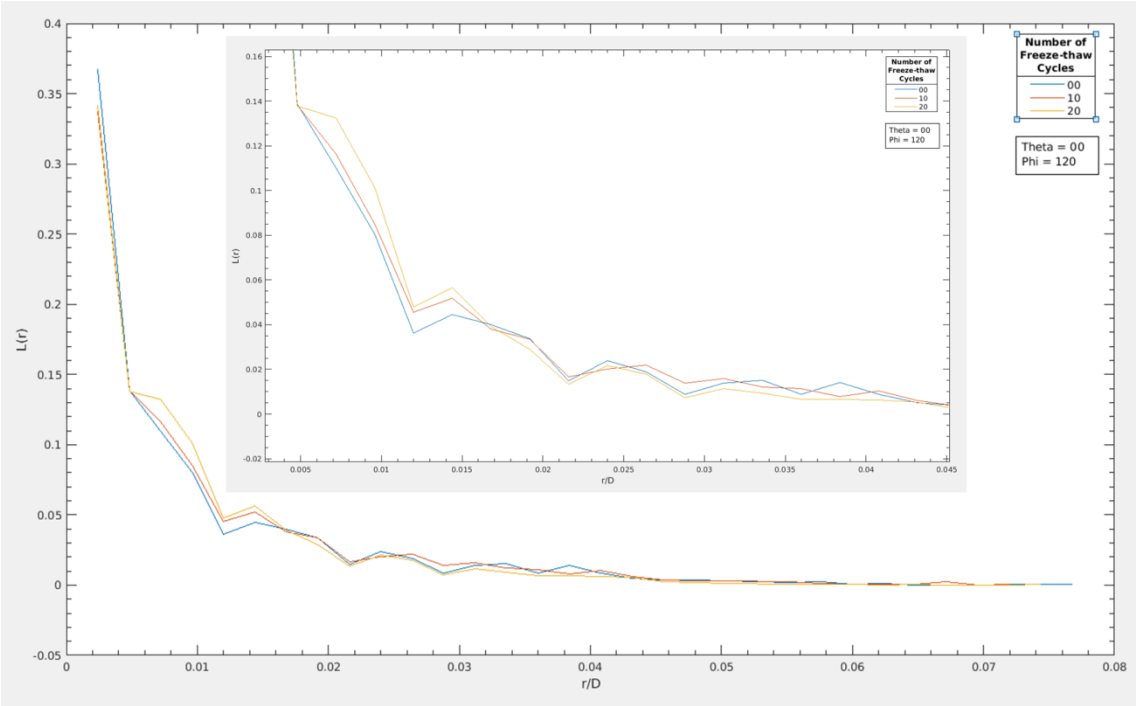
Number of Freeze-thaw Cycles
00
10
20
Theta = 00
Phi = 120
L(r)
r/D

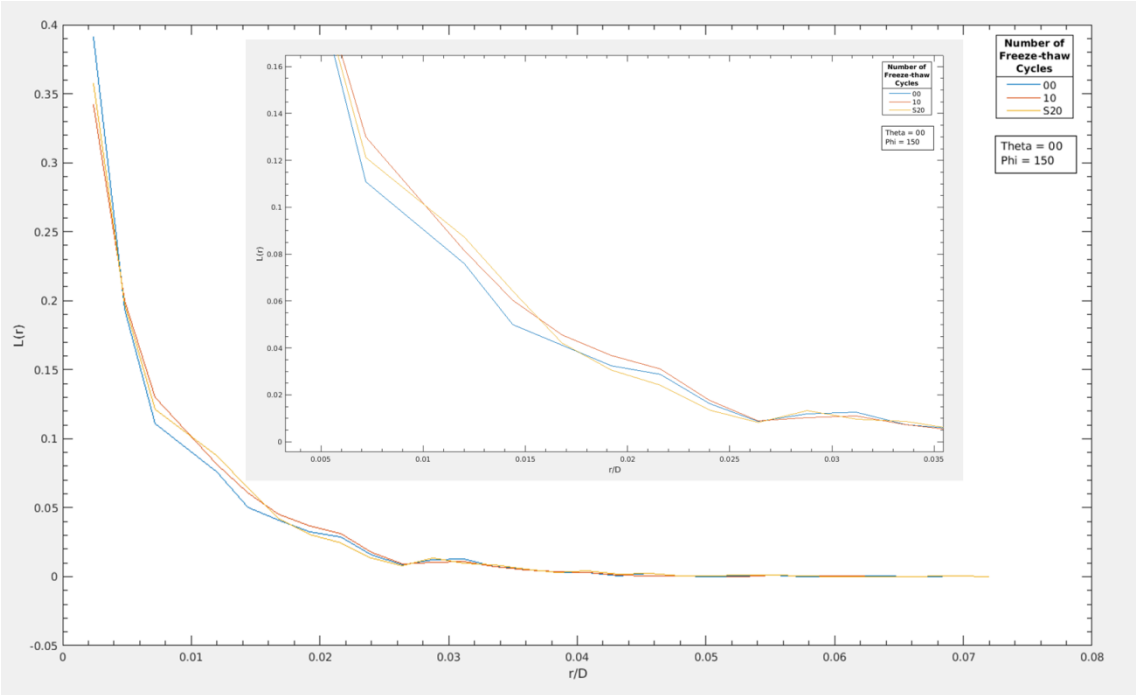
Number of Freeze-thaw Cycles
00
10
520
Theta = 00
Phi = 150
L(r)
r/D

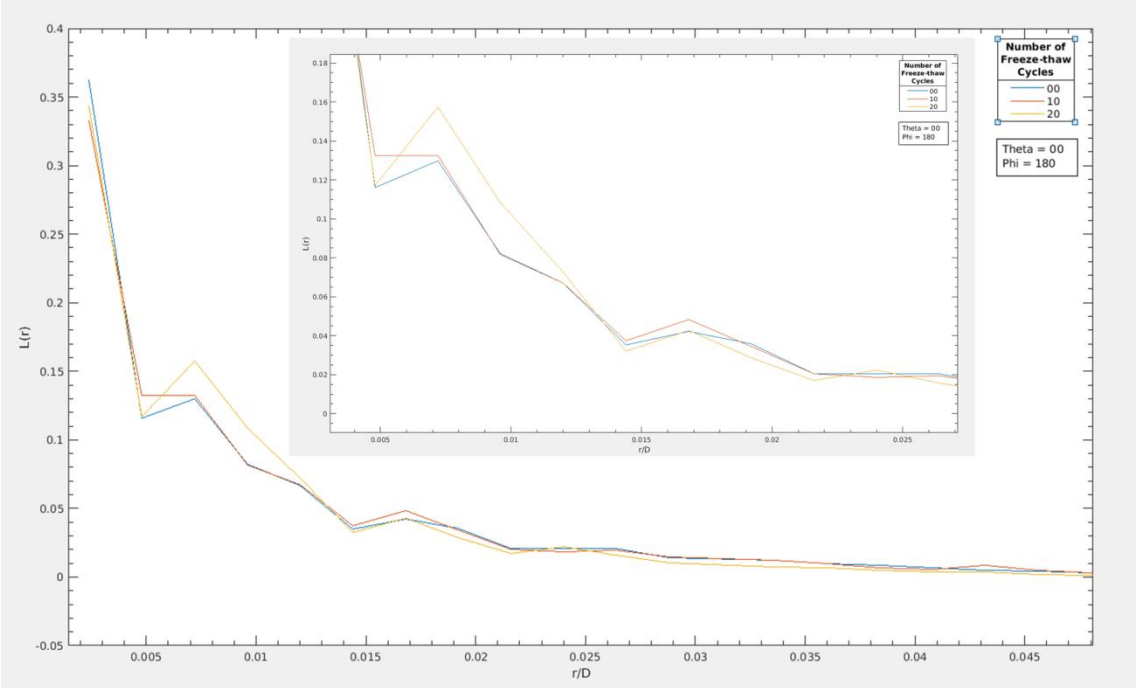
Number of Freeze-thaw Cycles
00
10
20
Theta = 00
Phi = 180
L(r)
r/D

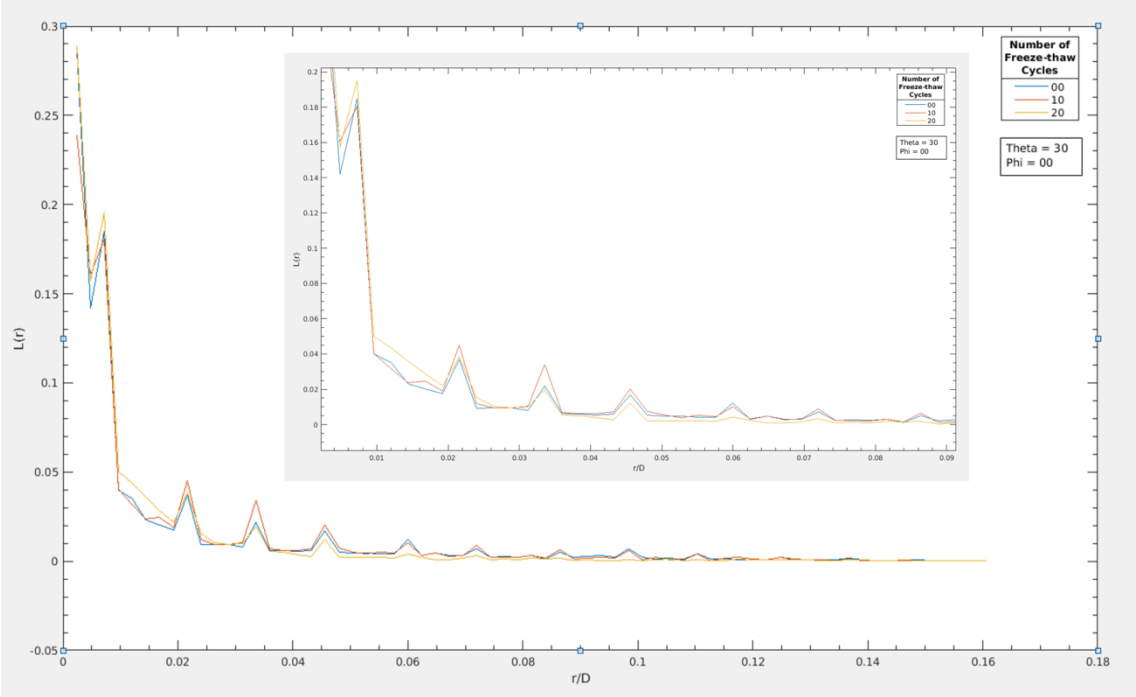
Number of Freeze-thaw Cycles
00
10
20
Theta = 30
Phi = 00
L(r)
r/D

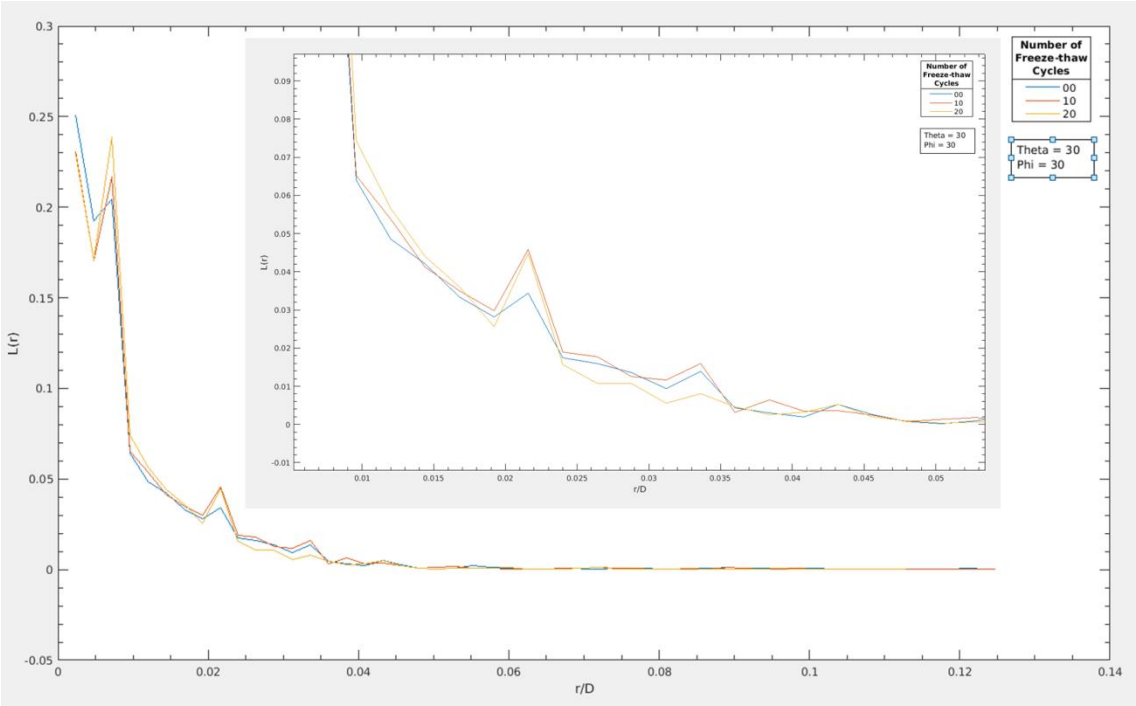
Number of Freeze-thaw Cycles
00
10
20
Theta = 30
Phi = 30
L(r)
r/D

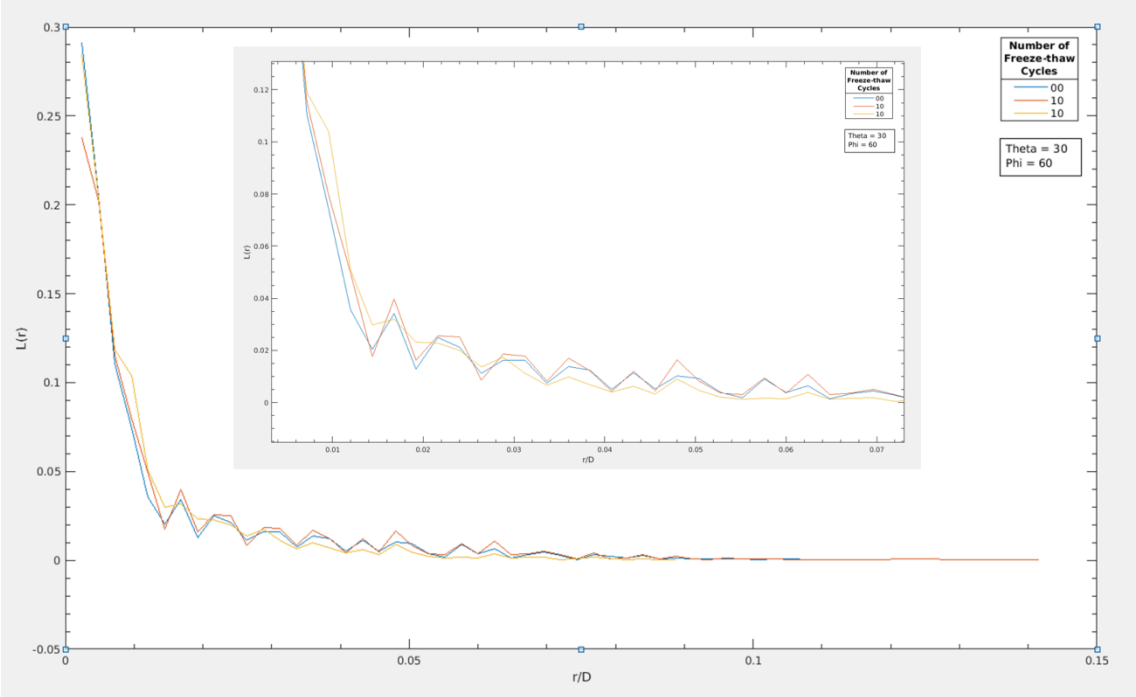
Number of Freeze-thaw Cycles
00
10
10
Theta = 30
Phi = 60
L(r)
r/D

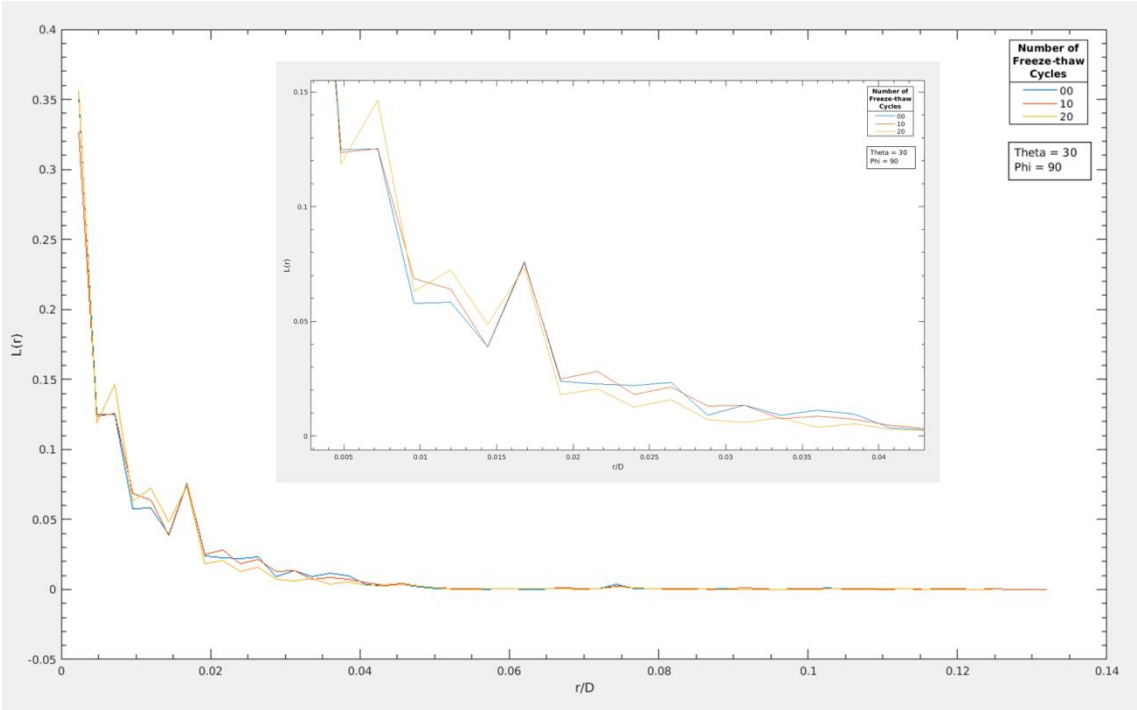
Number of Freeze-thaw Cycles
00
10
20
Theta = 30
Phi = 90
L(r)
r/D

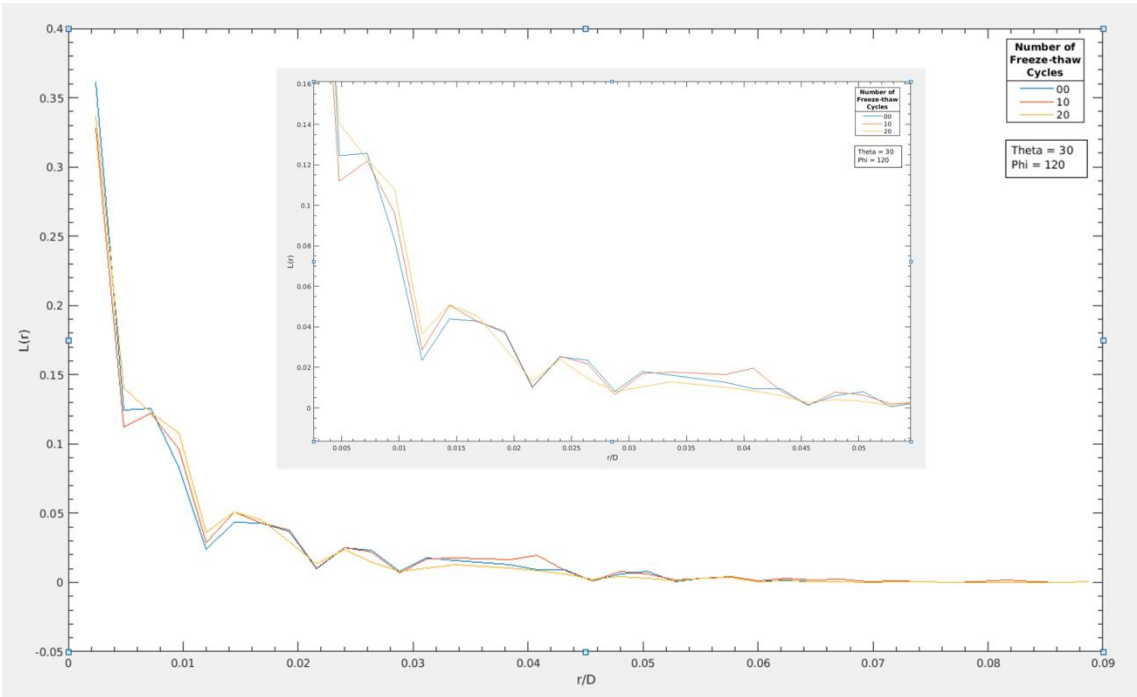
Number of Freeze-thaw Cycles
00
10
20
Theta = 30
Phi = 120
L(r)
r/D

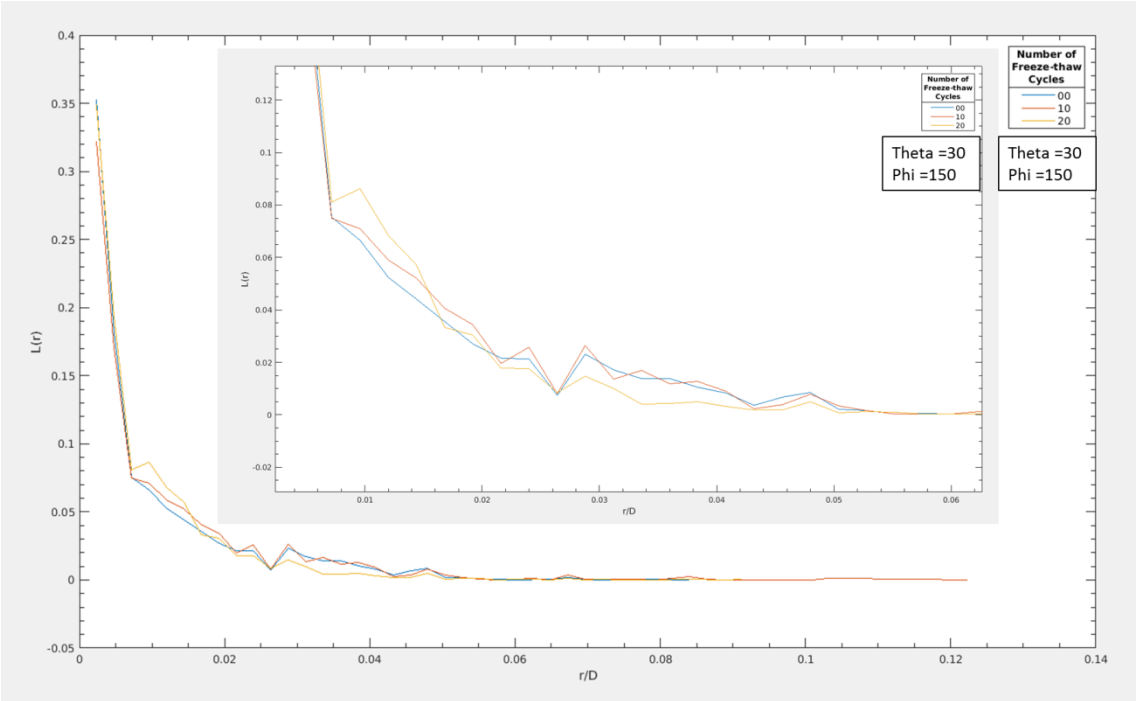
Number of Freeze-thaw Cycles
00
10
20
Theta =30
Phi =150
Theta =30
Phi =150
L(r)
r/D

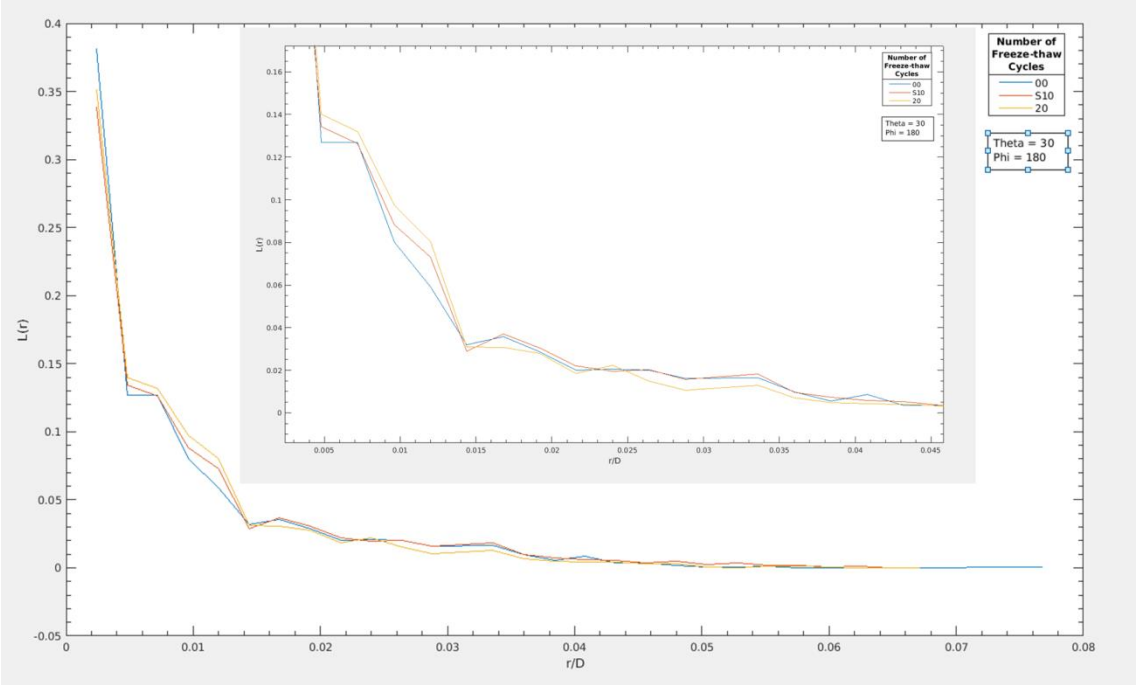
Number of Freeze-thaw Cycles
00
510
20
Theta = 30
Phi = 180
Theta = 30
Phi = 180
L(r)
r/D

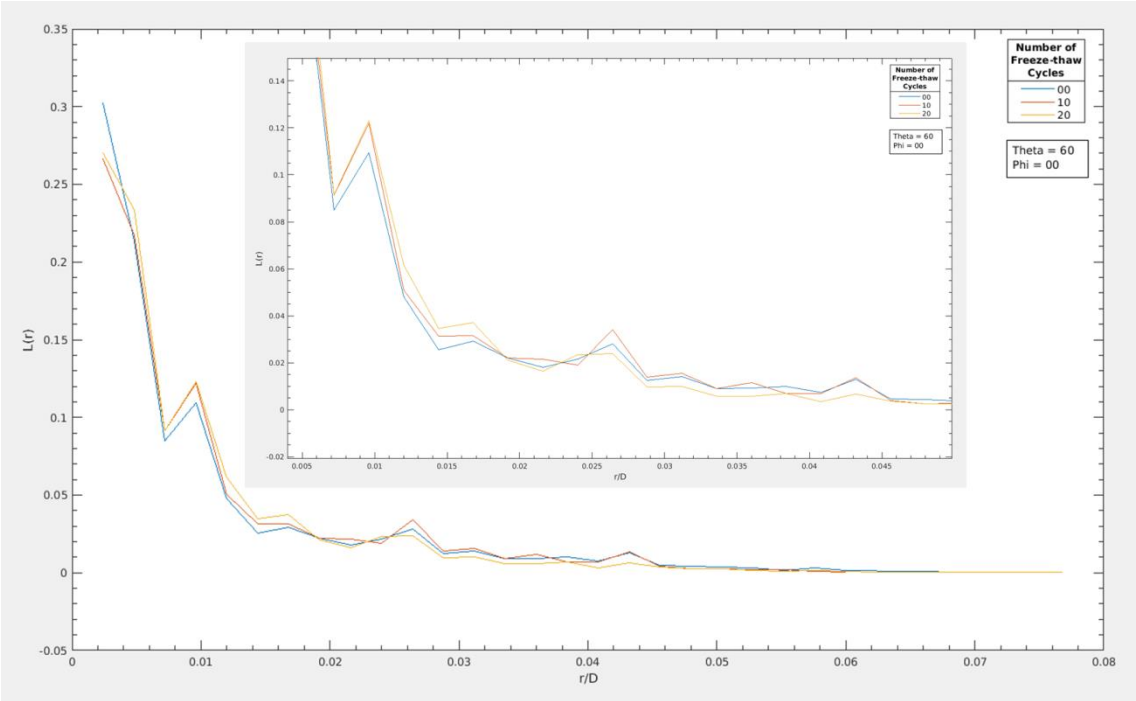
Number of Freeze-thaw Cycles
00
10
20
Theta = 60
Phi = 00
L(r)
r/D

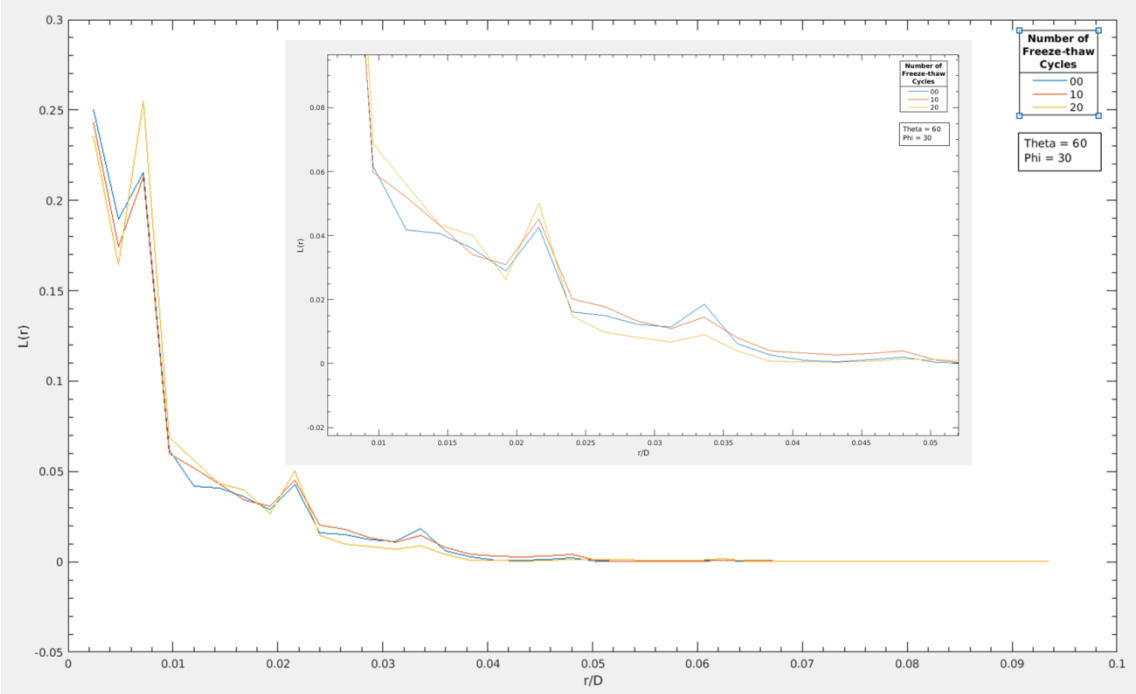
Number of Freeze-thaw Cycles
00
10
20
Theta = 60
Phi = 30
L(r)
r/D

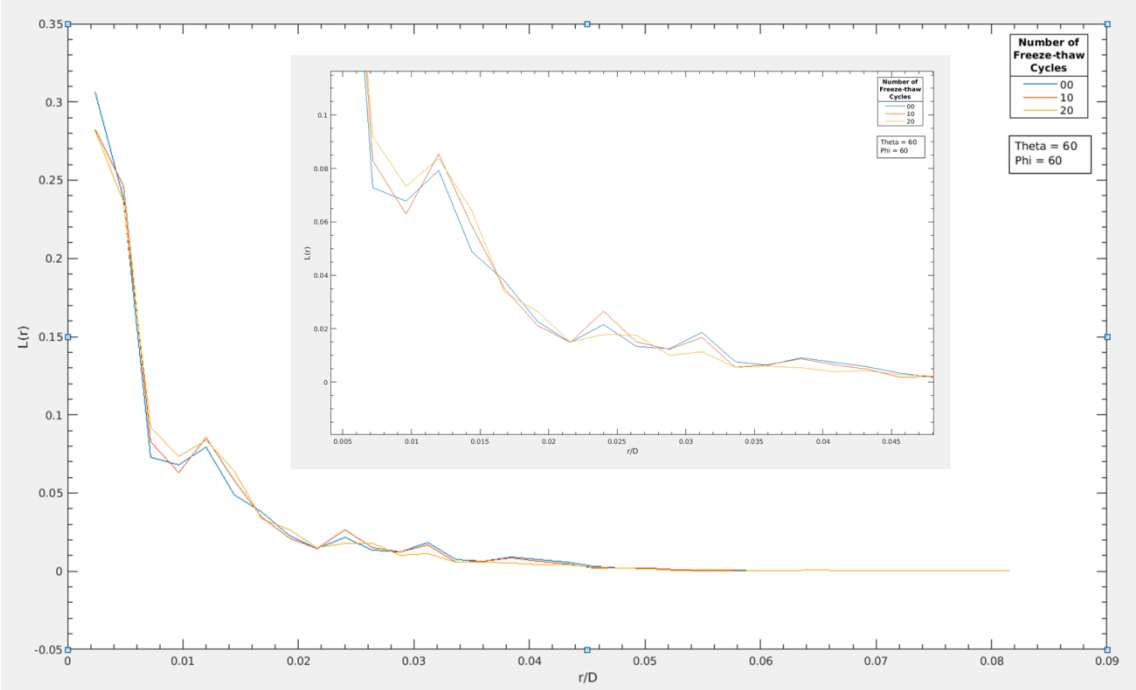
Number of Freeze-thaw Cycles
00
10
20
Theta = 60
Phi = 60
L(r)
r/D

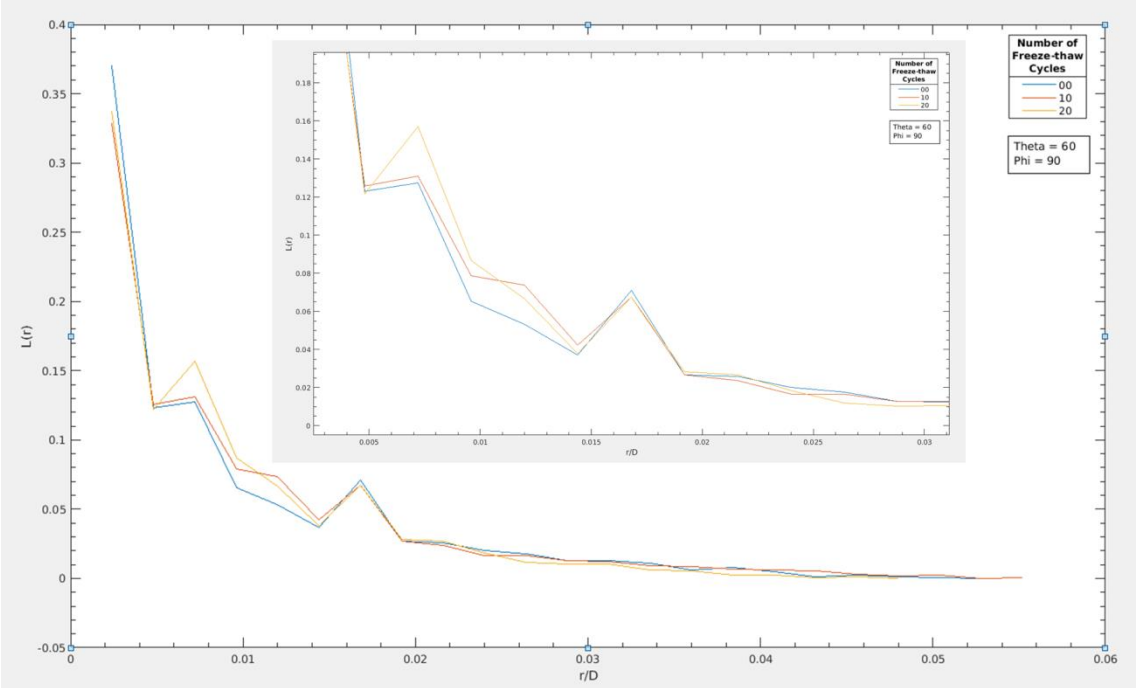
Number of Freeze-thaw Cycles
00
10
20
Theta = 60
Phi = 90
L(r)
r/D

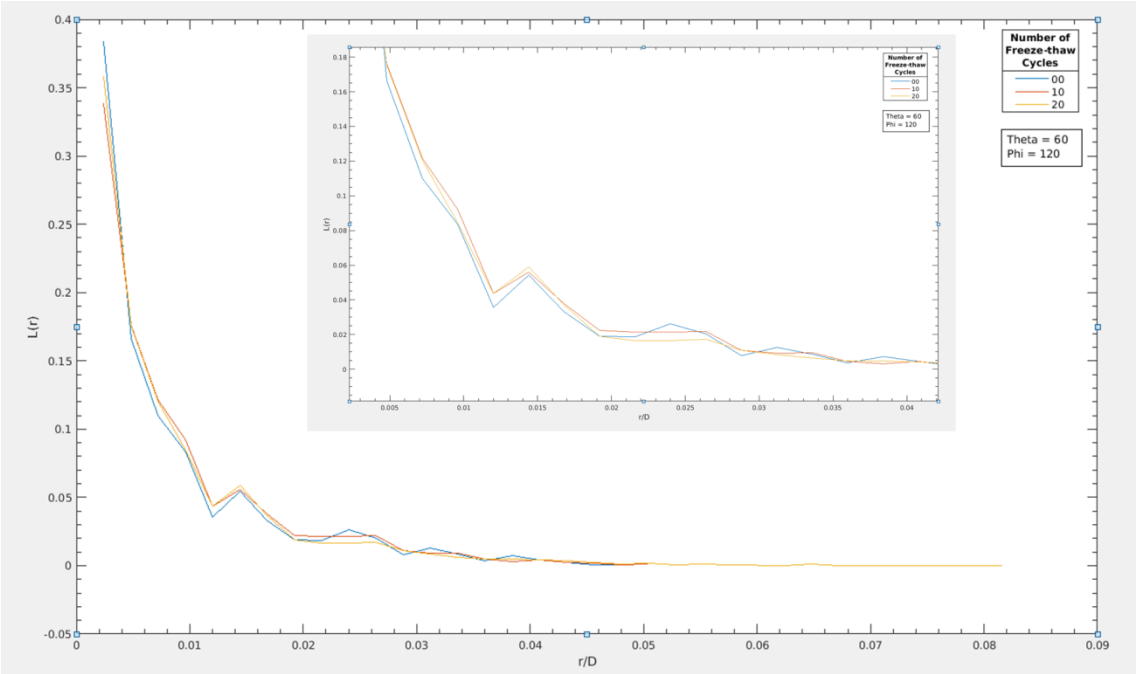
Number of Freeze-thaw Cycles
00
10
20
Theta = 60
Phi = 120
L(r)
r/D

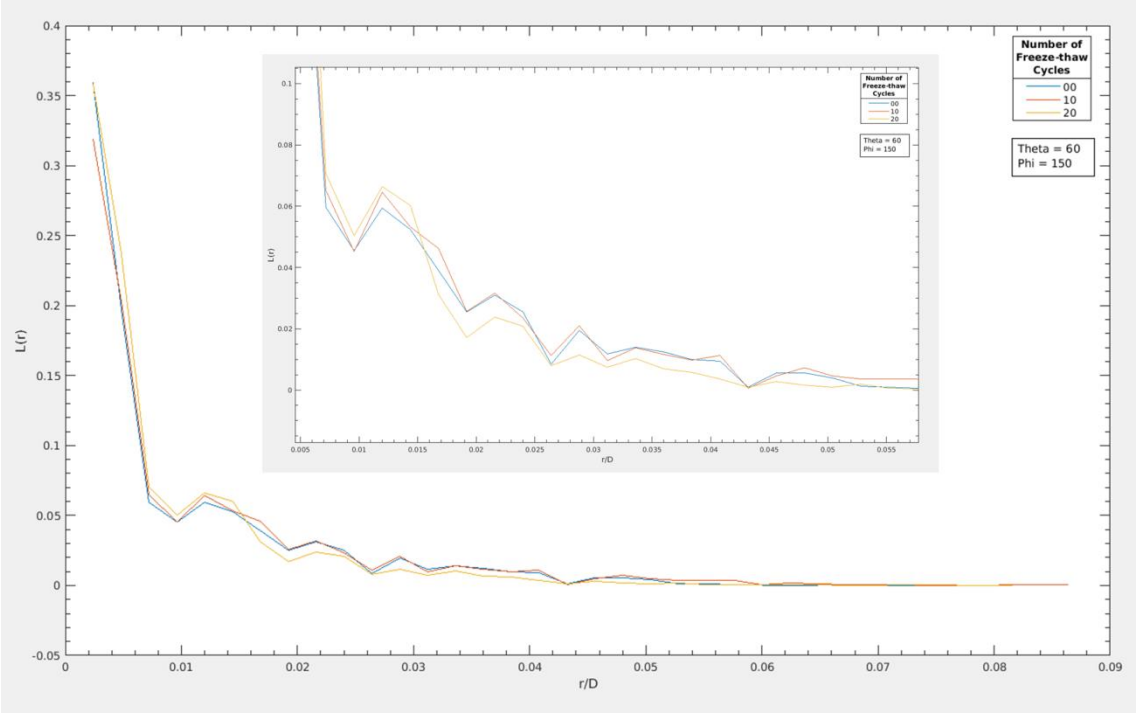
Number of Freeze-thaw Cycles
00
10
20
Theta = 60
Phi = 150
L(r)
r/D

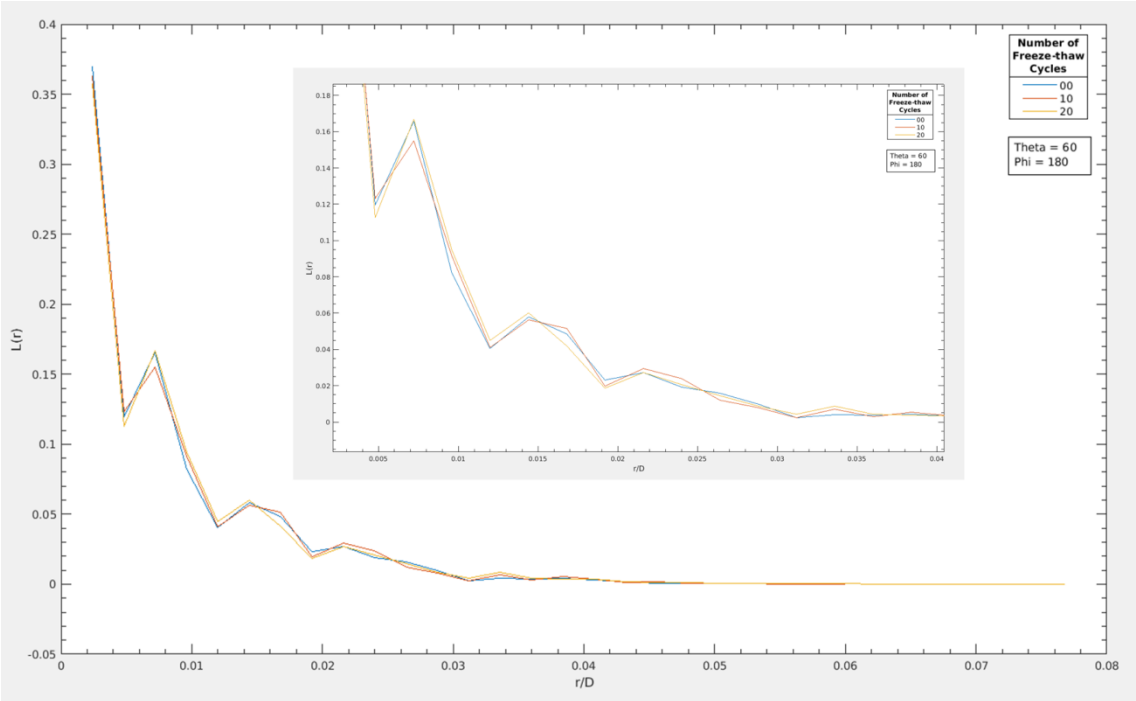
Number of Freeze-thaw Cycles
00
10
20
Theta = 60
Phi = 180
L(r)
r/D

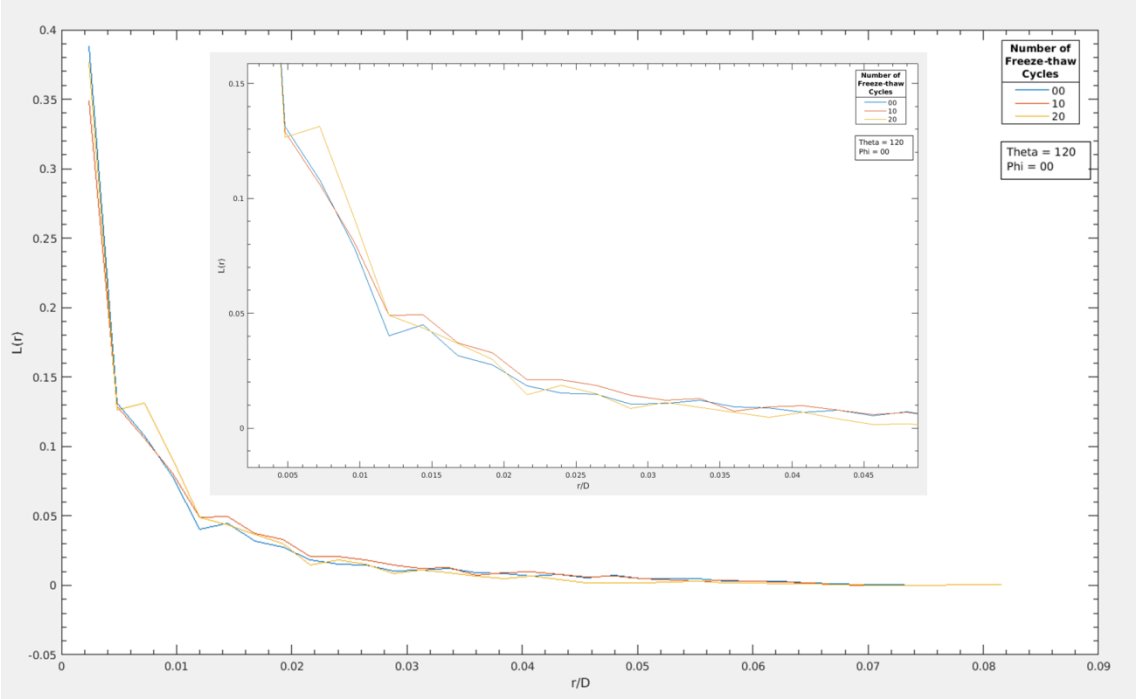
Number of Freeze-thaw Cycles
00
10
20
Theta = 120
Phi = 00
L(r)
r/D

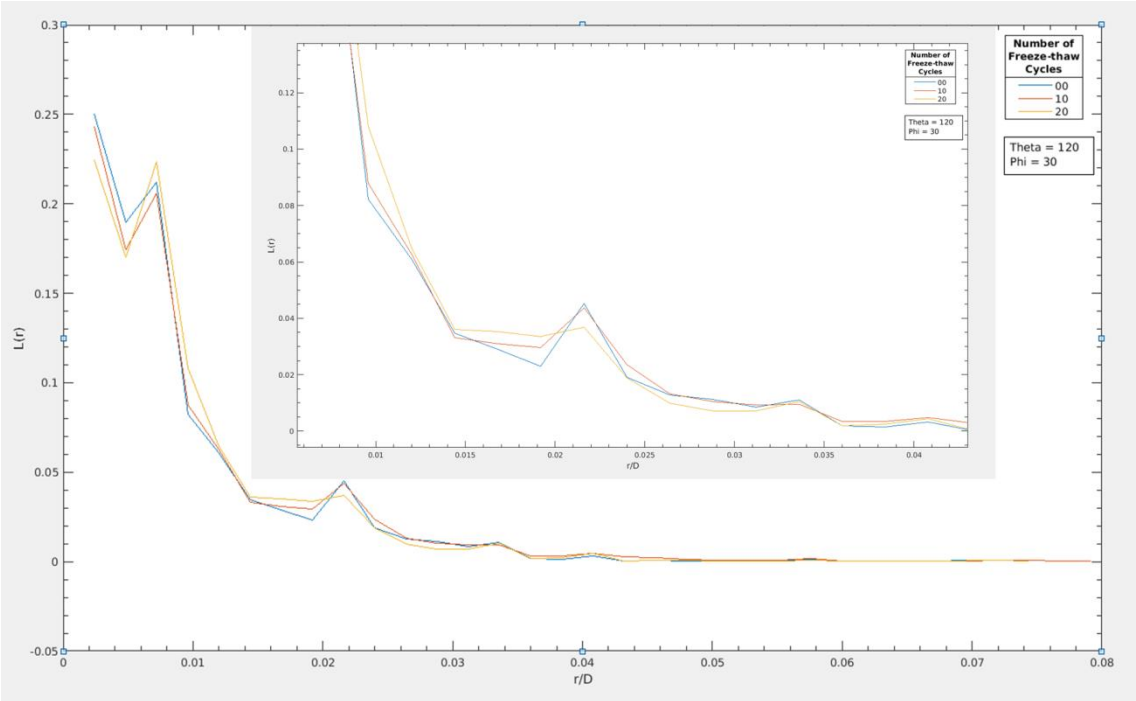
Number of Freeze-thaw Cycles
00
10
20
Theta = 120
Phi = 30
L(r)
r/D

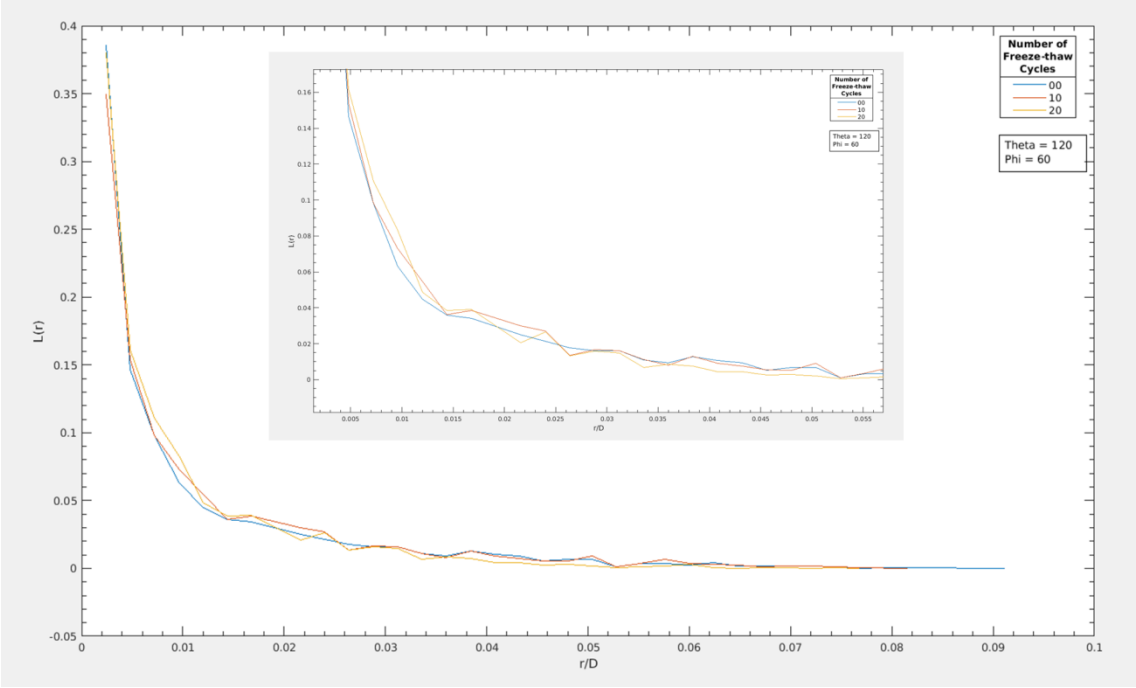
Number of Freeze-thaw Cycles
00
10
20
Theta = 120
Phi = 60
L(r)
r/D

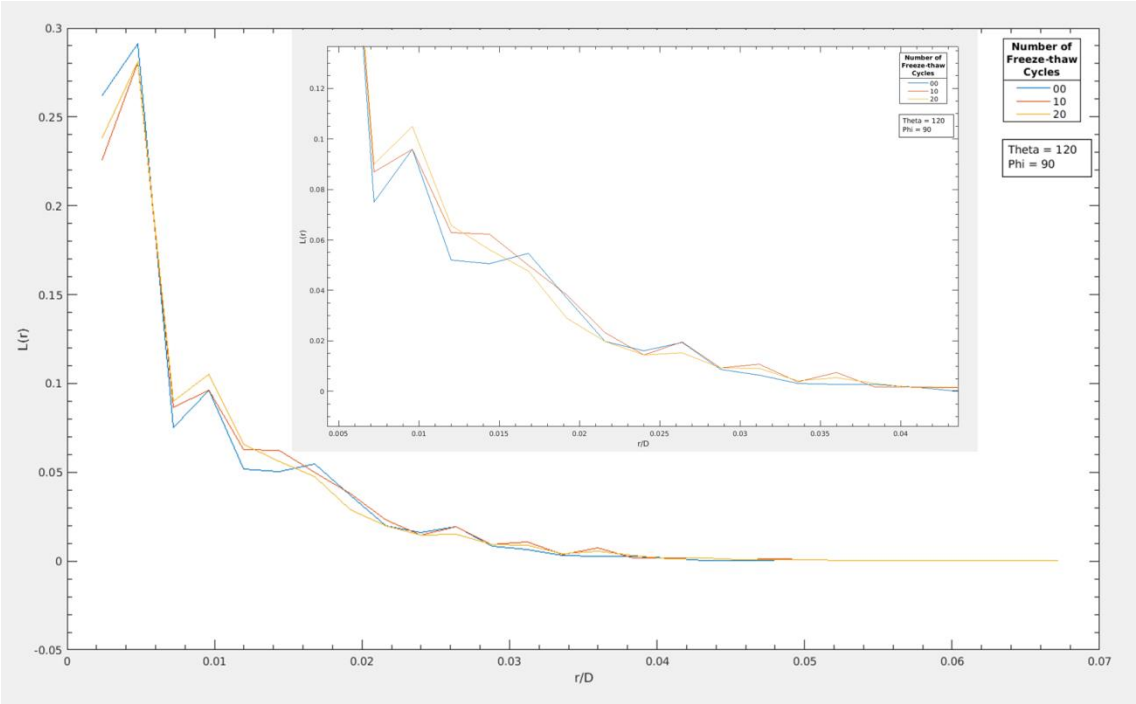
Number of Freeze-thaw Cycles
00
10
20
Theta = 120
Phi = 90
L(r)
r/D

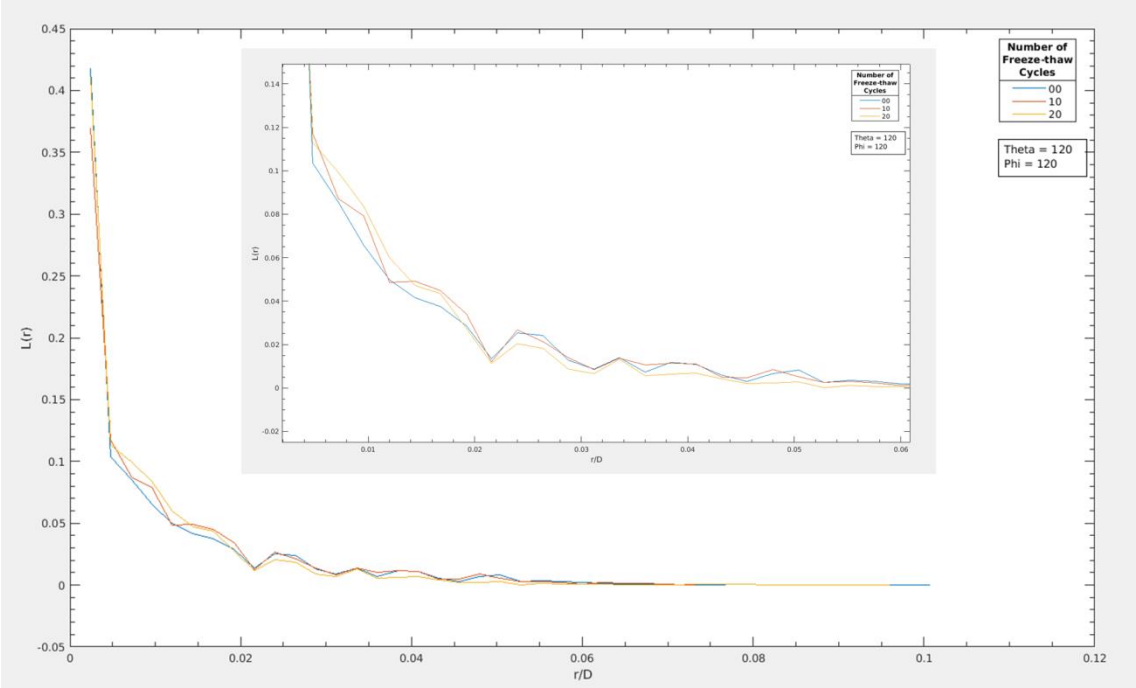
Number of Freeze-thaw Cycles
00
10
20
Theta = 120
Phi = 120
L(r)
r/D

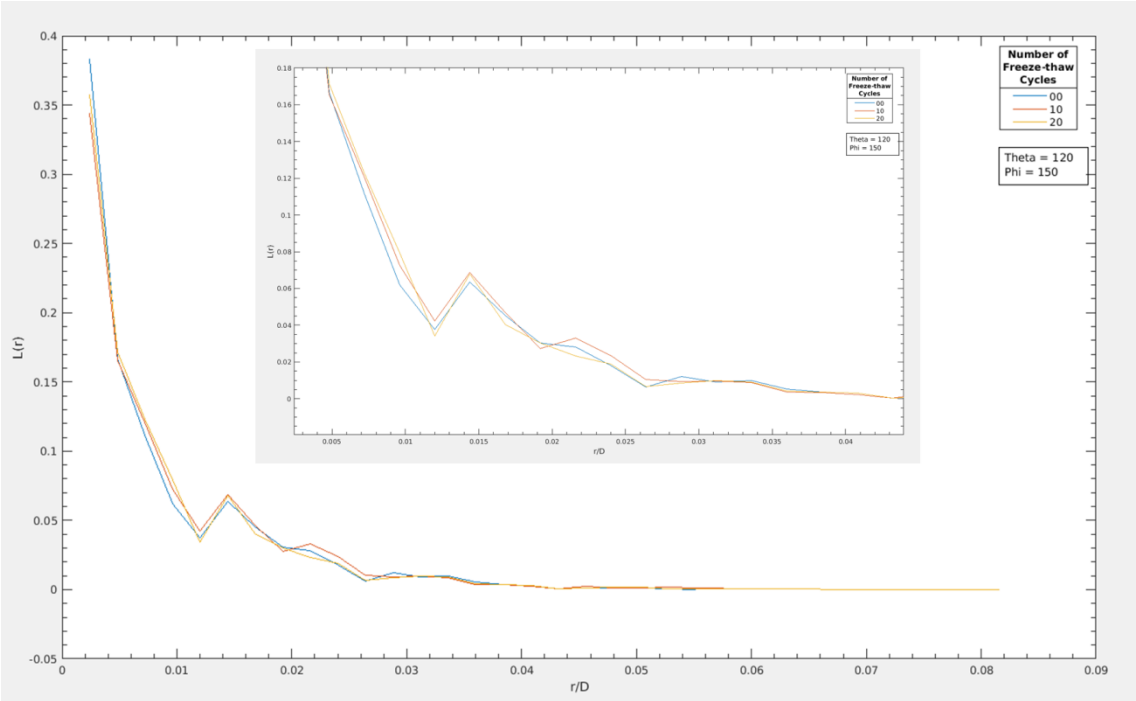
Number of Freeze-thaw Cycles
00
10
20
Theta = 120
Phi = 150
L(r)
r/D

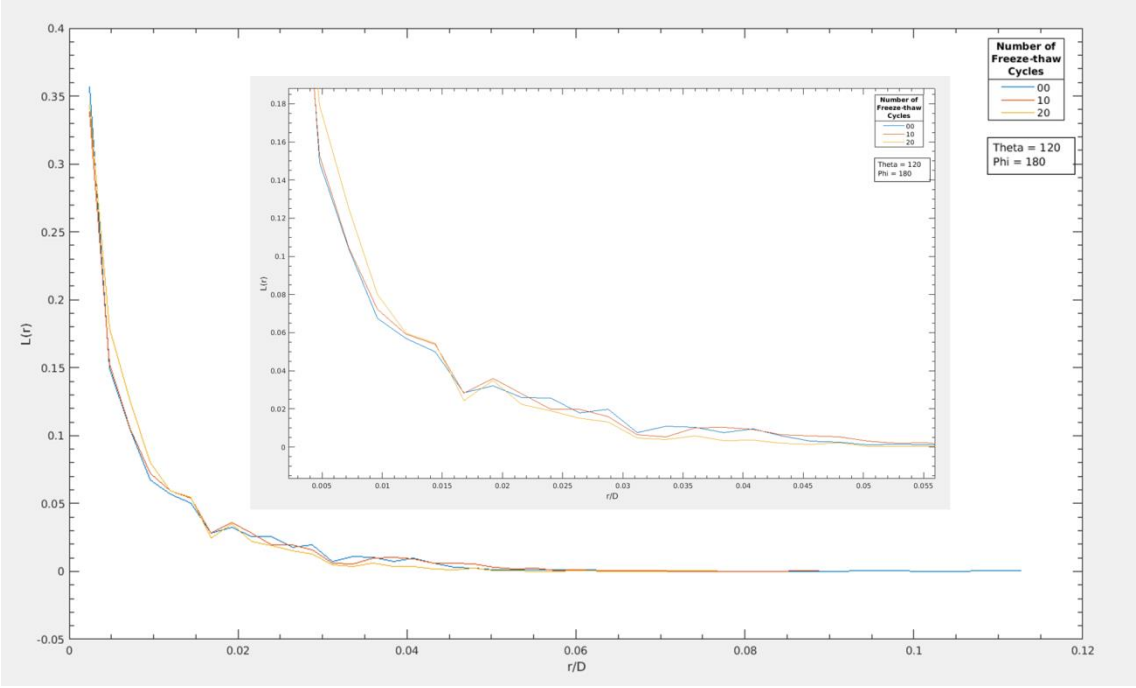
Number of Freeze-thaw Cycles
00
10
20
Theta = 120
Phi = 180
L(r)
r/D

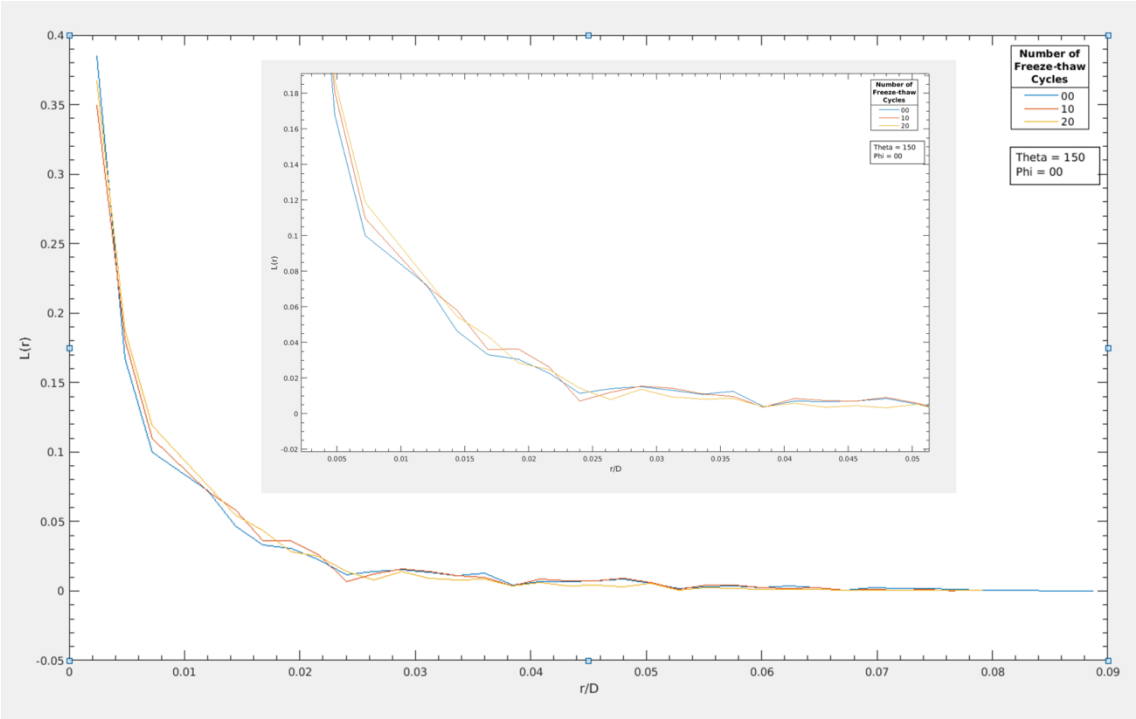
Number of Freeze-thaw Cycles
00
10
20
Theta = 150
Phi = 00
L(r)
r/D

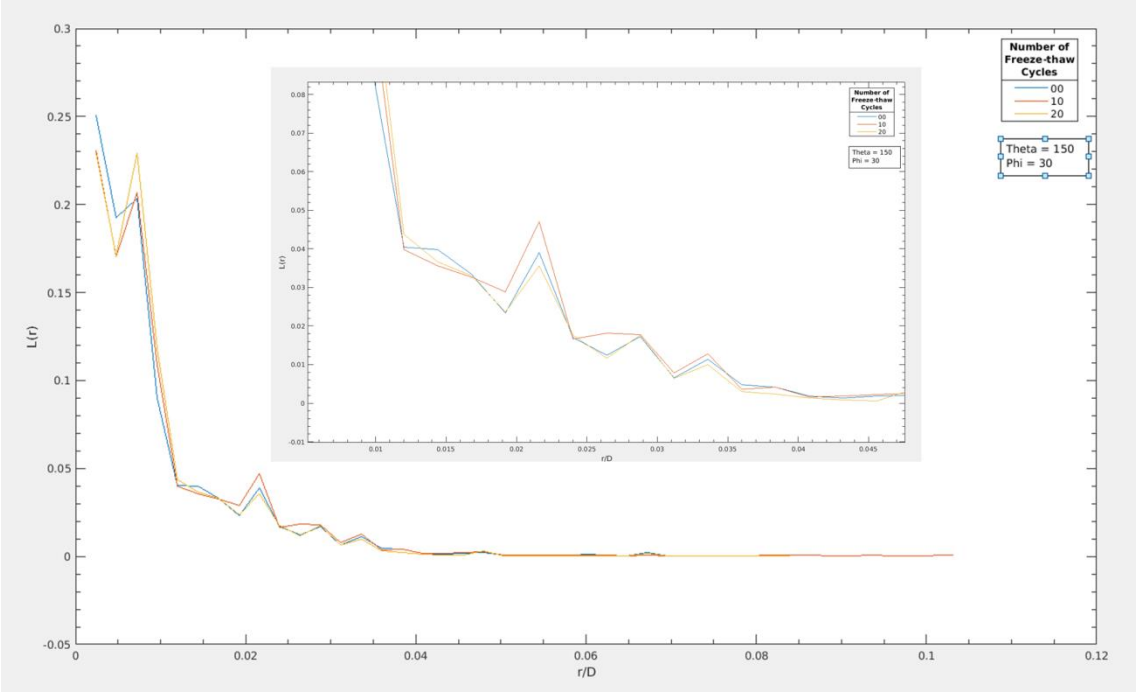
Number of Freeze-thaw Cycles
00
10
20
Theta = 150
Phi = 30
L(r)
r/D

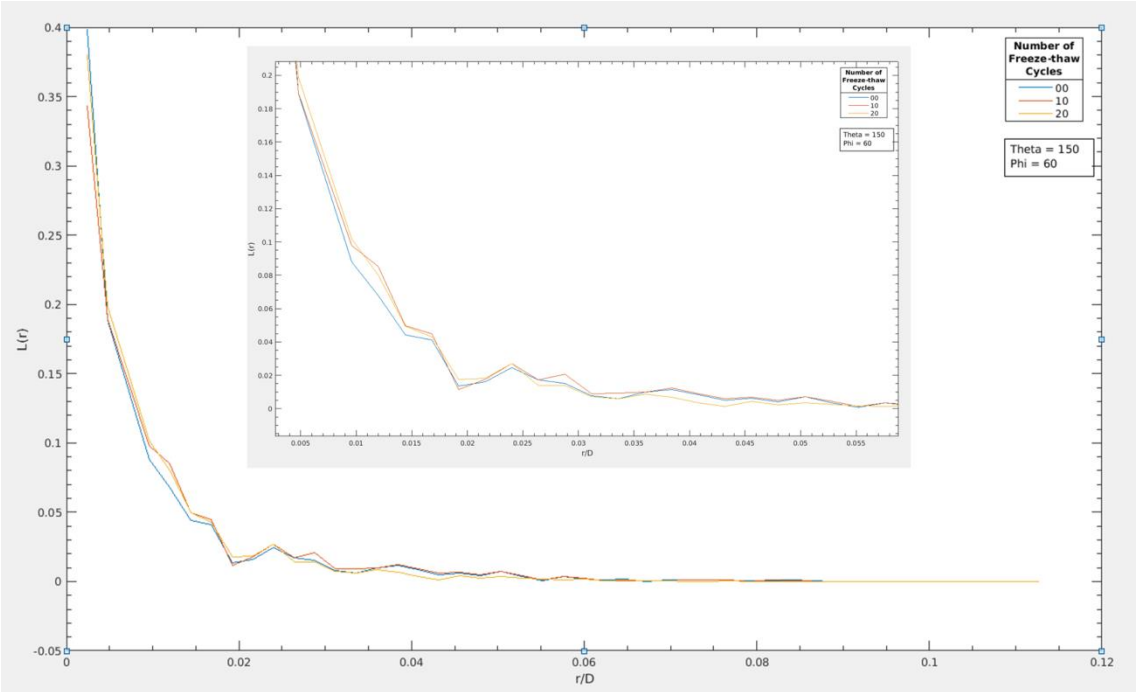
Number of Freeze-thaw Cycles
00
10
20
Theta = 150
Phi = 60
L(r)
r/D

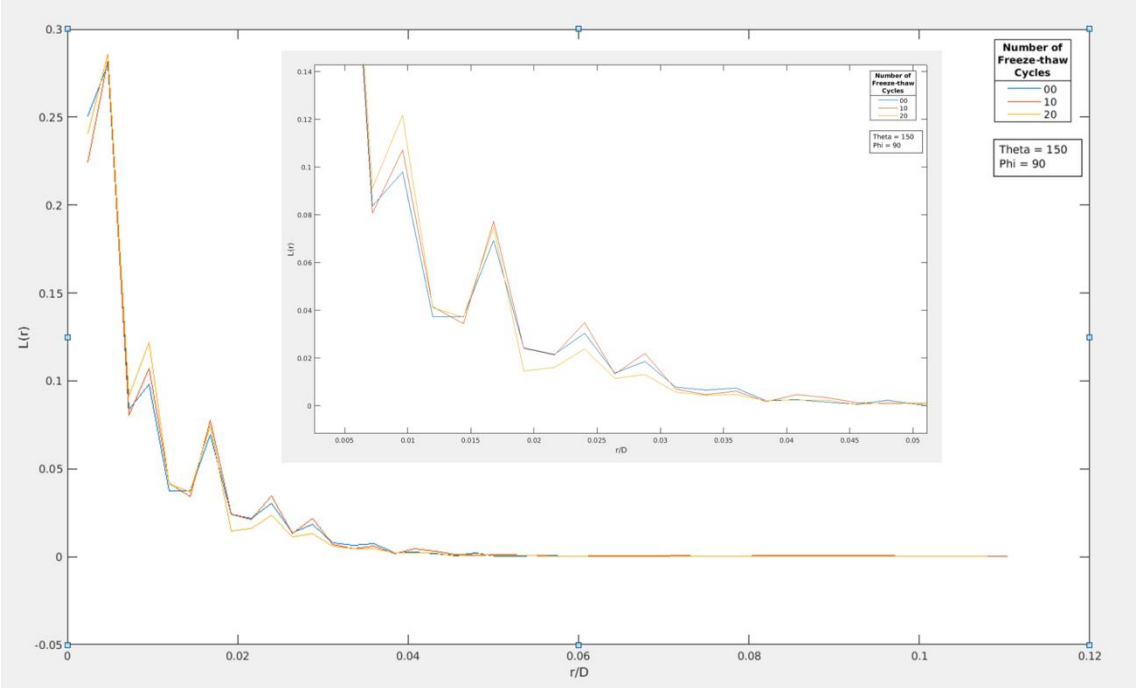
Number of Freeze-thaw Cycles
00
10
20
Theta = 150
Phi = 90
L(r)
r/D

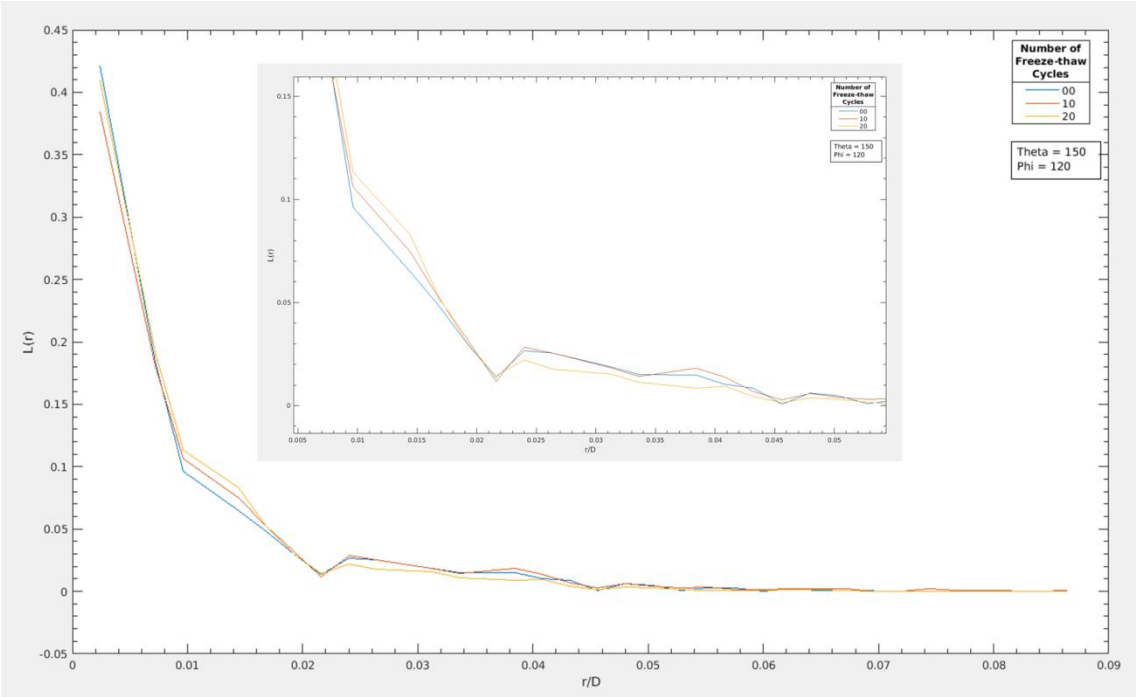
Number of Freeze-thaw Cycles
00
10
20
Theta = 150
Phi = 120
L(r)
r/D

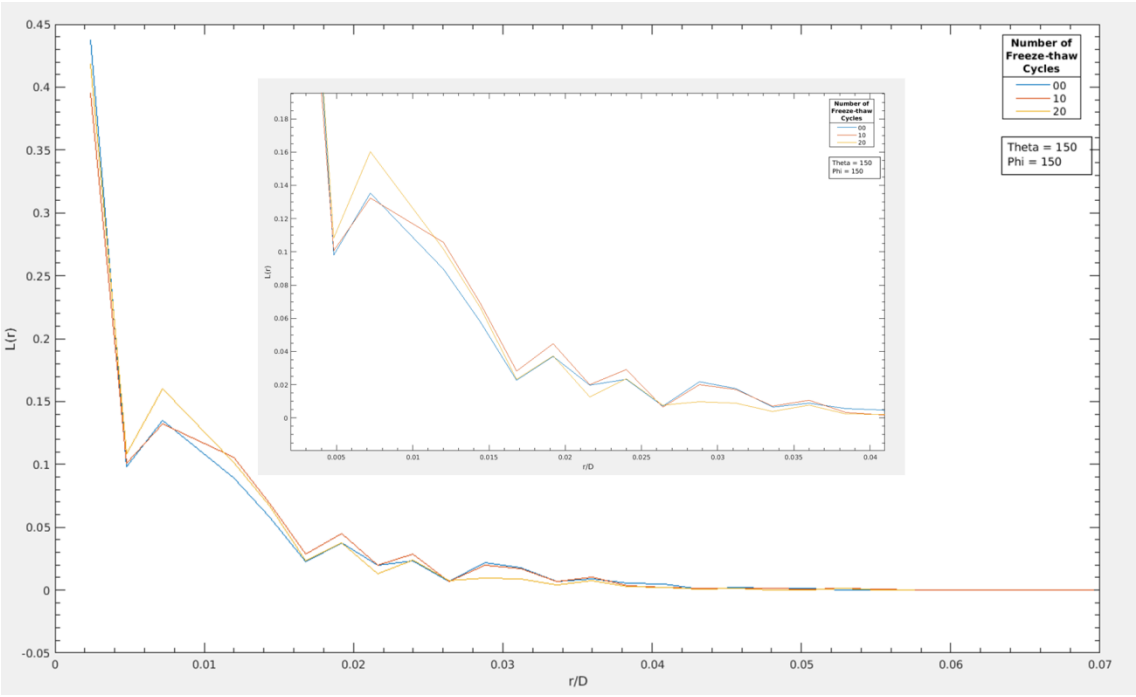
Number of Freeze-thaw Cycles
00
10
20
Theta = 150
Phi = 150
L(r)
r/D

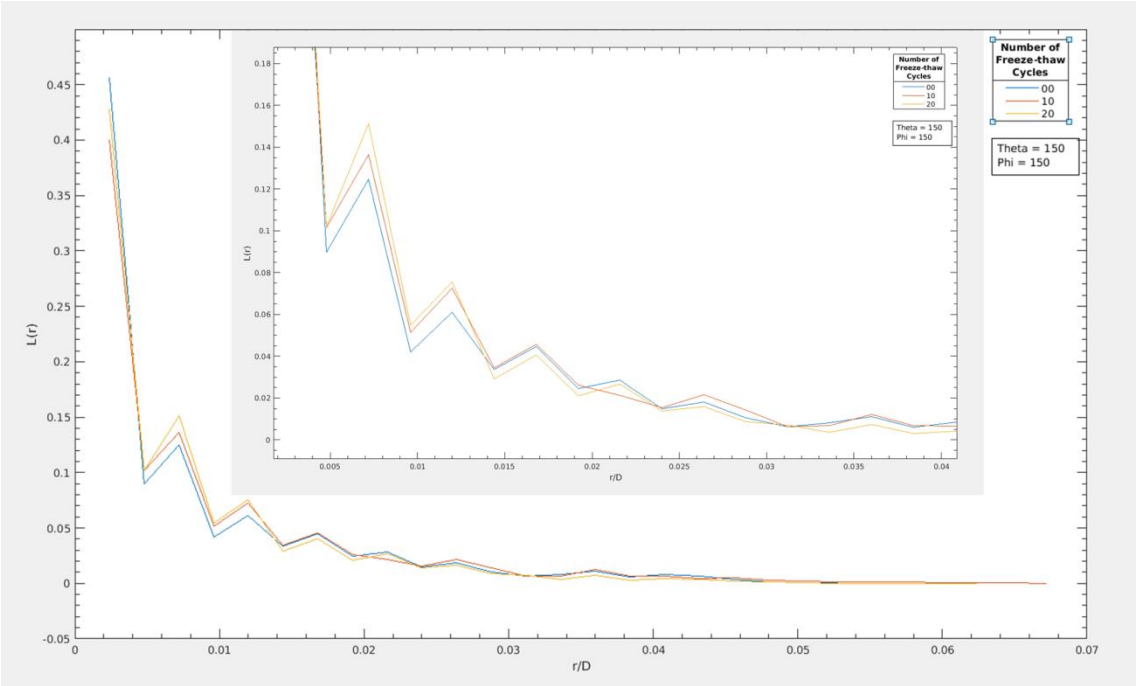
L(r)
r/D
Number of Freeze-thaw Cycles
00
10
20
Theta = 150
Phi = 150

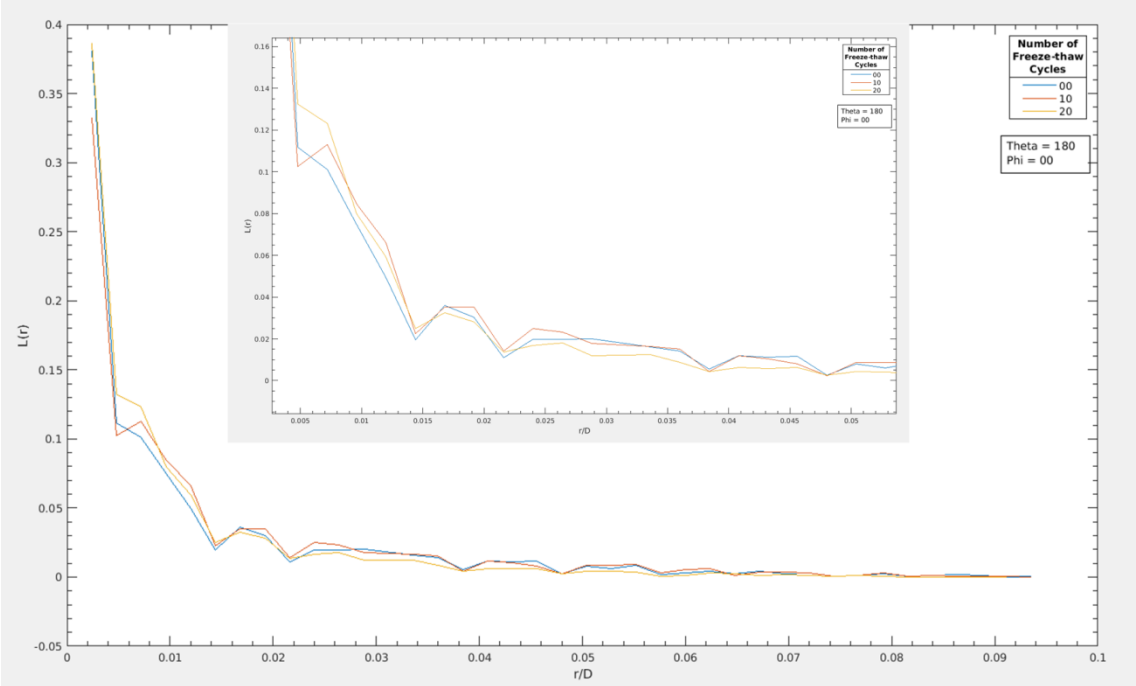
L(r)
r/D
Number of Freeze-thaw Cycles
00
10
20
Theta = 180
Phi = 00

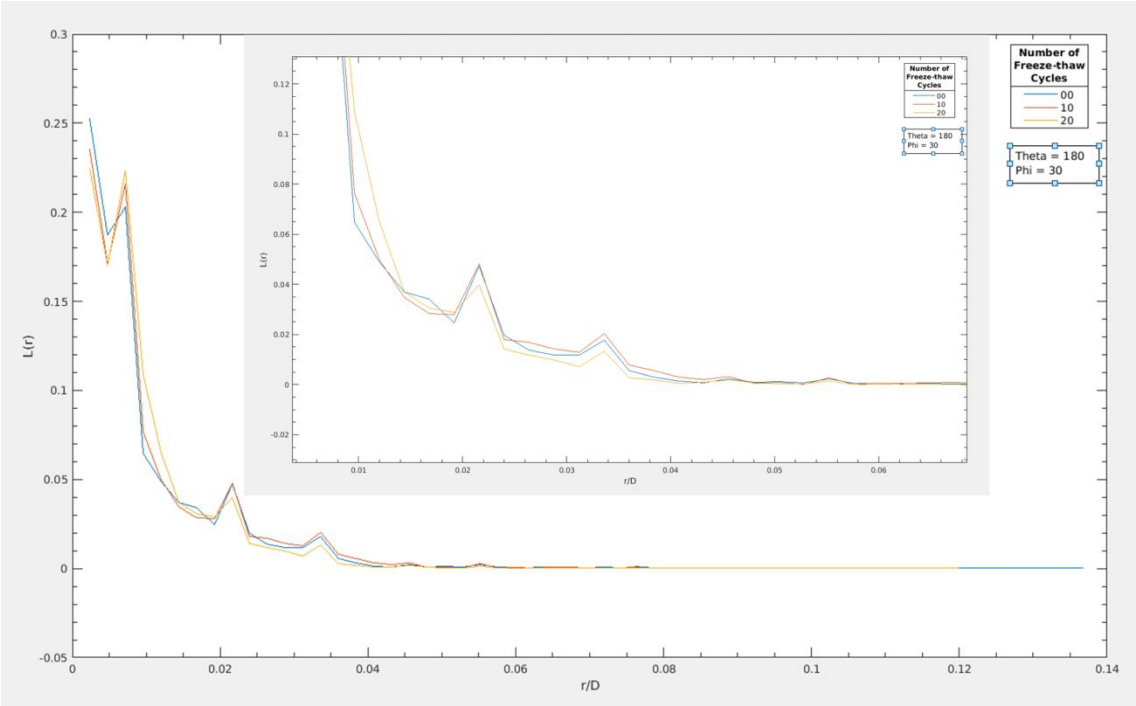
Number of Freeze-thaw Cycles
00
10
20
Theta = 180
Phi = 30
L(r)
r/D

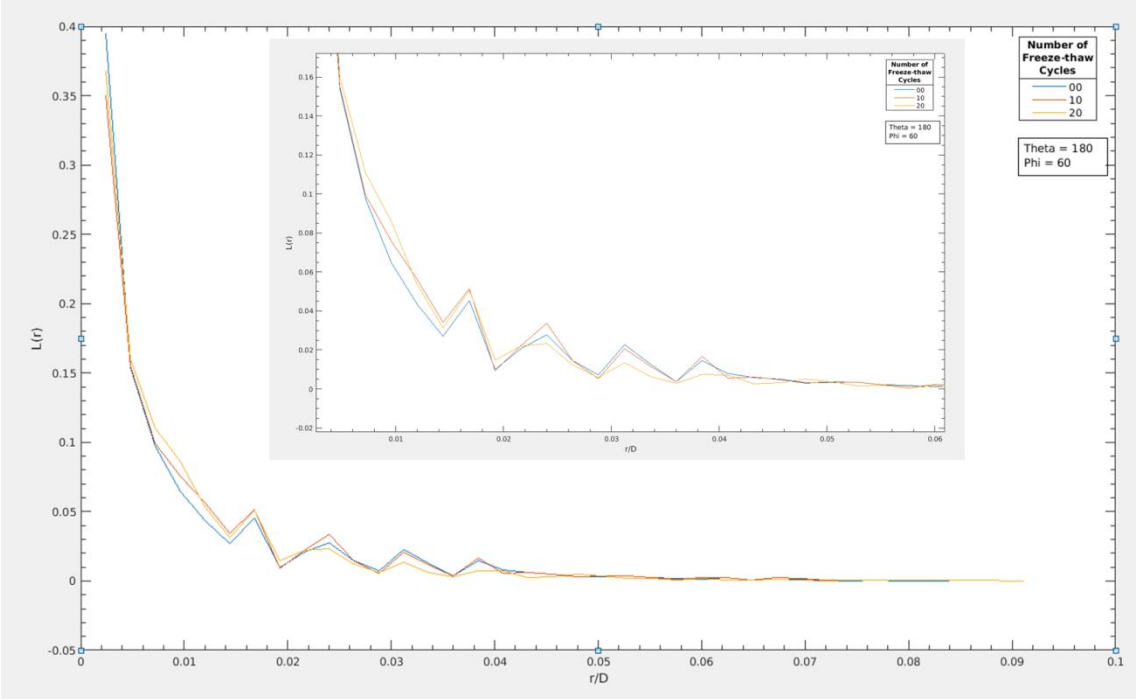
Number of Freeze-thaw Cycles
00
10
20
Theta = 180
Phi = 60
L(r)
r/D

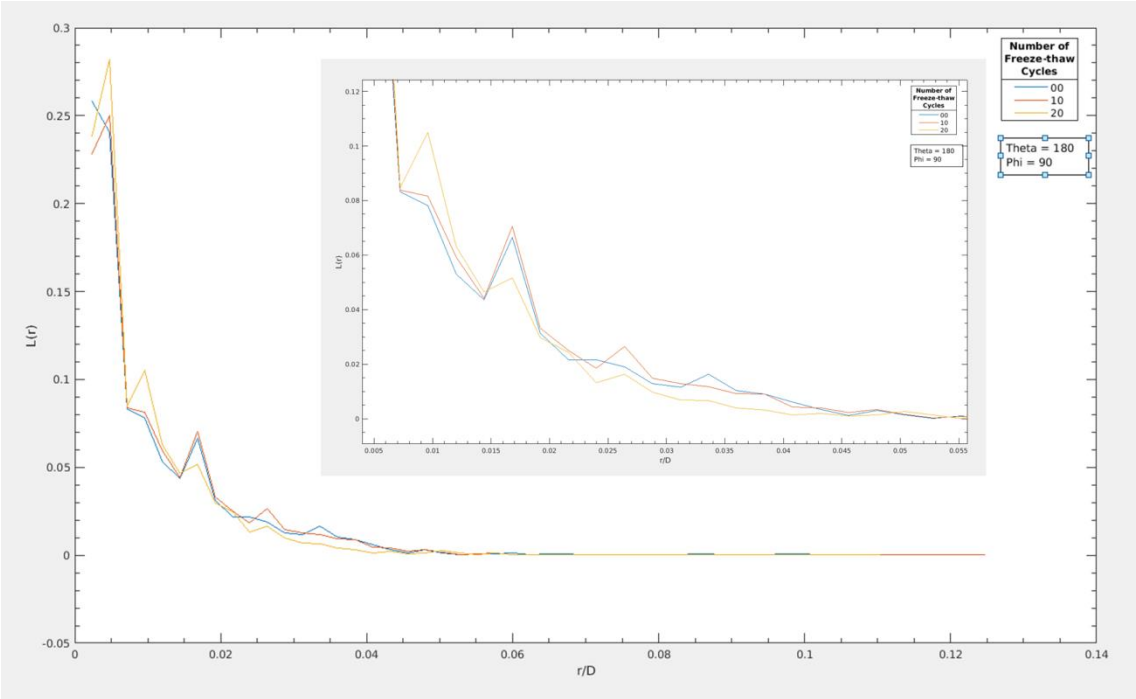
Number of Freeze-thaw Cycles
00
10
20
Theta = 180
Phi = 90
L(r)
r/D

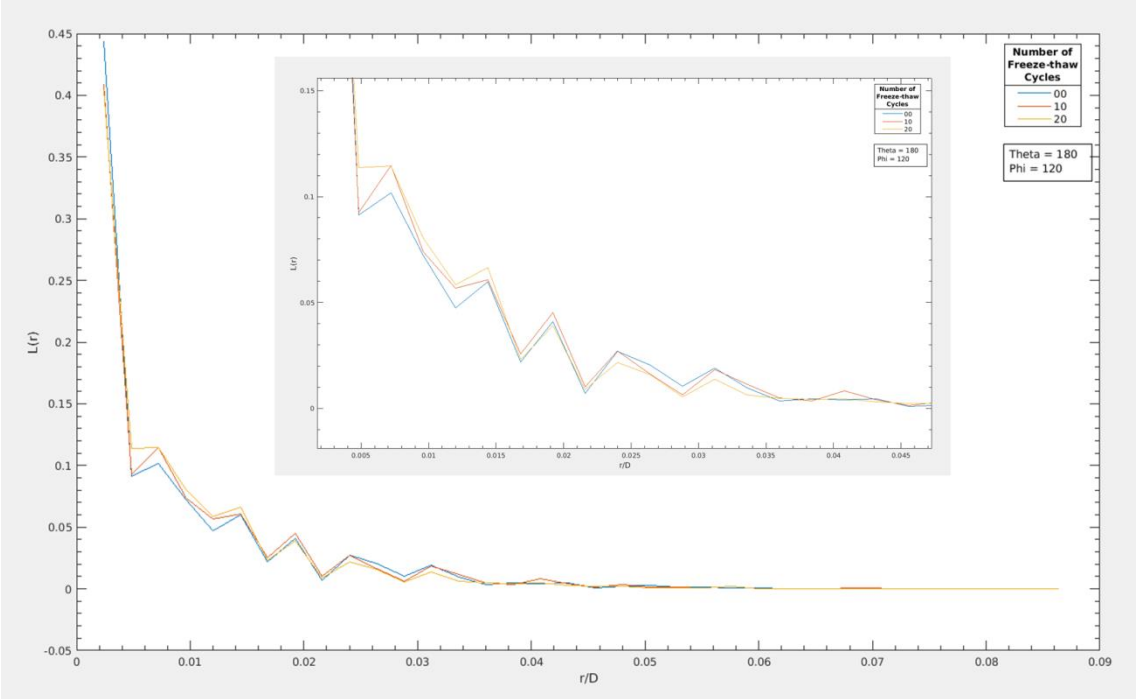
Number of Freeze-thaw Cycles
00
10
20
Theta = 180
Phi = 120
L(r)
r/D

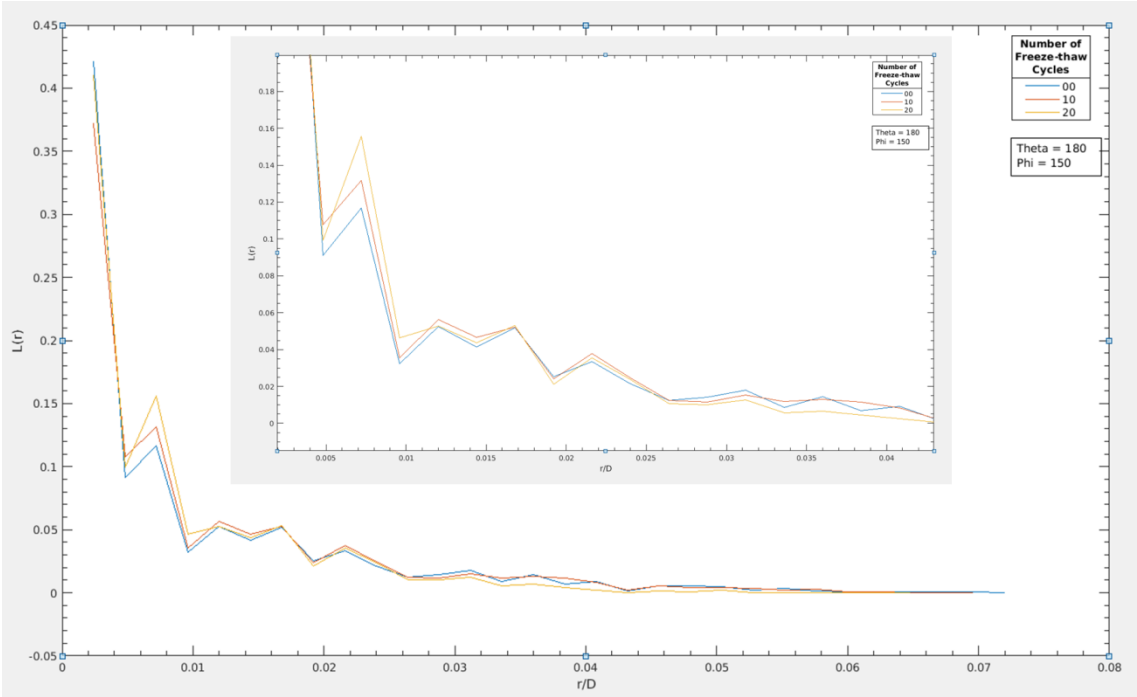
Number of Freeze-thaw Cycles
00
10
20
Theta = 180
Phi = 150
L(r)
r/D

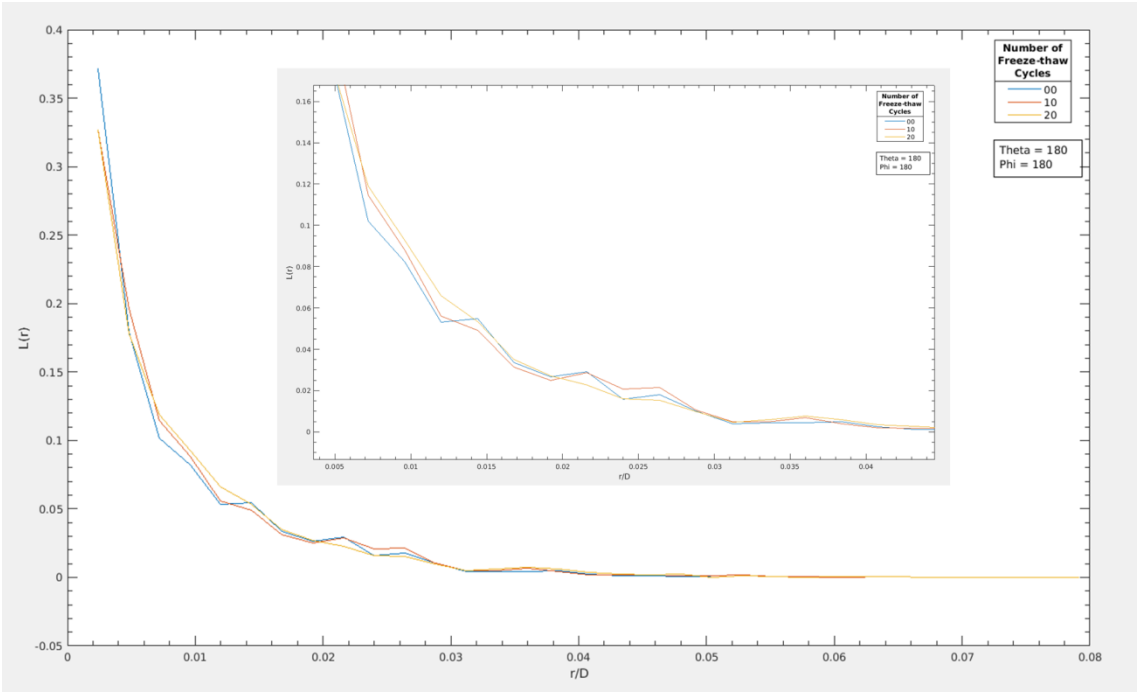
Number of Freeze-thaw Cycles
00
10
20
Theta = 180
Phi = 180
L(r)
r/D

C. Acoustic emission waveform parameters

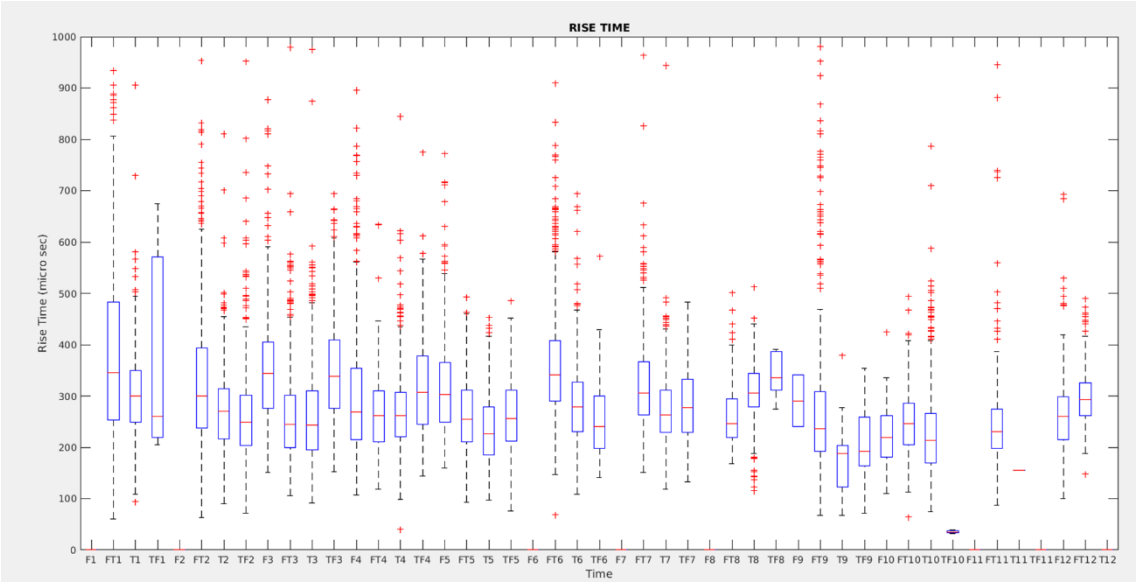

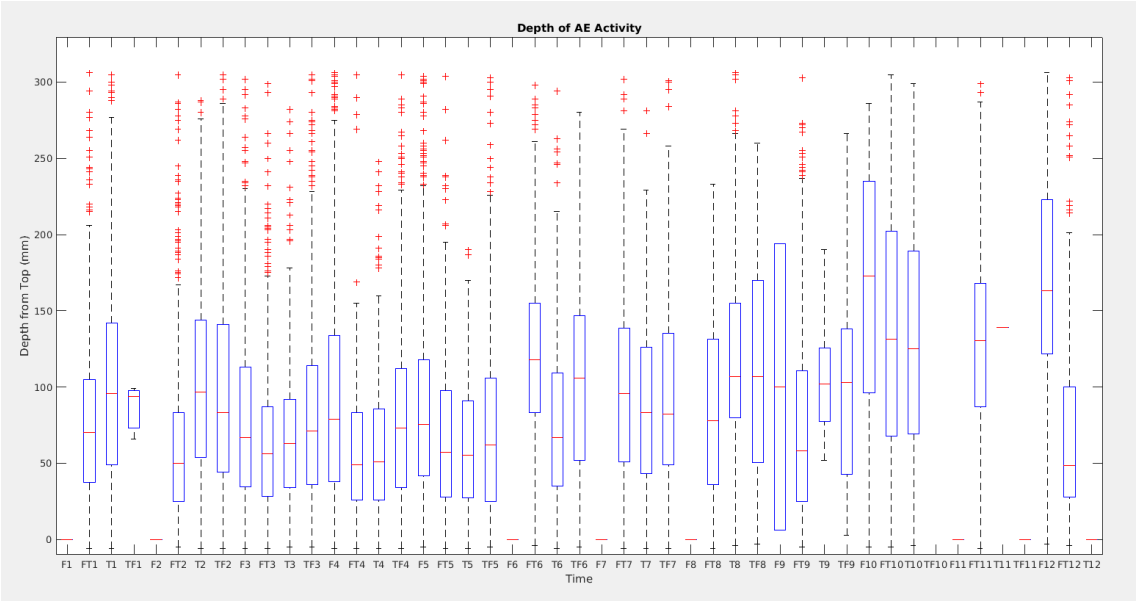

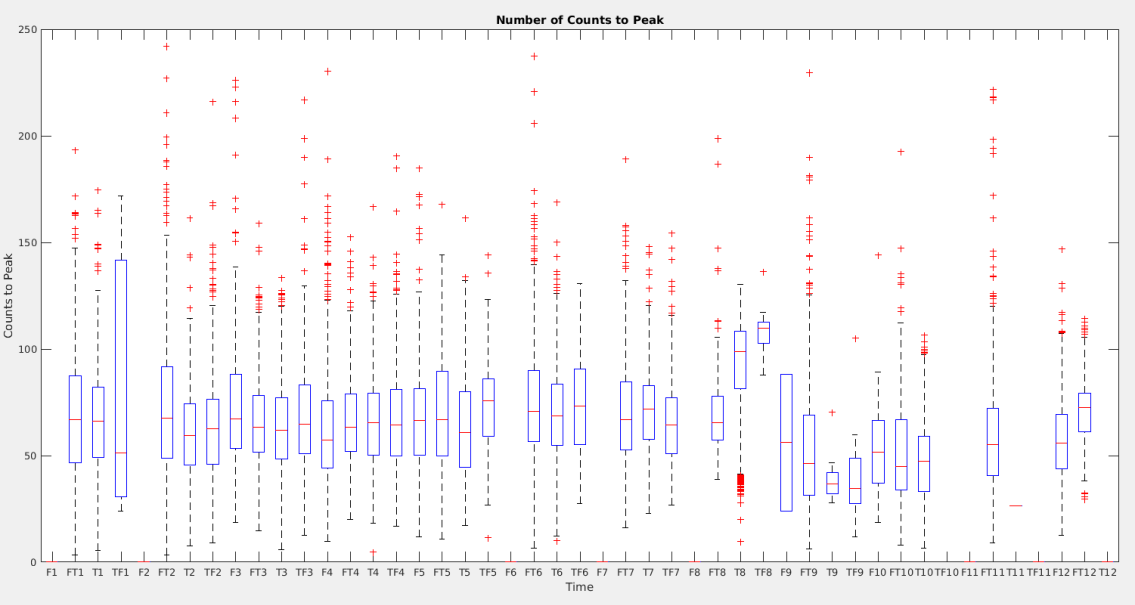
Number of Counts to Peak
Counts to Peak
Time
0
50
100
150
200
250
F1 FT1 T1 TF1 F2 FT2 T2 TF2 F3 FT3 T3 TF3 F4 FT4 T4 TF4 F5 FT5 T5 TF5 F6 FT6 T6 TF6 F7 FT7 T7 TF7 F8 FT8 T8 TF8 F9 FT9 T9 TF9 F10 FT10 T10 TF10 F11 FT11 T11 TF11 F12 FT12 T12

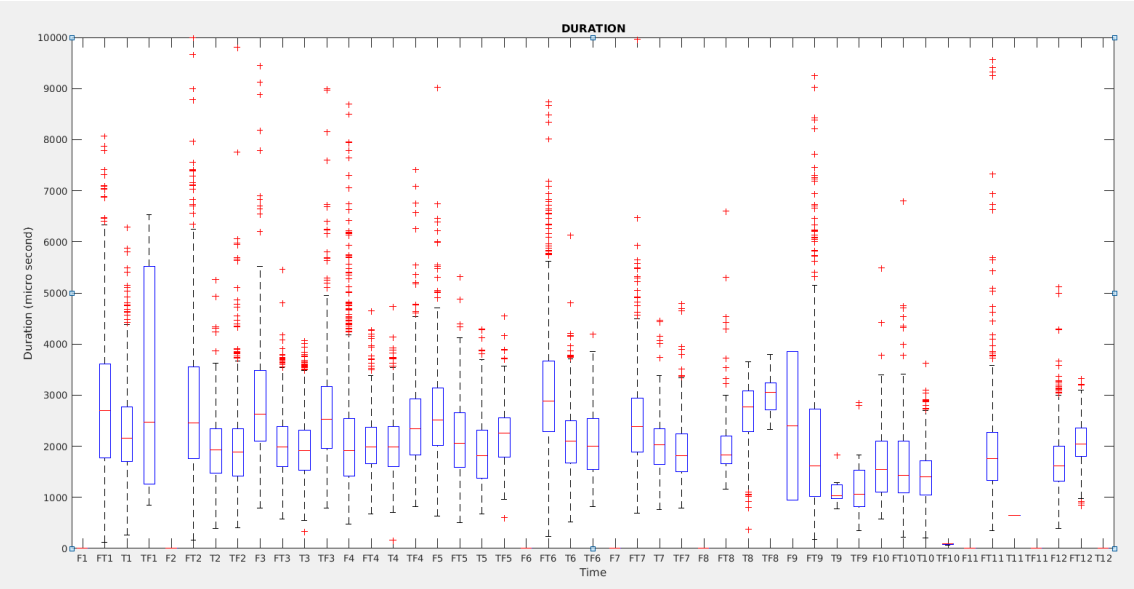
DURATION
Duration (micro second)
Time
0
1000
2000
3000
4000
5000
6000
7000
8000
9000
10000
F1 FT1 T1 TF1 F2 FT2 T2 TF2 F3 FT3 T3 TF3 F4 FT4 T4 TF4 F5 FT5 T5 TF5 F6 FT6 T6 TF6 F7 FT7 T7 TF7 F8 FT8 T8 TF8 F9 FT9 T9 TF9 F10 FT10 T10 TF10 F11 FT11 T11 TF11 F12 FT12 T12

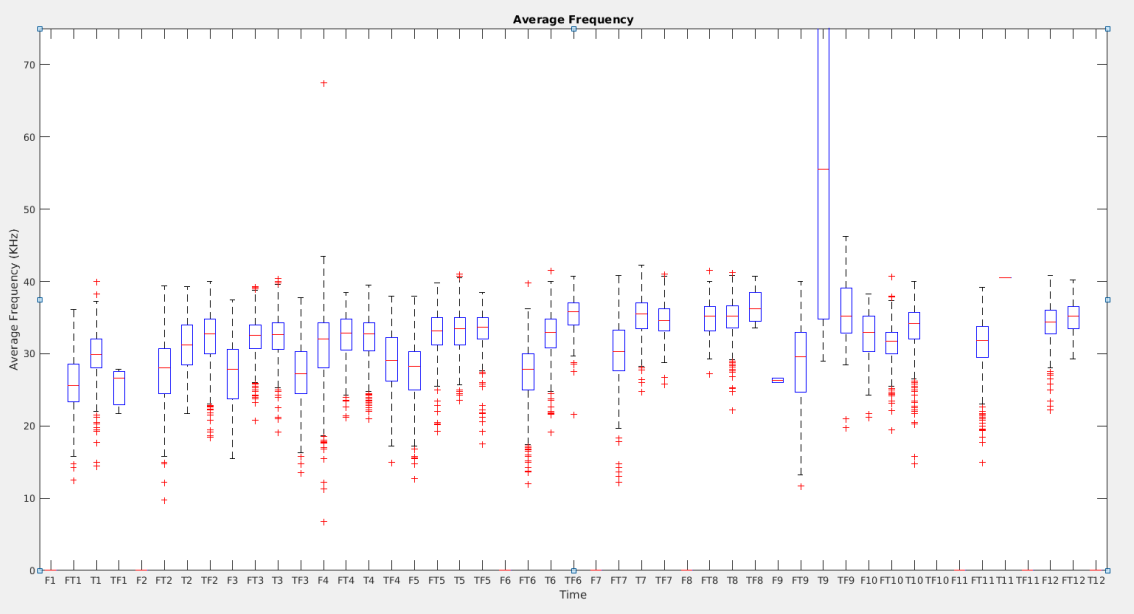
Average Frequency
Average Frequency (KHz)
Time

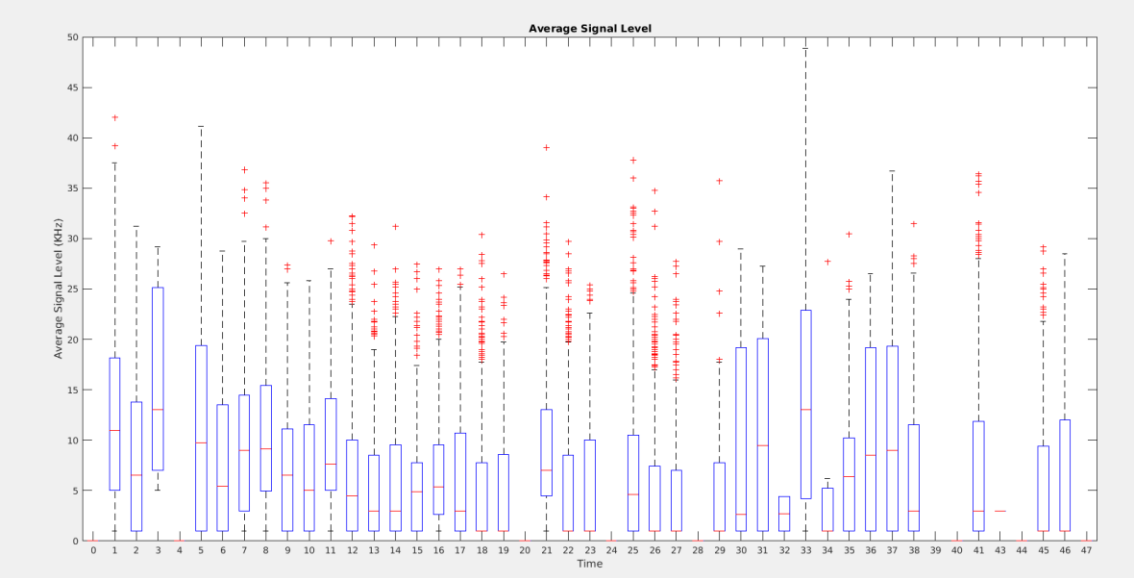
Average Signal Level
Average Signal Level (KHz)
Time

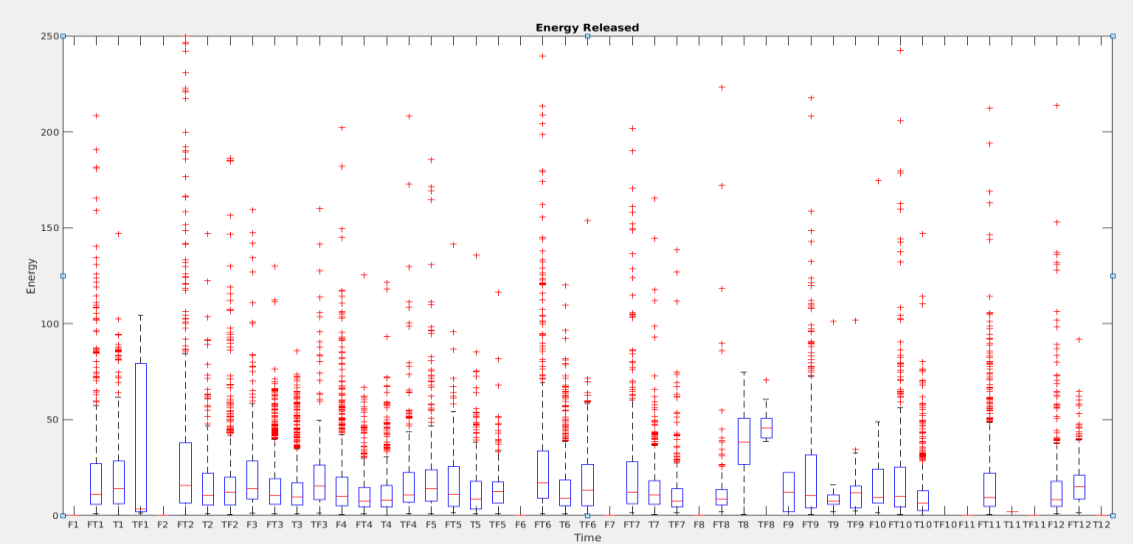
Energy Released
Energy
Time